

THEORETICAL STUDY OF WATER OXIDATION AND REDUCTION MECHANISMS BY AMINOPYRIDINE FIRST ROW TRANSITION METAL CATALYSTS

Ferran Acuña Pares

Per citar o enllaçar aquest document:

Para citar o enlazar este documento:

Use this url to cite or link to this publication:

<http://hdl.handle.net/10803/398411>

ADVERTIMENT. L'accés als continguts d'aquesta tesi doctoral i la seva utilització ha de respectar els drets de la persona autora. Pot ser utilitzada per a consulta o estudi personal, així com en activitats o materials d'investigació i docència en els termes establerts a l'art. 32 del Text Refós de la Llei de Propietat Intel·lectual (RDL 1/1996). Per altres utilitzacions es requereix l'autorització prèvia i expressa de la persona autora. En qualsevol cas, en la utilització dels seus continguts caldrà indicar de forma clara el nom i cognoms de la persona autora i el títol de la tesi doctoral. No s'autoritza la seva reproducció o altres formes d'explotació efectuades amb finalitats de lucre ni la seva comunicació pública des d'un lloc aliè al servei TDX. Tampoc s'autoritza la presentació del seu contingut en una finestra o marc aliè a TDX (framing). Aquesta reserva de drets afecta tant als continguts de la tesi com als seus resums i índexs.

ADVERTENCIA. El acceso a los contenidos de esta tesis doctoral y su utilización debe respetar los derechos de la persona autora. Puede ser utilizada para consulta o estudio personal, así como en actividades o materiales de investigación y docencia en los términos establecidos en el art. 32 del Texto Refundido de la Ley de Propiedad Intelectual (RDL 1/1996). Para otros usos se requiere la autorización previa y expresa de la persona autora. En cualquier caso, en la utilización de sus contenidos se deberá indicar de forma clara el nombre y apellidos de la persona autora y el título de la tesis doctoral. No se autoriza su reproducción u otras formas de explotación efectuadas con fines lucrativos ni su comunicación pública desde un sitio ajeno al servicio TDR. Tampoco se autoriza la presentación de su contenido en una ventana o marco ajeno a TDR (framing). Esta reserva de derechos afecta tanto al contenido de la tesis como a sus resúmenes e índices.

WARNING. Access to the contents of this doctoral thesis and its use must respect the rights of the author. It can be used for reference or private study, as well as research and learning activities or materials in the terms established by the 32nd article of the Spanish Consolidated Copyright Act (RDL 1/1996). Express and previous authorization of the author is required for any other uses. In any case, when using its content, full name of the author and title of the thesis must be clearly indicated. Reproduction or other forms of for profit use or public communication from outside TDX service is not allowed. Presentation of its content in a window or frame external to TDX (framing) is not authorized either. These rights affect both the content of the thesis and its abstracts and indexes.



DOCTORAL THESIS

**Theoretical Study of Water Oxidation and Reduction Mechanisms by
Aminopyridine First Row Transition Metal Catalysts**

Ferran Acuña Pares

2016

Doctoral programme in Chemistry

Supervised by: Dr. Julio Lloret Fillol and Dr. Josep M. Luis Luis

Tutor: Dr. Josep M. Luis Luis

Presented in partial fulfilment of the requirements for a doctoral degree from
the University of Girona



Dr. Julio Lloret Fillol and Dr. Josep M. Luis Luis, of Institut Català d'Investigació Química (ICIQ) and Universitat de Girona, respectively,

WE DECLARE:

That the thesis entitled Theoretical study of water oxidation and reduction mechanisms by aminopyridine first row transition metal catalysts, presented by Ferran Acuña Pares to obtain the doctoral degree, has been completed under our supervision and meets the requirements to opt for an International Doctorate.

For all the intents and purposes, We hereby sign this document.

Dr. Julio Lloret Fillol

Dr. Josep M. Luis Luis

Girona, June 21th, 2016

Dedicated to my family

If one way be better than another, that you may be sure is nature's way.

Aristotle

Full list of publications

List of publications resulting from this thesis

- 1) Codolà, Z.; Garcia-Bosch, I.; Acuña-Parés, F.; Prat, I.; Luis, J.M.; Costas, M.; Lloret-Fillol, J. Electronic Effects on Single-Site Iron Catalysts for Water Oxidation. *Chem. Eur. J.* **2013**, *19*, 8042.
- 2) Acuña-Parés, F.; Codolà, Z.; Costas, M.; Luis, J.M.; Lloret-Fillol, J. Unravelling the mechanism of water oxidation catalysed by nonheme iron complexes. *Chem. Eur. J.* **2014**, *20*, 5696.
- 3) Acuña-Parés, F.; Costas, M.; Luis, J.M.; Lloret-Fillol, J. Theoretical Study of the Water Oxidation Mechanism with Non-heme Fe(Pytacn) Iron Complexes. Evidence That the FeIV(O)(Pytacn) Species Cannot React with the Water Molecule To Form the O-O Bond. *Inorg. Chem.* **2014**, *53*, 5474.
- 4) Call, A.; Codolà, Z.; Acuña-Parés, F.; Lloret-Fillol, J. Photo- and electro-catalytic H₂ production by new first-row transition metal complexes based on an aminopyridine pentadentate ligand. *Chem Eur J.* **2014**, *20*, 6171.
- 5) Hassanpour, A.; Acuña-Parés, F.; Luis, J.M.; Cussó, O.; Morales-delaRosa, S.; Campos Martín, J.M.; Fierro, J.L.G.; Costas, M.; Lloret-Fillol, J.; Mas Balleste, R. H₂ Oxidation versus organic substrate oxidation in non-heme iron mediated reactions with H₂O₂. *Chem. Commun.* **2015**, *51*, 14992.
- 6) Codolà, Z.; Acuña-Parés, F.; Casadevall, C.; Luis, J.M.; Costas, M.; Lloret-Fillol, J. A new N-pentadentate iron (II) complex as an active homogeneous catalyst for water oxidation. In manuscript.
- 7) Acuña-Parés, F.; Luis, J.M.; Lloret-Fillol, J.; Christopher, C. Iron-cerium adducts as intermediates in the water oxidation reaction. In manuscript.
- 8) Acuña-Parés, F.; Luis, J.M.; Lloret-Fillol, J. Computational study of electrochemical hydrogen production mechanisms by cobalt catalysts based on an aminopyridine ligand. In manuscript.
- 9) Acuña-Parés, F.; Luis, J.M.; Lloret-Fillol, J. Computational study of photochemical hydrogen production mechanisms by cobalt catalysts based on an aminopyridine ligand. In manuscript.

My contribution to the publications discussed: As the first author, I carried out the calculations and the writing of the draft for articles 2, 3, 7, 8 and 9. As a co-author, I carried out the theoretical study, discussion and revision of papers 1, 4, 5 and 6.

List of publications not included in this thesis

- 10) Rovira, M.; Font, M.; Acuña-Parés F.; Parella, T.; Luis, J.M.; Lloret-Fillol, J.; Ribas, X. Aryl-copper(III)-acetylides as key intermediates in Csp²-Csp model couplings under mild conditions. *Chem. Eur. J.* **2014**, *20*, 10005.

- 11) Font, M.; Acuña-Parés, F.; Parella, T.; Serra, J.; Luis, J.M.; Lloret-Fillol, J.; Miquel Costas, M.; Ribas, X. Direct observation of two-electron Ag(I)/Ag(III) redox cycles in coupling catalysis. *Nat. Commun.*, **2014**, *5*, 4373.
- 12) Corona, T.; Pfaff, F.F.; Acuña-Parés, F.; Draksharapu, A.; Whiteoak, C.J.; Martin-Diaconescu, V.; Lloret-Fillol, J.; Browne, W.R.; Ray, K.; Company, A. Reactivity of a Nickel(II) Bis(amidate) Complex with meta-Chloroperbenzoic Acid: Formation of a Potent Oxidizing Species. *Chem. Eur. J.* **2015**, *21*, 15029.
- 13) Serra, J.; Whiteoak, C.J. ; Acuña-Parés, F.; Font, M.; Luis, Josep M.; Lloret-Fillol, J.; Ribas, X. Oxidant-Free Au(I)-Catalyzed Halide Exchange and Csp²-O Bond Forming Reactions. *J. Am. Chem. Soc.* **2015**, *137*, 13389.
- 14) Corona, T.; Draksharapu, A.; Padamati, S.K.; Gamba, I; Martin-Diaconescu, V.; Acuña-Parés, F.; Browne, W.R.; Company, A. Spectroscopy and reactivity studies on a well-defined high-valent Ni-OCl species. *J. Am. Chem. Soc.* **2016**, Submitted.
- 15) Rovira, M.; Soler, M.; Güell, I.; Wang, M.-Z.; Acuña-Parés, F.; Luis, J.M.; Gomez, L.; Andris, E.; Roithova, J.; Ribas, X. A practical guide in Ullmann-type C-O and C-N couplings: the quest for orthogonal discrimination among functional groups. In manuscript.
- 16) Call, A.; Acuña-Parés, F.; Lloret-Fillol, J. Cobalt-Catalyzed Light-Driven Reduction of Ketones and Aldehydes using Water and Et₃N as Hydride Source. In manuscript.

LIST OF ABBREVIATIONS

4Fe4S	Iron-sulfur cluster
55'bc bpy	5,5'-bis(carbamoyl)-2,2'-bipyridine
bdt	bis(dithiolene)
bpm	2,2'-bypyrimidine
BPMAN	2,7-[bis(2-pyridylmethyl)aminomethyl]-1,8-naphthyridine
bpp	3,5-bis(2-pyridyl)pyrazolate
bpy	2,2'-bipyridine
bpydc	Dibenzoate-substituted 2,2'-bipyridine
bpyOH	6,6'-dihydroxy-2,2'-bipyridine
bpz	2,2'-bipyrazine
BQEN	N,N'-dimethyl-N,N'-bis(8-quinolyl)ethane-1,2-diamine
bztpen	N-benzyl-N,N',N'-tris(pyridine-2-ylmethyl)ethylenediamine
CAN	Cerium Ammonium Nitrate
CASPT2	Complete-Active-Space second-order Perturbation Theory
CASSCF	Complete Active Space SCF method
cbc	4,11-dimethyl-1,4,8,11-tetraazabicyclo[6.6.2]hexadecane
CC	Coupled Cluster
CI	Configuration Interaction
Cor-CO ₂ H	β -octafluoro hangman corrole
Cp*	1,2,3,4,5-pentamethylcyclopentadiene
CV	Cyclic Voltammetry
Cyclam	1,4,8,11-tetraazacyclotetradecane
DC	Direct Coupling
depp	1,2-bis(diethylphosphino)propane
DFT	Density Functional Theory
dmbpy	4,4'-dimethyl-2,2'-bipyridine
dmgBF ₂	difluoroboryldimethylglyoxime
(DOH)(DOH)pn	N ² ,N ² '-propanediylbis(2,3-butanedione-2-imine-3-oxime)
DLS	Time-dependent Diffraction Light Scattering
DPV	Differential pulse voltammogram
EDTA	Ethylenediaminetetraacetic Acid
EPR	Electron Paramagnetic Resonance
ESI-MS	Electrospray Ionization Mass Spectrometry
FDR	Ferredoxin-NADP ⁺ reductase
H ₂ bda	2,2'-bipyridine-6,6'-dicarboxylic acid
HF	Hartree-Fock method
Hmcbpen	N-methyl-N'-carboxymethyl-N,N'-bis(2-pyridylmethyl)ethane-1,2-diamine
HRMS	High Resolution Mass Spectrometry
HOMO	Highest Occupied Molecular Orbital
isoq	isoquinoline
IRC	Intrinsic Reaction Coordinate
KIE	Kinetic Isotope Effect
LUMO	Lowest Unoccupied Molecular Orbital
MALDI-TOF-MS	Matrix-Assisted Laser Desorption/Ionization-Time-Of-Flight Mass Spectrometry
Mebimpy	2,6-bis(1-methylbenzimidazol-2-yl)pyridine
MeCN	Acetonitrile
Me ₂ NHC	N-dimethylimidazolin-2-ylidene
Me ₂ oxpn	N,N'-bis(2,2'-dimethyl-3-aminopropyl)oxamido

mep	N,N'-bis(2-pyridylmethyl)-N,N'-dimethyl ethane-1,2-diamine
mcp	N,N'-bis(2-pyridylmethyl)- <i>trans</i> -1,2-diaminocyclohexane
MO	Molecular Orbital
MOF	Meta-Organic Framework
MPn	Møller-Plesset Perturbation theory
MCSCF	Multi-Configuration Self-Consistent Field approach
MVio ²⁺	Methylviologen
NADP ⁺ /NADPH	Nicotinamide Adenine Dinucleotide Phosphate
NHE	Normal Hydrogen Electrode
NHC	3-methyl-1-(1-phenylethyl)-imidazole-2-ylidene
NMR	Nuclear Magnetic Resonance
OEC	Oxygen Evolving Complex
opba	<i>o</i> -phenylenebis(oxamate)
Oxone	potassium peroxydisulfate
oxpn	N,N'-bis(3-aminopropyl)oxamido
P680	Electron donor in PSII
P700	Electron donor in PSI
Pbn	2,2'-[4-(<i>tert</i> -butyl)pyridine-2,6-diyl]bis(1,8-naphthyridine)
PC	Plastoncyanin
PCET	Proton-coupled electron transfer
phpy	2-phenylpyridine
pic	4-picoline
PNP	Et ₂ PCH ₂ NMeCH ₂ PEt ₂
pp	2-pyrazolylpyridine
ppy	phenylpyridine
PQ	plastoquinone
Por	<i>meso</i> -tetrakis(4-N-methylpyridyl)porphyrin
PR	Proton Reduction
PRC	Proton Reduction Catalyst
PSI	Photosystem I
PSII	Photosystem II
PY5	2,6-(bis(bis-2-pyridyl)methoxy-ethane)-pyridine
PY5Me ₂	2,6-bis(1,1-bis(2-pyridyl)ethyl)-pyridine
Py ₂ CH-tacn	N-(dipyridin-2-yl)methyl)-N',N''-dimethyl-1,4,7-triazacyclononane
pylac	2-(20-pyridyl)-2-propanolate
pyr	pyridine
Pytacn	1-(2'-pyridylmethyl)-4,7-dimethyl-1,4,7-triazacyclononane
Py ₂ ^{Ts} tacn	1,4-di(picolyl)-7-(<i>p</i> -toluenesulfonyl)-1,4,7-triazacyclononane
(pz) ₃ BH	tris(pyrazol-1-yl)-borate
qpd	quinoxaline-pyran-fused dithiolene
qpy	2,2':6',2'':6'',2'''-quaterpyridine
RDS	Rate Determining Step
S ₀₋₄	Redox states involved in the Kok cycle
SHE	Standard Hydrogen Electrode
TAML	Tetra-amido macrocyclic ligand
TBHP	<i>tert</i> -butyl hydroperoxide
<i>t</i> -BuNC	<i>t</i> -Butyl isocyanide
TEA	Triethylamine
terpy	2,2':6',2''-terpyridine
TDTS	TOF Determining Transition State

TGG	Triglycylglycine
TMAP	<i>meso</i> -tetrakis(<i>N,N,N</i> -trimethylanilinium-4-yl)porphine
tmc	<i>N,N',N'',N'''</i> -tetramethylcyclam
TMPyP	<i>meso</i> -tetrakis(<i>N</i> -methylpyridinium-4-yl)porphine
TOF	Turnover frequency
TON	Turnover number
TPA	tris-(2-methylpyridil)amine
tpfc	5,10,15-tris-(pentafluorophenyl)corrole
TPyP	<i>meso</i> -tetrapyril-4-ylporphine
UV-Vis	Ultraviolet-Visible Spectroscopy
WNA	Water Nucleophilic Attack
WO	Water Oxidation
WOC	Water Oxidation Catalyst
WR	Water Reduction
WRC	Water Reduction Catalyst
Yz	Tyrosine residue

LIST OF FIGURES

- Figure 1:** Above, schematic representation of the photosynthetic process, with the light driven redox steps giving rise to O₂ evolution and NADPH formation. The P₆₈₀ and P₇₀₀ are chlorophyll photosensitizers, OEC = oxygen evolving complex, Ant = antennas, Ph = pheophytin, PQ = plastoquinone, Cyt-b₆f = Cytochrome-b₆f, PC = plastocyanin, FDR = ferredoxin-NADP⁺ reductase enzyme and NADP⁺ = nicotinamide adenine dinucleotide phosphate. Below, structure of oxygen-evolving complex (OEC), a Mn₄Ca cluster where the metal atoms are oxo bridged. The structure has been built from crystallographic data reported on ref. 12.....12
- Figure 2:** On the left, Kok cycle for the water oxidation mechanism in OEC cluster. On the right, some proposed O-O bond formation mechanisms at the S₄ state of the Mn₄CaO₅ cluster in the PSII.....13
- Figure 3:** Qualitative frontier MO splitting diagrams for an octahedral metal complex (left) and a metal-oxo residing in a tetragonal field (right). A d⁴ electron counting is shown.....16
- Figure 4:** The Meyer's blue dimer (**1**, left) and the Llobet's (**2**, right) Ru catalysts for water oxidation. TON and TOF values are shown in parentheses, respectively.....17
- Figure 5:** DFT proposed catalytic cycle for water oxidation in blue dimer (bottom) and Llobet (top) ruthenium catalysts.....18
- Figure 6:** Thummel's ruthenium(II) complexes for water oxidation. TON and TOF values are shown in parentheses, respectively.....19
- Figure 7:** Molecular structure of complexes [Ru^{II}(terpy)(bpm)(OH₂)₂]²⁺ (**6**), [Ru^{II}(terpy)(bpz)(OH₂)₂]²⁺ (**7**) and [Ru^{II}(Mebimpy)(bpy)(OH₂)₂]²⁺ (**8**). TON and TOF values are shown in parentheses, respectively.....20
- Figure 8:** a) Proposed catalytic cycle for water oxidation by complexes **6** and **7**. b) Schematic representation of the APT mechanism.....21
- Figure 9:** Molecular structure of complexes *cis*-[Ru^{II}(bpy)(OH₂)₂]²⁺ (**8**) and *trans*-[Ru^{II}(bpy)(OH₂)₂]²⁺ (**9**) and DFT computed WNA and DC mechanisms for O-O bond formation by complex **8**. TON value is shown in parentheses. Gibbs energies are in kcal·mol⁻¹.....22
- Figure 10:** Molecular structure of complexes [Ru^{II}(bda)(isoq)₂] (**10**) and [Ru^{II}(bda)(isoq)₂] (**11**) and illustration π -stacking interactions in the Ru^{IV}-O-O-Ru^{IV} dimer. TON and TOF values are shown in parentheses, respectively.....23
- Figure 11:** On the left, reaction mechanism postulated for iridium-catalyzed water oxidation. On the right, Bernhard [Ir^{III}(phpy)₂(OH₂)₂]⁺ catalysts for WO. TON and TOF values are shown in parentheses, respectively.....24
- Figure 12:** Postulated mechanisms for O-O bond formation in Bernhard water oxidation iridium catalyst [Ir(phpy)(O)(X)]⁺ at acidic pH (top), intermediate pH (middle) and basic pH (bottom).....25
- Figure 13:** Postulated mechanism for O-O bond formation in Crabtree water oxidation iridium catalyst.....26
- Figure 14:** On the left, molecular structure of [Cp*Ir^{III}(Me₂NHC)(OH)₂] (**13**). On the right, computed transition state for the O-O bond formation catalyzed by [Cp*Ir^{IV}(Me₂NHC)(O)(IO₃)]⁺ active species. TOF values are shown in parentheses.....26
- Figure 15:** Molecular structure of [Cp*Ir^{III}(NHC)Cl₂] (**14**). TON and TOF values are given in parentheses, respectively.....27
- Figure 16:** Molecular structures of iridium complexes [Cp*Ir^{III}(pp)Cl] (**15**) and [Cp*₂Ir₂(bpp)Cl₂]Cl (**16**).....27

Figure 17: Competition between Cp* degradation and O ₂ generation mechanisms in [Cp*IrL] complexes.....	28
Figure 18: a) Representation of the possible substructures present in the blue layer. b) Schematic generation of a Ir ^{IV} dimer from [Cp*Ir(pylac)(Cl)] (17).....	29
Figure 19: Water oxidation catalytic cycle proposed by means of DFT(B3LYP*-D ₃) calculations for [(bpydc)Ir ^{III} (H ₂ O) ₂ (CH ₃ COO)Cl] ⁺ . Gibbs energies are in kcal·mol ⁻¹ . TON and TOF values are shown in parentheses, respectively.....	30
Figure 20: Molecular structures of the three [Mn(TPP)] dimers. TON and TOF values for complex 21 are shown in parentheses, respectively.....	31
Figure 21: On the left, Mn-dimer complex [(terpy)(H ₂ O)Mn ^{IV} (μ-O) ₂ Mn ^{III} (H ₂ O)(terpy)] ³⁺ (22) with water oxidation catalytic activity. TON and TOF values are shown in parentheses, respectively. On the right, computational model used in ref. 53 for study the O-O bond formation step.....	32
Figure 22: Proposed O-O bond formation mechanism performed by 22.....	32
Figure 23: OCl ⁻ driven water oxidation mechanism proposed by complex 22 on the basis of DFT(B3LYP) calculations. The Gibbs energy barrier is in kcal·mol ⁻¹	33
Figure 24: Molecular structure of [(mcbpen)Mn ₂ ^{II} (H ₂ O) ₂ (mcbpen)] ²⁺ (23). TON value is shown in parentheses.....	34
Figure 25: DFT proposed water oxidation mechanism by complex 23.....	35
Figure 26: Molecular structure of cationic monomeric and dimeric manganese corrole complexes (24-25)....	36
Figure 27: Fe ^{III} -TAML catalyst family. The most active catalyst reported has R ₁ = R ₂ = Cl, R ₃ = R ₄ = F and X = H ₂ O (complex 26).....	37
Figure 28: Catalytic water oxidation cycle postulated for the most active reported Fe ^{III} -TAML complex 26. Gibbs energy barriers are in kcal·mol ⁻¹ . Oxidation potentials are calculated respect to the NHE.....	38
Figure 29: Family of catalytic water oxidation iron complexes. OTf stands for CF ₃ SO ₃ ⁻ anion.....	39
Figure 30: [Fe(OTf) ₂ (^{4-E} Pytacn)] substituted iron water oxidation catalyst.....	40
Figure 31: Proposed mechanism for water oxidation by non-heme iron complexes based on tetradentate ligands (L ^{N4}).....	40
Figure 32: Structure of mononuclear iron complexes based on <i>N</i> -tetradentate ligands. TON and TOF values are shown in parentheses, respectively.....	41
Figure 33: Proposed pathways for 29-catalyzed water oxidation with CAN or NaIO ₄ . Labels “Ox” and “Red” mean the sacrificial oxidant and its reduced form, respectively. Gibbs energy barrier is in kcal·mol ⁻¹	42
Figure 34: Structure of binuclear iron complexes. TON and TOF values are shown in parentheses, respectively.....	42
Figure 35: Molecular structure of [Co ^{II} (PY5)(OH ₂) ₂] ²⁺ (32) and DFT proposed catalytic cycle for water oxidation. TOF value is shown in parentheses. Oxidation potentials are calculated respect to the NHE at pH 9.2.....	44

Figure 36: Molecular structure of $[(\text{Cor-CO}_2\text{H})\text{Co}^{\text{III}}(\text{OH}_2)]^{3+}$ (33) and DFT proposed catalytic cycle for water oxidation. TOF value is shown in parentheses. Oxidation potentials are calculated respect to the NHE.....	45
Figure 37: Molecular structure of $[\text{Co}(\text{tpfc})(\text{pyr})_2]$ (34). TON and TOF values are given in parentheses.....	46
Figure 38: Molecular structure of $[\text{Co}(\text{terpy})_2(\mu\text{-bpp})(\mu\text{-1,2-O}_2)]^{3+}$ (35) and $[\text{Co}(\text{Me}_2\text{bimpy})_2(\mu\text{-bpp})(\mu\text{-1,2-O}_2)]^{3+}$ (36). b) Schematic representation of the O-O bond formation mechanism by formal $\text{Co}^{\text{IV}}=\text{O}$ species derived from 35 and 36	47
Figure 39: Water oxidation catalytic cycle by <i>trans</i> - $[\text{Ni}^{\text{II}}(\text{L})](\text{ClO}_4)_2$ (37). Oxidation potentials are calculated respect to the NHE. Gibbs energy barrier is in $\text{kcal}\cdot\text{mol}^{-1}$	48
Figure 40: Water oxidation catalytic cycle by $[(\text{Por})\text{Ni}^{\text{II}}]^{4+}$ (38). Oxidation potentials are calculated respect to the NHE. Gibbs energies are in $\text{kcal}\cdot\text{mol}^{-1}$	49
Figure 41: Proposed water oxidation catalytic cycle by $[\text{Ni}^{\text{II}}(\text{PY5})\text{Cl}]^+$ (39), consistent with electrochemical data.....	50
Figure 42: Aqueous speciation of the copper(II)-bipyridine system. TON and TOF values are given in parentheses, respectively.....	50
Figure 43: Proposed water oxidation mechanism by $[(\text{TGG})\text{Cu}^{\text{II}}(\text{OH}_2)]^{2-}$ species (41). TON and TOF values are given in parentheses, respectively.....	51
Figure 44: Proposed water oxidation mechanism by $[\text{Cu}^{\text{II}}(\text{bpyOH})(\text{OH})_2]^{2+}$ species (42). Oxidation potentials are calculated respect to the NHE. TON and TOF values are given in parentheses, respectively.....	52
Figure 45: DFT computed water oxidation catalytic cycle by $[(\text{L}_1)\text{Cu}^{\text{II}}]^{2-}$ species (43) consistent with CV data. Oxidation potentials are calculated respect to the NHE. Gibbs energies are in $\text{kcal}\cdot\text{mol}^{-1}$. TOF value is shown in parentheses.....	53
Figure 46: a) Above, molecular structure of $[\text{Cu}^{\text{II}}_2(\text{BPMAN})(\mu\text{-OH})](\text{OTf})_3$ (44). TON and TOF values are given in parentheses, respectively. Below, generation of $[\text{Cu}^{\text{III}}(\text{OH})(\mu\text{-O})\text{Cu}^{\text{III}}(\text{BPMAN})]^{3+}$ species from $[\text{Cu}^{\text{II}}(\text{OH}_2)(\mu\text{-O})\text{Cu}^{\text{II}}(\text{BPMAN})]^{3+}$. Oxidation potentials are calculated respect to the NHE.....	54
Figure 47: Structure of the active sites of $[\text{FeFe}]$ (A), $[\text{Fe}]$ (B) and $[\text{NiFe}]$ -hydrogenases (C).....	55
Figure 48: a) Molecular structure of $[\text{PtMe}_2(\text{bpy})]$ (45) and $[\text{PtMe}_2\{(\text{pz})_3\text{BH}\}]^-$ (46). b) Proposed mechanisms for H_2 generation by $\text{Pt}^{\text{IV}}\text{-H}$ active species.....	58
Figure 49: Photochemical pathway for H_2 generation from water by Pt^{II} complexes.....	59
Figure 50: a) Molecular structure of $[\text{PtCl}_2(\text{en})]$ derivatives with two (47), four (48) and six (49) viologen groups. b) DFT proposed mechanisms for H_2 generation performed by $[\text{PtCl}_2(\text{en})]$ and $[\text{PtCl}_2(55'\text{bcbpy})]$ complexes when the source of protons is a H_3O^+ ion.....	60
Figure 51: a) Molecular structure of $[\text{PdMe}_2\{(\text{pz})_3\text{BH}\}]^-$ (50) and $[\text{Pd}(\text{CH}_2\text{CH}_2\text{CH}_2\text{CH}_2)\{(\text{pz})_3\text{BH}\}]^-$ (51). b) MP2 supported mechanism for the reaction of 50 with water.....	61
Figure 52: Left, proposed mechanism for H_2 generation by 52 . The label "Ox" means the oxidized form of the electron donor (EDTA or TEOA) and "Red" the reduced form. Right, molecular structures of complexes $[\text{Rh}^{\text{III}}(\text{bpy})_3]^{3+}$ (52) and $[\text{Rh}^{\text{III}}(\text{dtbbpy})_3]^{3+}$ (53). TON values are in parenthesis.....	62
Figure 53: The DFT proposed mechanism for H_2 generation for $[\text{Rh}^{\text{III}}(\text{dmbpy})_2\text{Cl}_2]^+$ (54) complex. TON and TOF values are in parenthesis, respectively.....	64

Figure 54: Metal-hydride and H-H bond formation steps through PCET reactions performed by a rhodium(II) dimer with quadruply bridged carboxylate ligands (55). TON values are in parenthesis.....	65
Figure 55: Molecular structures of the Co ^{II} tetraazamacrocyclic (58), cobalt porphyrins (59-61), the bis(1,4,7-triazacyclodecane)cobalt(III) complex (62) and [Co ^{III} (CR)(OH) ₂] ³⁺ (63). TON and TOF value are in parenthesis, respectively.....	66
Figure 56: Molecular structures of cobaloximes [Co ^{II} (dmgBF ₂) ₂ (OH) ₂] (64) and [Co ^{III} {(DO)(DOH)pn}Cl ₂] ⁺ (65) and the Co bis-dithiolene complex (66). TON value is in parenthesis.....	67
Figure 57: Proposed mononuclear and binuclear H ₂ evolution pathways for cobaloxime catalysts. The green labeled arrows indicate the most energetically favored pathway according to DFT calculations.....	68
Figure 58: DFT(BP86) computed H ₂ evolution catalytic cycle performed by cobaloxime 65 with the <i>p</i> -cyanoanilinium acid as proton source. Gibbs energies are in kcal·mol ⁻¹ . The reduction potentials were originally reported vs. the Fc ⁺ /Fc couple. Here in, an empirical correction of 675 mV was used to convert the potentials respect to the SHE electrode.....	68
Figure 59: a) Molecular structures of [Co ^{II} (R-PY5Me ₂)(OH) ₂] ²⁺ (67-69) and [Co ^{II} (DPA-Bpy)(OH) ₂] ²⁺ (70). TON values are in parenthesis. b) Proposed rate determining step proposed by 70	70
Figure 60: Molecular structures of [Co ^{II} (OTf) ₂ (Py ₂ ^{Ts} tacn)], [Ni ^{II} (OTf) ₂ (Py ₂ ^{Ts} tacn)] and [Fe ^{II} (OTf) ₂ (Py ₂ ^{Ts} tacn)]. TOF value under electrochemical conditions is in parenthesis.....	71
Figure 61: Molecular structures of the Ni ^{II} tetraazamacrocyclic (71), [Ni ^{II} (cyclam)] ²⁺ (72) and [Ni ₂ ^{II} (biscyclam)] ⁴⁺ (73). TON and TOF values are in parenthesis, respectively.....	72
Figure 62: Above, molecular structures of [Ni(PNP) ₂] ²⁺ (74), [Ni ^{II} (P ^{Ph} ₂ N ^{Ph} ₂)(NCCH ₃)] ²⁺ (75) and [Ni ^{II} (P ^{Cy} ₂ N ^{Bz} ₂)] ²⁺ (76). TOF values are in parenthesis. Below, schematic representation of the Ni-H ₂ adduct derived from 76 and its conversion into the Ni-H intermediate.....	73
Figure 63: Catalytic cycle for H ₂ oxidation and production by the [Ni(P ^R ₂ N ^{R'} ₂) ₂] ²⁺ family of catalyst.....	74
Figure 64: Molecular structures of [Ni ^{II} (P ^{Ph} ₂ N ^R ₂)] ²⁺ (77) and [Ni ^{II} (P ^{Ph} ₂ N ^{Ph} ₂)] ²⁺ (78). TOF values are in parenthesis.....	75
Figure 65: DFT proposed mechanism for H ₂ generation for 79 . TOF value is in parenthesis. Gibbs energies are in kcal·mol ⁻¹ . The reduction potentials are relative to the NHE electrode at pH = 0.....	76
Figure 66: Molecular structure of complex [(PY5Me ₂)Mo ^{IV} (O)] ²⁺ (80) and DFT proposed mechanism for H ₂ production. TON and TOF values are in parenthesis, respectively. Gibbs energy barriers are in kcal·mol ⁻¹ . Redox potentials respect to the SHE electrode.....	77
Figure 67: Left, molecular structure of [Mo ^{IV} (bdt) ₂ (<i>t</i> -BuNC) ₂] (81). Right, proposed mechanism for H ₂ production. TON value is in parenthesis.....	78
Figure 68: DFT computed mechanism for H ₂ production by [Mo ^{IV} (O)(qpdt) ₂] ²⁻ (82). TON and TOF values are in parenthesis, respectively. Gibbs energies are in kcal·mol ⁻¹	79
Figure 69: Molecular structures of copper complexes [Cu(opba)] ²⁻ (83), [Cu(Me ₂ oxpn)Cu(OH) ₂] (84) and [Cu(oxpn)Cu(OH) ₂] (85). TOF values are in parenthesis.....	80
Figure 70: DFT computed H ₂ production mechanism for complex 86 . The Gibbs energy barrier is given in kcal·mol ⁻¹	81
Figure 71: Selected iron complexes for study the WO mechanism.....	97
Figure 72: Selected aminopyridine complexes for study the proton reduction mechanism.....	98

- Figure 73:** Schematic diagram of iron complexes $[\text{Fe}(\text{OTf})_2(\text{L}^{\text{N}4})]$ and $[\text{Fe}(\text{NCCH}_3)(\text{L}^{\text{N}5})](\text{OTf})_2$ used in this study. OTf stands for CF_3SO_3^- anion.....101
- Figure 74:** Proposed catalytic cycle for water oxidation reaction by iron complexes based on tetradentate nitrogen ligands with *cis*-labile positions ($\text{L}^{\text{N}4}$).....102
- Figure 75:** Energy profile for O-O bond formation with complexes **1** and **2**. Values indicate solvent state Gibbs energies corrected with a D2-Grimme dispersion model ($\text{kcal}\cdot\text{mol}^{-1}$). The subscripts d and q represent spin states of $S = 1/2$ and $S = 3/2$, respectively. The ground state $S = 5/2$ Fe^{III} hydroperoxo intermediate energies are also included.....107
- Figure 76:** Doublet and quadruplet spin state surfaces of complex **1** in gas phase. Values indicate Gibbs energies corrected with a D2-Grimme dispersion model ($\text{kcal}\cdot\text{mol}^{-1}$). The subscripts d and q represent spin states of $S = 1/2$ and $S = 3/2$, respectively. L_1 is the Pytacn ligand.....109
- Figure 77:** Free energy profile of O-O bond formation event for complex **1b** in solvent phase when the proton transfer is assisted by an external cluster of three water molecule. Values indicate Gibbs energies ($\text{kcal}\cdot\text{mol}^{-1}$). L_1 represents the Pytacn ligand.....111
- Figure 78:** Solvent phase mechanisms for the assisted O-O bond formation performed by $[\text{Fe}^{\text{V}}(\text{O})(\text{tmc})]^{3+}$ species, generated from complex **3**. Values indicate Gibbs energies ($\text{kcal}\cdot\text{mol}^{-1}$). L_3 represents the tmc ligand. The ground state $S = 5/2$ Fe^{III} hydroperoxo intermediate is also included.....112
- Figure 79:** Solvent phase energy profile for water assisted O-O bond formation with complex **4**. Values indicate Gibbs energies ($\text{kcal}\cdot\text{mol}^{-1}$). L_4 represents the $^{\text{Me}}\text{Py}_2\text{CH-tacn}$ ligand.....113
- Figure 80:** a) Viable O_2 generation mechanism from the $\text{Fe}^{\text{III}}(\text{OOH})$ to $\text{Fe}^{\text{IV}}(\text{O})$. Values shown in the figure indicate the Mulliken spin densities for selected atoms. All redox potentials have been calculated at $\text{pH} = 1$. b) Comparison of spin densities contours (iso-value of 0.01) of $\mathbf{1V}_d$ (left) and $\mathbf{1V}_q$ (right) species.....115
- Figure 81:** Second viable mechanistic proposal for the evolution from $\text{Fe}^{\text{III}}(\text{OOH})$ to $\text{Fe}^{\text{IV}}(\text{O})$ species. Values shown in the figure indicate the Mulliken spin densities for selected atoms. All redox potentials have been calculated at $\text{pH} = 1$116
- Figure 82:** Computed WO catalytic cycle catalyzed by **1**. Inset: the optimized geometry for the $\mathbf{1TS}_{(\text{III-IV})d}$ with the most relevant bond distances (\AA). Values represent redox potentials (V) and those in parenthesis report the free energies ($\text{kcal}\cdot\text{mol}^{-1}$).....117
- Figure 83:** Free energy profile ($\text{kcal}\cdot\text{mol}^{-1}$) for water oxidation reaction by catalyst **1**. The H_2O and O_2 molecules necessary to ensure the correct energetic balance in all the steps of the catalytic cycle are included in the calculation, but are omitted in the Figure for clarity.....100
- Figure 84:** Theoretical proposal by Kasapbasi and co-workers which occurs exclusively at Fe^{IV} oxidation state.²⁰⁸.....123
- Figure 85:** O-O bond formation profiles found for the **a** tautomer of $[\text{Fe}^{\text{IV}}(\text{O})(\text{OH}_2)(\text{Pytacn})]^{2+}\cdot 4\text{H}_2\text{O}$ for the $S = 0, 1$ and 2 spin states. Gibbs energy values are given in $\text{kcal}\cdot\text{mol}^{-1}$. Figures inserted correspond to the $S = 2$ spin state, where selected bond distances (\AA) are presented.....129
- Figure 86:** Internal (top) and external (bottom) base assisted O-O bond formation mechanisms from the tautomer **a** $[\text{Fe}^{\text{IV}}(\text{O})(\text{OH})(\text{Pytacn})]^+$ intermediate. Gibbs energy values are given in $\text{kcal}\cdot\text{mol}^{-1}$. Selected bond distances in \AA are indicated in the figures corresponding to the stationary points of the $S = 2$ reaction profile.....132
- Figure 87:** Internal base assisted O-O bond formation mechanisms from the tautomer **a** of $[\text{Fe}^{\text{IV}}(\text{OH})(\text{OH})(\text{Pytacn})]^{2+}$ intermediate. Gibbs energy values are given in $\text{kcal}\cdot\text{mol}^{-1}$. Selected bond distances (\AA) of stationary points on the $S = 2$ reaction profile are indicated in the figures.133

- Figure 88:** Iron complexes based on *N*-(quinolin-8-yl)acetamidyl fragment. a) iron(III) complex [Fe^{III}(dpaq)(H₂O)]²⁺ reported by Kodera *et al.*^{218b} b) New iron(II) complex based on the tacn moiety.....143
- Figure 89:** Spin density plots of complexes [Fe^{IV}(•AQ^{Me2}tacn)(O)]²⁺ (left) and [Fe^{IV}(•dpaq)(O)]²⁺ (right) (iso value = 0.01).....146
- Figure 90:** O-O bond formation free energy profiles found for [Fe^{IV}(•AQ^{Me2}tacn)(O)]²⁺ in the S = 1/2, 3/2 and 5/2 spin states. Gibbs energy values are given in kcal·mol⁻¹. The oxidized AQ^{Me2}tacn ligand is represented by •L₁.....147
- Figure 91:** Optimized geometries of the lowest energy species involved in the external O-O bond formation mechanism performed by [Fe^{IV}(•AQ^{Me2}tacn)(O)]²⁺, with the most relevant bond distances (Å). The oxidized AQ^{Me2}tacn ligand is represented by •L₅. Hydrogen atoms of the AQ^{Me2}tacn ligand are omitted for clarity.....147
- Figure 92:** Optimized geometries of the lowest energy species involved in the internal base assisted O-O bond formation mechanism performed by [Fe^{IV}(•AQ^{Me2}tacn)(O)]²⁺, with the most relevant bond distances (Å). The oxidized AQ^{Me2}tacn ligand is represented by •L₅. Hydrogen atoms of the AQ^{Me2}tacn ligand are omitted for clarity.....148
- Figure 93:** O-O bond formation free energy profiles found for [Fe^{IV}(•dpaq)(O)]²⁺ in the S = 1/2, 3/2 and 5/2 spin states. Gibbs energy values are given in kcal·mol⁻¹. The dpaq ligand is represented by L₂.....149
- Figure 94:** Optimized geometries of the lowest energy species involved in the O-O bond formation mechanism performed by [Fe^{IV}(•dpaq)(O)]²⁺, with the most relevant bond distances (Å). The oxidized dpaq ligand is represented by •L₆. Hydrogen atoms of the dpaq ligand are omitted for clarity.....150
- Figure 95:** Optimized geometries for [Ce^{IV}(H₂O)₉]⁴⁺ (left, capped square antiprismatic) and [Ce^{IV}(H₂O)₈]⁴⁺ (right, square antiprismatic) mononuclear aqua complexes. Bond distances in Å.....158
- Figure 96:** Optimized geometries for the most stable hydroxide (left: **8-Ce^{IV}(H₂O)₇(OH)**) and oxo (right: **4-Ce^{IV}(H₂O)₇(O)**) mononuclear cerium(IV) species. Bond distances in Å. The dashed lines indicate the hydrogen bonds between the coordinated and uncoordinated (or weakly interacting) water molecules.....158
- Figure 97:** Optimized geometries for the most stable aqua (left: [(H₂O)₇Ce^{IV}-O-Ce^{IV}(H₂O)₇]⁶⁺) and hydroxide (right: **8-(H₂O)₇Ce^{IV}-O-Ce^{IV}(OH)(H₂O)₆**) binuclear cerium(IV) species. Bond distances in Å.....160
- Figure 98:** Optimized geometries for the **1-α + Ce** (left) and **1-β + Ce** (right) aqua heterobimetallic iron-cerium species. Relevant bond distances in Å. Irrelevant hydrogen atoms are omitted for clarity.....162
- Figure 99:** a) Reaction equation for the generation of the **1-α + Ce** aqua iron-cerium intermediate from α-[Fe^{IV}(O)(OH₂)(mcp)]²⁺ and **8-(H₂O)₇Ce^{IV}-O-Ce^{IV}(OH)(H₂O)₆**. b) Generation of the iron based Fe^{III}-O-O-Ce^{III} Sakai intermediate. Gibbs energies are in kcal·mol⁻¹. The free energy balances have been performed with two iron complexes to avoid the generation of free mononuclear Ce^{IV} species as byproducts. L stands for the mcp ligand.....164
- Figure 100:** Space-filling models of **1-β + Ce** (left) and **1-α + Ce** (right) aqua heterobimetallic iron-cerium species. The purple arrows indicate the steric crowding that exists between the aqua ligands and the mcp ligand. Yellow arrows indicate the “push effect” exerted by the equatorial pyridine on the Ce^{IV}(H₂O)₇ fragment.....165
- Figure 101:** a) Optimized geometries for the **2-α + Ce** (left) and **2-β + Ce** (right) Fe^V-OH-Ce^{III} species. Relevant bond distances in Å. Irrelevant hydrogen atoms are omitted for clarity. b) Inner-sphere thermodynamics and estimated electron transfer barriers. The free energy values related with the **1-α + Ce** and **1-β + Ce** adducts are labeled in red and green, respectively.....166

Figure 102: Optimized geometries for 7-[2-α + Ce(OH)] (left) and 5-[2-α + Ce(OH)] (right) intermediate. The hydroxide group on cerium is circled. Relevant bond distances in Å. Irrelevant hydrogen atoms are omitted for clarity.....	167
Figure 103: Spin natural orbitals (isovalue = 0.05) of 5-[2-α + Ce(OH)] and possible O-O bond formation mechanisms.....	169
Figure 104: Triplet and quintuplet free energy profiles for the WNA to the oxo ligand in 5-[2-α + Ce(OH)] , assisted by the Ce ^{IV} -OH fragment. Inserted figure correspond to the 1TS_(I-II) structure. Relevant bond distances in Å and irrelevant hydrogens are omitted for clarity. Gibbs energies are in kcal·mol ⁻¹ . L stands for the mcp ligand. The transition state in the S = 2 spin state surface has not been located.....	170
Figure 105: a) Global free energy profile for the O-O bond formation mechanism performed by 5-[2-α + Ce(OH)] . b) Comparison of the O-O bond formation mechanisms performed by [Fe ^V (O)(OH)(mcp)] ²⁺ and 5-[2-α + Ce(OH)] species. Gibbs energies are in kcal·mol ⁻¹ . L stands for the mcp ligand.....	171
Figure 106: Free energy cost for the [Fe ^V (O)(OH)(mcp)] ²⁺ generation by 1-α (above) and 1-β (below) complexes respect to Fe ^{IV} species. The Marcus barrier for the inner-sphere electron transfer (ET) is also indicated. Gibbs energies are in kcal·mol ⁻¹ . L ₁ stands for the mcp ligand.....	172
Figure 107: a) Methyl oxidation mechanism by 1Fe^V-β in the S = 1/2 and S = 3/2 spin states. Inserted figure correspond to the transition state structure. Relevant bond distances in Å. b) Comparison between the O-O bond formation and methyl oxidation mechanisms for 1Fe^V-β . Gibbs energies are in kcal·mol ⁻¹ . L ₁ stands for the mcp ligand.	173
Figure 108: a) Methylene oxidation mechanism by 1Fe^V-α in the S = 1/2 and S = 3/2 spin states. Inserted figure correspond to the transition state structure. Relevant bond distances in Å. b) Comparison between the O-O bond formation and methylene oxidation mechanisms for 1Fe^V-α . Gibbs energies are in kcal·mol ⁻¹ . L ₁ stands for the mcp ligand.....	174
Figure 109: Experimentally proposed oxidation reactions and active species when acetic acid is present (left) or absent (right) in the reaction media. Green arrows indicate the most favorable reaction pathways. L stands for the mcp ligand.....	179
Figure 110: Homolytic <i>vs</i> heterolytic minimum free energy profiles for the H ₂ oxidation by [Fe ^V (O)(OH)(mcp)] ²⁺ . All species are labeled with its ground spin state. Gibbs energy values are given in kcal·mol ⁻¹	181
Figure 111: Optimized structures of the ground spin state intermediates and transition states involved in the heterolytic and 2+3 homolytic H-H cleavage mechanisms by [Fe ^V (O)(OH)(mcp)] ²⁺ . Bond distances in Å. Irrelevant hydrogen atoms are omitted for clarity.	182
Figure 112: Homolytic H ₂ oxidation free energy profiles found for [Fe ^{IV} (O)(·OAc)(mcp)] ²⁺ in the S = 1/2 and 3/2 spin states. Gibbs energy values are given in kcal·mol ⁻¹	184
Figure 113: Optimized structures of the ground spin state intermediates and transition states involved in the 2+4 homolytic H-H cleavage mechanism by [Fe ^{IV} (O)(·OAc)(mcp)] ²⁺ . Bond distances in Å. Irrelevant hydrogen atoms are omitted for clarity.	184
Figure 115: Experimentally proposed mechanism for the generation of metal-hydride active species under photochemical and electrochemical conditions. The reactivity differences between 1Co^{II} , 1Ni^{II} and 1Fe^{II} complexes are shown.....	189
Figure 116: Optimized geometries of Ni^I_A-NCCH₃ (left) and Ni^I_B-NCCH₃ (right) intermediates. The bond distances values are in angstroms (Å). Irrelevant hydrogen atoms are omitted for clarity.....	193

Figure 117: Single occupied molecular frontier orbitals of Co-OH ₂ (top), Ni-OH ₂ (middle) and Fe-OH ₂ (bottom) intermediates (isovalue of 0.0432) involved in the reduction step from M ^{II} to M ^I . The M ^{II} -OH ₂ and M ^I -OH ₂ structures are inserted in the left and right columns, respectively.....	196
Figure 118: Experimentally proposed proton reduction mechanism under electrochemical conditions by 1Co^{II}	203
Figure 119: Heterolytic and homolytic reaction pathways for H ₂ evolution by [Co ^{II} (H)(Py ₂ ^{Ts} tacn)] ⁺ and [Co ^{III} (H)(Py ₂ ^{Ts} tacn)] ²⁺ intermediates in acetonitrile solution.....	204
Figure 120: Possible electrochemical catalytic cycles for the proton reduction reaction by 1Co^{II} through Co ^{III} -H and Co ^{II} -H intermediates. Both the heterolytic and the homolytic pathways for H ₂ generation are considered. Reaction free energies are in kcal·mol ⁻¹	206
Figure 121: Intermolecular HAT mechanism in the S = 0 and S = 1 spin free energy surfaces for [Co ^{III} (H)(Py ₂ ^{Ts} tacn)] ²⁺ generation under electrochemical conditions. Hydrogen atoms of ligands in the inserted figures are omitted for clarity. Bond distances in Å. Free energies are in kcal·mol ⁻¹	207
Figure 122: Graphical representation of hydricity values (kcal·mol ⁻¹) for selected compounds. ^{266,267,268,269} ...	208
Figure 123: a) Stability of protonated pyridine cobalt species derived from the key intermediates involved in the electrochemical proton reduction reaction. The pK _a values for the protonated species in acetonitrile are also indicated. Free energies are in kcal·mol ⁻¹ . b) Spin density plot of [Co ^{II} (H-Py ₂ ^{Ts} tacn·)] ²⁺ (isovalue = 0.01)....	210
Figure 124: Possible involvement of the pyridine ligand in the electrochemical catalytic cycle for proton reduction by 1Co^{II} . Free energies are in kcal·mol ⁻¹ (free energy barriers in parenthesis).....	211
Figure 125: Intramolecular HAT mechanism in the S = 0 and S = 1 spin free energy surfaces for [Co ^{III} (H)(Py ₂ ^{Ts} tacn)] ²⁺ generation under electrochemical conditions. Hydrogen atoms of ligands in the inserted figures are omitted for clarity. Bond distances in Å. Free energies are in kcal·mol ⁻¹	212
Figure 126: a) Different pyridinium arm conformations for [Co ^{II} (H)(H-Py ₂ ^{Ts} tacn)] ²⁺ species. b) Intramolecular coupling between Co ^{II} -H and pyridinium fragments in the S = 1/2 and S = 3/2 spin free energy surfaces by [Co ^{II} (H)(H-Py ₂ ^{Ts} tacn)] ²⁺ under electrochemical conditions. Hydrogen atoms of ligands in the inserted figures are omitted for clarity. Bond distances in Å. Free energies are in kcal·mol ⁻¹	214
Figure 127: Free energy profile for our proposed mechanism of the whole proton reduction reaction catalyzed by 1Co^{II} (applied potential of -1.60 V vs SCE). The CH ₃ CN, H ⁺ and H ₂ molecules necessary to ensure the correct energetic balance in all the steps of the catalytic cycle are included in the calculation, but are omitted in the Figure for clarity.....	215
Figure 128: Experimentally proposed water/proton reduction mechanism under photochemical conditions by 1Co^{II} . The reactivity differences between 1Co^{II} , 1Ni^{II} and 1Fe^{II} complexes are also indicated.....	220
Figure 129: Heterolytic and homolytic reaction pathways for H ₂ evolution in water by [Co ^{II} (H)(Py ₂ ^{Ts} tacn)] ⁺ and [Co ^{III} (H)(Py ₂ ^{Ts} tacn)] ²⁺ intermediates.....	220
Figure 130: Solvent ligand exchange reactions experimented by 1Co^{II} and 1Co^I intermediates under photochemical conditions (H ₂ O/CH ₃ CN 7:3 solvent mixture).....	222
Figure 131: Proton reduction catalytic cycle under photochemical conditions by complex 1Co^{II} . Reactive protons ([H ⁺]) could originate from H ₃ O ⁺ or water solvent molecules. The electrons are delivered to cobalt intermediates by the reduced photosensitizer PSIr^{II} . Both the heterolytic and the homolytic pathways for H ₂ generation are considered.....	223
Figure 132: a) Pyridine protonation mechanism by [Co ^I (NCCH ₃)(Py ₂ ^{Ts} tacn)] ⁺ and a H ₃ O ⁺ (H ₂ O) ₂ cluster. b) Cobalt (III) hydride generation mechanism by [Co ^I (NCCH ₃)(Py ₂ ^{Ts} tacn)] ⁺ and a H ₃ O ⁺ (H ₂ O) ₂ cluster. Hydrogen atoms of the ligands have been omitted for clarity. Bond distances in Å. Free energies are in kcal·mol ⁻¹	225

- Figure 133:** Water O-H bond cleavage mechanism catalyzed by $[\text{Co}^{\text{I}}(\text{NCCH}_3)(\text{Py}_2^{\text{Ts}}\text{tacn})]^+$. Hydrogen atoms of the ligands have been omitted for clarity. Bond distances in Å. Free energies are in $\text{kcal}\cdot\text{mol}^{-1}$226
- Figure 134:** a) Water O-H bond cleavage mechanism catalyzed by $[\text{Co}^{\text{III}}(\text{H})(\text{Py}_2^{\text{Ts}}\text{tacn})]^{2+}$. b) H_2 generation mechanism by $[\text{Co}^{\text{III}}(\text{H})(\text{Py}_2^{\text{Ts}}\text{tacn})]^+$ and a $\text{H}_3\text{O}^+(\text{H}_2\text{O})_3$ cluster. Hydrogen atoms of the ligands have been omitted for clarity. Bond distances in Å. Free energies are in $\text{kcal}\cdot\text{mol}^{-1}$228
- Figure 135:** Water O-H bond cleavage catalyzed by $[\text{Co}^{\text{II}}(\text{H})(\text{Py}_2^{\text{Ts}}\text{tacn})]^+$. Hydrogen atoms of the ligands have been omitted for clarity. Bond distances in Å. Free energies are in $\text{kcal}\cdot\text{mol}^{-1}$229
- Figure 136:** Above, optimized geometry of the cobalt (III) hydride dimer in the ground spin state ($S = 0$). Below, optimized geometry of the $\text{Co}^{\text{II}}\cdot\cdot\text{H}\cdot\text{H}\cdot\cdot\text{Co}^{\text{II}}$ dimer in the ground spin state ($S = 2$). Irrelevant hydrogen atoms were omitted for clarity. Bond distances in Å.....230
- Figure 137:** Above, optimized geometry of the cobalt (II) hydride dimer in the ground spin state ($S = 2$). Below, optimized geometry of the $\text{Co}^{\text{I}}\cdot\cdot\text{H}\cdot\text{H}\cdot\cdot\text{Co}^{\text{I}}$ dimer in the ground spin state ($S = 2$). Irrelevant hydrogen atoms were omitted for clarity. Bond distances in Å.....231
- Figure 138:** Free energy profile of the computed proton reduction mechanism catalyzed by 1Co^{II} under photochemical conditions. The $\text{H}_2\text{O}/\text{OH}/\text{H}_3\text{O}^+$ clusters and H_2 molecules necessary to ensure the correct energetic balance in all the steps of the catalytic cycle are included in the calculation, but are omitted in the Figure for clarity.....232
- Figure 139:** Spin density plots of open shell cobalt intermediates. The blue color is associated with the alpha spin.....233
- Figure 140:** Spin natural orbitals (SNO) of $\text{Co}^{\text{II}}\text{-NCCH}_3$ (above) and $\text{Co}^{\text{I}}\text{-NCCH}_3$ (below) related with the $\text{Co}\text{-NCCH}_3$ bond.....233
- Figure 141:** a) Electrostatic potential surfaces for cobalt hydride species. The color coding is from blue (large positive potential) to red (large negative potential). b) Relevant occupied frontier molecular orbitals for cobalt hydride species (isovalue = 0.01). From the above plots, it is evident that the $\text{Co}^{\text{II}}\text{-H}$ moiety presents a higher hydride character than $\text{Co}^{\text{III}}\text{-H}$234

LIST OF SCHEMES

- Scheme 1:** Fundamental description of the WNA and the DC mechanism of water oxidation.....15
- Scheme 2:** a) Proposed molecular hydrogen evolution mechanisms promoted by common metal-hydride active species. b) Water oxidative addition on the metal center to generate metal-hydride species.....57
- Scheme 3:** Studied O-O bond formation pathways involving Fe^{IV} species. The microsolvation of the iron complex was modeled by three explicit water molecules. WNA stands for Water Nucleophilic Attack.....124
- Scheme 4:** O_2 evolution and regeneration of the $[\text{Fe}^{\text{IV}}(\text{O})(\text{OH}_2)(\text{Pytacn})]^{2+}$ resting state through hydroperoxo intermediates.....126
- Scheme 5:** Summary of all the O-O bond formation pathways involving $\text{Fe}^{\text{IV}}(\text{O})$ and $\text{Fe}^{\text{V}}(\text{O})$ species. The lowest energy barrier for the O-O bond formation starting from $\{\text{Fe}^{\text{IV}}\}$ species is around $28 \text{ kcal}\cdot\text{mol}^{-1}$. In addition, we also reported that the redox couple $\text{Fe}^{\text{V/VI}}$ is not accessible under catalytic conditions. The redox values are relative to the SHE electrode at $\text{pH} = 1$. The free energies of the TS are relative to the $[\text{Fe}^{\text{IV}}(\text{O})(\text{OH}_2)(\text{Pytacn})]^{2+}$ and $[\text{Fe}^{\text{V}}(\text{O})(\text{OH})(\text{Pytacn})]^{2+}$, respectively. The WNA stands for Water Nucleophilic Attack.....138
- Scheme 6:** Reactivity differences between **1- α** and **1- β** topological isomers and some possible O-O bond formation mechanisms performed by the **1- α + Ce** intermediate. Figure adapted from reference 70.....155
- Scheme 7:** a) Possible 2+3 homolytic H-H and heterolytic bond breaking mechanisms catalyzed by $[\text{Fe}^{\text{V}}(\text{O})(\text{OH})(\text{mcp})]^{2+}$ species. b) 2+4 homolytic mechanism for $[\text{Fe}^{\text{V}}(\text{O})(\cdot\text{OAc})(\text{mcp})]^{2+}$179
- Scheme 8:** Summary of reactivity differences between **1Co^{II}**, **1Ni^{II}** and **1Fe^{II}** complexes under photochemical conditions. Reduction potentials (vs. SHE electrode) and pK_a values have been derived by DFT calculations.....198
- Scheme 9:** Proposed heterolytic (purple) and homolytic (red) proton reduction pathways for cobaloxime catalysts.....202

LIST OF TABLES

Table 1: Redox potentials E° , $E_{1/2}(\text{PCET})$ and pK_a values of the thermodynamic cycle involving $\text{Fe}^{\text{IV}}/\text{Fe}^{\text{V}}$ transformations. ^a	105
Table 2: Mulliken atomic spin populations, $\text{Fe}-\text{O}_a$ and O_a-O_c bond distances for key species involved in the O-O bond formation mechanism for complex 1	107
Table 3: Theoretical and experimental values of the activation parameters (ΔH^\ddagger , ΔS^\ddagger and ΔG^\ddagger) for iron complex 1	118
Table 4: Spin states relative free energies ($\text{kcal}\cdot\text{mol}^{-1}$) of the Fe^{IV} intermediates for complex 1 in the two <i>cis</i> -tautomers a and b	127
Table 5: Selected Mulliken spin densities and bond distances for the stationary points obtained in the formation of the O-O bond by an external water nucleophilic attack to the $S = 2$ $[\text{Fe}^{\text{IV}}(\text{O})(\text{OH}_2)(\text{Pytacn})]^{2+}$ complex.....	128
Table 6: Selected Mulliken spin densities and bond distances for the $S = 2$ stationary points involved in the O-O bond formation mechanism from $[\text{Fe}^{\text{IV}}(\text{O})(\text{OH})(\text{Pytacn})]^+$ species.....	131
Table 7: Selected Mulliken spin densities and bond distances for the stationary points obtained in the formation of the O-O bond by external water nucleophilic attack to $S = 2$ $[\text{Fe}^{\text{IV}}(\text{OH})(\text{OH})(\text{Pytacn})]^{2+}$ complex.....	134
Table 8: Free energy differences (ΔG) and pK_a values for the proton dissociation of HNO_3 assisted by several water clusters.....	135
Table 9: Redox potentials E° , PCET (V) and pK_a values of the thermodynamic cycle involving all the possible iron intermediates that could be formed in aqueous solution from $[\text{Fe}^{\text{II}}(\text{AQ}^{\text{Me}_2}\text{tacn})(\text{OH}_2)]^+$ and $[\text{Fe}^{\text{III}}(\text{dpaq})(\text{OH}_2)]^{2+}$. ^[a]	145
Table 10: Relative free energy differences ($\text{kcal}\cdot\text{mol}^{-1}$) for $[\text{Ce}^{\text{IV}}(\text{H}_2\text{O})_7(\text{OH})]^{3+}$ isomers, and deprotonation free energies and pK_a values respect to the $[\text{Ce}^{\text{IV}}(\text{H}_2\text{O})_8]^{4+}$ aqua complex.....	159
Table 11: Relative free energy differences ($\text{kcal}\cdot\text{mol}^{-1}$) for $[\text{Ce}^{\text{IV}}(\text{H}_2\text{O})_7(\text{O})]^{2+}$ isomers, deprotonation free energies and pK_a values respect to the corresponding hydroxo intermediates.....	159
Table 12: Relative free energy differences ($\text{kcal}\cdot\text{mol}^{-1}$) of $[(\text{H}_2\text{O})_7\text{Ce}^{\text{IV}}-\text{O}-\text{Ce}^{\text{IV}}(\text{OH})(\text{H}_2\text{O})_6]^{5+}$ isomers, and deprotonation free energies and pK_a values respect to $[(\text{H}_2\text{O})_7\text{Ce}^{\text{IV}}-\text{O}-\text{Ce}^{\text{IV}}(\text{H}_2\text{O})_7]^{6+}$	160
Table 13: Relative free energy differences ($\text{kcal}\cdot\text{mol}^{-1}$) for a representative subgroup of bis-hydroxide binuclear Ce^{IV} isomers, and deprotonation free energies and pK_a values respect to 8-(H₂O)₇Ce^{IV}-O-Ce^{IV}(OH)(H₂O)₆	161
Table 14: Relative free energy differences ($\text{kcal}\cdot\text{mol}^{-1}$) for α - $[(\text{mcp})\text{Fe}^{\text{IV}}(\text{O})(\mu\text{-O})(\text{Ce}^{\text{IV}})(\text{OH})(\text{H}_2\text{O})_6]^{3+}$ isomers, and deprotonation free energies and pK_a values respect to 1-α + Ce	162
Table 15: Spin states relative free energies ($\text{kcal}\cdot\text{mol}^{-1}$) of the Fe^{IV} intermediates for complex 1-β in the two <i>cis</i> -tautomers 1a-β and 1b-β	163

Table 16: Relative free energy differences (kcal·mol ⁻¹) for β-[(mcp)Fe ^{IV} (O)(μ-O)(Ce ^{IV})(OH)(H ₂ O) ₆] ³⁺ isomers, and deprotonation free energies and pK _a values respect to 1-β + Ce	163
Table 17: Relative free energy differences (kcal·mol ⁻¹) for all the α-[(mcp)Fe ^{IV} (O)(μ-OH)(Ce ^{IV})(OH)(H ₂ O) ₆] ⁴⁺ isomers, and deprotonation free energies and pK _a values respect to 2-α + Ce	167
Table 18: Relative free energy differences (kcal·mol ⁻¹) for all the β-[(mcp)Fe ^{IV} (O)(μ-OH)(Ce ^{IV})(OH)(H ₂ O) ₆] ⁴⁺ isomers, deprotonation free energies and pK _a values respect to 2-β + Ce	168
Table 19: Mulliken spin population, Fe-O _a and H _a -H _b bond distances for key species involved in the 2+3 homolytic H-H bond activation mechanism for [Fe ^V (O)(OH)(mcp)] ²⁺ active species.	158
Table 20: Mulliken spin populations Fe-O _a and H _a -H _b bond distances for key species involved in the 2+3 homolytic H-H bond activation mechanism for complex [Fe ^{IV} (O)(·OAc)(mcp)] ²⁺	185
Table 21: Relevant bond distances (Å) of the most stable spin states for M ^{II} -L geometries: ^a	192
Table 22: Computed free energy (ΔG) for coordination of CH ₃ CN and H ₂ O to 1M and for ligand exchange reactions: ^a	194
Table 23: Stabilization energies (ΔE _{LM}) for the dominant donor-acceptor interactions (n _L → n _M *) between 1M complexes and L solvent ligands: ^a	194
Table 24: Electronegativity (χ) and electrophilicity (ω) descriptors for cobalt, nickel and iron complexes and solvent ligands: ^a	195
Table 25: DFT computed reduction potentials (V) and pK _a values of the proposed iron, cobalt and nickel intermediates. ^a	195
Table 26: Hydricities, bonding dissociation energies (BDE) and pK _a values for the Co-H bond in cobalt hydride species.....	208
Table 27: Partial atomic charges, spin densities (in parenthesis) and Mayer bond order index (B.O.) for the cobalt atom and hydride moiety in reduced Py ₂ ^{Ts} tacn compounds. ^a	233

ACKNOWLEDGMENTS

I would like to start by thanking a lot my supervisors Dr. Julio Lloret and Dr. Josep M. Luis for their confidence in me, their patience, guidance and the very useful discussions. The work of this thesis would not have been possible without them.

Many thanks to my colleagues of the QBIS-CAT group, especially to Dr. Zoel Codolà, Arnau Call, Mireia Rovira, Marc Font, Jordi Serra, Teresa Corona, Joan Serrano, Dr. Miquel Costas, Dr. Xavi Ribas and Dr. Anna Company, for give me the opportunity to be involved in their research projects. These collaborations have helped me to grow as chemist.

Great thanks to Prof. Dr. Christopher Cramer from the University of Minnesota (Minneapolis, USA) for hosting a scientific visit and the collaborative research in the computational study of the $\text{Fe}^{\text{IV}}\text{-O-Ce}^{\text{IV}}$ adducts involved in the water oxidation reaction.

Great thanks to the Institute of Computational Chemistry and Catalysis (IQCC), the “Consorci de Serveis Universitaris de Catalunya” (CSUC) and the Minnesota Supercomputing Institute (MSI) for the computational resources.

Special thanks to the University of Girona for the predoctoral (BR-UdG) and mobility (MOB2014) grants, the European Research Foundation for projects FP7-PEOPLE-2010-ERG-268445, ERC-2009-StG-239910 and ERC-2015-CoG, the MINECO for projects CTQ2009-08464, CTQ2011-23156/BQU and CTQ2014-52525-P and the Generalitat de Catalunya for projects 2009SGR637 and 2014SGR931.

Finally, but not least, I want to thank immensely my family for their support, my girlfriend for her huge love and patience and especially my parents, whom have taken care of me in the worst moments and have helped me to achieve my dreams. I will love you forever.

TABLE OF CONTENTS

Abstract.....	1
Resum.....	3
Resumen.....	5
Chapter 1. General Introduction.....	8
1.1. World Energetic Problem.....	10
1.2. The Photosynthesis.....	10
1.3. Artificial Photosynthesis.....	13
1.4. Artificial Water Oxidation Catalysts.....	14
1.4.1 O-O bond formation pathways.....	14
1.4.2 Earth-scarce Transition Metal-based WOCs.....	16
1.4.2.1 Ruthenium based WOCs.....	16
1.4.2.2 Iridium based WOCs.....	24
1.4.3 First row Transition Metal-based WOCs.....	30
1.4.3.1 Manganese based WOCs.....	30
1.4.3.2 Iron based WOCs.....	36
1.4.3.3 Cobalt based WOCs.....	43
1.4.3.4 Nickel based WOCs.....	47
1.4.3.5 Copper based WOCs.....	50
1.5. Hydrogenase Enzymes.....	55
1.6. Artificial Hydrogen Production Catalysts.....	56
1.6.1 Mechanisms for Molecular Hydrogen Production.....	56
1.6.2 Earth-scarce Transition Metal-based H ₂ Production Catalysts.....	58
1.6.2.1 Platinum based H ₂ Production Catalysts.....	58
1.6.2.2 Palladium based H ₂ Production Catalysts.....	60
1.6.2.3 Rhodium based H ₂ Production Catalysts.....	62
1.6.3 First row Transition Metal-based H ₂ Production Catalysts.....	65
1.6.3.1 Cobalt based H ₂ Production Catalysts.....	65

1.6.3.2 Nickel based H ₂ Production Catalysts.....	71
1.6.3.3 Molybdenum based H ₂ Production Catalysts.....	76
1.6.3.4 Copper based H ₂ Production Catalysts.....	79
Chapter 2. Theoretical methodology.....	83
2.1. Basics of quantum mechanics.....	85
2.2. <i>Ab initio</i> methods.....	85
2.3. Density Functional Theory (DFT).....	86
2.3.1 DFT foundations.....	86
2.3.2 Efficiency and applications.....	89
2.4. pKa calculations.....	89
2.5. Thermodynamics and kinetics of redox reactions.....	90
2.6. Broken spin symmetry methodology.....	92
Chapter 3. Main Objectives.....	94
Chapter 4. Unravelling the Mechanism of Water Oxidation Catalyzed by Non-Heme Iron Complexes.....	99
4.1. State-of-the-art.....	101
4.2. Results and discussion.....	103
4.2.1 O-O bond formation reaction pathway.....	106
4.2.1.1 O-O bond formation for <i>cis</i> -site complexes 1 and 2	106
4.2.1.2 <i>cis</i> -OH ligand-assisted- versus external-water attack in the Fe ^V =O mechanism.....	110
4.2.1.3 O-O bond formation mechanism for complex 3	111
4.2.1.4 O-O bond formation mechanism for complex 4	113
4.2.2 Reaction pathway for O ₂ generation from the Fe ^{III} -OOH species.....	114
4.2.3 Global catalytic cycle.....	116
Chapter 5. Theoretical Study of the Water Oxidation Mechanism with Non-heme Fe(Pytacn) Iron Complexes. Evidence that the Fe^{IV}(O)(Pytacn) Species Cannot React with the Water Molecule to Form the O-O Bond.....	120
5.1. State-of-the-art.....	122
5.2. Results and discussion.....	124

5.2.1 O-O bond formation mechanism through $[\text{Fe}^{\text{IV}}(\text{O})(\text{OH}_2)(\text{Pytacn})]^{2+}$	125
5.2.2 O-O bond formation mechanism through $[\text{Fe}^{\text{IV}}(\text{O})(\text{OH})(\text{Pytacn})]^+$	129
5.2.3 O-O bond formation mechanism through $[\text{Fe}^{\text{IV}}(\text{OH})(\text{OH})(\text{Pytacn})]^{2+}$	133
5.2.4 Comparison with the catalytic cycle proposed by Kasapbasi <i>et al.</i>	135
Chapter 6. Water oxidation reaction mechanism with N-pentadentate iron catalysts	140
6.1. State-of-the-art	142
6.2. Results and discussion	143
6.2.1 O-O bond formation mechanisms	146
6.2.1.1. O-O bond formation reaction pathway by complex 5	146
6.2.1.2. O-O bond formation reaction pathway by complex 6	148
Chapter 7. Iron-Cerium adducts as intermediates in the water oxidation reaction	152
7.1. State-of-the-art	154
7.2. Results and discussion	156
7.2.1 Speciation of CAN in acidic aqueous solution	157
7.2.2 Iron-Cerium adducts structure and generation	161
7.2.3 Inner-sphere oxidation of the $\text{Fe}^{\text{IV}}\text{-O-Ce}^{\text{IV}}$ adduct	165
7.2.4 O-O bond formation mechanisms for iron-cerium adduct	168
7.2.5 Decomposition pathways for the mcp ligand	171
Chapter 8. H_2 versus organic substrate oxidation by high valent non-heme iron species	176
8.1. State-of-the-art	178
8.2. Results and discussion	180
8.2.1 H-H bond cleavage mechanisms for $[\text{Fe}^{\text{V}}(\text{O})(\text{OH})(\text{mcp})]^{2+}$	180
8.2.2 Internal base assisted H-H bond cleavage mechanism for $[\text{Fe}^{\text{V}}(\text{O})(\text{OAc})(\text{mcp})]^{2+}$	183
Chapter 9. Influence of the metal identity and solvent on the proton reduction activity of aminopyridine complexes	187
9.1. State-of-the-art	189
9.2. Results and discussion	190

9.2.1 Geometrical description of M^{II}/I -L intermediates.....	191
9.2.2 Origin of the solvent ligand coordination preference.....	193
9.2.3 Influence of solvent ligands on the proton reduction activity.....	195
Chapter 10. Computational study of electrochemical hydrogen production mechanisms by cobalt catalysts based on an aminopyridine ligand.....	200
10.1. State-of-the-art.....	202
10.2. Results and discussion.....	204
10.2.1 Proton reduction catalytic cycle in acidic media.....	205
10.2.2 Protonation of the pyridine ligands.....	209
10.2.3 Mechanistic role of pyridine moieties in the generation of cobalt hydride species.....	212
10.2.4 Intramolecular mechanism for hydrogen production.....	213
10.2.5 Global energy profile of the proton reduction catalytic cycle.....	214
Chapter 11. Computational study of photochemical hydrogen production by cobalt catalysts based on an aminopyridine ligand.....	217
11.1. State-of-the-art.....	219
11.2. Results and discussion.....	221
11.2.1 Solvent molecules exchange by $1Co^{II}$ under photochemical conditions.....	221
11.2.2 Electron transfer reactions between Et_3N , $[Ir^{II}(ppy)_2(bpy)]$ and $1Co^{II}$ catalyst.....	222
11.2.3 Protonation of the Cobalt(I) species in aqueous basic media.....	223
11.2.4 Heterolytic H-H bond formation mechanism.....	227
11.2.5 Homolytic H-H bond formation mechanism.....	229
11.2.6 Global energy profile of the photocatalytic proton reduction reaction.....	231
11.2.7 Electronic structure of relevant cobalt intermediates.....	232
Chapter 12. General Conclusions.....	236
References.....	242

ABSTRACT

One of the major technological and scientific challenges of our world is the substitution of fossil fuels by sustainable, renewable and clean energy sources. At present, the only resource that could cover the global energy demand and satisfy the previous requirements is sunlight. Catalytic transformations may allow the conversion of solar energy into a chemical fuel, facilitating its transport and storage. Nature has accomplished this goal through the photosynthesis process used by plants and cyanobacteria. In this process, the solar energy is converted to chemical energy and stored in carbohydrate molecules, which are generated from water and CO₂. The water oxidation (WO) reaction provides the necessary electrons and protons for the reduction of CO₂. This multiple proton-coupled electron transfer may be used to produce new fuels, as for instance the H₂ gas, which is considered a promising energy carrier. Unfortunately, efficient artificial catalysts are required to overcome the high energetic barriers that suppose the WO.

Many research groups are focusing their work in the development of artificial photosynthetic devices capable to produce H₂ and O₂ from the water splitting reaction. To achieve this goal, a water oxidation catalyst (WOC) and a proton reduction catalyst should work in a synergetic manner. The detailed knowledge of the mechanism will allow to enhance the catalytic performance and to ensure the compatibility of the two catalysts under the same reaction conditions. At this point, the Density Functional Theory (DFT) has proven to be very useful method to explore the reaction mechanisms and identify the active species. For this reason, this thesis centers its goals in the computational elucidation of the key steps and structural features that benefit both the water oxidation and proton reduction (PR) reactions.

The first part of this thesis focuses in the water oxidation reaction. Iron can be seen as a particularly attractive metal for designing WOCs because it is abundant, environmentally benign, and inexpensive. With this consideration in mind, our group reported a new family of non-heme Fe^{II} complexes for WO based on nitrogen chelating ligands. These complexes are among the first-row transition-metal systems with highest WO activity. Experimental data show that only tetradentate complexes with two labile *cis* positions are active when NaIO₄ or CAN sacrificial oxidants were used. In order to understand how these iron catalysts work, DFT calculations have been performed to: *i*) propose a catalytic cycle consistent with the experimental data and *ii*) to unravel the role of the ligand coordination number and mode in the WO activity. The key O-O bond formation step was modelled considering different oxidation states for the iron atom (IV and V). Computational studies supported by experimental data permitted to understand which factors make feasible the WO process and opened a new way for the *in silico* design of more efficient iron based WOCs. We have also investigated the H₂ activation by the α -[Fe^{II}(CF₃SO₃)₂(mcp)] complex, and discussed its convenience in the construction of water splitting devices.

It was recently reported the first example of a well-characterized inner-sphere complex to be formed in the CAN-mediated water oxidation, based on the complex α -[Fe^{II}(CF₃SO₃)₂(mcp)]. The Fe^{IV}(O)-O-Ce^{IV} intermediate is an iron-based analog of the oxygen evolving complex present in the photosystem II. To achieve a complete mechanistic picture of the iron catalyzed WO, we have carried also a computational study to elucidate the structure, speciation and reactivity of the Fe^{IV}(O)-O-Ce^{IV} adduct. DFT calculations reveal that the Lewis acid role of the cerium cation strongly benefits the kinetics of the O-O bond formation event.

The second part of this thesis focuses in the proton reduction reaction. Recently, we reported the synthesis and characterization of new cobalt, nickel and iron aminopyridine complexes with

electrocatalytic activity for PR. However, the cobalt complex is also active under photochemical conditions. In order to understand how these catalysts work, we have carried DFT calculations to: *i*) identify the active species; *ii*) to propose viable catalytic cycles for the photochemical and electrochemical driven H₂ generation and *iii*) to understand the role of the ligand, the reaction conditions and the metal on the proton reduction activity. Quantum mechanical analysis supported by experimental data unraveled the factors that benefit the proton reduction reaction. This data may guide the synthesis of more efficient proton reduction catalysts.

RESUM

Un dels principals reptes tecnològics i científics del nostre món és la substitució dels combustibles fòssils per fonts d'energia sostenibles, renovables i netes. Actualment, l'únic recurs que podria cobrir la demanda mundial d'energia i satisfer aquests requisits és la llum solar. Transformacions catalítiques permetrien la conversió de l'energia solar en un combustible químic, facilitant el seu transport i emmagatzematge. La naturalesa ha aconseguit aquest objectiu gràcies al procés de la fotosíntesi utilitzat per les plantes i cianobacteris. En aquest procés l'energia solar es converteix en energia química i s'emmagatzema en molècules d'hidrats de carboni, que es generen a partir d'aigua i CO_2 . La reacció d'oxidació de l'aigua (OA) proporciona els electrons i protons necessaris per a la reducció del CO_2 . Aquesta transferència múltiple i acoblada d'electrons i protons pot ser utilitzada per produir nous combustibles, com per exemple el gas H_2 , el qual es considera un portador d'energia prometedora. Malauradament, es requereixen catalitzadors artificials que puguin superar l'elevada barrera energètica que suposa el procés d'OA.

Molts grups de recerca estan centrant el seu treball en el desenvolupament de dispositius fotosintètics artificials capaços de produir H_2 i O_2 a partir de la reacció de dissociació de l'aigua. Per aconseguir aquest objectiu, un catalitzador d'oxidació de l'aigua (COA) i un catalitzador de reducció de protons (CRP) han de treballar de manera sinèrgica. El coneixement detallat del mecanisme permetrà millorar el rendiment catalític i garantir la compatibilitat dels dos catalitzadors sota les mateixes condicions de reacció. En aquest punt, la Teoria del Funcional de la Densitat (DFT) ha demostrat ser un mètode molt útil per explorar els mecanismes de reacció i identificar les espècies actives. Per aquesta raó, aquesta tesi centra el seus objectius en l'elucidació computacional de les etapes fonamentals i les característiques estructurals que beneficien tant les reaccions d'OA com la reducció de protons (RP).

La primera part d'aquesta tesi es centra en l'oxidació de l'aigua. El ferro és un metall particularment atractiu per al disseny de COAs, ja que és abundant, ambientalment benigne, i barat. Amb aquesta consideració en ment, el nostre grup va publicar una nova família de complexos de Fe^{II} no hemo per a l'OA basada en lligands quelants de nitrogen. Aquests complexos són uns dels catalitzadors basats en un metall de la primera sèrie de transició que presenten activitats de OA més altes. Les dades experimentals mostren que només els complexos amb dues posicions *cis* làbils són actius quan s'utilitzen NaIO_4 o CAN com a oxidants de sacrifici. Per tal de comprendre com funcionen aquests catalitzadors de ferro s'han realitzat càlculs DFT per a: *i*) proposar un cicle catalític coherent amb les dades experimentals i *ii*) per descobrir el rol que tenen el nombre i el mode de coordinació del lligand en l'activitat d'OA. El pas clau de la formació de l'enllaç O-O es va modelar tenint en compte diferents estats d'oxidació per l'àtom de ferro (IV i V). Estudis computacionals recolzats per les dades experimentals van permetre comprendre els factors que fan possible el procés d'OA i van obrir un nou camí per al disseny *in silico* de COA més eficients basats en ferro. També hem investigat l'activació de l' H_2 per part del complex $\alpha\text{-}[\text{Fe}^{\text{II}}(\text{CF}_3\text{SO}_3)_2(\text{mcp})]$ i discutit la seva conveniència en la construcció de dispositius de dissociació de l'aigua.

Recentment es va publicar el primer exemple d'un complex d'esfera interna ben caracteritzat format en la reacció d'oxidació amb CAN, basat en el complex $\alpha\text{-}[\text{Fe}^{\text{II}}(\text{CF}_3\text{SO}_3)_2(\text{mcp})]$. L'intermedi $\text{Fe}^{\text{IV}}(\text{O})\text{-O-Ce}^{\text{IV}}$ és un anàleg basat en ferro del complex generador d'oxigen present en el fotosistema II. Per aconseguir una imatge completa del mecanisme de l'OA catalitzada amb ferro, hem realitzat també un estudi computacional per a elucidar l'estructura, la especiació i la reactivitat de l'adducte $\text{Fe}^{\text{IV}}(\text{O})\text{-O-Ce}^{\text{IV}}$. Els càlculs DFT revelen que el paper d'àcid de Lewis del catió ceri afavoreix dràsticament la cinètica de la formació de l'enllaç O-O.

La segona part d'aquesta tesi es centra en la reducció de protons. Recentment, vam publicar la síntesi i caracterització de nous complexos aminopiridínics de cobalt, níquel i ferro amb activitat electrocatalítica per a la RP. No obstant, el complex de cobalt també és actiu en condicions fotoquímiques. Per tal d'entendre com funcionen aquests catalitzadors, hem realitzat càlculs DFT per a: *i*) identificar les espècies actives; *ii*) proposar cicles catalítics viables per a la generació fotoquímica i electroquímica del H₂ i *iii*) per entendre el paper del lligand, les condicions de reacció i el metall en l'activitat catalítica. L'anàlisi mecanoquàntic recolzat per dades experimentals ha desentranyat els factors que beneficien la reacció de reducció de protons. Aquestes dades poden guiar la síntesi de catalitzadors més eficients per a la reducció de protons.

RESUMEN

Uno de los principales retos tecnológicos y científicos de nuestro mundo es la sustitución de los combustibles fósiles por fuentes de energía sostenibles, renovables y limpias. Actualmente, el único recurso que podría cubrir la demanda mundial de energía y satisfacer estos requisitos es la luz solar. Transformaciones catalíticas permitirían la conversión de la energía solar en un combustible químico, facilitando su transporte y almacenamiento. La naturaleza ha conseguido este objetivo gracias al proceso de la fotosíntesis utilizado por las plantas y cianobacterias. En este proceso la energía solar se convierte en energía química y se almacena en moléculas de hidratos de carbono, que se generan a partir de agua y CO_2 . La reacción de oxidación del agua (OA) proporciona los electrones y los protones necesarios para la reducción del CO_2 . Esta transferencia múltiple y acoplada de electrones y protones puede ser utilizada para producir nuevos combustibles, como por ejemplo el gas H_2 , el cual se considera un portador de energía prometedor. Desgraciadamente, se requieren catalizadores artificiales que puedan superar la elevada barrera energética que supone el proceso de OA.

Muchos grupos de investigación están centrando su trabajo en el desarrollo de dispositivos fotosintéticos artificiales capaces de producir H_2 y O_2 a partir de la reacción de disociación del agua. Para conseguir este objetivo, un catalizador de oxidación del agua (COA) y un catalizador de reducción de protones deben trabajar de manera sinérgica. El conocimiento detallado del mecanismo permitirá mejorar el rendimiento catalítico y garantizar la compatibilidad de los dos catalizadores bajo las mismas condiciones de reacción. En este punto, la Teoría del Funcional de la Densidad (DFT) ha demostrado ser un método muy útil para explorar los mecanismos de reacción e identificar las especies activas. Por ello, esta tesis centra sus objetivos en la elucidación computacional de las etapas fundamentales y las características estructurales que benefician tanto las reacciones de oxidación del agua como la reducción de protones (RP).

La primera parte de esta tesis se centra en la oxidación del agua. El hierro es un metal particularmente atractivo para el diseño de COAs, ya que es abundante, inocuo para el medio ambiente y barato. Con esta consideración en mente, nuestro grupo publicó una nueva familia de complejos de Fe^{II} no hemo para la OA basada en ligandos quelantes de nitrógeno. Estos complejos son unos de los catalizadores basados en un metal de la primera serie de transición que presentan actividades de OA más altas. Los datos experimentales muestran que sólo los complejos con dos posiciones *cis* lábiles son activos cuando se utilizan NaIO_4 o CAN como oxidantes de sacrificio. Para comprender cómo funcionan estos catalizadores de hierro, se han realizado cálculos DFT para: *i*) proponer un ciclo catalítico coherente con los datos experimentales y *ii*) para desentrañar el rol que tienen el número y el modo de coordinación del ligando en el actividad de OA. El paso clave de la formación del enlace O-O se modeló teniendo en cuenta diferentes estados de oxidación para el átomo de hierro (IV y V). Estudios computacionales apoyados por los datos experimentales permitieron comprender los factores que hacen posible el proceso de OA y abrir un nuevo camino para el diseño *in silico* de COA más eficientes basados en hierro. También hemos investigado la activación del H_2 por parte del complejo $\alpha\text{-}[\text{Fe}^{\text{II}}(\text{CF}_3\text{SO}_3)_2(\text{mcp})]$ y discutido su conveniencia en la construcción de dispositivos de disociación del agua.

Recientemente se publicó el primer ejemplo de un complejo de esfera interna bien caracterizado formado en la reacción de oxidación con CAN, basado en el complejo $\alpha\text{-}[\text{Fe}^{\text{II}}(\text{CF}_3\text{SO}_3)_2(\text{mcp})]$. El intermedio $\text{Fe}^{\text{IV}}(\text{O})\text{-O-Ce}^{\text{IV}}$ es un análogo basado en hierro del complejo generador de oxígeno presente en el fotosistema II. Para conseguir una imagen completa del mecanismo de la OA catalizada con hierro, hemos realizado también un estudio computacional para elucidar la estructura,

la especiación y la reactividad del aducto $\text{Fe}^{\text{IV}}(\text{O})\text{-O-Ce}^{\text{IV}}$. Los cálculos DFT revelan que el papel de ácido de Lewis del catión cerio favorece drásticamente la cinética de la formación del enlace O-O.

La segunda parte de esta tesis se centra en la generación de H_2 . Recientemente, publicamos la síntesis y caracterización de nuevos complejos aminopiridínicos de cobalto, níquel y hierro con actividad electrocatalítica para la RP. No obstante, el complejo de cobalto también es activo en condiciones fotoquímicas. Para entender cómo funcionan estos catalizadores, hemos realizado cálculos DFT para: *i*) identificar las especies activas; *ii*) proponer ciclos catalíticos viables para la generación fotoquímica y electroquímica del H_2 y *iii*) para entender el papel del ligando, las condiciones de reacción y el metal en la actividad catalítica. El análisis mecanocuántico apoyado por datos experimentales ha desentrañado los factores que benefician la reacción de reducción de protones. Estos datos pueden guiar la síntesis de catalizadores más eficientes para la reducción de protones.

CHAPTER 1:

GENERAL INTRODUCTION

1. GENERAL INTRODUCTION

1.1. World Energetic Problem

The increasing world energy demand as a result of the fast expansion of the population, combined with the depletion of the petroleum supplies, makes the current energy consumption model unsustainable. Recent statistics reveal that in 2013 the industrialized countries consumed an average power of 18 TW¹ and predicted to increase by 56% between 2010 and 2040.² Moreover, the CO₂ derived from the combustion of fossil fuels is considered one of the main greenhouse gases responsible for global warming, which may have catastrophic consequences for all life forms. For these reasons, a lot of efforts have been focused in the development of alternative fuels which should be environmentally friendly, present an affordable economic cost and ensure the future energy demands of humanity. The only energy source that meets these requirements and presents a high availability in most regions of the planet is sunlight.³

Currently, photovoltaic cells are used to capture solar energy and then transform it into electricity. However, the permanent energy supply is limited by the day/night cycles. Therefore, new ways to harvest and store the sunlight are required. One strategy to achieve this goal is the employment of catalytic transformations to directly convert the solar energy into chemical fuels. Among the proposals, the light driven catalyzed decomposition of water into molecular hydrogen and molecular oxygen is one of the most promising solutions, since the produced energy carrier H₂ can be used as a carbon-free and environmentally benign fuel. The construction of efficient artificial photoelectrochemical devices requires a detailed understanding of the interplay between the reductive and oxidative catalytic sites and the light harvesting components. A recent analysis of the performance of the large scale H₂ production shows that the optimization of the engineering aspects related to the sizing of photochemical devices and the use of light capturing components may reduce the costs of one kg of H₂ below \$2.90. Therefore, molecular hydrogen is a promising future fuel.⁴

1.2. The Photosynthesis

In Nature, the harvesting and storing of sunlight energy into chemical compounds is achieved in the so-called photosynthesis, which occurs in the thylakoid membrane of the chloroplast of green plants, algae and cyanobacteria.^{5,6} It is a complex chemical process in which water, carbon dioxide and sunlight are combined to generate valuable natural products such as carbohydrates and oxygen.



The photosynthesis proceeds through light dependent and light independent reactions. Three enzymes cooperate in the photosynthesis reaction steps: the photosystem II (PSII), the cytochrome-b₆f and the photosystem I (PSI). The photosynthetic mechanism starts with an initial light absorption by a group of chlorophylls and carotenoid antennas (Ant) in PSII, reaching the corresponding excited states (Figure 1). The previous light harvesting complexes deliver the energy to the reduced form of photosensitizer chlorophyll dimer P₆₈₀. The excited state P₆₈₀^{*} transfers one electron to a pheophytin (Ph) molecule generating the oxidized form of P₆₈₀ (P₆₈₀⁺). Then, the PSII catalyzes several proton-coupled electron transfer reactions on plastoquinone molecules (PQ_A and PQ_B) to generate plastoquinol (PQH₂) species. The subsequent electron transfer from PQH₂ to a plastocyanin (PC, copper based protein) is catalyzed by cytochrome-b₆f. In the last step of the electron transfer chain, the PSI enzyme aids to mediate the electron transfer from the PC to the ferredoxin-NADP⁺ reductase enzyme (FDR), an iron-sulfur protein which reduces the nicotinamide adenine

dinucleotide phosphate (NADP^+) molecule to NADPH. Finally, the NADPH is consumed in the Calvin cycle to convert the CO_2 to carbohydrates.

P_{680}^+ has enough oxidizing power (1.2 V vs. NHE) to generate a radical on a tyrosine residue (Yz), which in turn will oxidize a manganese based cluster known as oxygen evolving complex (OEC) present in PSII.⁷ The latter can recover the extracted electrons by oxidizing a nearby water molecule. Consequently, the water oxidation (WO) in PSII generates the electrons and the protons required to reduce the CO_2 to carbohydrates.⁸ The PSII metalloprotein system oxidizes water more efficiently than any synthetic catalyst, with a turnover number (TON) of 180,000 molecules of O_2 per site and a turnover frequency (TOF) above 300 s^{-1} .^{9,10} Only two artificial systems have been reported that proceed at similar rates.^{10,11}

During the past decades sustainable efforts have been directed at the elucidation of the WO mechanism and the OEC structure from experimental and computational points of view. Technical advances in X-ray structure analysis have led to great progress in the characterization of OEC cluster. Most recent experimental data about the PSII structure, published by Nobuo and co-workers in 2011, provided the most accurate OEC structure.¹² The X-ray structure shows that three manganese and one calcium atoms are linked by four oxygen atoms, forming a cubane-like structure; a fourth manganese atom dangles outside the cubane center and is linked to it by two oxygen atoms. Five water molecules interact with the Mn_4Ca cluster: one to an oxo group, two coordinate to the dangling manganese, and the other two to the calcium atom.

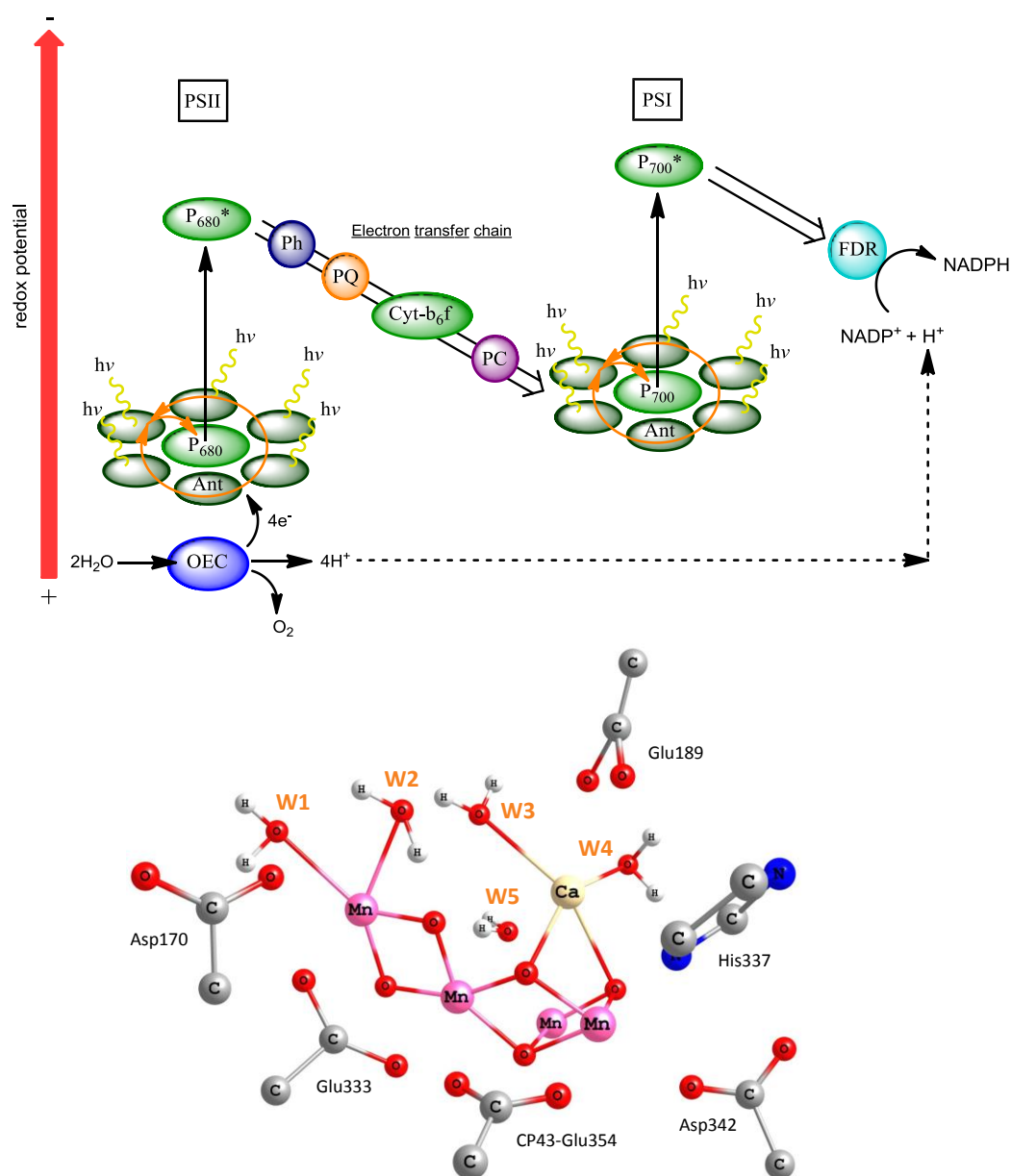


Figure 1: Above, schematic representation of the photosynthetic process, with the light driven redox steps giving rise to O_2 evolution and NADPH formation. The P_{680} and P_{700} are chlorophyll photosensitizers, OEC = oxygen evolving complex, Ant = antennas, Ph = pheophytin, PQ = plastoquinone, Cyt- b_6/f = Cytochrome- b_6/f , PC = plastocyanin, FDR = ferredoxin- NADP^+ reductase enzyme and NADP^+ = nicotinamide adenine dinucleotide phosphate. Below, structure of oxygen-evolving complex (OEC), a Mn_4Ca cluster where the metal atoms are oxo bridged. The structure has been built from crystallographic data reported on ref. 12.

There has been also much interest in the water oxidation mechanism at OEC, and some mechanisms have been proposed relating the structure of the distorted Mn_4CaO_5 cubane to its WO activity.¹³ Despite the wealth of experimental information available, the mechanism for this fundamental reaction is not yet fully understood. It is well-known to occur *via* four successive light driven proton-coupled electron transfer steps, that convert the most reduced S_0 state of the Mn_4Ca cluster to the active S_4 state, step where O_2 is released, in the so-called Kok cycle (Figure 2a). Finally, two water molecules coordinate to the manganese cluster, recovering the S_0 state. The

oxidation states of the manganese atoms involved in the various S states are uncertain and it has been proposed various possible structures for the S₄ Kok cycle. In all cases, oxygen evolution is proposed to arise from oxo groups associated with a highly oxidized Mn₄Ca cluster.¹⁴ One of the mechanisms proposed for the O-O bond formation involves the nucleophilic attack of water molecule on a Mn^V-oxo group (Figure 2A),¹⁵ which can be previously activated by the interaction with the calcium atom (Figure 2B). Alternatively, the O-O bond formation could occur by coupling of two Mn^{IV}=O centers with radical character (Figure 2C) or two oxo bridging groups (Figure 2D).⁶

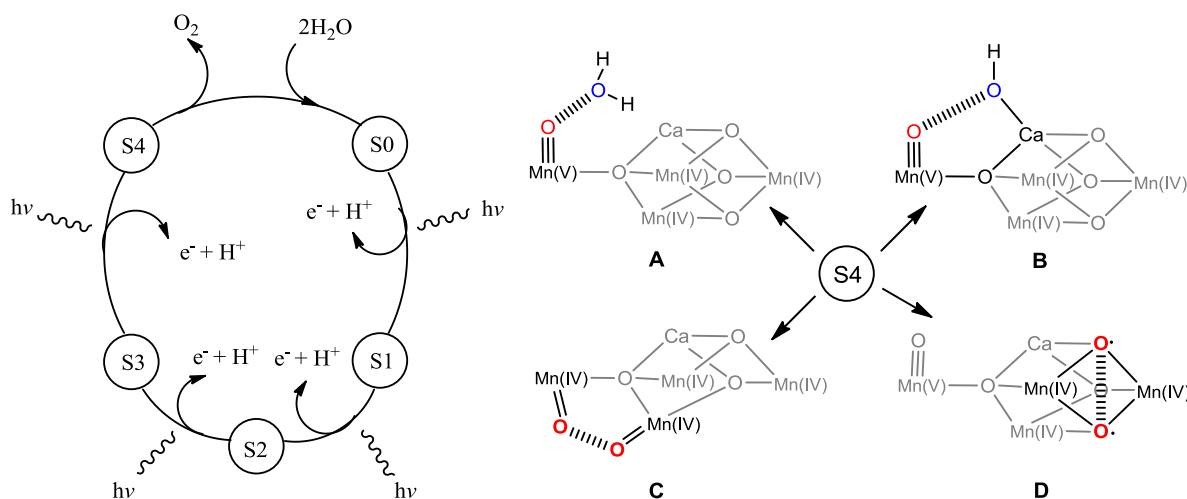
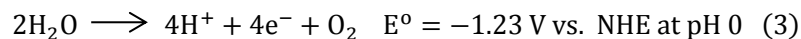
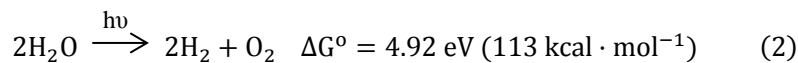


Figure 2: On the left, Kok cycle for the water oxidation mechanism in OEC cluster. On the right, some proposed O-O bond formation mechanisms at the S₄ state of the Mn₄CaO₅ cluster in the PSII.

1.3. Artificial Photosynthesis

Chemists have been inspired in the natural Photosynthesis to develop synthetic systems to catalyze the light driven decomposition of water. The water splitting reaction (Eq. 2) is a multiple proton-coupled electron transfer (PCET) process which can be divided in two half-reactions: the water oxidation (Eq. 3) and the proton reduction (PR) (Eq. 4):¹⁶



Water oxidation is energy demanding half-reaction and then it is the bottleneck of the whole water splitting process. Therefore, the design of optimal water oxidation catalysts (WOCs) is imperative to construct efficient artificial photosynthetic systems. The WOCs have to reach a high oxidation state and form M-O bonds to produce O₂. This coupled chemical and redox processes can be accomplished by different oxidative methods such the use of electric current, photosensitizers ([Ru^{II}(bpy)₃]²⁺), single electrons transfer reagents ((NH₄)₂Ce^{IV}(NO₃)₆ and [Co^{III}(NH₃)₅Cl]²⁺) or oxo-transfer salts such sodium hypochlorite (NaOCl), Oxone (KSO₅) and sodium periodate (NaIO₄).

On the other hand, the structural and/or functional design of proton reduction catalysts (PRC) has found inspiration in the Hydrogenase metalloprotein systems (see section 1.5). The PR reaction

can be achieved by electrochemical or photochemical methods. In the latter, it is required the combination of a photosensitizer, the catalyst and a sacrificial electron donor like ascorbate or trimethylamine (Et_3N). The general photochemical mechanism starts with the electron transfer from the excited state of the photosensitizer to the proton reduction catalyst. Then, the reduced catalyst generates H_2 and the photosensitizer recovers its initial state by accepting electrons from the sacrificial reductant.

1.4. Artificial Water Oxidation Catalysts

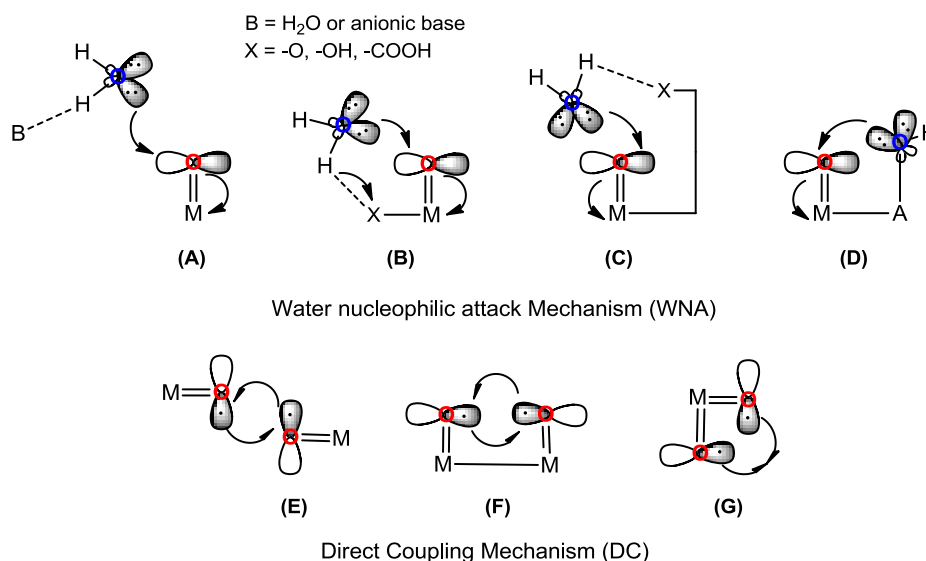
The carboxylate groups from the amino acid residues surrounding the OEC and the oxo bridging ligands are essential to stabilize the high oxidation state of intermediates in the Mn_4Ca cluster.^{16b} This structural arrangement has inspired chemists to design homogeneous WOCs based on transition metals and organic moieties containing N and O chelating atoms. These systems avoid the protein scaffolding that often complicates the comprehension of the WO mechanism of the natural systems. Therefore, the homogeneous molecular WOCs are ideal platforms to understand the key steps of the WO mechanism and which factors enhance this reactivity. In this section, the mechanistic studies of some relevant homogeneous WOCs will be summarized based on electrochemical, kinetic, spectroscopic and computational data. This information permits the construction of a comprehensive picture of the WO reaction at a molecular level.

1.4.1 O-O bond formation pathways

The development of transition metal complexes that efficiently catalyze the water oxidation to O_2 requires a detailed mechanistic knowledge of the different steps of the catalytic process. Among the main steps elucidated contributing to the WO (M-OH_2 oxidation to M=O , O-O bond formation and O_2 release) one of the most important is the O-O bond formation event. There are two main pathways for the O-O bond formation mechanism, known as the water nucleophilic attack (WNA) and the direct coupling (DC) (Scheme 1).^{14,17} The former implies the nucleophilic attack of a water molecule or hydroxide group to a metal-oxo electrophilic group, resulting in a formal two electron reduction of the metal center. The nucleophilic attack leads to the formation of an O-O bond with σ symmetry along with the reduction of the M-O π bond character and oxidation state at the metal center. Different strategies can be used to achieve catalytic water oxidation through the WNA pathway. One is the assistance of an external base, which might facilitate the O-O bond formation by enhancing the nucleophilic character of the water molecule (Scheme 1A). The basic fragment can be also introduced in the coordination sphere of the metal, for instance in *cis* position respect to the oxo ligand (Scheme 1B). This allows the reduction of the entropy contribution to the O-O bond formation barrier. Furthermore, a basic pendant ligand can be incorporated over the complex active site to ensure the proper orientation of the water substrate to the oxo group (Scheme 1C). In both cases the basic motive might facilitate the reactants interaction in the right geometric disposition. A second strategy consists in the employment of external or internal (present in the complex structure) Lewis acids to assist the O-O bond formation (Scheme 1D).

The DC mechanism implies the interaction of two metal-oxo groups with radical character, forming a peroxo intermediate. This picture has been implicated in the design of two center WOCs, in which the reduction of the intermolecular repulsion and the increase of the spin density on the oxo moiety will encourage the coupling. The DC pathway can proceed with the coupling of two metal-oxo fragments from different metal complex (Scheme 1E) or embedded in the same catalyst (Scheme 1F). In the latter case, flexible ligand architecture should be considered to allow the system

to approach the metal-oxo moieties. Alternatively, the O-O bond formation can be triggered by the coupling of two *cis*-oxo ligands present on the same metal center (Scheme 1G).



Scheme 1: Fundamental description of the WNA and the DC mechanisms of water oxidation.

On the basis of the ligand field theory, a qualitative explanation can be provided of how the WNA or DC reactivity is determined by the local geometry of the metal-oxo complex and the electron configuration.¹⁴ In most of the reported WOCs, the metal-oxo moiety resides in a pseudooctahedral or square pyramidal coordination environment. For these two geometries, the frontier molecular orbital (MO) splitting pattern respect to an O_h field is very similar to that exerted by a tetragonal field (Figure 3). According to the tetragonal MO splitting diagram, the number of d-electrons and the occupation of the M-O π* orbitals determine the electrophilic or radical character of the M-O moiety.¹⁸ The WNA mechanism requires the occupation of a half-filled or empty e(d_{xz}, d_{yz}) LUMO orbital by the electron pair of the water molecule. Only even electron systems with a d⁰, d² or d⁴ electronic configurations satisfy this condition. On the other hand, the DC mechanism is only possible for d¹ or d³ odd electron configurations, which give rise to the radical character of the metal-oxo. However, this qualitative explanation does not take into account the differences between low and high spin state electron configurations, which determine the strength of the metal-oxo bond and the preferred reaction pathway, and the steric effects. The spin influence depends of the electronic structure and geometry of the system under study and it can only be addressed computationally.

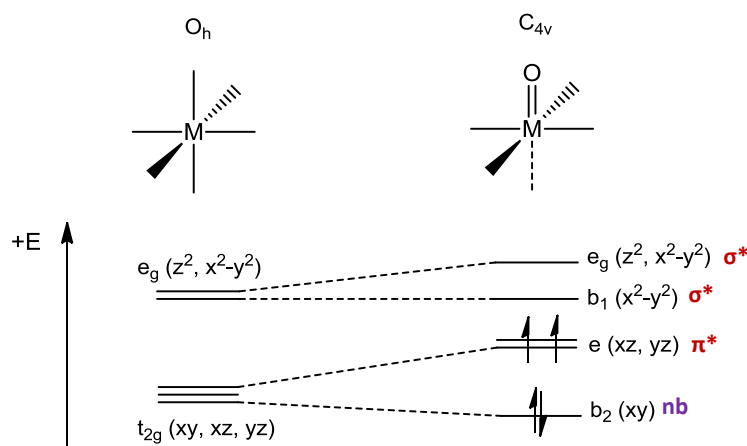


Figure 3: Qualitative frontier MO splitting diagrams for an octahedral metal complex (left) and a metal-oxo residing in a tetragonal field (right). A d^4 electron counting is shown

Many studies try to adjust the electronic and geometric parameters of the catalysts to induce WO reactivity following the WNA or DC mechanisms. However, the emergence of single center WOCs demonstrates that one metal center is enough to oxidize the water molecule through a WNA mechanism.

The O-O bond formation reaction is one of the main topics of the presented thesis. Detailed knowledge about how the O-O bond forms and how can be controlled through computational studies. Likewise, different oxidation states and electronic configurations can be examined. Therefore, the following mechanistic review will mainly focus on the generation of the O-O bond. In addition, other relevant aspects, such as the nature of active species and catalyst decomposition pathways, will be considered.

1.4.2 Earth-scarce Transition Metal-based WOCs

1.4.2.1 Ruthenium based WOCs

Since the early work of Meyer and co-workers¹⁹ on the blue dimer catalyst $[(bpy)_2(OH_2)Ru^{III}-O-Ru^{III}(OH_2)(bpy)_2]^{4+}$ (**1**, Figure 4; $bpy = 2,2'$ -bipyridine) back in 1982, a large quantity of Ru based WOCs have been synthesized. Up to date, Ru complexes are the best studied family of WOC from the experimental and mechanistic point of view.²⁰ Beside the blue dimer, and among other dimeric ruthenium systems, the Llobet's catalyst $[(terpy)_2(OH_2)Ru^{II}-L-Ru^{II}(terpy)_2(OH_2)]$ (**2**, Figure 4; $terpy = 2,2':6',2''$ -terpyridine, $L = bis(2\text{-pyridyl})\text{-}3,5\text{-pyrazolate}$),²¹ has been shown to be a WOC. The key intermediates that lead to the O-H bond formation in these complexes are obtained after a stepwise PCET events promoted by the addition of four equivalents of oxidant (cerium ammonium nitrate, CAN), after which the O-O bond formation occurs. Like is the Kok cycle in PSII, the catalyst evolves through series of each time more oxidized stages until the O-O bond is form.

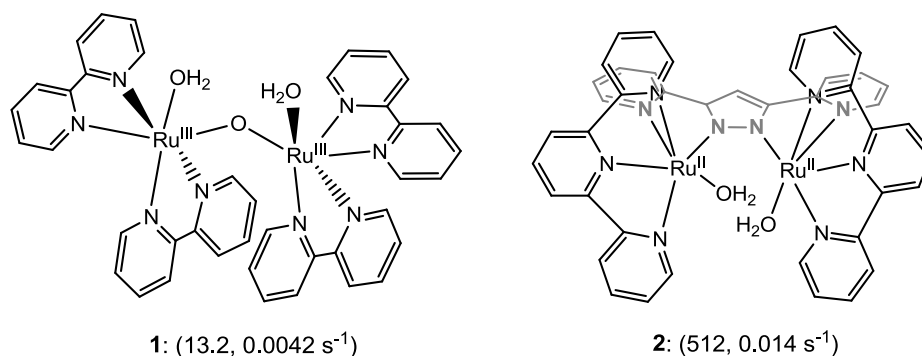


Figure 4: The Meyer's blue dimer (**1**, left) and the Llobet's (**2**, right) Ru catalysts for water oxidation. TON and TOF values are shown in parentheses, respectively.

Complex **1** presented a TON of 13.2 and a TOF of 0.004 s⁻¹. On the other hand, complex **2** is more active with a TON of 512 and TOF of 0.014 s⁻¹. By kinetic and ¹⁸O isotopic labeling studies, a water oxidation mechanism for both catalysts, **1** and **2**, has been proposed. The results suggested that the DC mechanism was more favored for Llobet's catalyst,¹⁷ while the WNA mechanism was more probable for the blue dimer.²²

Later on, Siegbahn and co-workers performed a theoretical investigation of the entire cycle for both catalysts and mechanisms at DFT(B3LYP*) level²³ (in Figure 5). The authors studied the postulated WNA and DC mechanism and in addition they and additional pathway where one of the two oxo groups at the ruthenium centers is protonated. For the blue dimer, the most favorable pathway implies the formation of a high valent dinuclear Ru^V(OH)-O-Ru^V(O) species after several redox steps. The water nucleophilic attack to form a O-O bond is induced by the assistance of an adjacent hydroxyl ligand, obtaining a Ru^{IV}(OH₂)-O-Ru^{IV}(OOH) intermediate. The deprotonation of the hydroperoxo group leads to O₂ releasing and generates an open vacant site on a dinuclear Ru^{III} species. The open vacant site is then occupied by a water molecule, recovering the initial state of the catalyst. Thus, the blue dimer induces the O-O bonding through a WNA mechanism, with a DFT computed O-O bond formation energy barrier of 17.6 kcal·mol⁻¹, while the energy barrier for the DC mechanism is 21.5 kcal·mol⁻¹. However, the TOF-determining transition state (TDTS) of the process is found in the earlier redox steps ($\Delta G^\ddagger = 22.0$ kcal·mol⁻¹, in agreement with the 20-21 kcal·mol⁻¹ derived from the TOF). The oxygen release is easier to achieve for the blue dimer, since O₂ is weakly bonded to Ru^{IV}.

Hurst and coworkers proposed an alternative mechanism in which the WNA occurs on an activated bpy ligand instead of a Ru^V=O moiety. The oxidation of the bpy ligand favors the nucleophilic attack of a second water molecule on the bi-pyridine (bpy). Finally, the O-O coupling takes place on the bpy scaffold. It is expected that this type of reactivity may be related to the catalyst degradation under aqueous solution.

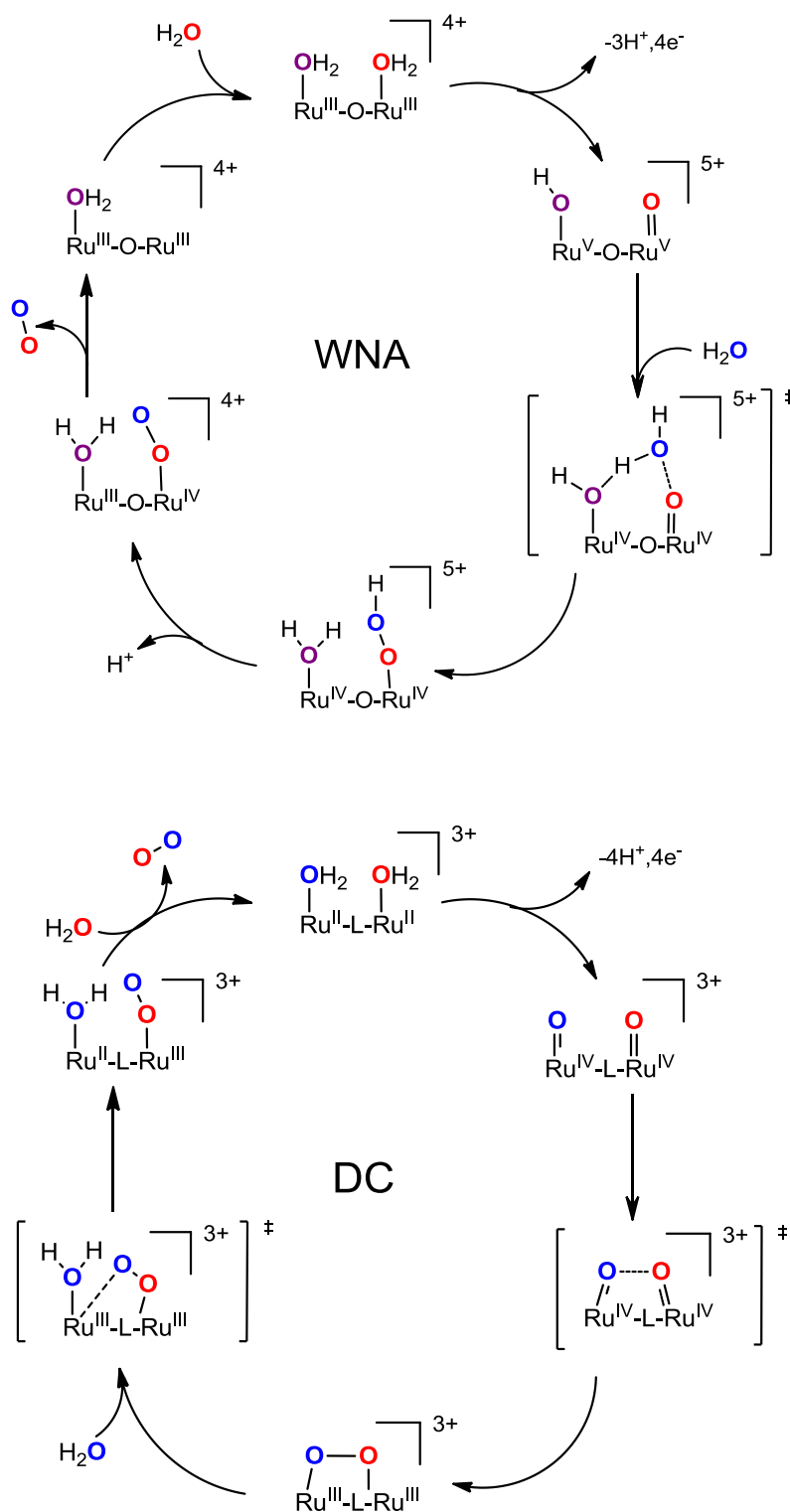


Figure 5: DFT proposed catalytic cycle for water oxidation in blue dimer (bottom) and Llobet (top) ruthenium catalysts.

The Llobet's catalyst cycle starts with the formation of a dinuclear $\text{Ru}^{\text{IV}}=\text{O}$ from the oxidation of $\text{Ru}^{\text{II}}(\text{OH}_2)\text{-L-Ru}^{\text{II}}(\text{OH}_2)$. A direct coupling of these metal-oxo radicaloid groups forms a dinuclear Ru^{III} peroxo intermediate. The incorporation of a water molecule in the coordination sphere of a Ru center favors the decooordination of the peroxo group and the subsequent O_2 releasing. Finally, the open vacant site is occupied by a water molecule, recovering the initial state of the catalyst. In

Llobet's catalyst the O-O bond formation involves a DC mechanism and the O₂ release is the rate limiting step with a DFT energy barrier of 21.9 kcal·mol⁻¹. On the contrary, for this catalyst the O-O bond formation event is the rate limiting step ($\Delta G^\ddagger = 32.2$ kcal·mol⁻¹) of the WNA mechanism.

Since the discovery of mononuclear Ru WOCs, it has been realized that a multimetallic framework is not an intrinsic design to obtain water oxidation catalysis. In the last decade, a huge number of single center Ru WOCs has been synthesized and their catalytic mechanisms were studied by spectroscopic, electrochemical, and kinetic experiments. In 2005, Thummel's group reported the first family of mononuclear ruthenium(II) complexes based on the tridentate polypyridyl ligand pbn (2,2'-[4-(tert-butyl)pyridine-2,6-diyl]bis(1,8-naphthyridine)) (**3-5**, Figure 6) capable to oxidize water using CAN as oxidant.²⁴ These aqua complexes are stabilized thanks to a hydrogen bond interaction between the uncoordinated naphthyridine nitrogens moieties and the aqua ligand. UV-Vis studies reveal that the incorporation of a NMe₂ electro-donating group in the *para* position of the axial pyridine rings (complex **3**) favors the oxidation to the corresponding Ru^{III} intermediate, although his complex presents the lower WO activity. The authors did not conduct any mechanistic study, although preliminary DFT(B3LYP) calculation were performed suggesting that high valent active species may possess a seven-coordination sphere.²⁵

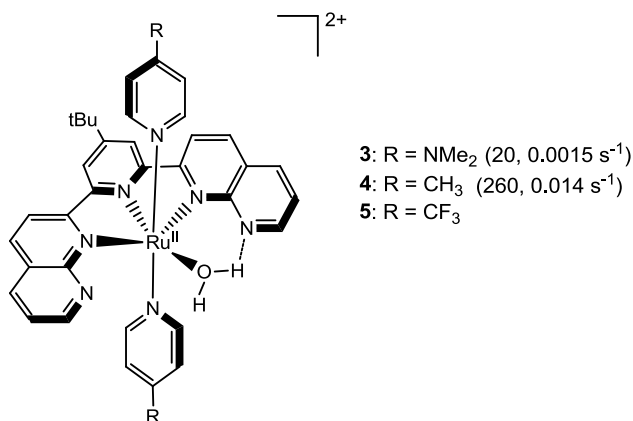


Figure 6: Thummel's ruthenium(II) complexes for water oxidation. TON and TOF values are shown in parentheses, respectively.

The water oxidation mechanistic study for complexes [Ru^{II}(terpy)(bpm)(OH₂)²⁺] (**6**; bpm = 2,2'-bypyrimidine) and [Ru^{II}(terpy)(bpz)(OH₂)²⁺] (**7**; bpz = 2,2'-bipyrazine) was performed by Meyer and coworkers in 2008 (Figure 7).²⁶ Thermodynamic and kinetic data reported suggests that the starting [Ru^{II}-OH₂]²⁺ reactant is oxidized and deprotonated by CAN to reach [Ru^V=O]³⁺ active species. A WNA on this high valent intermediate produces a [Ru^{III}-OOH]²⁺ intermediate. Further oxidation and deprotonation of the later species may form the [Ru^{IV}-OO]²⁺. At this point, two proposed mechanisms may be followed by the ruthenium system to produce O₂: 1) a water molecule attacks the Ru^{IV} center and displace the molecular oxygen, or 2) [Ru^{IV}-OO]²⁺ is oxidized to [Ru^V-OO]³⁺ and then a water molecule displaces the molecular oxygen forming [Ru^{III}-OH]²⁺, restarting the catalytic cycle (Figure 8a). Experimental data suggest that, for systems **6** and **7**, O₂ release from [Ru^{IV}-OO]²⁺ is the rate determining-step.

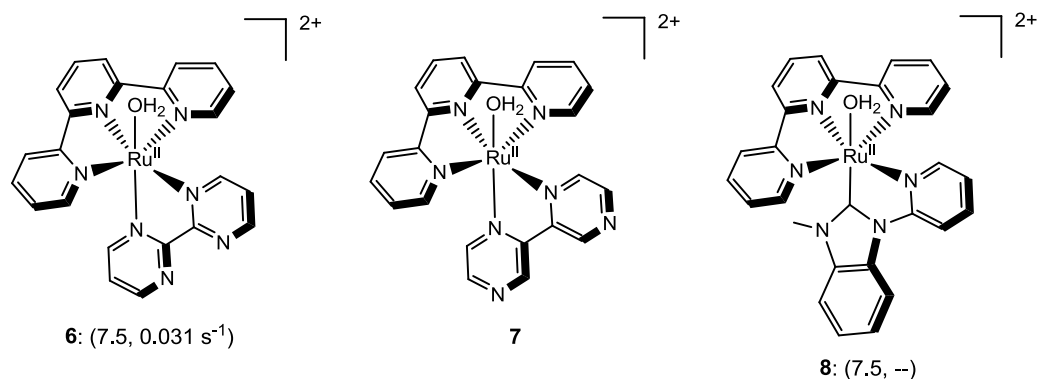


Figure 7: Molecular structure of complexes $[\text{Ru}^{\text{II}}(\text{terpy})(\text{bpm})(\text{OH}_2)]^{2+}$ (**6**), $[\text{Ru}^{\text{II}}(\text{terpy})(\text{bpz})(\text{OH}_2)]^{2+}$ (**7**) and $[\text{Ru}^{\text{II}}(\text{Mebimpy})(\text{bpy})(\text{OH}_2)]^{2+}$ (**8**). TON and TOF values are shown in parentheses, respectively.

Voorhis *et al.*, and later Meyer, Yang and coworkers, confirm this catalytic cycle by means of QM/MM (molecular mechanics) minimal free energy path simulations on complex **6** with the B3LYP density functional.^{27,28} These computational studies provided valuable information about the operational O-O bond formation mechanism. According to that, the WNA on the $\text{Ru}^{\text{V}}=\text{O}$ moiety is assisted by the bulk aqueous solvent, which accepts a proton from the nucleophilic water. Moreover, Meyer's group showed that the addition of a base (AcO^- , H_2PO_4^- and HPO_4^-) greatly enhanced the rates of electrocatalytic water oxidation for the catalyst $[\text{Ru}^{\text{II}}(\text{Mebimpy})(\text{bpy})(\text{OH}_2)]^{2+}$ (**8**, Figure 7; Mebimpy = 2,6-bis(1-methylbenzimidazol-2-yl)pyridine) and QM/MM minimal free energy path calculations confirm that the origin of this phenomena is the concerted atom-proton transfer (APT) to the base during the O-O bond formation event (Figure 8b).²⁹ Therefore, the structure of the first solvation shell and/or the presence of a base play a key role in the O_2 generation. Quantum mechanical calculations also indicate that the oxidation from Ru^{IV} to Ru^{V} presents a remarkable redox potential of 1.6-1.8 V vs NHE.

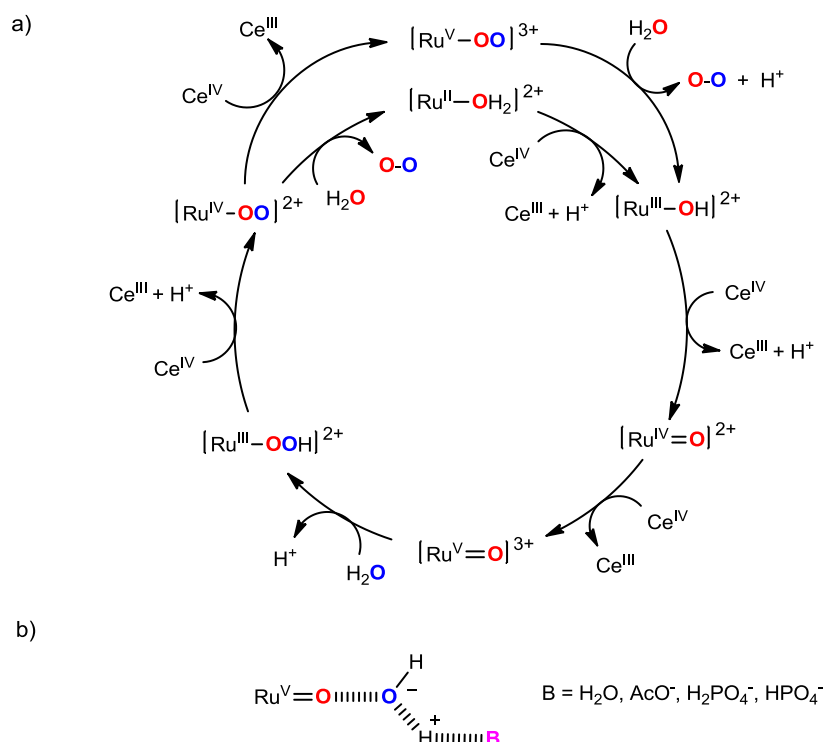


Figure 8: a) Proposed catalytic cycle for water oxidation by complexes **6** and **7**. b) Schematic representation of the APT mechanism.

In contrast with the previous single-site ruthenium systems, mechanistic studies and DFT calculations carried out by Fujita and Thummel in 2013 indicate that, under both neutral and basic conditions, complex **4** show an onset potential for catalytic WO that is lower than the $[\text{Ru}^{\text{V}}=\text{O}]^{3+}/[\text{Ru}^{\text{IV}}=\text{O}]^{2+}$ redox couple. This result is consistent with the preference for a direct PCET process coupled of $[\text{Ru}^{\text{IV}}=\text{O}]^{2+}\cdots(\text{H}_2\text{O})$ to yield the corresponding $[\text{Ru}^{\text{III}}-\text{OOH}]^{2+}$, which avoids the generation of high energetic $[\text{Ru}^{\text{V}}=\text{O}]^{3+}$ species.³⁰

It is well-known that, under photochemical conditions the excited state of polypyridyl-based ruthenium complexes such $[\text{Ru}^{\text{II}}(\text{bpy})_3]^{2+}$ can act as sacrificial oxidants in the WO reaction, but few have been found to catalyze this reaction. One example is complex $[\text{Ru}(\text{bpy})_2(\text{OH})_2]^{2+}$ (**8**, Figure 9), which can experiment a *cis/trans* photoisomerization to give the *trans* isomers **9**. In 1988, Meyer and coworkers anticipated on the basis of electrochemical experiments that complexes **8** and **9** may reach Ru^{VI}-bis-oxo species.³¹ They also suggested that the Ru^{VI} intermediate can participate as active species in the WO reaction. In 2010, Llobet *et al.* revealed that the *cis* isomer is more active than the *trans* one. Isotopic labelling studies and quantum mechanical calculations at M06-L and CASSCF/CASPT2 levels support a mechanism in which the O-O bond is generated by a WNA on a formal Ru^{VI}-bis-oxo ($\Delta G^\ddagger = 24.5 \text{ kcal}\cdot\text{mol}^{-1}$), instead of the intramolecular coupling of the two oxo moieties ($\Delta G^\ddagger = 57.5 \text{ kcal}\cdot\text{mol}^{-1}$) (Figure 9). The molecular orbital analysis of the RuO₂ π system reveals an electronic structure consistent with a $[\text{Ru}^{\text{III}}(\text{bpy})_2(\text{O}\cdot)(\text{O}^-)]^{2+}$, indicating that the Ru oxidation state is below the formal limit of VI.³²

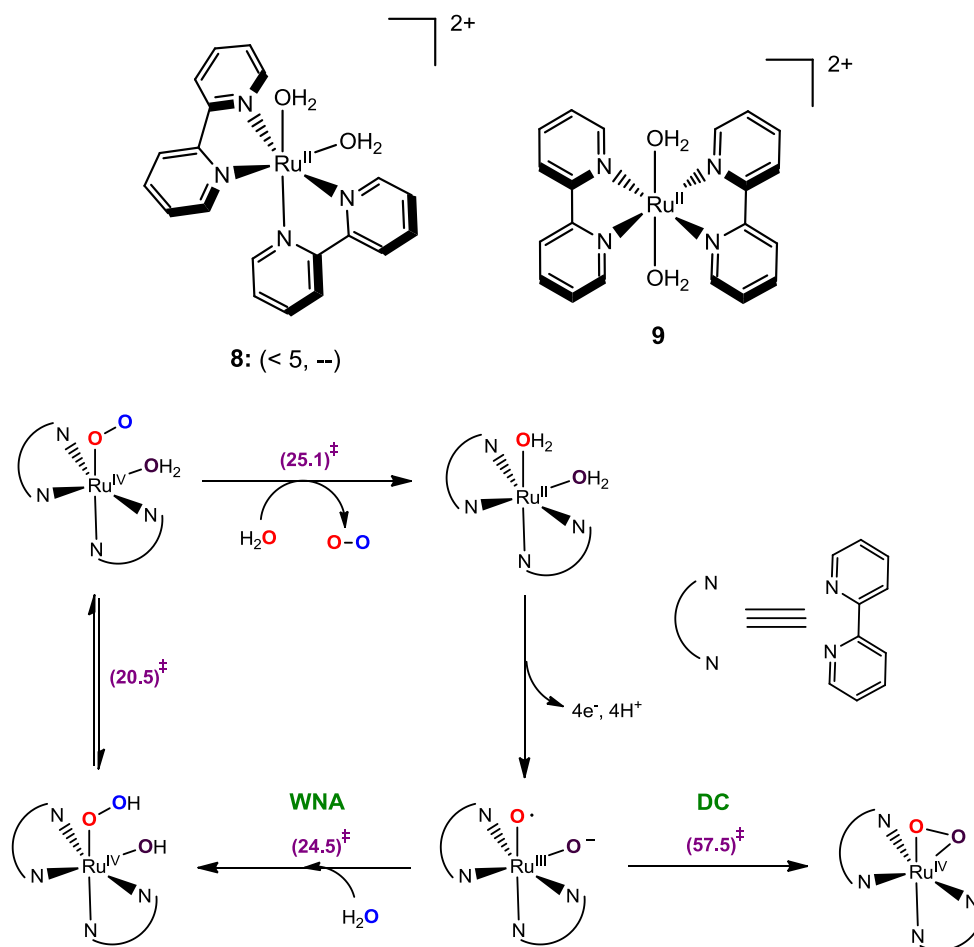


Figure 9: Molecular structure of complexes cis -[Ru^{II}(bpy)(OH₂)₂]²⁺ (**8**) and $trans$ -[Ru^{II}(bpy)(OH₂)₂]²⁺ (**9**) and DFT computed WNA and DC mechanisms for O-O bond formation by complex **8**. TON value is shown in parentheses. Gibbs energies are in kcal·mol⁻¹.

One can envision that inducing electronic perturbations on the metal by modification of ligand's structure may be a good strategy to optimize the energetic cost all the steps involved in the catalytic cycle. The most successful result in this direction was obtained introducing ligands with negatively charged functional groups, which increase the electron density on the ruthenium center. This results in a lower oxidation potential to reach the active high valent species. Moreover, these negatively charged moieties stabilize the high oxidation intermediates by interactions between the empty d-orbitals of the metal and filled p-orbitals of the negatively charged moieties. In 2012, Sun and coworkers reported that [Ru^{II}(bda)(isoq)₂] complex (**10**, Figure 10; H₂bda = 2,2'-bipyridine-6,6'-dicarboxylic acid; isoq = isoquinoline) catalyze the WO reaction with a TOF > 300 s⁻¹, comparable with the 100-400 s⁻¹ of the *in vivo* OEC.¹⁰ Differential pulse voltammograms (DPV) reveal a low redox potential of 1.25 V for the Ru^{IV}-OH/Ru^V=O couple. Interestingly, stopped-flow kinetic measurements and DFT(M06-2X) calculations affirmed that the O-O bond formation event takes place through a DC mechanism between two monomeric Ru^V=O fragments, with a free energy barrier of only 8.4 kcal·mol⁻¹. The DFT data also reveals that in the analogous [Ru^{II}(bda)(pic)₂] complex (**11**, Figure 10; pic = 4-picoline), the steric hindrance between the methyl groups of the picoline moieties inhibits the molecular orbital overlap between the two oxo ligands. In contrast, the π -stacking interactions between the isoquinoline moieties in complex **10** favors the coupling between the Ru^V=O fragments, improving the catalytic performance of the bda type catalysts (Figure 10).

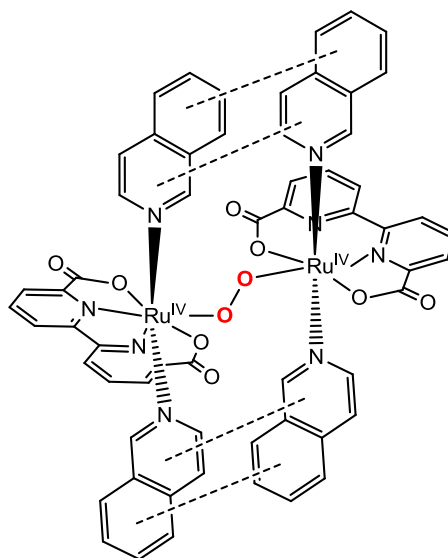
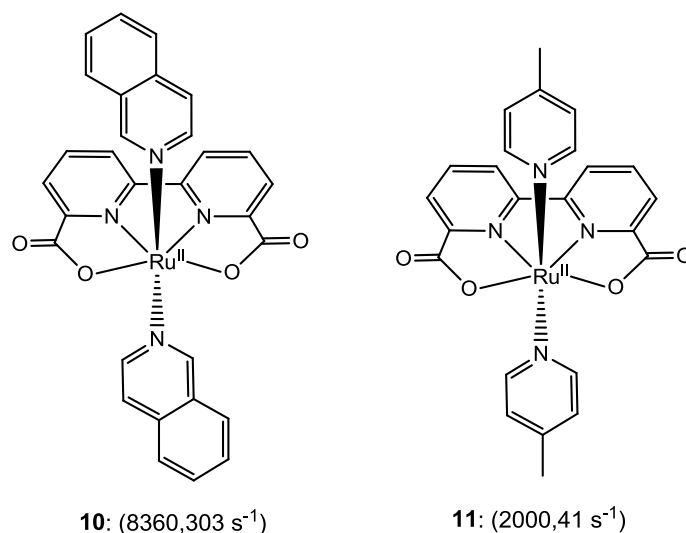


Figure 10: Molecular structure of complexes $[\text{Ru}^{\text{II}}(\text{bda})(\text{isoq})_2]$ (**10**) and $[\text{Ru}^{\text{II}}(\text{bda})(\text{isoq})_2]$ (**11**) and illustration π -stacking interactions in the $\text{Ru}^{\text{IV}}\text{-O-O-Ru}^{\text{IV}}$ dimer. TON and TOF values are shown in parentheses, respectively.

In the last decades, impressive efforts have been conducted to elucidate the precise mechanism of the Ru-catalyzed water oxidation reaction, but new data suggest that different Ru WOCs may follow different reaction mechanisms. Thus, some studies indicate that the Ce^{IV} oxidant and the nitrate anions may be directly involved in the O-O bond formation event.³³ Moreover, it was also recently observed that a single-site ruthenium complex can form a dinuclear system which is active in the water oxidation reaction, questioning if one ruthenium center is enough to perform this reaction.³⁴ Finally, a recent spectroscopic of several single-site Ru WOCs has been unable to identify the EPR signal related with $\text{Ru}^{\text{V}}=\text{O}$ species.³⁵ As a result, the previously reported mechanisms and kinetic constant for the O-O bond formation event are highly speculative. However, all the collected structural and mechanistic data from Ru WOCs has been used as a guide for the development of efficient WOCs based on other transition metals.

1.4.2.2 Iridium based WOCs

In 2008, Bernhard and co-workers reported for the first time the WO activity of a family of easily tunable mononuclear iridium complexes analogues of $[\text{Ir}^{\text{III}}(\text{phpy})_2(\text{OH}_2)_2]^+$ (**12**, Figure 11; phpy = 2-phenylpyridine), which are easily synthesized, robust and water-soluble.³⁶ The turnover numbers of this complexes are high, but their catalytic rates are relatively low. By analogy with ruthenium mononuclear systems, the proposed reaction mechanism²⁷ (Figure 11) involves the two electron oxidation of $\text{Ir}^{\text{III}}\text{-OH}_2$ species, using Ce^{IV} as oxidant, to form an $\text{Ir}^{\text{V}}=\text{O}$ complex which is the active species. The key step is the O-O bond formation through a WNA mechanism, where a water molecule attacks $\text{Ir}^{\text{V}}=\text{O}$ moiety. This generates an $\text{Ir}^{\text{III}}\text{-hydroperoxo}$ species that can release molecular oxygen by further oxidation. O_2 evolution was accompanied by the binding of water and the loss of one proton and two electrons.

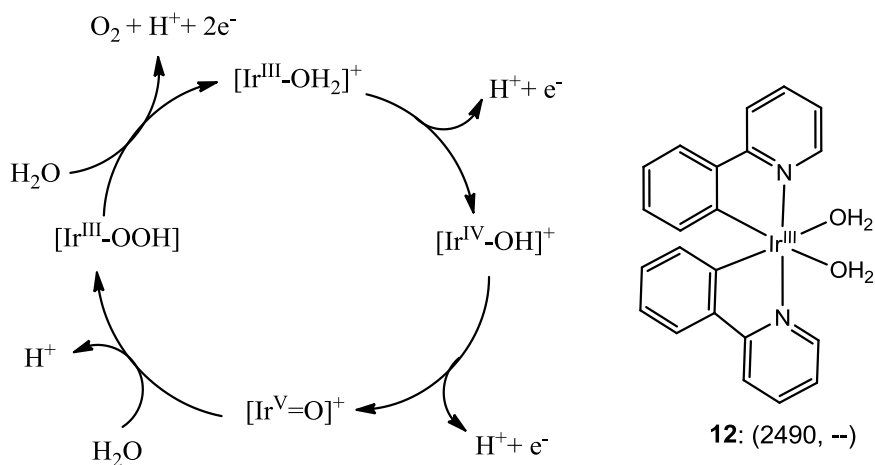


Figure 11: On the left, reaction mechanism postulated for iridium-catalyzed water oxidation. On the right, Bernhard $[\text{Ir}^{\text{III}}(\text{phpy})_2(\text{OH}_2)_2]^+$ catalysts for WO. TON and TOF values are shown in parentheses, respectively.

The reactivity of $\text{Ir}^{\text{V}}=\text{O}$ species and the details of the O-O bond formation steps, were studied at DFT(B3LYP) level by Balcells and co-workers.³⁷ They postulated three kind of different $\text{Ir}^{\text{V}}=\text{O}$ active species present in solution, depending on the pH. The general formula for these complexes is $[\text{Ir}(\text{phpy})_2(\text{O})(\text{X})]^q$, where $\text{X} = \text{OH}_2$ ($q = +1$), OH^- ($q = 0$) or O^{2-} ($q = -1$). These protonation states of the oxo species have different reactivity and therefore, water oxidation follows different mechanism (Figure 12). At acidic pH, the most feasible intermediate $[\text{Ir}(\text{phpy})_2(\text{O})(\text{OH}_2)]^+$ leads to a five-coordinated trigonal bipyramidal complex (**I-OH₂**) by H_2O decoordination the metal (due to the presence of low-lying antibonding $d_\pi(\text{Ir})\text{-}p_\pi(\text{O})$ orbitals), forming a H-bond with the oxo ligand. The formed **I-OH₂** is more reactive than the parent complex and through a water nucleophilic attack (**TS_{(I-II)-OH₂}**), the O-O bond is form with concomitant a proton transfers to the Oxo and the second water molecule coordinated to the vacant position at the metal. IRC calculations yield an octahedral $\eta^1\text{-H}_2\text{O}_2$ complex (**II-OH₂**) as a product. The process is endergonic ($5.0 \text{ kcal}\cdot\text{mol}^{-1}$) and has a free energy barrier of $25.9 \text{ kcal}\cdot\text{mol}^{-1}$. Less acidic conditions is represented by the the oxo-hydroxo iridium complex $[\text{Ir}(\text{phpy})_2(\text{O})(\text{OH})]$ (**I-OH**), where an external water molecule bridges the oxo and hydroxo ligands by H-bonds. The transition state (**TS_{(I-II)-OH}**) involves the attack of the water molecule to the electrophilic $\text{Ir}^{\text{V}}=\text{O}$ group helped by the assistance of the hydroxo ligand, which acts as an internal base capturing the proton. to yield **II-OH**. The O-O bond formation process is endergonic ($3.6 \text{ kcal}\cdot\text{mol}^{-1}$) and has a lower energy barrier than the previous mechanism ($20.2 \text{ kcal}\cdot\text{mol}^{-1}$). In basic conditions, the complex $[\text{Ir}(\text{phpy})_2(\text{O}_2)]^-$ (**I-O**) is dominant. In this case, the O-

O bond formation transition state ($\text{TS}_{(\text{I-III})-\text{O}}$) involves the proton transfer from a water molecule to one oxo group whereas the other yields the O-O bond. This mechanism has the lowest barrier (14.5 kcal·mol⁻¹). Interestingly, the increase of the basicity of the ligand in *cis* position to the oxo moiety, not only compensates the fact that an additional negative charge (OH vs Oxo) stabilize the electrophilicity of the iridium but reduces the free energy barrier. However, the energetic cost for the deprotonation has not been considered, which could increase the total free energy barrier significantly.

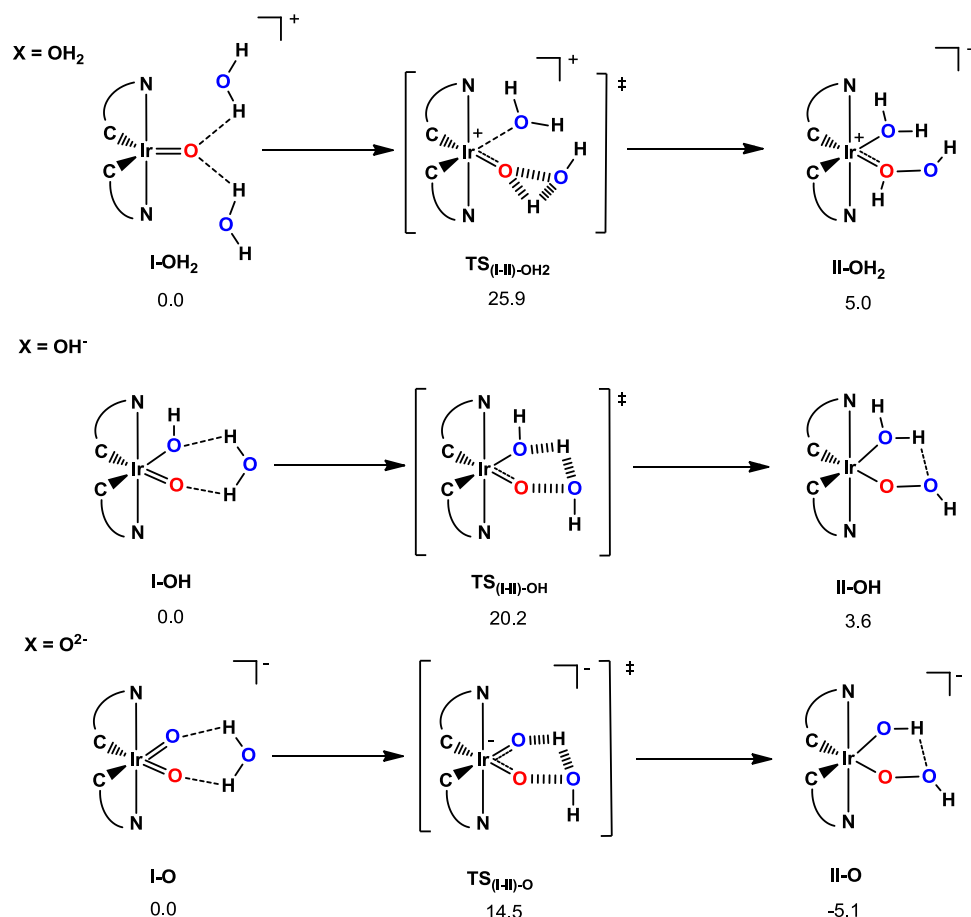


Figure 12: Postulated mechanisms for O-O bond formation in Bernhard water oxidation iridium catalyst $[\text{Ir}(\text{ppy})(\text{O})(\text{X})]^+$ at acidic pH (top), intermediate pH (middle) and basic pH (bottom).

Brudvig and Crabtree were the first to study half sandwiched iridium complexes with a relatively strong donating pentamethylcyclopentadienyl ligand (Cp*) in water oxidation.³⁸ These semi-stool complexes achieve an oxygen generation rate up to 0.17 s⁻¹ when bear a *N,N*-dimethylimidazolium carbene (ppy) and CAN is used as a sacrificial oxidant. The proposed whole catalytic cycle for these iridium complexes is similar to the one reported in the Bernhard's system. Crabtree and co-workers performed an study of the O-O bond formation step for catalyst $[\text{Cp}^*\text{Ir}^{\text{III}}(\text{ppy})\text{Cl}]$ by DFT(B3LYP) calculations and kinetic experiments.^{38b} This catalyst was computationally modeled by replacing the Cp* ligand by Cp. As in the case of Bernhard catalyst, the WO follows a WNA mechanism, where a water molecule acts as a nucleophile and the Ir^V=O species as an electrophile (Figure 13). The most feasible pathway involves a second water molecule assisting the proton transfer to the oxo group, obtaining a five membered-ring in the transition state. The analysis of the Ir^V=O electronic structure show that the donor-acceptor interaction in the O-O bond formation step is promoted by the characteristic electronic structure of $[\text{Cp}^*\text{Ir}^{\text{III}}(\text{ppy})\text{Cl}]$. The

presence of a doubly occupied π^* orbital, which is preferentially located on Ir rather than on O, increases the electrophilicity of O and weakens the Ir=O bond. The electrophilicity of the Ir=O moiety is also promoted by the presence of an empty π^* orbital, which lies low in energy at the LUMO level, and can accept the electron density from the water molecule. However, the DFT barrier of this mechanism has a significant energy barrier of $24.0 \text{ kcal}\cdot\text{mol}^{-1}$, which is significantly higher than the $18.5 \text{ kcal}\cdot\text{mol}^{-1}$ derived from the experimental TOF value.

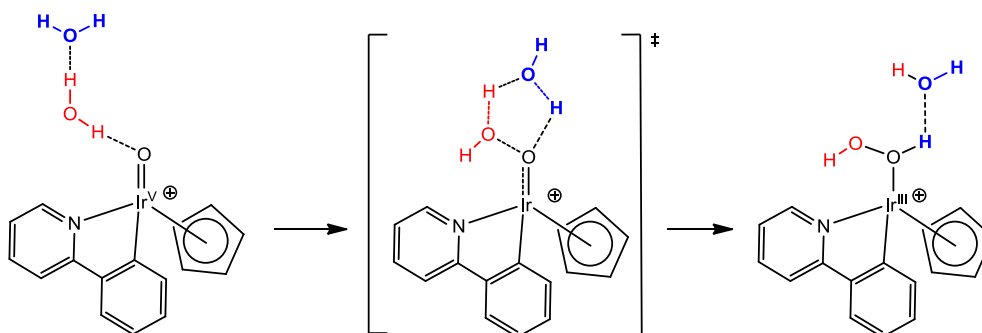


Figure 13: Postulated mechanism for O-O bond formation in Crabtree water oxidation iridium catalyst.

Sodium periodate (NaIO_4) can be used as an alternative to CAN, as it is a much weaker oxidant ($E^\circ = 1.2 \text{ V}$ at pH 7) and is stable under mild conditions. However, it is known that NaIO_4 is a two electron inner-sphere oxidant or oxygen atom transfer reagent, and this chemical behavior of NaIO_4 may completely change the mechanistic scenario. For this reason, Reek and coworkers carried out in situ ESI-MS experiments and DFT(B3LYP) calculations on $[\text{Cp}^*\text{Ir}^{\text{III}}(\text{Me}_2\text{NHC})(\text{OH})_2]$ (where $\text{Me}_2\text{NHC} = N$ -dimethylimidazolin-2-ylidene) (**13**, Figure 14) to elucidate the sodium periodate driven WO mechanism.³⁹ The ESI-MS data indicate that Ir=O intermediates with IO_3^- or IO_4^- coordinated to the metal were generated. DFT calculation reveal that $[\text{Cp}^*\text{Ir}^{\text{IV}}(\text{Me}_2\text{NHC})(\text{O})(\text{IO}_3)]^+$ may perform the O-O bond formation event through a nucleophilic attack of IO_3^- on the $\text{Ir}^{\text{IV}}=\text{O}$ moiety (Figure 14). The DFT free energy barrier is $21.8 \text{ kcal}\cdot\text{mol}^{-1}$ in agreement with the turnover frequency of 0.27 s^{-1} . The WNA on the $\text{Ir}^{\text{IV}}=\text{O}$ assisted by the IO_3^- internal base has an energy barrier of $36.5 \text{ kcal}\cdot\text{mol}^{-1}$, which cannot be reached at room temperature.

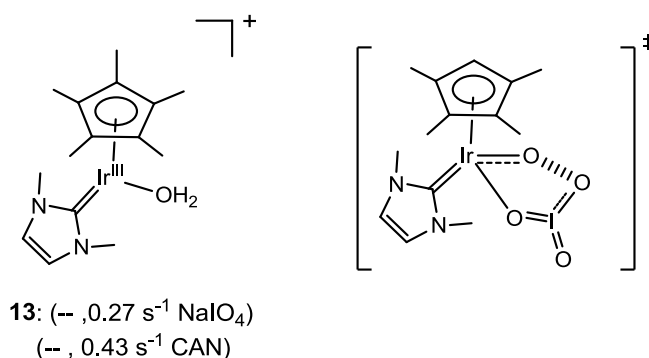
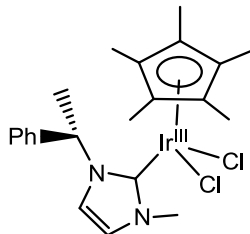


Figure 14: On the left, molecular structure of $[\text{Cp}^*\text{Ir}^{\text{III}}(\text{Me}_2\text{NHC})(\text{OH})_2]$ (**13**). On the right, computed transition state for the O-O bond formation catalyzed by $[\text{Cp}^*\text{Ir}^{\text{IV}}(\text{Me}_2\text{NHC})(\text{O})(\text{IO}_3)]^+$ active species. TOF values are shown in parentheses.

The Lloret-Fillol group also reported the iridium complex $[\text{Cp}^*\text{Ir}^{\text{III}}(\text{NHC})\text{Cl}_2]$ (**14**, Figure 15; NHC = 3-methyl-1-(1-phenylethyl)-imidazole-2-ylidene), which shows an incredible high WO activity employing NaIO_4 as a sacrificial oxidant, with a TON of 400000 with a sustained TOF of 2.5 s^{-1} .⁴⁰ Interestingly, no relevant inhibition of the WO activity was observed if the reaction mixture is stored during several months. This makes $[\text{Cp}^*\text{Ir}^{\text{III}}(\text{NHC})\text{Cl}_2]$ a good candidate to be incorporated in water splitting devices.



14: (400000, 2.5 s^{-1})

Figure 15: Molecular structure of $[\text{Cp}^*\text{Ir}^{\text{III}}(\text{NHC})\text{Cl}_2]$ (**14**). TON and TOF values are given in parentheses, respectively.

The precedent studies consider that the operational O-O bond formation mechanism always involves the nucleophilic attack of some oxygen moiety to the $\text{Ir}^{\text{V}}=\text{O}$ moiety. However, as occurred with ruthenium WOCs, the DC mechanism may be an alternative route to the O-O bond generation. Previous calculations indicate that the singlet-triplet gap in $\text{Ir}^{\text{V}}=\text{O}$ species is about $5 \text{ kcal}\cdot\text{mol}^{-1}$ and in the $S = 1$ the metal-oxo moiety present significant spin density. Therefore the coupling between two $\text{Ir}^{\text{IV}}-\text{O}\cdot$ could be possible.³⁸ For this reason, Crabtree and coworkers synthesized an iridium dimer $[\text{Cp}^*_2\text{Ir}_2(\text{bpp})\text{Cl}_2]\text{Cl}$ based on a doubly chelating bis-pyridine-pyrazolide ligand (**15**, Figure 16) and the analogous monomer $[\text{Cp}^*\text{Ir}^{\text{III}}(\text{pp})\text{Cl}]$ (**16**; Figure 16; pp = 2-pyrazolylpyridine) to check if a DC mechanism for the O-O bond formation is preferred over the WNA ones.⁴¹ Both systems present first-order kinetics respect to catalyst concentration, but the dimer ($k_{\text{obs}} = 0.83 \pm 0.06 \text{ min}^{-1}$) present lower rates for O_2 evolution with NaIO_4 compared to the monomer ($k_{\text{obs}} = 4.77 \pm 0.12 \text{ min}^{-1}$). No significant differences were observed between the aqueous electrochemistry of the monomer and the dimer, suggesting that the DC pathway is inoperative in the investigated iridium based WOCs.

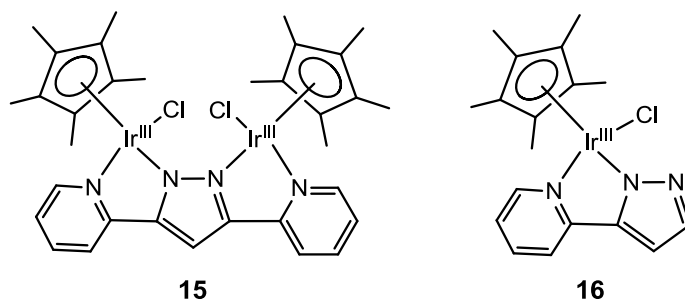


Figure 16: Molecular structures of iridium complexes $[\text{Cp}^*_2\text{Ir}_2(\text{bpp})\text{Cl}_2]\text{Cl}$ (**15**) and $[\text{Cp}^*\text{Ir}^{\text{III}}(\text{pp})\text{Cl}]$ (**16**).

However, since the discovery of the Cp^* ligand degradation in half sandwiched iridium WOC by Grotjahn and co-workers in 2011,⁴² there is an open debate about the real identity of catalytic species in Ir water oxidation. Determination of the molecular or heterogeneous nature of the active species has been an active area of research. By a combination of kinetic, UV-Vis, DFT(OPBE) and NMR studies Macchioni and coworkers observed that three iridium complexes of general formula

$[\text{Cp}^*\text{Ir}^{\text{III}}\text{L}]$ for WO reaction suffer the oxidative functionalization of a Cp^* quaternary carbon and a methyl group when CAN is used as oxidant.⁴³ The authors suggested that the WO reaction competes with the ligand degradation process: after the WNA attack on the $\text{Cp}^*\text{Ir}^{\text{V}}=\text{O}$ moiety, the already generated $\text{Ir}^{\text{III}}\text{-OOH}$ product is further oxidized and deprotonated to generate $\text{Cp}^*\text{Ir}^{\text{IV}}(\eta^2\text{-O}_2)$ that is in equilibrium with $\text{Cp}^*\text{Ir}^{\text{III}}(\eta^1\text{-O}_2\cdot)$ superoxide species (Figure 17). The latter intermediate is considered the responsible for initiating the oxidative degradation pathway, leading to acetic, formic, glycolic acids and other iridium intermediates.

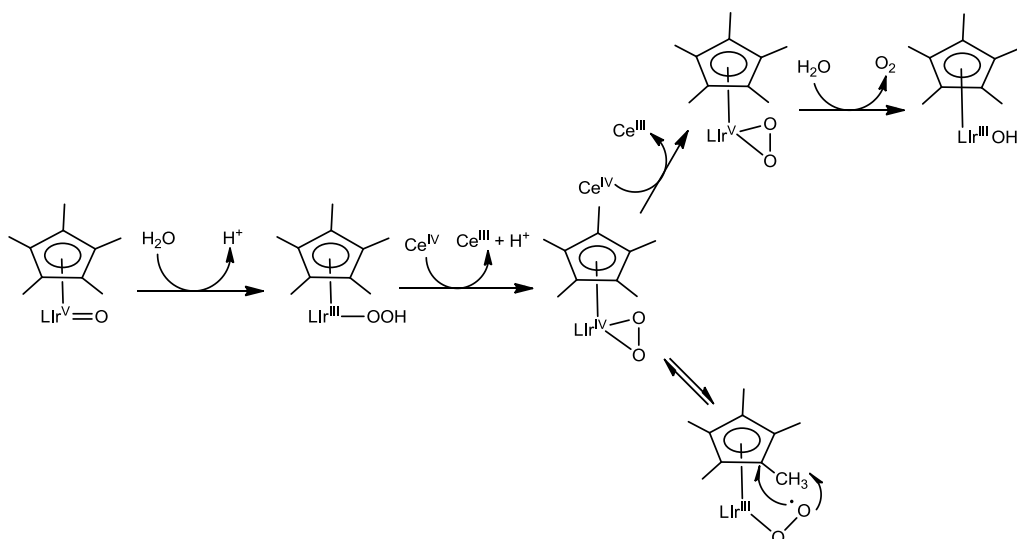


Figure 17: Competition between Cp^* degradation and O_2 generation mechanisms in $[\text{Cp}^*\text{IrL}]$ complexes.

In contrast with ruthenium WOC, the degradation of the ligand may increase the WO activity of the system due to the formation of other IrO_x heterogeneous species.⁴⁴ A new kind of heterogeneous system was discovered when Brudvig *et al.* studied the electrochemical oxidation of the precursor complexes $[\text{Cp}^*\text{Ir}(\text{H}_2\text{O})_3](\text{SO}_4)$ and $[(\text{Cp}^*\text{Ir})_2(\text{OH})_3](\text{OH})$. They detected that a blue layer of an amorphous iridium oxide containing carbon atoms is deposited onto the anode, which is more active for WO reaction than crystalline IrO_2 .⁴⁵ IR and X-ray absorption spectroscopies show that the six ligands to iridium in the blue layer are likely oxygen atoms, consistent with the formation of iridium oxide, and present C=O and C-H bonds intact. According to X-ray scattering and pair distribution function analysis, the blue layer is composed by small iridium oxide domains of about 7 Å. DFT(B3LYP) and simulated annealing Monte Carlo calculations were carried out to propose two plausible structures of the blue layer consistent with the experimental data (Figure 18a). The iridium oxide domains may present one or two Ir^{IV} centers surrounded by hydroxide or aqua groups. The two substructures may be also linked by μ -oxo/hydroxo bridging groups, or through hydrogen bonding interaction, favoring an extended amorphous structure of the blue layer. The small carbon content may come from the presence of coordinated ketomalonate fragments, which are known to come from the oxidation of the Cp^* ligand and may be stable under the highly oxidizing conditions. They also observed that when Cp^* or cyclooctadiene (cod) moieties and chelating ligands (bpy, 2-phenylpyridine and 2-(20-pyridyl)-2-propanolate) are present in the iridium complex structure, the NaIO_4 driven WO reaction occurs without the formation of nanoparticles or the blue layer.⁴⁶ Instead, spectroscopic data and MALDI-TOF-MS spectrometry derived from $[\text{Cp}^*\text{Ir}(\text{pylac})(\text{Cl})]$ (17, Figure 18b; pylac = 2-(20-pyridyl)-2-propanolate) point to the degradation of the Cp^* to form Ir^{IV} dimers as active species. These binuclear species may contain the pylac moiety intact. Consequently, the

real catalyst has a complex structure, which may depend of the nature of corresponding precursors, and mechanistic investigations should be taken with reserve.

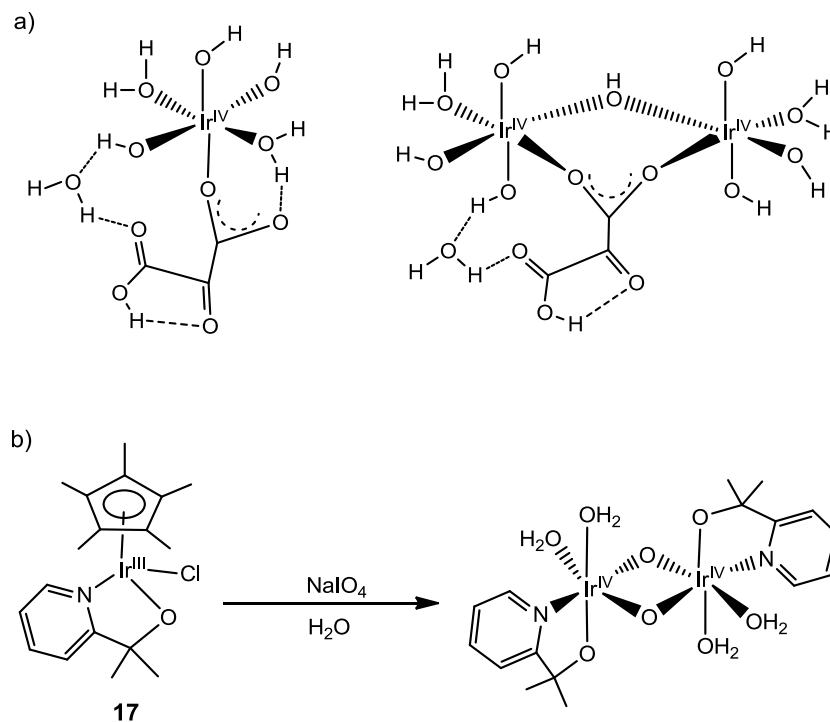


Figure 18: a) Representation of the possible substructures present in the blue layer. b) Schematic generation of a Ir^{IV} dimer from [Cp*Ir(py)ac](Cl) (**17**).

A proper characterization of the precatalyst structure after oxidative degradation of Cp* moiety may help to shed some light on the identity and activity of active species. Thus, Lin *et al.* recently reported the design of a stable Zirconium based metal–organic framework (MOF) using [Cp*Ir^{III}(bpydc)Cl]⁺ (**18**, Figure 19; bpydc = dibenzoate-substituted 2,2'-bipyridine) as a building block.⁴⁷ ESI-MS spectrometric analysis of the digested sample suggested that when CAN is added to the aqueous solution, the precatalyst may be [(bpydc)Ir^{III}(H₂O)₂(CH₃COO)Cl]⁺, in which the bpydc remains intact. Siegbahn and coworkers explored by means of DFT calculations the whole WO catalytic cycle with different functionals (Figure 19).⁴⁸ They identified that the WNA on Ir^V=O moiety assisted by the acetate ligand functioning as a base has a free energy barrier about 30 kcal·mol⁻¹, which is too demanding. Instead, Ir^{VI} and Ir^{VII} oxidation states may be reached through PCET steps and present lower O-O bond formation energy barriers than Ir^V species (Ir^{VI}: 14.7 kcal·mol⁻¹ and Ir^{VII}: 16.3 kcal·mol⁻¹ at B3LYP*-D₃). The calculated barriers are in good agreement with the 20.3 kcal·mol⁻¹ derived from the measured TOF of 0.008 s⁻¹. Finally, further deprotonation and oxidation of the Ir-OOH products lead to the recovering of Ir^{III}-OH₂ and the O₂ release. The theoretical determination of this Ir^{VI} / Ir^{VII} new WO mechanism may stimulate the design of more efficient iridium WOCs.

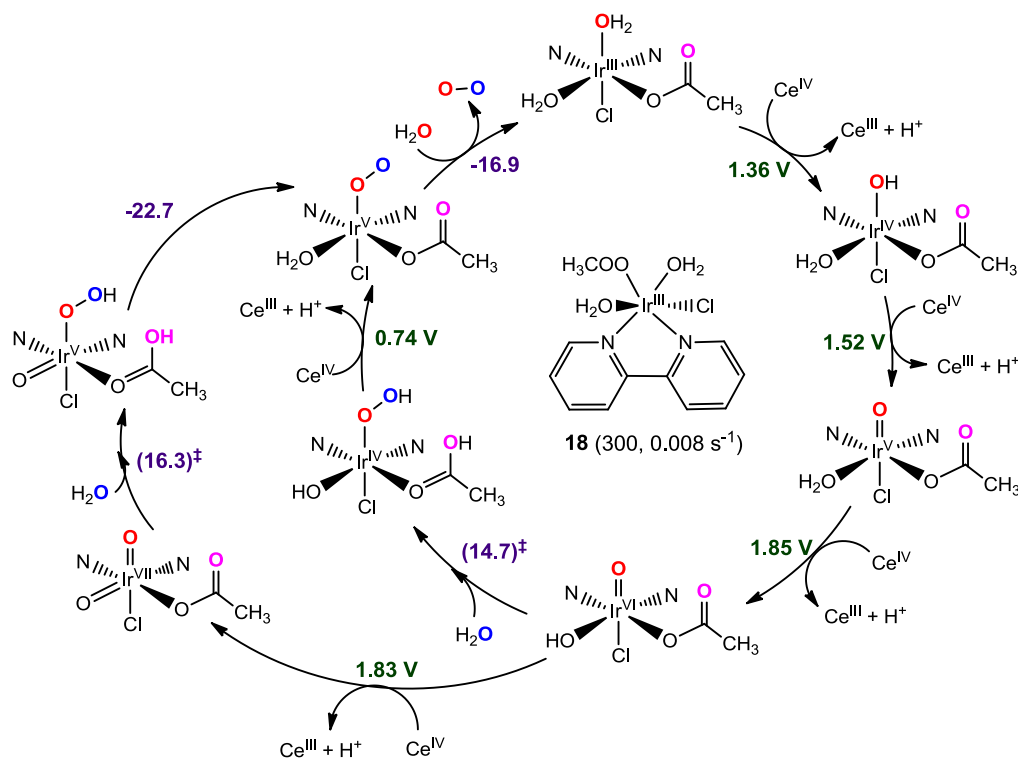


Figure 19: Water oxidation catalytic cycle proposed by means of DFT(B3LYP*-D₃) calculations for [(bpydc)Ir^{III}(H₂O)₂(CH₃COO)Cl]⁺. Gibbs energies are in kcal·mol⁻¹. TON and TOF values are shown in parentheses, respectively.

1.4.3 First Row Transition Metal-based WOCs

The earth-scarce ruthenium and iridium WOCs have shown high water oxidation efficiencies. However, the high costs of Ru and Ir limits their use on a large scale application. On the other hand, WOCs based on earth-abundant transition metals such as Mn, Fe, Co, Cu, and Ni has many advantages, including low cost, lower toxicities, tunable redox properties and simple assemblies to other devices. However, the search for water oxidation systems based on first row transition metals that can work at neutral pH and low overpotentials remain a chemical challenge. In this section, the mechanistic studies on some relevant WOCs based on earth-abundant transition metals are summarized.

1.4.3.1 Manganese based WOCs

In contrast with ruthenium or iridium systems, only few reported manganese complexes exists with the capacity of catalyzing water oxidation. The first example of a homogenous manganese complex that undergo oxidation of water to O₂ was reported by Naruta's group in 1994.⁴⁹ They synthesized three manganese triphenylporphyrin (TPP) dimers linked by an *o*-phenylene bridge (Figure 20). The WO activity of these complexes was studied by cyclic voltammetry in an aqueous acetonitrile solution (5% v/v H₂O in acetonitrile). The three manganese complexes showed an irreversible discharge current at a redox potential higher than 1.4 V vs. NHE, related with the WO onset. The rate of O₂ evolution was found to depend on the complex concentration, indicating the involvement of manganese porphyrin dimers in the rate-determining step. The corresponding monomeric manganese porphyrin did not show O₂ evolution, a clear indication of the need of two manganese centers in close proximity to generate the O-O bond. Isotopic ¹⁸O-labelling studies confirm that the oxygen atoms of the evolved O₂ come from water solvent. On the basis of experimental data, they

proposed a mechanism which starts with the oxidation of two $\text{Mn}^{\text{III}}\text{-OH}$ moieties to reach the $\text{Mn}^{\text{V}}\text{=O}$ species. Then, the close proximity of the two $\text{Mn}^{\text{V}}\text{=O}$ groups triggers the formation of a $\text{M}^{\text{IV}}\text{-O-O-Mn}^{\text{IV}}$ intermediate. Finally, two OH^- may replace the peroxo fragment, leading to the O_2 release and the regeneration of the starting manganese(III) dimer. In a later paper, the authors characterized the $\text{Mn}^{\text{V}}\equiv\text{O}$ dimeric active species using *meta*-chloroperoxybenzoic acid (*mcpBA*) as oxidant.⁵⁰

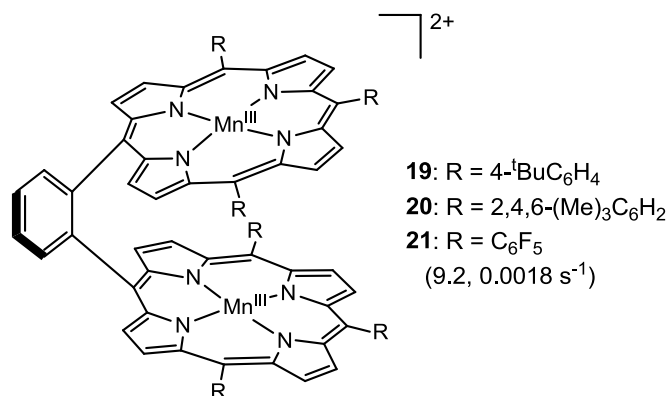


Figure 20: Molecular structures of the three [Mn(TPP)] dimers. TON and TOF values for complex **21** are shown in parentheses, respectively.

In 1999, Limburg *et al.* reported the first manganese catalyst capable catalyze oxygen evolution from an oxidant in aqueous solution, the Mn dimer $[(\text{terpy})(\text{H}_2\text{O})\text{Mn}^{\text{IV}}(\mu\text{-O})_2\text{Mn}^{\text{III}}(\text{H}_2\text{O})(\text{terpy})]^{3+}$ (**22**, Figure 21).⁵¹ A very low TON value of 4 was obtained for complex **22** when sodium hypochlorite (NaOCl) was used a sacrificial oxidant. This was a consequence of the complex degradation and the formation of inactive MnO_4^- ions, the latter observed by UV-Vis spectroscopy. Isotopic labeling studies using H_2^{18}O confirmed that 75% of the atomic oxygen in the O_2 product derived from the water solvent, while 25% come from the oxidant ClO^- . Taking into account the isotopic distribution, the authors proposed that the WO catalytic cycle starts with the exchange of one aqua ligand with ClO^- to form $[(\text{terpy})(\text{H}_2\text{O})\text{Mn}^{\text{IV}}(\mu\text{-O})_2\text{Mn}^{\text{III}}(\text{OCl})(\text{terpy})]^{2+}$. Then, the chloride dissociation leads to the generation of a highly oxidized $[(\text{terpy})(\text{H}_2\text{O})\text{Mn}^{\text{IV}}(\mu\text{-O})_2\text{Mn}^{\text{V}}(\text{O})(\text{terpy})]^{3+}$ intermediate, which was considered the responsible of the O-O bond formation. It was also shown that the O_2 evolution becomes more efficient with Oxone as oxidant (KHSO_5).⁵² The rate constant for O_2 evolution from Oxone was estimated to be $2420 \text{ mol O}_2 \text{ h}^{-1} \text{ mol}^{-1}$, which corresponds to a reaction barrier of $18 \text{ kcal}\cdot\text{mol}^{-1}$. Isotopic labelling studies allow distinguishing between the O-O bond formation with water and the competing reaction with oxone. According to labelling studies, the reaction with water may have a barrier $1\text{-}3 \text{ kcal}\cdot\text{mol}^{-1}$ higher than with oxone, which translates in a barrier of $19\text{-}21 \text{ kcal}\cdot\text{mol}^{-1}$.

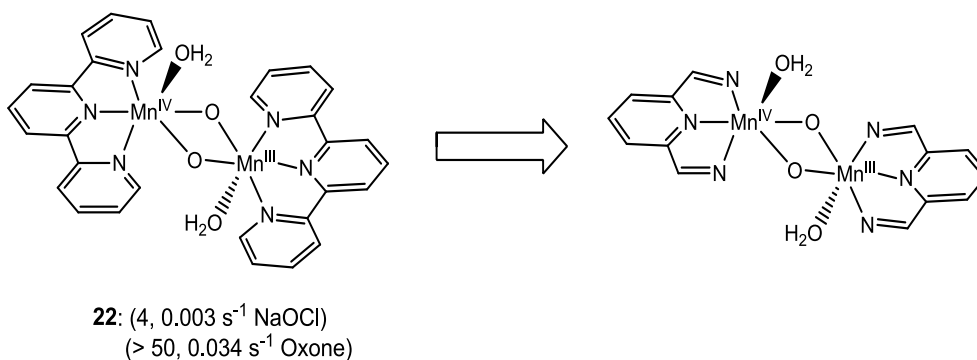


Figure 21: On the left, Mn-dimer complex [(terpy)(H₂O)Mn^{IV}(μ-O)₂Mn^{III}(H₂O)(terpy)]³⁺ (**22**) with water oxidation catalytic activity. TON and TOF values are shown in parentheses, respectively. On the right, computational model used in ref. 53 for study the O-O bond formation step.

Siegbahn, Lundberg and co-workers present a computational investigation at DFT(B3LYP*) level,⁵³ to analyze the nature of the high valence species and the factors to enhance the O-O bond formation in this Mn-dimer complex. Since DFT was unable to accurately describe the electronic structure of the oxone-Mn dimer system, the computational study focuses on the undergoing O-O bond formation by a water molecule. To reduce the computational effort, a model structure of the [(terpy)(H₂O)Mn^{IV}(μ-O)₂Mn^{III}(H₂O)(terpy)]³⁺ dimer was computationally modeled (Figure 21). Well-characterized Mn^V≡O complexes exist and they are not active in O-O bond formation, so formation of a high valent state Mn≡O center is not only requirement for the O-O bond formation. Moreover, some studies performed on OEC models suggested an oxygen radical WO mechanism, where a Mn^{IV}=O· (oxyl) radical is formed instead of Mn^V≡O. The Mulliken spin population in the manganese dimer confirms that the most stable active species are better described as a Mn^{IV}=O· radical state. The radical character of Mn^{IV}=O· is rather independent of the theoretical model used. They also demonstrated that the electronic structure of previously reported Mn^V≡O complexes, which are inactive in O₂ formation, have ground singlet and triplet spin states with no radical oxyl character. Therefore, it was concluded that the oxyl character is a requirement for the O-O bond formation.

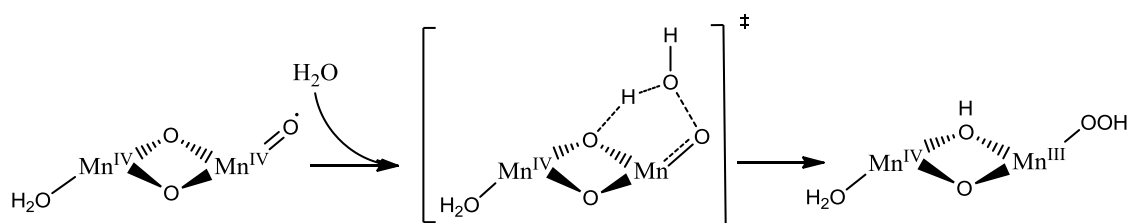


Figure 22: Proposed O-O bond formation mechanism performed by **22**.

The O-O bond formation mechanism was explored in the triplet and quintet spin states for the Mn^{IV}=O· moiety. In the transition state, the water molecule attacks the oxyl group while one of the bridging oxygen assists the proton transfer (Figure 22). The lowest calculated barrier (23.4 kcal·mol⁻¹) is close to the expected 19-21 kcal·mol⁻¹ for the WNA mechanism based on experimental rate measurements. The existence of a spin crossing could indicate that the highest energy point on the reaction path is actually be lower than any of the calculated transition states and, in another paper, the authors confirmed that none of the located minimum energy crossing points (MECP) is rate limiting.⁵⁴

The Siegbahn-Lundberg model only considers the O-O bond formation triggered by water. However, the reaction proceeds with an excess of oxidants, suggesting that NaOCl and KHSO₅ may play other important roles. Nakamura and coworkers proposed an alternative mechanism in which the direct involvement of the OCl⁻ oxidant in the O-O bond formation event and the counter ion effect were considered (Figure 23).⁵⁵ DFT(B3LYP) calculations show that the introduction of three ClO⁻ to electroneutralize the 3+ charge of **22** provokes the proton transfer from the aqua ligands to ClO⁻ ions. Then, one of the generated HOCl molecules can migrate from the Mn^{IV}-OH moiety and establish a hydrogen bond interaction with an oxo bridging moiety. This transfer enables the O-O bond formation event: in the transition state, the O-Cl bond dissociates enabling the formation of an O-O bond between the Mn^{IV}-OH fragment and the HO moiety of HOCl. This is accompanied by the transfer of an electron from the Mn^{IV}-OH to the Cl atom of HOCl, and a simultaneous acid-base reaction between the Mn^{IV}-OH and the attached OCl⁻. After the pivotal attack, the hydroperoxide product [(terpy)(OOH)Mn^{IV}(μ-O)₂Mn^{III}(OH)(terpy)]Cl(HOCl)₂ is obtained. The free energy barrier of this pivotal mechanism is 14.0 kcal·mol⁻¹, in fair agreement with the experimental data. The subsequent PCET from the -OOH group to one oxo bridging group generates a superoxide [(terpy)(•O₂)Mn^{III}(μ-O)(μ-OH)Mn^{III}(OH)(terpy)]Cl(HOCl)₂ intermediate. Finally, the dissociation of the superoxide moiety on the Mn^{III} center leads to the O₂ release. The exchange interactions between the transferred electron of the superoxide moiety and that of the Mn center explain how the triplet molecular oxygen is produced. In contrast with the Limburg and Lundberg proposals, the O-O bond formation by ClO⁻ does not require the formation of high valent Mn^V≡O species.

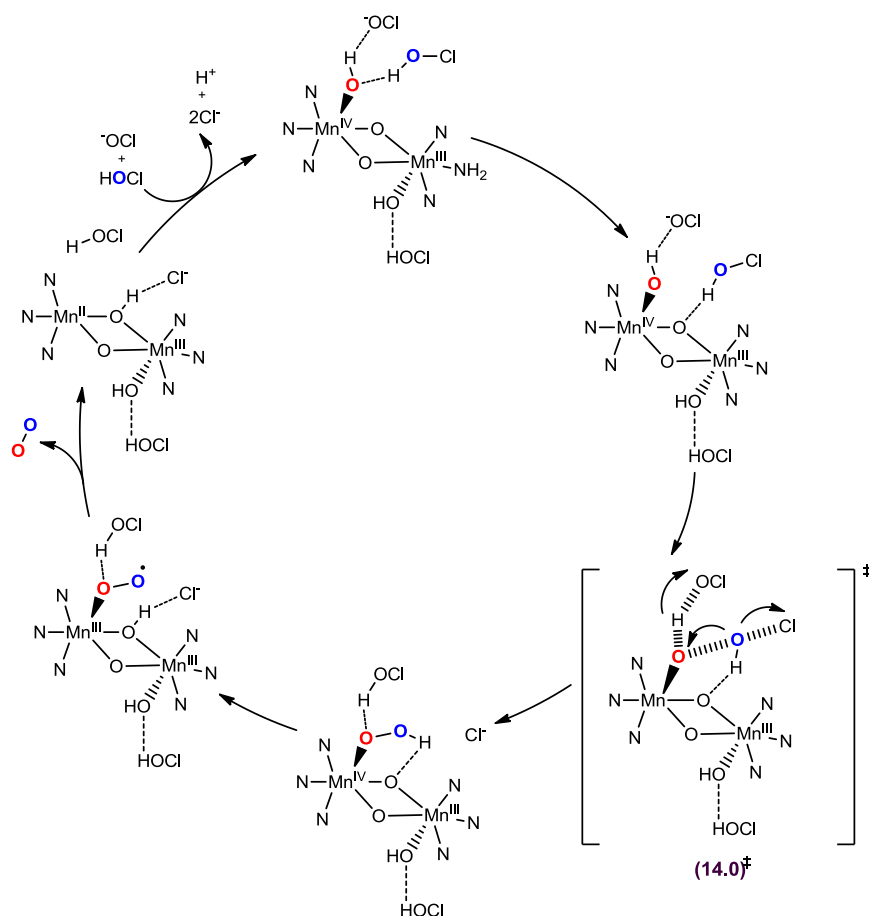
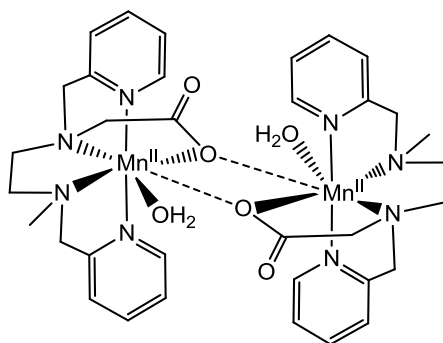


Figure 23: OCl⁻ driven water oxidation mechanism proposed by complex **22** on the basis of DFT(B3LYP) calculations. The Gibbs energy barrier is in kcal·mol⁻¹.

The degradation of catalyst **22** was studied by Buda and coworkers with *ab initio* molecular dynamics simulations and DFT(BLYP) calculations.⁵⁶ They observed that the $\text{Mn}_2^{\text{IV,V}}$ dimer undergo the breakage of one of the oxo bridges and a release of a water ligand leading to two pentacoordinated Mn sites. The new intermediate is less active in the formation of the O-O bond, in agreement with the experimentally observed decrease of the catalytic activity of **22** in aqueous solution after a few catalytic cycles. These mechanistic studies should be taken with reserve, since it has been recently shown that oxidation of **22** leads to the formation of a possible active tetranuclear manganese complex.⁵⁷ However, there is some controversial about its capacity to oxidize water electrochemically.⁵⁸ The incorporation of complex **22** onto materials such as kaolin allows the utilization of the one-electron oxidant CAN to drive the water oxidation reaction instead of an oxygen transfer reagent.⁵⁹

In 2003, McKenzie and co-workers reported the synthesis and characterization of a dimeric manganese(II) complex based on the pentadentate anionic ligand *N*-methyl-*N'*-carboxymethyl-*N,N'*-bis(2-pyridylmethyl)ethane-1,2-diamine (Hmcbpen) (**23**, Figure 24).⁶⁰ Complex **23** can catalyze the water oxidation reaction using *tert*-butyl hydroperoxide (TBHP) as oxidant in acetonitrile or protic solvents (H_2O and MeOH). EPR and UV-Vis data indicate that the treatment of complex **23** with TBHP in a protic solvent generates $\text{Mn}^{\text{III}}\text{-OX}$ ($\text{X} = \text{-H}$ or -R) monomeric species and, when H_2O was used as solvent, O_2 evolution catalyzed by **23** is also observed.⁶¹ On the other hand, in acetonitrile solution two new species were formed, identified as the mono- μ -oxo-bridged $\text{Mn}_2^{\text{III,III}}$ and bis- μ -oxo-bridged $\text{Mn}_2^{\text{IV,IV}}$ complexes, which may have a short lifetime in H_2O and MeOH solvents. Isotopic ^{18}O labelling studies showed that the O_2 product present one oxygen atom from a water molecule and one from the TBHP. Taking into account all this data, the authors propose a catalytic cycle in which two $\text{Mn}^{\text{III}}\text{-OH}$ interact to form μ -oxo-bridged $\text{Mn}_2^{\text{III,III}}$ and $\text{Mn}_2^{\text{IV,IV}}$ structures. The O-O bond formation reaction may occur through an intramolecular coupling between two oxo-bridging moieties in a bis- μ -oxo-bridged $\text{Mn}_2^{\text{IV,IV}}$ complex.



23: (20, -- TBPH)

Figure 24: Molecular structure of $[(\text{mcbpen})\text{Mn}_2^{\text{II}}(\text{H}_2\text{O})_2(\text{mcbpen})]^{2+}$ (**23**). TON value is shown in parentheses.

The mechanistic proposal was further refined by DFT(B3LYP) calculations (Figure 25).⁶² Sameera *et al.* show that complex **23** can be in equilibria with monomeric $[\text{Mn}^{\text{II}}(\text{mcbpen})(\text{H}_2\text{O})]^+$ species. The TBHP oxidizes the $[\text{Mn}^{\text{II}}(\text{mcbpen})(\text{H}_2\text{O})]^+$ to reach a $[\text{Mn}^{\text{IV}}(\text{mcbpen})(\text{O})]^+$ intermediate. The authors propose that the dimerization of $[\text{Mn}^{\text{IV}}(\text{mcbpen})(\text{O})]^+$ forms $[(\text{mcbpen})\text{Mn}^{\text{III}}(\mu\text{-O})\text{Mn}^{\text{IV}}(\text{O}\cdot)(\text{mcbpen})]^{2+}$ species, in which the Mn^{IV} center present a decoordinated pyridine ring. The O-O bond formation reaction proceeds through a WNA on the $\text{Mn}^{\text{IV}}\text{-O}\cdot$ moiety assisted by one carboxylate ligand. Then, one proton transfer occurs from the hydroperoxide group in $[(\text{mcbpen})\text{Mn}^{\text{III}}(\mu\text{-O})\text{Mn}^{\text{III}}(\text{OOH})(\text{mcbpen}\text{-COOH})]^{2+}$ to the oxo bridge. Finally, the molecular

oxygen is displaced by a water molecule, recovering the initial two $[\text{Mn}^{\text{II}}(\text{mcbpen})(\text{H}_2\text{O})]^+$ monomer. According to this mechanism, the carboxylate moieties of the mcbpen ligand play two important roles in the WO reaction. The COO^- group may act as an internal base, enhancing the nucleophilic character of water, but it also establishes weak bonding interactions between the Mn fragments which allow the generation of high valent monomeric intermediates.

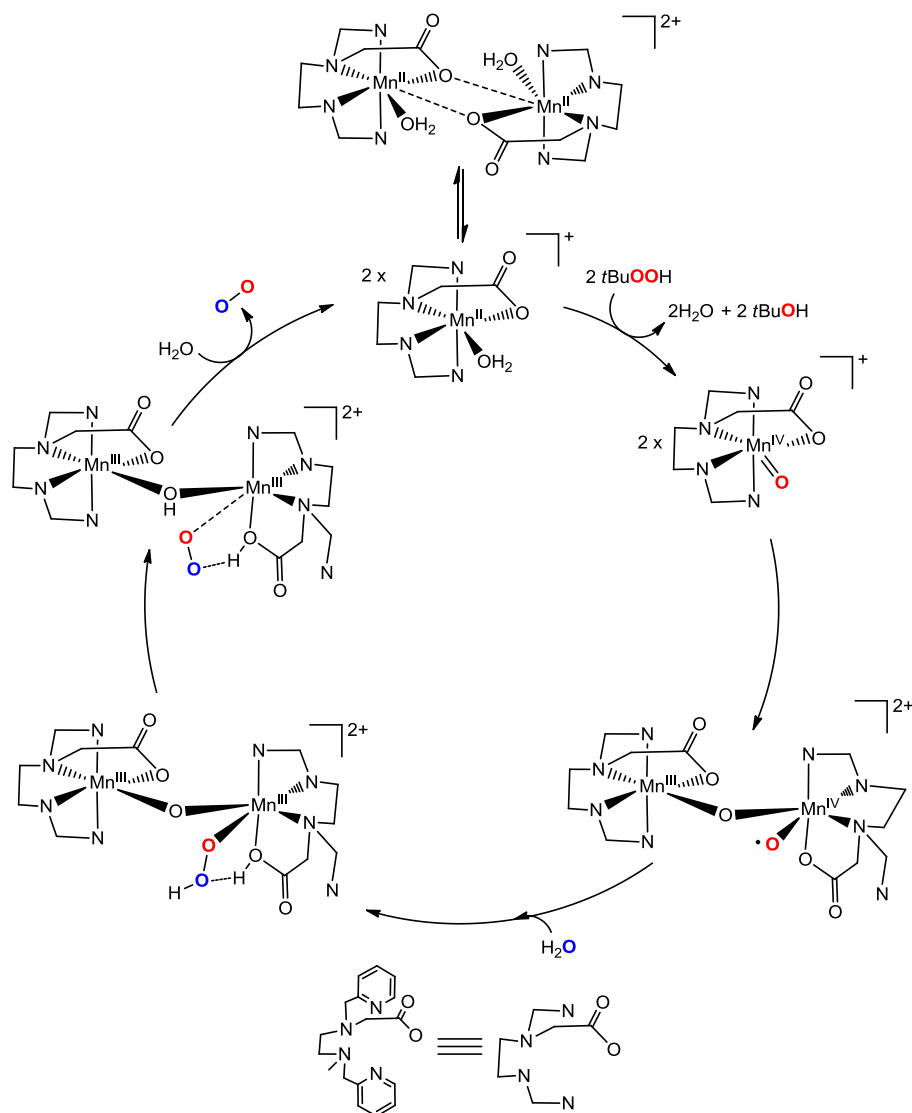


Figure 25: DFT proposed water oxidation mechanism by complex **23**.

The binuclear structure is not a requirement to oxidize water with Mn complexes. In analogy with Naruta's complexes, Åkermark and Sun prepared the cationic monomeric and dimeric manganese corrole complexes capable to catalyze the oxidation of water under a basic solution of dichloromethane-acetonitrile (**24-25**, Figure 26).⁶³ In contrast with complexes **19-21**, the bridging group is a xanthene moiety instead of an aryl ring, being the former more flexible. Electrochemical studies reveal that the two systems may reach high valent active species with relatively low potentials. Privalov, Sun and coworkers computationally studied the O-O bond formation by this $\text{Mn}^{\text{V}}\equiv\text{O}$ species derived from **24** and **25**.⁶⁴ The influence of the first solvation shell on the O-O bond formation mechanism was modelled introducing a cluster of four water molecules surrounding the manganese active centers. DFT(B3LYP) calculations about the expected DC mechanism for **24** indicate that the generation of a $\text{Mn}^{\text{III}}\text{-O-O-Mn}^{\text{III}}$ intermediate presents a high energetic cost (20

kcal·mol⁻¹). In contrast, the flexibility of the xanthene group enables the system to accommodate several water molecules between the two manganese centers. This suggested that the O-O bond formation in the dimer structure **24** may proceed through an OH⁻ nucleophilic attack on a Mn^V=O moiety or a WNA assisted by another oxo ligand. On the other hand, the nucleophilic attack of an OH⁻ group on a monomeric Mn^V=O intermediate presented a very low energy barrier of only 8 kcal·mol⁻¹. Taking into account the experimental and computational results, it was proposed that complex **25** may follow an analogous Ru WO mechanism, in which the generated Mn^{III}-OOH is further oxidized and deprotonated to produce O₂.

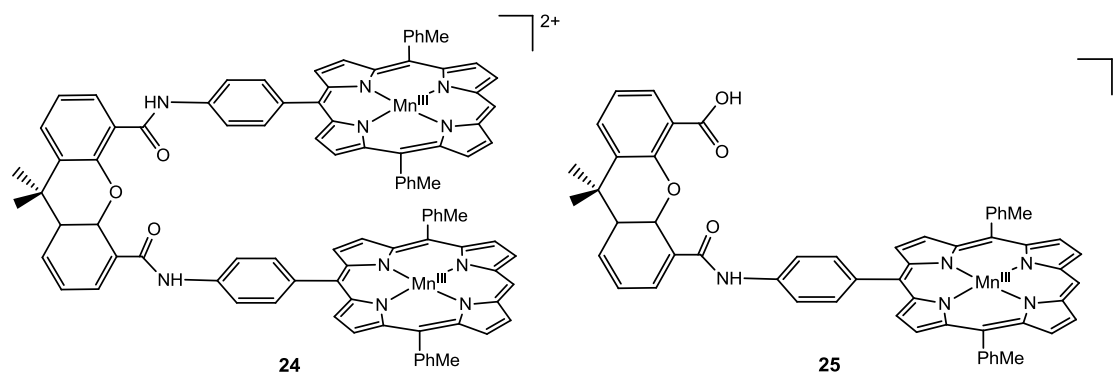


Figure 26: Molecular structure of cationic monomeric and dimeric manganese corrole complexes (**24-25**).

1.4.3.2 Iron based WOCs

Iron is the most attractive metal for the design of catalysts because is abundant, economic and environmentally friendly. In 2010, Ellis *et al.* reported the first iron WOC. A series of iron(III)-centered tetraamido macrocyclic ligand (Fe^{III}-TAML) complexes were synthesized (Figure 27), some of them capable of catalyze efficiently the oxidation of water to molecular dioxygen using CAN as oxidant.⁶⁵ A study of on-line O₂ evolution shows that the introduction of electron-withdrawing substituents into the ligand increase the rates of O₂ generation. The catalyst with R₁ = R₂ = Cl, R₃ = R₄ = F and X = H₂O (**26**) exhibited the lowest turnover number (TON > 16) for an iron WOC but a high turnover frequency (TOF > 1.3 s⁻¹), and its initial rate was first-order. Recently, Fe^V=O TAML intermediate has been generated photochemically with [Ru^{II}(bpy)₃]²⁺ as a photosensitizer and Na₂S₂O₈ as a sacrificial oxidant in a 50% acetonitrile-borate mixture, being the active species under photochemical conditions.⁶⁶

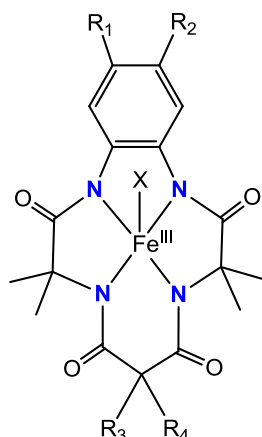


Figure 27: Fe^{III}-TAML catalyst family. The most active catalyst reported has R₁ = R₂ = Cl, R₃ = R₄ = F and X = H₂O (complex **26**).

The mechanism of thermal water oxidation by **26** and the nature of the various reactive intermediates participating in the catalytic cycle, were studied computationally by Cramer and co-workers through a combination of M06-L and multireference second-order perturbation theory (CASSCF/CASPT2) calculations.^{67a} The proposed catalytic cycle (Figure 28) starts with two proton-coupled electron transfer (PCET) reactions from [TAML-Fe^{III}-OH₂]⁻ to the [TAML-Fe^V-O]⁻ species. Then, one electron oxidation process on [TAML-Fe^V-O]⁻ leads to a highly oxidized [TAML⁺-Fe^V-O] (1.09 V vs. NHE), in which the TAML platform acts as an electron reservoir. Water nucleophilic attack on this high oxidized iron-oxo species to form an O-O bond is facilitated by a cluster of three adjacent water molecules to which proton transfer occur concomitant with O-O bond formation (30 kcal·mol⁻¹). The approach of a single water molecule to the oxo group was found to be repulsive at all distances. This solvent shell serves to relay a proton away from the product [TAML-Fe^{IV}-OOH]⁻. A subsequent PCET step generates formal peroxo [TAML-Fe^V-OO]⁻ (0.38 V) species. Finally, a transition state structure for displacement of O₂ by H₂O leads to oxygen releasing and catalyst regeneration, with a low free energy barrier (8.8 kcal·mol⁻¹).

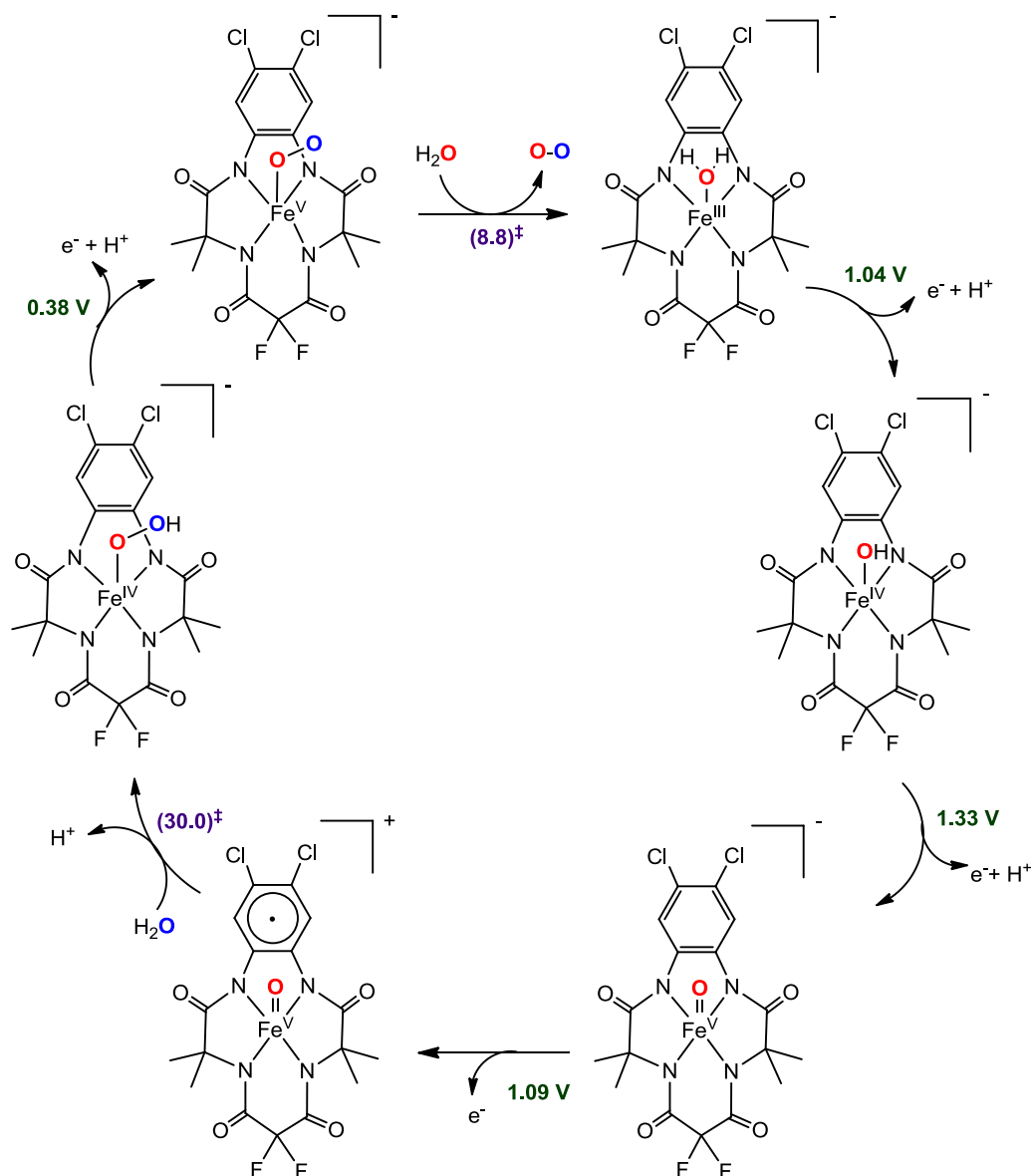


Figure 28: Catalytic water oxidation cycle postulated for the most active reported Fe^{III} -TAML complex **26**. Gibbs energy barriers are in $\text{kcal}\cdot\text{mol}^{-1}$. Oxidation potentials are calculated respect to the NHE.

The O-O bond formation step has a high energy barrier of $30.0 \text{ kcal}\cdot\text{mol}^{-1}$, but TOF value suggests a maximum activation free energy for the TDTS of about $20 \text{ kcal}\cdot\text{mol}^{-1}$. The lack of quantitative prediction was attributed to the complexity of the DFT accurate description of the electronic structure of the active species, which is very sensitive to the theoretical method employed. Following this direction, Siegbahn and coworkers revisited the previous WO mechanism comparing the data obtained from the M06-L and B3LYP- D_2 functionals.^{67b} The ligand degradation pathways that may experiment the TAML system and the involvement of nitrate anions in the O-O bond formation event were also considered. Representing the full energy diagram for the WO catalytic cycle, the authors observed that the M06-L favors the nitrate nucleophilic attack on the oxo moiety while B3LYP- D_2 the WNA mechanism. Interestingly, in the WNA on the TAML ligand ($\Delta G^\ddagger(\text{B3LYP-}\text{D}_2) = 10.9 \text{ kcal}\cdot\text{mol}^{-1}$) proceed faster than the O_2 formation ($\Delta G^\ddagger(\text{B3LYP-}\text{D}_2) = 15.4 \text{ kcal}\cdot\text{mol}^{-1}$), in agreement with the fast decomposition observed for the TAML iron complex.⁶⁵ The B3LYP- D_2 free energy barrier for the O-O bond formation is consistent with the TOF value.

In 2011, Lloret-Fillol *et al.* presented a new family of Fe^{II} catalysts for water oxidation (Figure 29), which has reached one of the highest turnover number described to date for a homogeneous system based on a first row transition metal.⁶⁸ These catalysts are formed by tetra- and pentadentate nitrogen chelating ligands, which coordinate to the iron center. The coordination sphere of Fe^{II} complexes is completed by labile anions (OTf = triflate). The accessibility and flexibility of these ligands has yielded preliminary information about the reaction mechanism. It was found that only iron catalysts with tetradentate ligands and two available positions in *cis* are effective, obtaining for the [Fe(OTf)₂(mcp)] (Figure 29; mcp = N,N'-bis(2-pyridylmethyl)-*trans*-1,2-diaminocyclohexane) catalyst 350 TON and more than 1000 TON when using CAN and NaIO₄ as oxidizing, respectively. Mechanistic studies conducted with the catalyst [Fe(OTf)₂(Pytacn)] showed that water oxidation is centered on a single metal center. The intermediate [Fe^{IV}(O)(OH₂)(Pytacn)]²⁺ was initially considered as the *resting state* of the catalytic cycle. Only O₂ formation is detected when an excess of oxidant is added to a solution of [Fe^{IV}(O)(OH₂)(Pytacn)]²⁺, showing that the O-O bond formation could take place through a higher iron oxidation state. The rate dependence with the concentration could be divided in two different regions: i) water oxidation reaction is first order respect both [Fe^{IV}(O)(OH₂)(Pytacn)]²⁺ and CAN at low concentrations; ii) but as the concentration of the oxidant increases the order of reaction respect to CAN tends to zero. The authors proposed that this phenomenon can be attributed to formation of a new intermediate before the determining step reaction.⁶⁹ Kinetic studies were consistent with a rate-determining WNA.

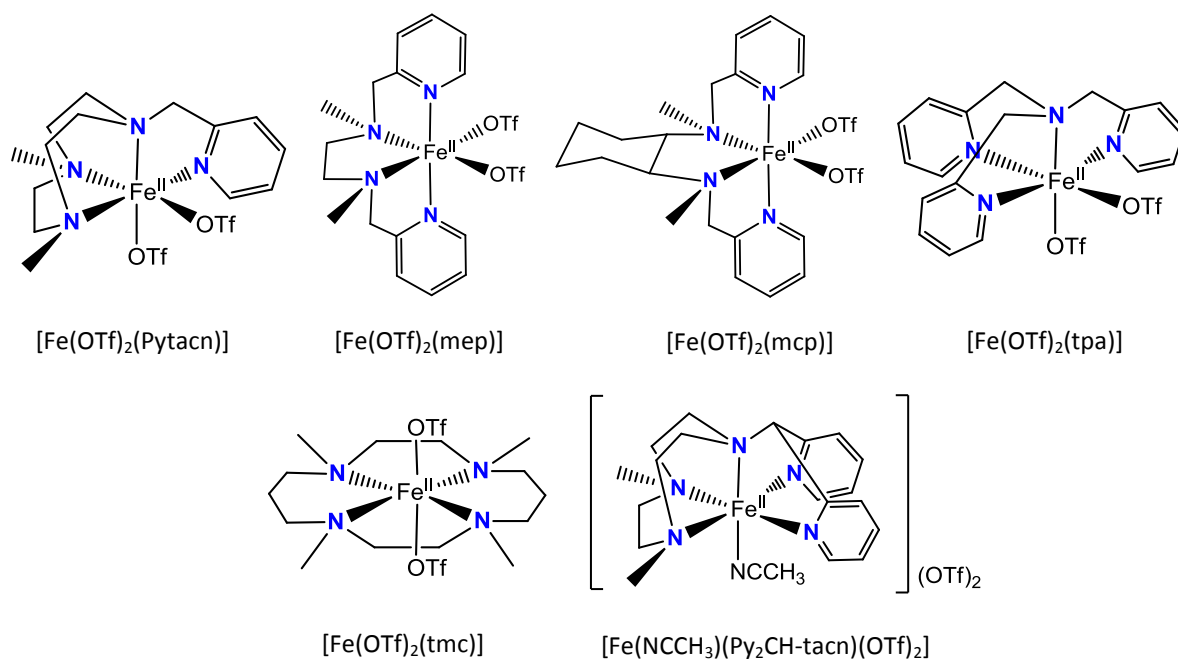


Figure 29: Family of catalytic water oxidation iron complexes. OTf stands for CF₃SO₃⁻ anion.

In a posterior publication the authors studied the electronic effects by introduction of substituents at the para-position of the pyridine in catalyst with general formula [Fe(OTf)₂(^{4-E}Pytacn)] (E = -Cl, -CO₂Et, -NO₂, Figure 30), observing a substantial increase of the rate and catalytic activity of the reaction with electron withdrawing group.⁶⁹ This observation shows that there is an evident correlation between catalytic activity and electronic nature of the catalyst. They also confirm by UV-Vis spectroscopy studies that the Ce^{IV} oxidant interacts with the aqua ligand of [Fe^{IV}(O)(OH₂)]²⁺ species as a Lewis acid, being the resulting adduct the resting state of the catalytic cycle under large excess of CAN.⁶⁹ The Fe^{IV}-Ce^{IV} intermediate derived from complex

[Fe(OTf)₂(mcp)] was recently characterized by rRaman and ESI-MS spectrometry, suggesting that an oxo bridge connects the two metals.⁷⁰

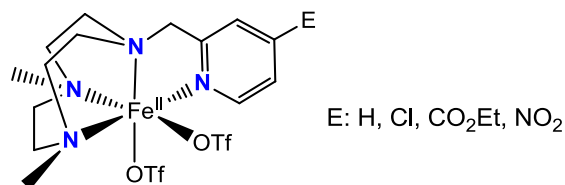


Figure 30: [Fe(OTf)₂(^{4-E}Pytacn)] substituted iron water oxidation catalyst.

All this data allowed the authors to propose the mechanism depicted in Figure 31. The resting state Fe^{IV}-O-Ce^{IV} may exist in equilibrium with the corresponding inner-sphere oxidized Fe^V-O(H)-Ce^{III} species. Then, the previous intermediate or free [Fe^V(O)(OH)]²⁺ species may constitute the key intermediate undergoing the WNA prior to O-O bond formation. However, many mechanistic details of the WO catalytic cycle remain unclear. For this reason, this thesis focuses on the computational mechanistic study of the water oxidation reaction by these iron systems. It is important to notice that the experimental work of the water oxidation with iron complexes was developed in parallel to this thesis, which provides a very intense experiment – theory / theory – experiment feedbacks.

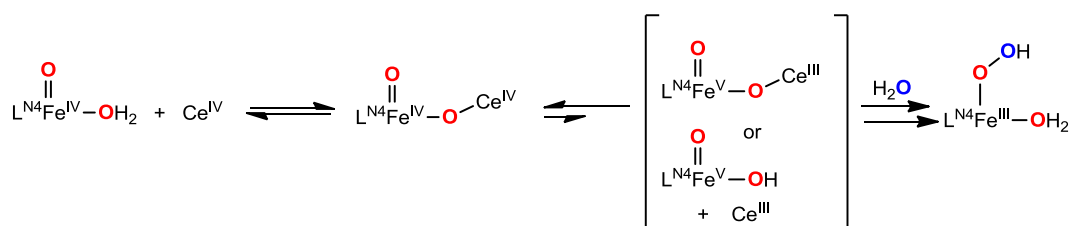


Figure 31: Proposed mechanism for water oxidation by non-heme iron complexes based on tetradentate ligands (L^{N4}).

In the last four years, other mononuclear iron WOC based on *N*-donor pyridyl/amine ligands with *cis* labile coordinating sites has been synthesized (Figure 32). From all this studies is clearly shown that the ligand design is very important. For instance, Llobet and coworkers report the capacity of [Fe^{II}(BQEN)(OTf₂)] (BQEN = N,N'-dimethyl-N,N'-bis(8-quinolyl)-ethane-1,2-diamine) (**27**) to oxidize water by CAN (TON: 80±10),⁷¹ but with competition of ligand degradation. UV-Vis spectroscopy, ESI-MS experiments confirm the formation of [Fe^{IV}(BQEN)(O)(OH₂)]²⁺ species.

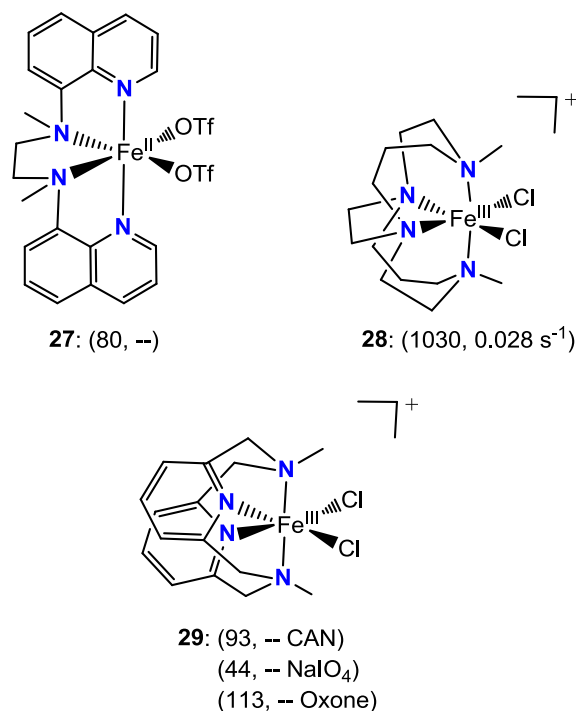


Figure 32: Structure of mononuclear iron complexes based on *N*-tetradentate ligands. TON and TOF values are shown in parentheses, respectively.

Lau and coworkers show that the iron(III) complex $cis\text{-[Fe}^{\text{III}}(\text{cbc})\text{Cl}_2]^+$ (**28**, Figure 32; $\text{cbc} = 4,11\text{-dimethyl-1,4,8,11-tetraazabicyclo[6.6.2]hexadecane}$) is capable to oxidize efficiently water at pH range 1-7 by using NaIO_4 as a sacrificial oxidant, with a maximum TON of 1030 and TOF of 0.028 s^{-1} .⁷² Cyclic voltammetry, UV-Vis, ESI-MS and ¹⁸O-labeling studies suggest that the active species should be a $[\text{Fe}^{\text{V}}(\text{cbc})(\text{O})(\text{OH})]^{2+}$ intermediate, following the Lloret-Fillol *et al.* initial proposal.

The *cis* effect was also identified in the macrocyclic $[\text{Fe}^{\text{III}}(\text{L}_2)\text{Cl}_2]^+$ (**29**, Figure 32; $\text{L}_2 = \text{N,N}^2\text{-dimethyl-2,11-diaza[3,3](2,6)pyridinophane}$). Che *et al.* studied the WO capacity of **29** using CAN, NaIO_4 and Oxone as oxidants in acid and neutral aqueous media.⁷³ The maximum TON values were 93, 44, 113 when CAN, NaIO_4 and Oxone were employed, respectively. Spectroscopic techniques and ¹⁸O-labelling experiments on **29** reveal that $\text{Fe}^{\text{IV}}=\text{O}$ and $\text{Fe}^{\text{V}}=\text{O}$ species may be involved in the WO reaction. ESI-MS measurements suggest that $[\text{Fe}^{\text{IV}}(\text{L}_2)(\text{O})(\text{OH})]^+$ intermediates are generated using CAN at pH = 1 and further oxidation may lead to the $[\text{Fe}^{\text{V}}(\text{L}_2)(\text{O})(\text{OH})]^{2+}$ active species. However, $[\text{Fe}^{\text{V}}(\text{L}_2)(\text{O})_2]^+$ reactive species are formed in ESI-MS experiments when NaIO_4 or Oxone oxidants are used at the same pH. Taking into account that NaIO_4 and Oxone are typically two-electron oxidants, the authors proposed the catalytic cycle depicted in Figure 33. M06-L calculations were performed to evaluate the energetic feasibility of the O-O bond formation event catalyzed by $[\text{Fe}^{\text{V}}(\text{L}_2)(\text{O})_2]^+$. By analogy with the $[\text{Ir}(\text{phpy})_2(\text{OH})_2]^+$ system, the reaction proceeds through an internal base assisted WNA with a free energy barrier of only $15.4\text{ kcal}\cdot\text{mol}^{-1}$. Further oxidation and deprotonation of hydroperoxide moiety in the $[\text{Fe}^{\text{III}}(\text{L}_2)(\text{OOH})(\text{OH})]^+$ product may lead to the generation of $[\text{Fe}^{\text{III}}(\text{L}_2)(\text{OO}\cdot)(\text{OH})]^+$. Finally, a solvent water molecule may displace the molecular oxygen from the iron coordination sphere and the subsequent redox event allows the recovering of the resting state $[\text{Fe}^{\text{III}}(\text{L}_2)(\text{OH})_2]^+$ species. Interestingly in this study the authors didn't found accumulation of a $\text{Fe}^{\text{IV}}\text{-Ce}^{\text{IV}}$ intermediate prior O-O bond formation.

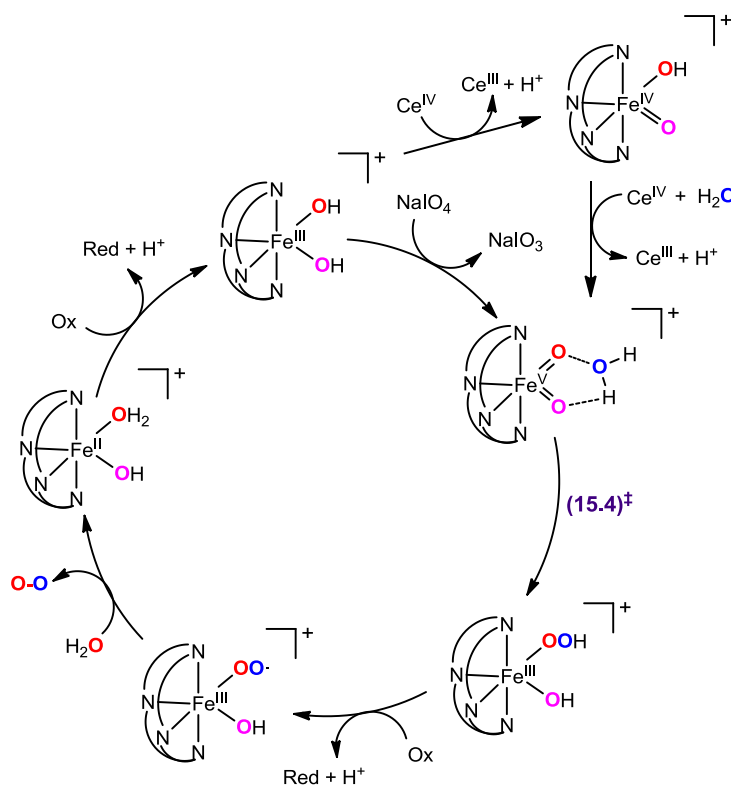


Figure 33: Proposed pathways for **29**-catalyzed water oxidation with CAN or NaIO₄. Labels “Ox” and “Red” mean the sacrificial oxidant and its reduced form, respectively. Gibbs energy barrier is in kcal·mol⁻¹.

Recently, the oxygen evolution capacity of some binuclear iron complexes has been corroborated. Larry Que and co-workers found that an electrochemically generated non-heme (μ -oxo)diiron(IV) (**30**, Figure 34) can oxidize water to a hydroxyl radical *via* a PCET process, instead of forming an O–O bond, with a rate constant of $0.73(3)\text{M}^{-2}\text{s}^{-1}$.⁷⁴ The absence of H₂O₂ or O₂ products and the linear dependence of the reaction rate on the square of the H₂O concentration, clearly point to a rate-determining step involving one oxidant iron dimer and two water molecules. The kinetic isotope effect (KIE) of 2.3 indicates that an O–H bond cleavage occurs in the rate-determining step. With this data in mind, the authors propose that WO reaction proceeds through an electron transfer (ET) from the water to **30**, being the activation barrier lowered by a proton transfer (PT) from one water molecule to another.

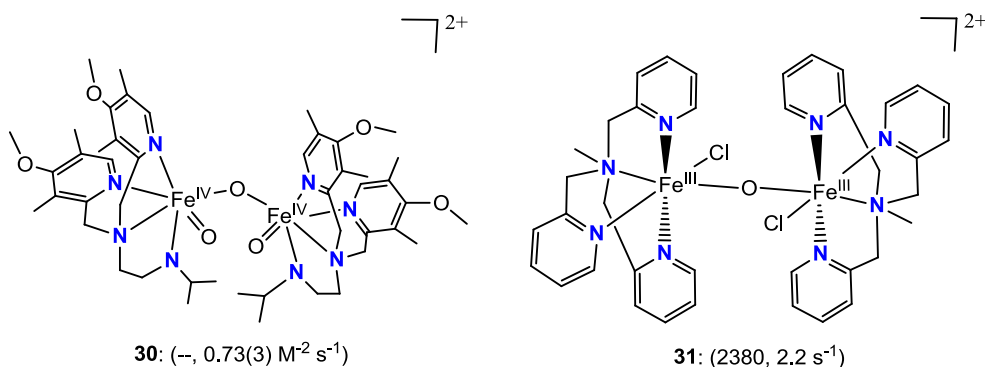


Figure 34: Structure of binuclear iron complexes. TON and TOF values are shown in parentheses, respectively.

Ma *et al.* observed that iron(III) compounds $[\text{Fe}^{\text{III}}(\text{TPA})\text{Cl}]^+$ and $[(\text{TPA})_2\text{Fe}^{\text{III}}_2(\mu\text{-O})\text{Cl}_2]^{2+}$ (**31**) in a acetate buffer convert to a $(\mu\text{-O})(\mu\text{-OAc})$ diiron(III) intermediate, which is responsible for the O-O bond formation when Oxone is employed.⁷⁵ UV-Vis spectral evolution of a mixture of diiron and Oxone in acetate buffer show the formation of a new intermediate which may correspond to a $\text{Fe}^{\text{IV}}=\text{O}$ dimer. Under optimal conditions, complex **37** presents a high TON value (2380) and a TOF of 2.2 s^{-1} . Although labelling studies showed that the O_2 molecule present oxygen atoms that come from water and Oxone, the latter is the major source of oxygen atoms. Thus, **37** cannot be considered a real WOC.

1.4.3.3 Cobalt based WOCs

Since the 1980s, it is known that some cobalt salts are able to catalyze the oxidation of water.⁷⁶ However, the search for cobalt based systems was stopped until Nocera and co-workers showed that an *in situ* generated cobalt phosphate system (Co-Pi) was capable of operating under neutral conditions with a low overpotential.⁷⁷ Since then, the number of reported cobalt-based WOCs has grown rapidly, including Co_3O_4 nanoparticles,⁷⁸ polyoxometalate clusters⁷⁹ and homogeneous mono- and binuclear cobalt molecular complexes. Herein, only the mechanistic aspects of some relevant homogeneous cobalt systems will be discussed.

In 2011, Berlinguette and coworkers reported the first cobalt electrocatalyst for water oxidation based on a pentadentate ligand 2,6-(bis(bis-2-pyridyl)methoxy-ethane)-pyridine (PY5) (**32**, Figure 35) that operates under basic media with a TOF of about 79 s^{-1} .⁸⁰ Electrochemical studies show a reversible redox wave at 0.75 V vs NHE at pH 2.2, which was attributed to the $[\text{Co}^{\text{III}}(\text{PY5})(\text{OH})]^{2+}/[\text{Co}^{\text{II}}(\text{PY5})(\text{OH}_2)]^{2+}$ redox couple. Thus, complex **26** operates through a PCET process, which allows the system to access to high oxidation states at lower redox potentials. A pH-independent oxidation event was also identified at 1.40 V in the range pH 7.6-10.3, corresponding to the $[\text{Co}^{\text{IV}}(\text{PY5})(\text{OH})]^{2+}/[\text{Co}^{\text{III}}(\text{PY5})(\text{OH})]^{2+}$ couple. At pH higher than 10.3, this process becomes pH-dependent (-59 mV/pH unit), which is consistent with the PCET process involving the $[\text{Co}^{\text{IV}}(\text{PY5})(\text{O})]^{2+}/[\text{Co}^{\text{III}}(\text{PY5})(\text{OH})]^{2+}$ couple. Further studies reveal that WO activity of **32** come from molecular species, although the participation of CoO_x nanoparticles cannot be ruled out.⁸¹ Considering the absence of the catalytic peak current in acidic media and the banned generation of formal $\text{Co}^{\text{IV}}=\text{O}$ species by the oxo-wall rule,⁸² the authors propose that the O-O bond formation in mildly to strongly basic media result from the WNA on the $[\text{Co}^{\text{IV}}(\text{PY5})(\text{OH})]^{2+}$ intermediate assisted by a base (OH⁻, phosphate buffer).

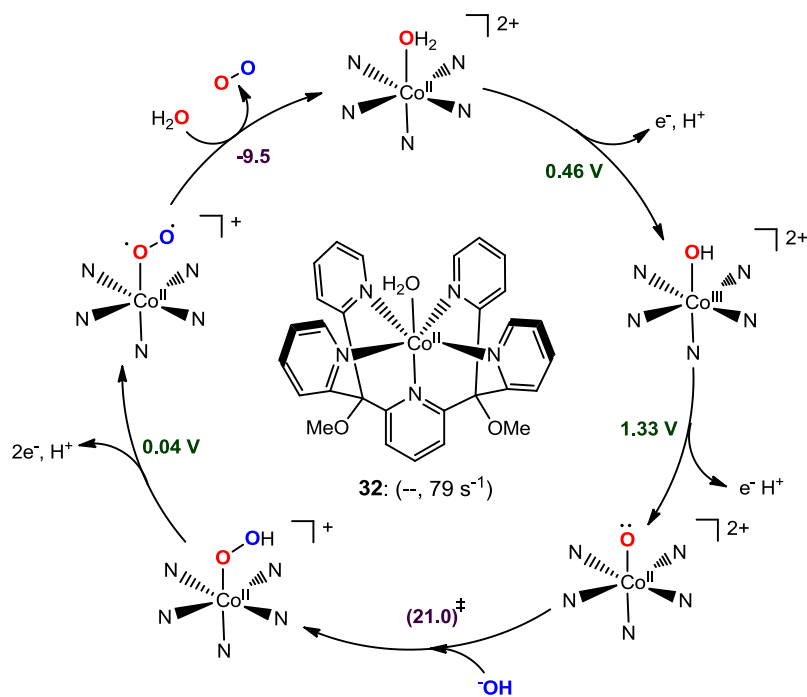


Figure 35: Molecular structure of $[\text{Co}^{\text{II}}(\text{PY5})(\text{OH}_2)]^{2+}$ (**32**) and DFT proposed catalytic cycle for water oxidation. TOF value is shown in parentheses. Oxidation potentials are calculated respect to the NHE at pH 9.2.

To get more insight into mechanistic details, Baik and coworkers carried out a DFT (B3LYP) study of the WO catalytic cycle performed by $[\text{Co}^{\text{II}}(\text{PY5})(\text{OH}_2)]^{2+}$ at pH 9.2 (Figure 35).⁸³ The computed redox potentials for the couples $[\text{Co}^{\text{III}}(\text{PY5})(\text{OH})]^{2+}/[\text{Co}^{\text{II}}(\text{PY5})(\text{OH}_2)]^{2+}$ (0.87 V) and $[\text{Co}^{\text{IV}}(\text{PY5})(\text{O})]^{2+}/[\text{Co}^{\text{III}}(\text{PY5})(\text{OH})]^{2+}$ (1.33 V) are close the experimental ones. The spin density and molecular orbitals analysis indicate that the Co-O moiety in $[\text{Co}^{\text{IV}}(\text{PY5})(\text{O})]^{2+}$ is best represented as a biradicaloid $\text{Co}^{\text{II}}-(\cdot\text{O}\cdot)$, due to an intramolecular electron transfer between the oxo ligand and cobalt. The Iron-oxene fragment has been proposed in the oxidation mechanism by cytochrome P450,⁸⁴ but this was the first that the oxene character was proposed for a synthetic complex. The free energy barrier for the nucleophilic attack of a hydroxide moiety on the $\text{Co}^{\text{II}}\text{-oxene}$ is $21.0 \text{ kcal}\cdot\text{mol}^{-1}$, which can be reached under catalytic conditions. They also consider the dissociation of a pyridine ligand and the incorporation of a hydroxide group in the coordination sphere of the cobalt center. However, the intramolecular O-O coupling between OH and $\text{Co}^{\text{II}}\text{-oxene}$ has a higher free energy cost than the intermolecular mechanism. Further oxidation and deprotonation of the generated hydroperoxide $[\text{Co}^{\text{II}}(\text{PY5})(\text{OOH})]^+$ results in the molecular oxygen evolution and the recovering of **32**. In contrast with Ru or Ir WOCs, the formal oxidation state of the cobalt center always remains and the oxygen moieties are the groups that suffer the oxidation processes. This allows the cobalt system to reach a high oxidation state with a reduced energetic cost.

Nocera and coworkers show that the cobalt β -octafluoro hangman corrole $[(\text{Cor-CO}_2\text{H})\text{Co}^{\text{III}}(\text{OH}_2)]^{3+}$ (**33**, Figure 36) not only reduces oxygen but also oxidize water under electrocatalytic conditions.⁸⁵ It was believed in the active form of the complex, the hanging carboxylic acid group ($-\text{COOH}$) positioned in close proximity to the cobalt-oxo group may act as a proton acceptor, assisting the WNA attack on the Co-O moiety. Moreover, it was expected that the fluoride groups may reduce the oxidation potential to reach high valent species. Complex **33** was found to display a catalytic onset at 1.45 V vs NHE under pH 7 with a TOF of 0.81 s^{-1} . The computational mechanistic analysis was addressed in a subsequent study by Cramer and Ertem,

using a model structure without the tBu and methyl groups in the xantheno moiety (Figure 36).⁸⁶ DFT(M06-L) calculations show that complex **33** may reach a $[(\cdot\text{Cor-CO}_2\text{H})\text{Co}^{\text{III}}(\text{O}\cdot)]^{3+}$ intermediate after two PCET events (low potentials of 0.69 V vs. NHE and 1.06 V vs. NHE), in which the extracted electrons derive from the corrole ligand and oxo group instead of the metal center. The subsequent deprotonation of the hanging carboxylic acid and the WNA on the Co^{III} -oxyl group assisted by the carboxylate base have a total energy barrier of $22.5 \text{ kcal}\cdot\text{mol}^{-1}$. A second water molecule is required to act as a proton shuttle from the nucleophilic water molecule to the carboxylate moiety. The generated cobalt hydroperoxide $[(\text{Cor-CO}_2\text{H})\text{Co}^{\text{III}}(\text{OOH})]^{2+}$ evolves to $[(\text{Cor-CO}_2\text{H})\text{Co}^{\text{III}}(\text{OO}\cdot)]^{2+}$ after a PCET reaction (0.10 V) and the latter species may follow different thermodynamically viable pathways until the molecular oxygen release takes place. As occurred with complex **32**, the corrole ligand and oxygen moieties have a lower oxidation potential than the cobalt center, remaining the latter in the III oxidation state in all the steps of the catalytic cycle.

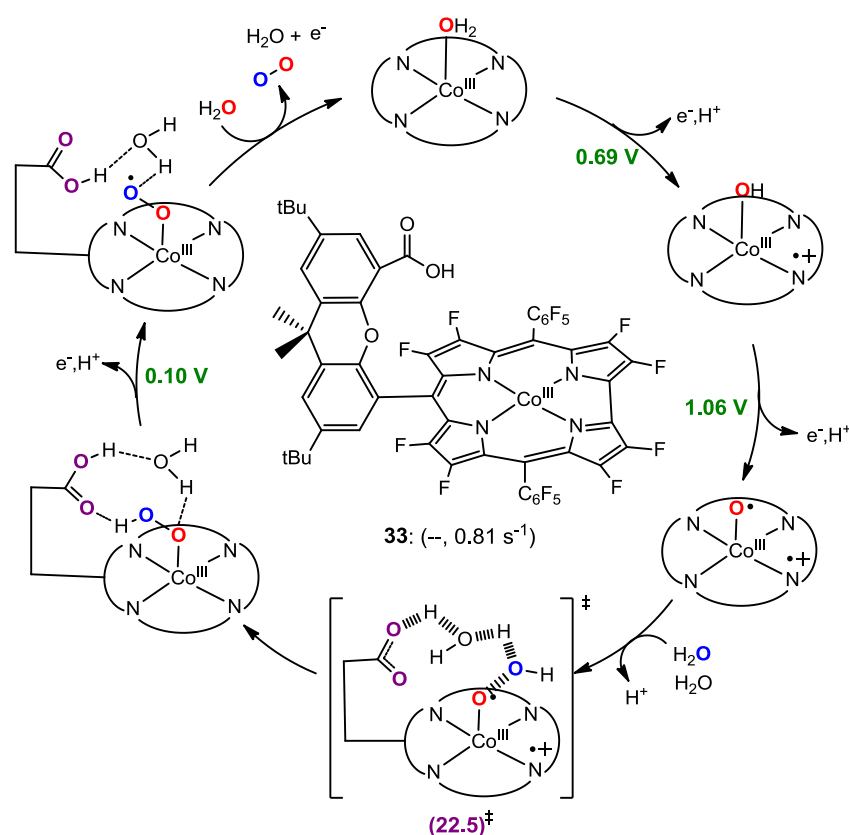
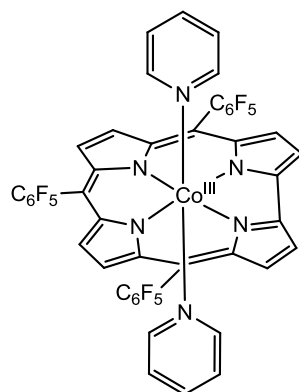


Figure 36: Molecular structure of $[(\text{Cor-CO}_2\text{H})\text{Co}^{\text{III}}(\text{OH}_2)]^{3+}$ (**33**) and DFT proposed catalytic cycle for water oxidation. TOF value is shown in parentheses. Oxidation potentials are calculated respect to the NHE.

Another interesting cobalt corrole complex $[\text{Co}(\text{tpfc})(\text{pyr})_2]$ (**34**, Figure 37; tpfc = 5,10,15-tris-(pentafluorophenyl)corrole; pyr = pyridine) capable to electrocatalyze the water oxidation and reduction was reported by Lei *et al.*⁸⁷ Experimental data and DFT(M06-L) calculations suggest that **34** follows a very similar operational WO mechanism described for **33**, with a TOF of 0.20 s^{-1} . The O-O bond formation also occurs through a WNA on a $\text{Co}^{\text{III}}\text{-O}\cdot$ moiety but, in contrast with **33**, the reaction is assisted by the acetate buffer anions. The computed free energy barrier for the O-O bond formation event is $18.0 \text{ kcal}\cdot\text{mol}^{-1}$, in agreement with the $18.4 \text{ kcal}\cdot\text{mol}^{-1}$ derived from the TOF value.



34: (–, 0.20 s^{–1})

Figure 37: Molecular structure of [Co(tpfc)(pyr)₂] (**34**). TON and TOF values are given in parentheses.

Some binuclear cobalt systems are also active in water oxidation reaction. Llobet, Stahl and co-workers reported the synthesis and characterization of two binuclear Co^{III}Co^{III}-(μ-peroxo) WO electrocatalysts, [Co(terpy)]₂(μ-bpp)(μ-1,2-O₂)³⁺ (**35**) and [Co(Me₂bimpy)]₂(μ-bpp)(μ-1,2-O₂)³⁺ (**36**) (Me₂bimpy = bis-(N-methylimidazolyl)-pyridine), based on a bispyridylpyrazolate (bpp) ligand (Figure 38a).⁸⁸ The use of the non-labile bpp ligand minimizes the ligand exchange reactions and the decomposition of the Co complex. The authors get inspired by a previous computational study about the involvement of dinuclear Co^{III}-Co^{III}-bridging peroxo intermediates in the WO mechanism catalyzed by heterogeneous Co oxides.⁸⁹ Both complexes were able to catalyze the electrochemical WO in aqueous 0.1 M, pH 2.1 phosphate. The first observed quasi-reversible wave (**35**: 1.56 V vs. NHE and **36**: 1.35 V vs. NHE) corresponds to the Co^{IV}Co^{III}/Co^{III}Co^{III} redox couple. A second oxidation wave at 1.82 V and 1.84 V by complexes **35** and **36**, respectively, belong to the Co^{IV}Co^{IV}/Co^{IV}Co^{III} redox couple. The two previous redox events were followed by a catalytic wave at 1.91 V vs NHE, suggesting that the WO reaction is triggered when the Co^{IV}Co^{IV} state is reached. Therefore, **35** and **36** share a common mechanism, where two oxidation reactions are necessary to reach the Co^{IV}Co^{IV} state before O₂ release. The two catalysts were stable for several hours without signs of nanoparticles generation. By analogy with the previous mechanistic studies conducted on a bpp-Ru WOC,²¹ they propose that an undetected Co^{III}(OH)Co^{III}(OH) dimeric intermediate may undergo two PCET reactions to afford formal Co^{IV}(O)Co^{IV}(O) active species (Figure 38b). Then, the O–O bond formation event takes place, generating the peroxo-bridged Co^{III}(O–O)Co^{III} structure. Further oxidation of Co^{III}(O–O)Co^{III} may lead to the molecular oxygen evolution.

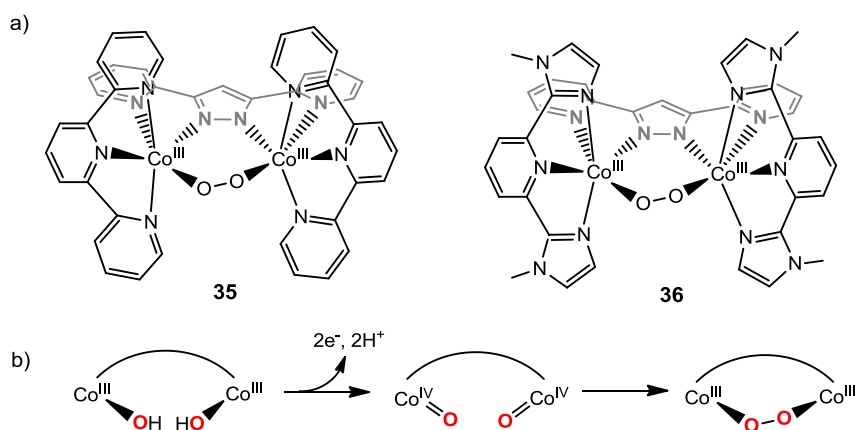


Figure 38: Molecular structure of $[\text{Co}(\text{terpy})]_2(\mu\text{-bpp})(\mu\text{-1,2-O}_2)]^{3+}$ (**35**) and $[\text{Co}(\text{Me}_2\text{bimpy})]_2(\mu\text{-bpp})(\mu\text{-1,2-O}_2)]^{3+}$ (**36**). b) Schematic representation of the O-O bond formation mechanism by formal $\text{Co}^{\text{IV}}=\text{O}$ species derived from **35** and **36**.

Other mononuclear cobalt based WOCs have been reported which can catalyze the WO reaction under photochemical conditions, such the *trans*- $[\text{Co}(\text{qpy})(\text{OH}_2)_2]^{2+}$ complex (qpy = 2,2':6',2'':6'',2''':6'''-quaterpyridine) prepared by Lau et al.⁹⁰ and cobalt salen complexes.⁹¹ However, the authors did not provide any detailed information about the structure of the catalytic intermediates and the way that the O-O bond formation occurs.

1.4.3.4 Nickel based WOCs

In 2014, Lu and coworkers reported the first nickel based homogeneous electrocatalyst for water oxidation, *trans*- $[\text{Ni}^{\text{II}}(\text{L})](\text{ClO}_4)_2$ (**37**, Figure 39; L = 5,5,7,12,12,14-hexamethyl-1,4,8,11-tetraazacyclotetradecane), that can operate at neutral pH and low overpotential (170 mV) in phosphate buffer.⁹² A long time induction was observed, attributed to the conversion of the *trans*-isomer to the active *cis*-isomer. Cyclic voltammetry, controlled potential electrolysis experiments and DFT calculations (with the B3P86 functional for geometry optimizations and BP86* for free energies evaluation) suggest that the reaction starts with the incorporation of two water molecules on the *trans* free vacant sites of the nickel complex followed by a PCET to generate *trans*- $[\text{Ni}^{\text{III}}(\text{L})(\text{OH})(\text{OH}_2)]^{2+}$ species (Figure 39). The computed potential for the generation of $[\text{Ni}^{\text{III}}(\text{L})(\text{OH})(\text{OH}_2)]^{2+}$ is 0.91 V, close to the measured potential of 0.87 V. Then, the system may follow two possible pathways to reach the Ni^{IV} oxidation state: a second PCET to form the formal $[\text{Ni}^{\text{IV}}(\text{L})(\text{O})(\text{OH}_2)]^{2+}$ (1.74 V) species; or the isomerization from the *trans*- $[\text{Ni}^{\text{III}}(\text{L})(\text{OH})(\text{OH}_2)]^{2+}$ to trigonal bipyramidal (TB) and the subsequent PCET to TB- $[\text{Ni}^{\text{IV}}(\text{L})(\text{O})(\text{OH}_2)]^{2+}$ (1.53 V). The second event is consistent with the observed redox potential of 1.41 V for the $\text{Ni}^{\text{III}}/\text{Ni}^{\text{IV}}$ couple. The spin density analysis reveals that the Ni-O moiety presents an important oxyl character and it is best represented as a $\text{Ni}^{\text{III}}\text{-O}\cdot$. The water O-H bond insertion and the WNA on the Ni-O bond always give barriers between 30 and 60 $\text{kcal}\cdot\text{mol}^{-1}$, which cannot be reached at room temperature. In contrast, the isomerization of the $\text{Ni}^{\text{III}}\text{-O}\cdot$ intermediate to *cis*- $[\text{Ni}^{\text{IV}}(\text{L})(\text{OH})(\text{OH})]^{2+}$ and the subsequent coupling of the two hydroxide groups has a reachable barrier of 26.4 $\text{kcal}\cdot\text{mol}^{-1}$. Therefore, *cis*-isomer becomes crucial for the catalytic activity, as it was observed in iron WOCs. Further oxidation and deprotonation of the HO-OH moiety in the *cis*- $[\text{Ni}^{\text{II}}(\text{L})(\text{HO-OH})]^{2+}$ product may lead to the molecular O_2 release. The O-O bond formation free energy barrier is close to the kinetic limit at room temperature (25 $\text{kcal}\cdot\text{mol}^{-1}$), which is in agreement with the rate limiting character attributed to this chemical step from electrochemical data.

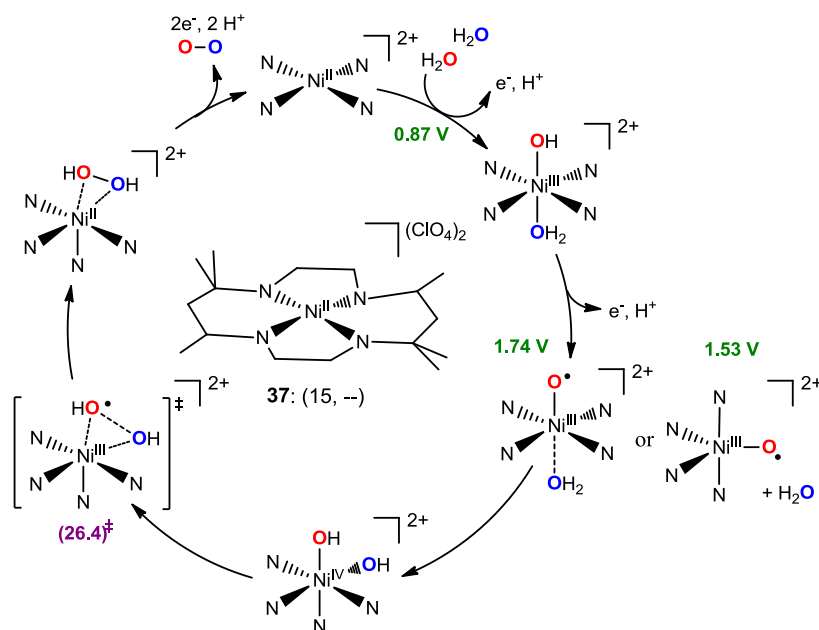


Figure 39: Water oxidation catalytic cycle by *trans*-[Ni^{II}(L)](ClO₄)₂ (**37**). Oxidation potentials are calculated respect to the NHE. Gibbs energy barrier is in kcal·mol⁻¹.

The electrocatalytic water oxidation capacity of a nickel(II) complex [(Por)Ni^{II}]⁴⁺ based on the *meso*-tetrakis(4-*N*-methylpyridyl)porphyrin ligand (**38**, Figure 40) was verified by Cao *et al.*⁹³ Catalyst **38** exhibited water oxidation activity in a pH range 2.0-8.0, with a TOF of 0.67 s⁻¹ at 20 °C. On the basis of kinetic isotope effect (KIE), inhibition and electrochemical studies in various buffer solutions with different anions and pHs, the authors suggest that “Por” is a redox non-innocent ligand and propose that the O-O bond formation occurs through a WNA on a formal Ni^{IV}=O moiety assisted by the buffer base. To provide more confidence in their results, the WO catalytic cycle was explored by means of DFT(B3LYP) calculations (Figure 40). Initially, complex **38** suffers a ligand-centered oxidation (1.63 V vs. NHE). This allows the nickel(II) system to accommodate a water molecule in an axial position ($\Delta G = 3.3$ kcal·mol⁻¹). Then, the first PCET on [(•Por)Ni^{II}-OH₂]⁵⁺ forms an unstable [(•Por)Ni^{III}-OH]⁵⁺ intermediate (1.89 V), which loses a proton to generate a [(Por)Ni^{III}-O•]⁴⁺ intermediate ($\Delta G = -5.2$ kcal·mol⁻¹). Two strategies were considered to model the O-O bond formation event: 1) the WNA on [(Por)Ni^{III}-O•]⁴⁺ assisted by the bulk solvent (represented by a cluster of four water molecules) or 2) the WNA assisted by the acetate buffer anions. The former mechanism present a free energy barrier of 24.9 kcal·mol⁻¹, close to the kinetic limit at room temperature, while the latter is the preferred pathway by 18.0 kcal·mol⁻¹. The calculated KIE for the later mechanism (1.44) is in excellent agreement with the experimental one (1.55) and the computed free energy barrier is consistent with that derived from the TOF (17.7 kcal·mol⁻¹). Finally, the loss of two electrons and a proton of the final hydroperoxide [(Por)Ni^{II}-OOH]³⁺ product results in the regeneration of **38** and the molecular oxygen release.

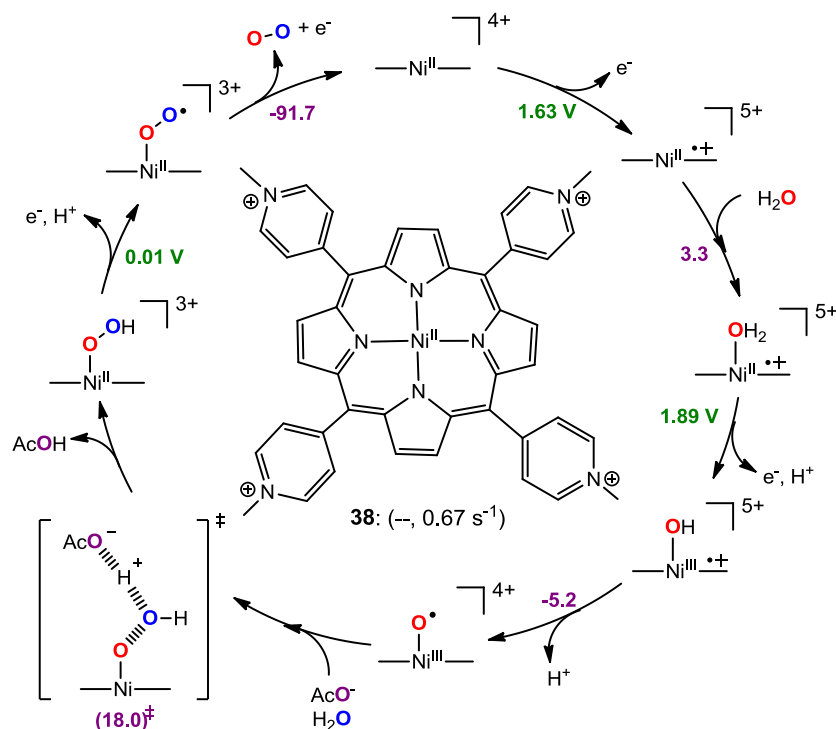


Figure 40: Water oxidation catalytic cycle by $[(\text{Por})\text{Ni}^{\text{II}}]^{4+}$ (**38**). Oxidation potentials are calculated respect to the NHE. Gibbs energies are in $\text{kcal}\cdot\text{mol}^{-1}$.

Sun and coworkers show that pentadentate complex $[\text{Ni}^{\text{II}}(\text{PY5})\text{Cl}]^+$ (**39**, Figure 41) is also an electrocatalyst for water oxidation in aqueous phosphate buffer solutions.⁹⁴ Long term bulk electrolysis experiments reveal an enhancement of the initial catalytic current after a short time. This could be consistent with the formation of nickel oxide particles or the ligand exchange chemical reaction from $-\text{Cl}$ to $-\text{OH}_2$. However, the DFT(M06) optimized $[\text{Ni}^{\text{II}}(\text{PY5})(\text{OH}_2)]^{2+}$ is in good agreement with the crystal structure obtained from the resulting solution after electrolysis, revealing that the origin of the current enhancement is due to the ligand exchange. Cyclic and differential pulse voltammetry studies were performed to construct a Pourbaix diagram over the pH range 6.2–12. Two PCET events were detected: the evolution from $[\text{Ni}^{\text{II}}(\text{PY5})(\text{OH}_2)]^{2+}$ to $[\text{Ni}^{\text{III}}(\text{PY5})(\text{OH})]^{2+}$ species (1.49 V vs. NHE at pH 6.2) and a second unusual oxidation process in which two e^- and one H^+ are transferred, attributed to the $[\text{Ni}^{\text{V}}(\text{PY5})(\text{O})]^{3+}/[\text{Ni}^{\text{III}}(\text{PY5})(\text{OH})]^{2+}$ couple (1.72 V at pH 6.2). Kinetic studies show an impressive TOF of about 2000 s^{-1} when 1.0 M phosphate buffer is applied. Moreover, the $\text{H}_2\text{O}/\text{D}_2\text{O}$ KIE was 2.06, consistent with a rate determining step O-O bond formation assisted by the phosphate base buffer. Taking into account all this data, the authors propose a WO catalytic cycle in which the WNA on formal $\text{Ni}^{\text{V}}=\text{O}$ species is the dominant pathway.

Meyer *et al.* reported the first polypeptide copper (II) complex formed by the self-assembly of the triglycylglycine macrocyclic ligand (TGG) and $\text{Cu}^{\text{II}}(\text{OH})_2$.⁹⁶ Cyclic voltammetry, controlled potential electrolysis and kinetic studies show that complex $[(\text{TGG})\text{Cu}^{\text{II}}(\text{OH}_2)]^{2-}$ (**41**, Figure 43; TGG = Triglycylglycine) efficiently catalyze the WO reaction in a phosphate buffer at pH 11. Based on electrochemical data, the authors proposed a WO mechanism analogous to that considered for Ru and Ir WOC (Figure 43). The O-O bond formation event was identified as the rate-determining step of the reaction, which may proceed through a water nucleophilic attack on $[(\text{TGG})\text{Cu}^{\text{III}}(\text{O}\cdot)]^{2-}$ moiety to give the hydroperoxide intermediate $\text{Cu}^{\text{II}}\text{-OOH}$. The catalytic peak current dependence on the buffer concentration suggests that the WNA is assisted by the phosphate buffer base. Complex **41** has a relevant TOF of 33 s^{-1} , which is comparable with that of **40**.

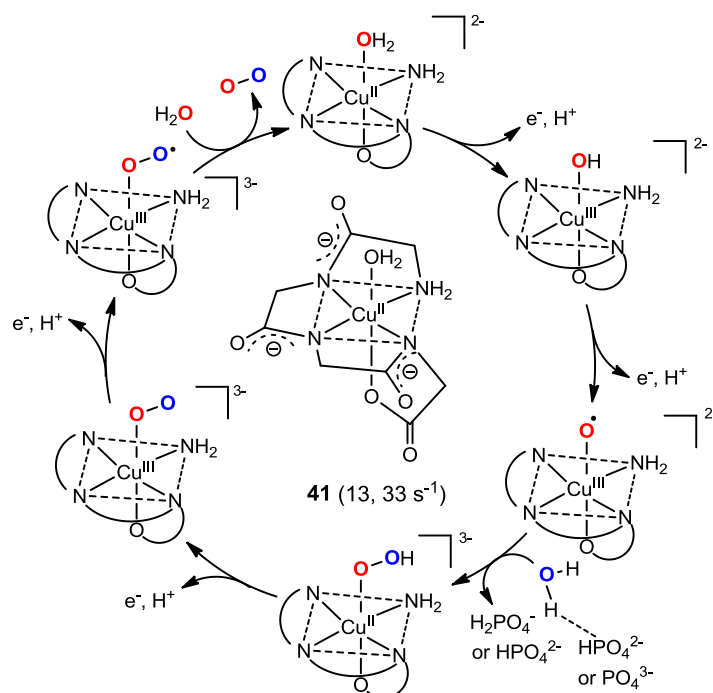


Figure 43: Proposed water oxidation mechanism by $[(\text{TGG})\text{Cu}^{\text{II}}(\text{OH}_2)]^{2-}$ species (**41**). TON and TOF values are given in parentheses, respectively.

Although the previous copper based WOCs show high current densities and good stabilities under basic pH, high oxidation state copper species (Cu^{III} / Cu^{IV}) are difficult to reach, leading to high overpotentials for WO that limit their practical utility. To solve this deficiency, Lin and coworkers introduced hydroxyl groups on the bpy ligand of complex **40** to mimic the role of tyrosine Z in Photosystem II, enabling the hydroxyl groups to participate in the PCET processes.⁹⁷ Moreover, the ligand becomes redox non-innocent, which may lower the overpotential and enhance the WO activity. Cyclic voltammetry studies on $[\text{Cu}^{\text{II}}(\text{bpyOH})(\text{OH})_2]^{2+}$ (**42**, Figure 44; bpyOH = 6,6'-dihydroxy-2,2'-bipyridine) from pH 12 to 14 show irreversible catalytic current with an onset potential of about 0.8 V versus the normal hydrogen electrode. Computational studies at B3LYP level reveal the energetically feasible redox pathways and acid-base equilibria experimented by the copper system under electrochemical conditions at pH 12.4 (Figure 44). The reaction starts with the deprotonation of one coordinated hydroxyl group under basic pH ($\text{pK}_a = 10.9$). Then, a PCET event enable the copper complex to reach a Cu^{III} intermediate (1.0 V vs. NHE), with the protons of the bipyridine hydroxide's groups totally transferred to the resulting oxygen moieties on the copper center. Then, a ligand centered oxidation reaction generates $[\text{Cu}^{\text{III}}(\cdot\text{bpyO})(\text{OH})_2]$ species (1.1 V). It

was proposed that the O-O bond formation reaction occurs through a WNA on $[\text{Cu}^{\text{III}}(\cdot\text{bpyO})(\text{OH})_2]$. The TOF of $[\text{Cu}^{\text{II}}(\text{bpyOH})(\text{OH})_2]^{2+}$ (0.4 s^{-1}) has a much lower value than the one obtained for $[\text{Cu}^{\text{II}}(\text{bpy})(\text{OH})_2]^{2+}$ (100 s^{-1}). Therefore, the redox-non innocent character of the bpyOH ligand translates into stabilization of the high-valent intermediates, lowering of the overpotential for H_2O oxidation.

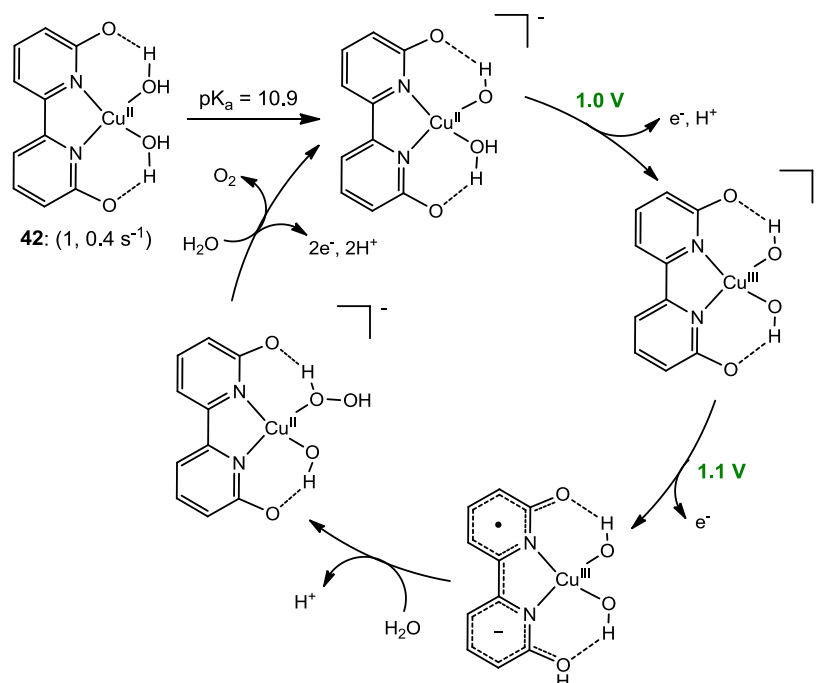


Figure 44: Proposed water oxidation mechanism by $[\text{Cu}^{\text{II}}(\text{bpyOH})(\text{OH})_2]^{2+}$ species (**42**). Oxidation potentials are calculated respect to the NHE. TON and TOF values are given in parentheses, respectively.

In 2015, Llobet, Feliu Maseras and coworkers reported the synthesis, characterization and computational study of a new family of copper WOC based on an anionic tetradentate amidate acyclic ligand H_4L_1 (N_1, N_1' -(1,2-phenylene)bis(N_2 -methyloxalamide)), containing electron-donating groups at the aromatic ring.⁹⁸ Cyclic voltammetry studies at pH 11.5 show that $[(\text{L}_1)\text{Cu}^{\text{II}}]^{2-}$ (**43**, Figure 45) first suffers a metal-centered oxidation to $[(\text{L}_1)\text{Cu}^{\text{III}}]$ with a low potential of 0.56 V versus NHE. On the contrary, the subsequent redox event is pH-dependent, with a modest oxidation potential of 1.26 V, and it was considered as ligand centered. The PCET involves the oxidation of the phenyl group together with the coordination of a hydroxide ligand, reaching $[(\cdot\text{L}_1)(\text{Cu}^{\text{III}}\text{OH})]$ species. As the electron-donating capacity at the aromatic ring increases, the overpotential is reduced by more than 500 mV, up to an overpotential of 170 mV, a clear fingerprint of the involvement of the ligand in the electrochemical activity of $[(\text{L}_1)\text{Cu}^{\text{II}}]^{2-}$. A catalytic rate constant of 3.6 s^{-1} was obtained through a foot-of-the-wave analysis. Furthermore, DFT calculations at B3LYP level were conducted to explore the complete WO catalytic cycle (Figure 45). According to the computed energy profile, the rate determining step involves the generation of $[(\cdot\text{L}_1)\text{Cu}^{\text{III}}(\text{OH})]$ species and its reaction with an OH^- moiety. Interestingly, the O-O bond formation does not follow a conventional nucleophilic attack mechanism on the Cu-OH moiety. Instead, one electron transfer occurs from the hydroxide moiety to the $\text{Cu}^{\text{III}}\text{-OH}$ group, generating a $[(\text{L}_1)\text{Cu}^{\text{III}}(\text{HO}\cdots\text{OH})\cdot]^{2-}$ radical anionic intermediate, in a type of mechanism labeled single-electron transfer water nucleophilic attack (SET-WNA). Then, after a second electron transfer, the $[(\text{L}_1)\text{Cu}^{\text{II}}(\text{HOOH})]^{2-}$ intermediate is achieved, and

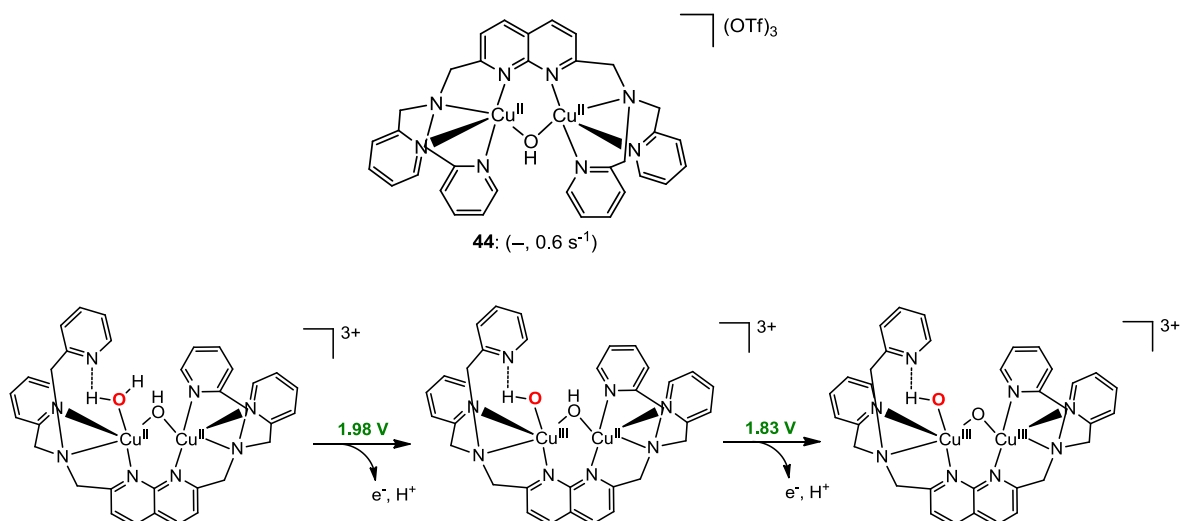


Figure 46: a) Above, molecular structure of $[\text{Cu}^{\text{II}}_2(\text{BPMAN})(\mu\text{-OH})](\text{OTf})_3$ (**44**). TON and TOF values are given in parentheses, respectively. Below, generation of $[\text{Cu}^{\text{III}}(\text{OH})(\mu\text{-O})\text{Cu}^{\text{III}}(\text{BPMAN})]^{3+}$ species from $[\text{Cu}^{\text{II}}(\text{OH}_2)(\mu\text{-O})\text{Cu}^{\text{II}}(\text{BPMAN})]^{3+}$. Oxidation potentials are calculated respect to the NHE.

Summarizing this section, the synergism between the computational and experimental studies has enabled a deep understanding of the key steps of the water oxidation process at atomic scale. This knowledge has been used to rationally design more efficient WOCs. Most of the structure-activity data has been obtained from the study of earth-scarce metal based catalysts (such as Ru or Ir). Unfortunately, less mechanistic research has been conducted on first row transition metal complexes (Mn, Fe, Co, Ni, Cu). In general, the proposed catalytic cycles fall in two different mechanism scenarios a water nucleophilic attack and direct coupling mechanism regardless of the metal and ligand employed. However, in contrast to the second and three row transition metal complexes, these systems may reach a variety of spin and oxidation states which lead to a larger variety of mechanistic scenarios. Furthermore, there is still a lack of information about: i) the influence of other species present in the reaction media (i.e. oxidants); ii) the decomposition pathways and robustness of the catalysts. A detailed knowledge of all the chemical transformations suffered by the earth abundant based systems will facilitate the development of efficient and low cost artificial photosynthetic devices.

The first part of this thesis is devoted to improve the understanding of the WO mechanism by Fe catalyst. To achieve this goal we have performed an extensive computational study of the WO reaction catalyzed by a family of non-heme iron complexes. In chapters 4-6, the mechanism and the influence of the ligand geometry on WO reaction are unrevealed. Then, to draw a complete picture of the process, the decomposition pathways and the influence of the oxidant (CAN) on the WO activity are analyzed in chapter 7. Finally, in chapter 8 the capacity of a non-hem iron complex to oxidize H_2 and the potential efficiency of water splitting devices based on high valent non-heme iron catalysts is discussed.

The water splitting devices requires also a catalyst operating in the reductive site to produce the fuel. H_2 produced by sun-light is one of the most convenient fuels for a CO_2 clean energy cycle. Moreover, water oxidation and water reduction can be classified as multi proton-electron

transformation, sharing common mechanism features. In this regard, the next section contains a mechanistic review of some of the most relevant proton/water reduction catalysts.

1.5. Hydrogenase Enzymes

In nature, the reversible conversion between protons and hydrogen is catalyzed by a class of redox enzymes called Hydrogenases, which are present in some prokaryote, archaea and algae species.⁶ These systems have remarkable TOF values between 1000-10000 s⁻¹ at 30°C.¹⁰⁰ Hydrogenases are classified into three classes based on the metal atoms composition of the active site (Figure 3):¹⁰¹

- 1) **[FeFe]-hydrogenases:** Contain a binuclear iron fragment, with the two metals connected through a CO and dithiolate bridging groups, and a cubane [4Fe4S] cluster (Figure 47A). Two CO and CN ligands and a water molecule complete the coordination sphere of the iron centers. The Fe-Fe hydrogenases usually work as proton reduction catalysts.^{101b}
- 2) **[Fe]-hydrogenases:** Contain one iron atom with two CO ligands, a water molecule and the methylenetetrahydromethanopterin (methylene-H4MPT) organic cofactor (Figure 47B).
- 3) **[NiFe]-hydrogenases:** Contain a binuclear Ni-Fe fragment. The coordination sphere of the iron atom is occupied by one CO and two CN ligands, while cysteine residues (Cys) are chelating the nickel center. The two metals are connected through two bridging cysteine groups (Figure 47C). Ni-Fe hydrogenases are primarily involved in the molecular hydrogen oxidation.^{101b} This class of hydrogenases is the most widely spread in nature.⁶

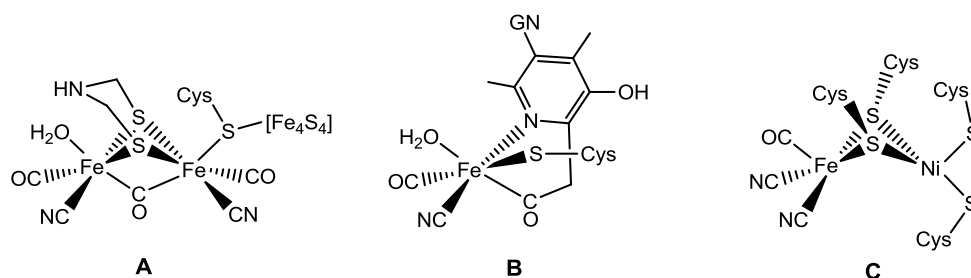


Figure 47: Structure of the active sites of [FeFe] (A), [Fe] (B) and [NiFe]-hydrogenases (C). GN = guanylnucleotide.

The proton reduction mechanism by hydrogenases is still under extensive debate and different approaches, such as mutagenesis¹⁰² or computational simulations,¹⁰³ were conducted to elucidate the key steps of the H⁺ reduction or H₂ oxidation. Most of the proposed mechanisms involve low valent active species, generated *via* PCET events, with terminal or bridging hydride moieties capable to interact with protons to produce H₂. In the case of [FeFe]-hydrogenases, it is also considered that the bridging amine in the dithiolate group can act as a base, delivering protons to the active site.¹⁰⁴

Iron and nickel hydrogenases are unstable under aerobic conditions and suffer from high production costs, making difficult their application in solar-driven water-splitting devices.^{101b} Therefore, understanding the catalytic proton reduction mechanism in hydrogenase enzymes may guide scientists into the design of more resistant and active catalysts to produce hydrogen.

1.6. Artificial Hydrogen Production Catalysts

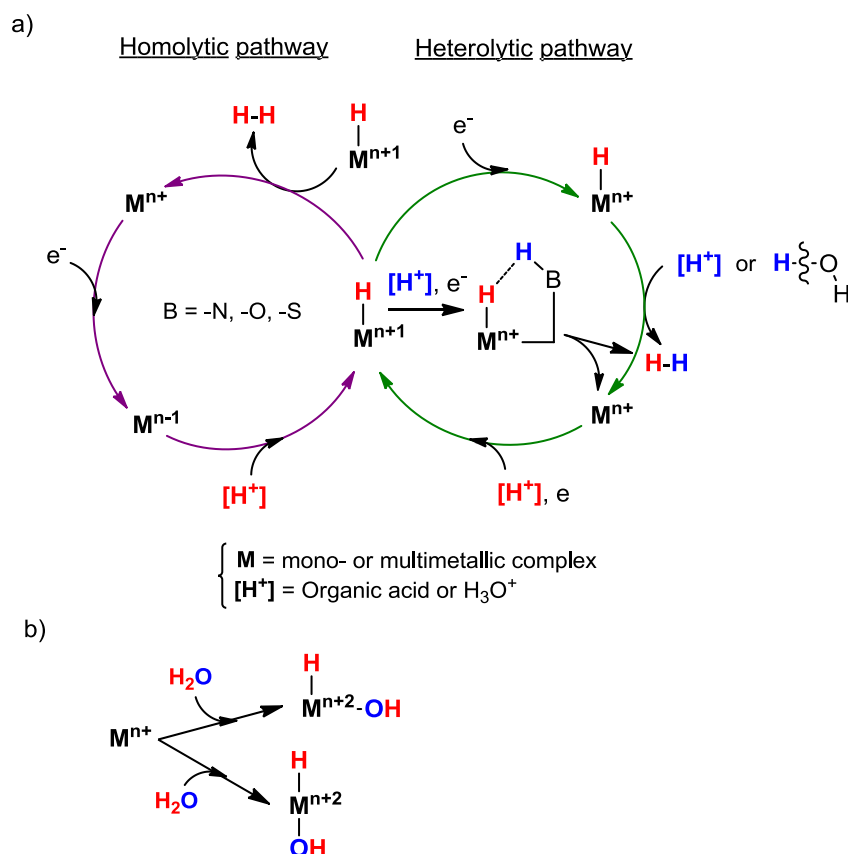
Currently, the most used and economically viable way to produce molecular hydrogen at large-scale is the steam reforming of methane.¹⁰⁵ However, this industrial process requires high temperature conditions and generate byproducts which cause a negative impact on the environment. Molecular hydrogen can be also produced/oxidized in a catalytic manner using heterogeneous materials based on Pt and other heavy metals,¹⁰⁶ but the expensive cost of these noble metals bans their large-scale application. Therefore, the development of water-splitting devices with the reductive site occupied by first row transition metal catalysts may become the most cheap and sustainable way to produce hydrogen.

The first step for the replacement of the most common and robust but expensive heterogeneous noble metal-based H₂ evolution catalyst by bio-inspired synthetic catalysts was the development of several structural and functional mimics of the active site of [FeFe]-hydrogenase, [Fe]-hydrogenase and [NiFe]-hydrogenase.^{107,108} However, in the last decades, many examples of mononuclear proton and water reduction electro- and photocatalysts based on other transition metals and ligand architectures have been reported. The simpler mononuclear catalysts are useful models to gain insight the H₂ evolution mechanism. In this section, the proposed proton or water reduction mechanisms for some relevant systems will be exposed based on electrochemical, kinetic, spectroscopic and computational data.

1.6.1 Mechanisms for Molecular Hydrogen Production

Although WO is recognized as the most challenging part of the water splitting process, the proton or water reductions reactions are far to be trivial. Certainly, electron transfer, proton transfer or PCET processes are at the core of the state-of-the-art chemical reactivity, however are not well understood. Water reduction (WR) or proton reduction to H₂ brings us the possibility to provide basic information about these concepts. Moreover, the mechanistic knowledge of the proton or WR reactions results essential for the design of effective hydrogen evolution catalysts.

Experimental and theoretical studies suggest that most of the homogeneous H₂ production systems based on first row transition metals share a common general catalytic cycle, in which mono- or multimetallic metal-hydride active species (Mⁿ⁺¹-H) are generated through sequential or concerted protonation and reduction (Scheme 2a).¹⁰⁹ Then, the metal-hydride group triggers the H-H bond formation event by following a homolytic or heterolytic reaction pathway. In the former, the reductive elimination of two Mⁿ⁺¹-H intermediates is required to produce molecular hydrogen. In contrast, the heterolytic pathway first usually implies the reduction of Mⁿ⁺¹-H moiety to Mⁿ⁺-H. Then the polarized metal-hydride intermediate establish electrostatic interactions with the proton source leading to the H₂ evolution. Alternatively, when the reaction occurs in aqueous solution, the Mⁿ⁺-H may perform a nucleophilic attack on a H₂O molecule, triggering the O-H bond cleavage and producing H₂. A third mechanism is presented in electron rich metals such Ir or Pt, which can promote the oxidative addition of a water molecule on the metal center and generate *cis*- or *trans*-Mⁿ⁺²(H)(OH) species (Scheme 2b). The Mⁿ⁺²(H)(OH) species may follow one of the previously discussed H-H bond formation mechanisms or, in the case of the *cis*-Mⁿ⁺²(H)(OH) species, the H-H bond can be formed by a coupling between the OH and hydride ligands.



Scheme 2: a) Proposed molecular hydrogen evolution mechanisms promoted by common metal-hydride active species. The reduction process could be ligand centered instead of metal centered. b) Water oxidative addition on the metal center to generate metal-hydride species.

The proton reduction studies of organometallic and coordination complexes are usually conducted under electrochemical or photochemical regimes. The former regime usually involves an organic (i.e. acetonitrile) or organic-aqueous media and an acid as a proton source, while in the latter the proton reduction reaction is performed in aqueous solution and using a photosensitizer as a reductor. Electrochemical studies performed in pure water are less common. Under electrochemical conditions, the reaction pathways can depend on the strength and concentration of the acid used as a source of protons, as well as the redox properties of the given system.

Different structural and electronic modifications can be introduced in the metal complex to lower the energetic barriers for some of the elementary steps of the catalytic cycle of proton reduction. The metal-hydride generation can be facilitated if the ancillary ligands are able to stabilize reduced intermediates and minimize the electrochemical overpotential needed for proton reduction. A possibility to accomplish metal-hydride at lower overpotential can be the use of redox non-innocent ligands, which present a high metal-ligand cooperation delocalizing the reducing equivalents on the ligand.¹¹⁰ The H_2 production *via* a heterolytic reaction pathway can be favored by the introduction of sterically-crowded ligands congesting the active site preventing bi-molecular reactions. Alternatively, the presence of a pendant donor group (nitrogen, sulfur or oxygen moieties) in the first or second coordination sphere of the metal system (Scheme 2a), *via* previous protonation can facilitate the release of protons to the metal-hydride accelerating the rate for this particular elementary step of the reaction.¹¹¹ Moreover, the protonation of the external donor groups can also reduce the redox overpotential of proton reduction. The latter structural modification is inspired on

the amine groups located at the second coordination sphere in natural [FeFe]-hydrogenase enzymes, which control the proton delivery to the metal center.

The following review will be focus on the metal-hydride generation and the H₂ release steps. In addition other aspects such as the electronic structure of the active species, the mechanistic role of the ligands or the origin of the reactive protons will be also discussed.

1.6.2 Earth-scarce Transition Metal-based H₂ Production Catalysts

1.6.2.1 Platinum based H₂ Production Catalysts

Fourth decades ago, Monaghan's group and Canty's groups reported the first examples of organometallic platinum(II) compounds that react with water to generate H₂.^{112,113} It was postulated that complexes such [PtMe₂(bpy)] (**45**, Figure 48a) and [PtMe₂{(pz)₃BH}]⁻ [(pz)₃BH = tris(pyrazol-1-yl)-borate] (**46**, Figure 48a) catalyze the oxidative addition of a water molecule on the Pt(II) center to generate transient undetected the hydridoplatinum(IV) intermediates {Pt^{IV}(OH)(H)} or {Pt^{IV}(H)}{OH}. Then, the interaction between the Pt^{IV}-H moiety and the water solvent produces molecular hydrogen (Figure 48b). This proposal was supported by the detection of H₂ gas in the reaction of **45** with methanol in almost dry acetone solution to obtain [PtMe₂(OMe)(bpy)(OH₂)]⁻[OH].¹¹³ However, no detailed mechanistic analysis was conducted to validate this mechanism.

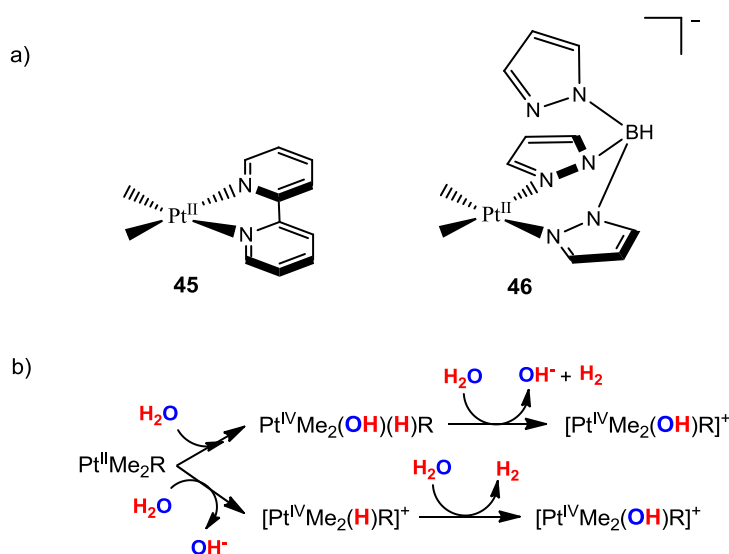


Figure 48: a) Molecular structure of [PtMe₂(bpy)] (**45**) and [PtMe₂{(pz)₃BH}]⁻ (**46**) b) Proposed mechanisms for H₂ generation by Pt^{IV}-H active species.

On the past three decades, Sakai *et al.* have reported several mononuclear and binuclear platinum(II) complexes which photocatalyze the H₂ generation reaction in water.¹¹⁴ The photocatalytic system is composed of a photosensitizer ([Ru^{III}(bpy)₃]³⁺), the platinum H₂-evolving catalyst, the methylviologen electron relay (MVio²⁺) and a sacrificial electron donor (EDTA = ethylenediaminetetraacetic acid) (Figure 49). The role of the photosensitizer is to trigger the electron transfer between EDTA, [Ru^{III}(bpy)₃]³⁺ and the MVio²⁺. This sequential process is initiated by light absorption of the reduced form of the photosensitizer ([Ru^{II}(bpy)₃]²⁺), generating an excited state that can be quenched by electron transfer to the MVio²⁺. Then, the platinum complex is reduced by the reduced form of the methylviologen (MVio^{•+}). Finally, the platinum system is activated and

reduces protons to H₂. Mechanistic studies reveal that the control of electronic and steric effects allows the fine tuning of the catalytic performance. The authors found that diplatinum(II) complexes with shorter Pt-Pt distances are more active than those with longer Pt-Pt distances and mononuclear complexes. This suggested that dimeric intermediate could be involved in the reaction. The incorporation of negatively charged -Cl ligands, like in [PtCl₂(en)] (en = ethylenediamine) and [PtCl₂(4,4'-dicarboxy-bpy)], show higher activity than containing only neutral ligands. Indeed, the introduction of electron-withdrawing groups exhibit higher activity than those systems without such groups. The last modifications may allow the stabilization of a low oxidation on the platinum center.

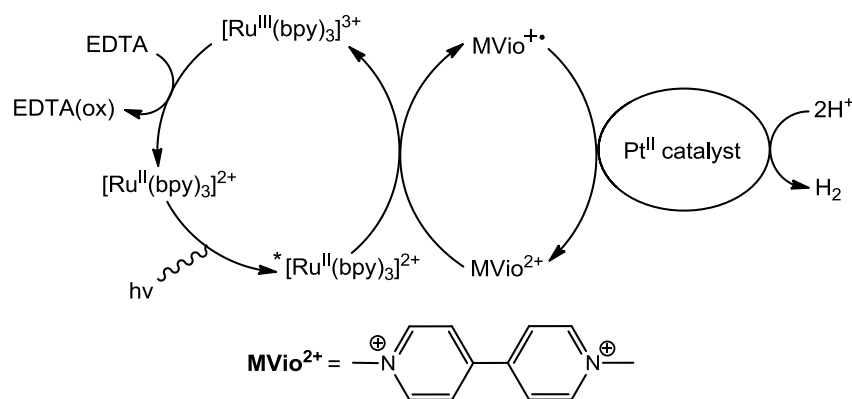


Figure 49: Photochemical pathway for H₂ generation from water by Pt^{II} complexes.

In 2011, Sakai's group presented three new derivatives of the mononuclear complex [PtCl₂(en)] which contain between two and six viologen units in the bpy scaffold (Figure 50a).¹¹⁵ The multiviologen groups were expected to serve as electron reservoirs close to the Pt^{II} center. On the basis of UV/Vis-NIR spectroscopy, electrochemistry studies and electrical conductivity measurements, the authors suggest that a binuclear intermediate should be generated with a Pt-Pt bond, through the stacking of two monomeric Pt fragments. Moreover, kinetic data indicate that the H₂ generation proceeds through a bimolecular reaction path. It was also observed that the complex with the minimum number of viologen groups exhibits the highest catalytic activity. A computational study was also performed to shed more light on the H₂ evolution mechanism. The molecular mechanics (MM3) analysis of the [PtCl₂(en)]-viologen systems show that the Coulombic repulsions rather than the steric effects account for the repulsion between the platinum(II) monomeric fragments. This result correlates with the highest catalytic activity observed for the system with less viologen groups, which is the complex with less positive charge (complex **47**). DFT(B3LYP) quantum mechanical calculations were carried out on [PtCl₂(en)] and [PtCl₂(55'bc bpy)] (55'bc bpy = 5,5'-bis(carbamoyl)-2,2'-bipyridine) systems to explore the thermodynamics of the H₂ evolution when methylviologen is used as a reductor (Figure 50b). The results indicate that the formation of Pt^{III}-H species by different acids (H₃O⁺, CH₃COOH, HCl) and MVio⁺ is always significant endergonic process for the two complexes, being more favored when the proton is transferred from a hydronium cation. Since experimental data show that a binuclear structure should be involved in the rate determining step, the authors propose that the active species may be a Pt^{II}-Pt^{III}-H dimeric intermediate. They estimate that the Pt^{II}-Pt^{III} bond has an energy of 20-30 kcal·mol⁻¹, which may stabilize the Pt^{III}-H fragment. This may reduce the energetic cost of the hydride generation. Finally, the heterolytic and homolytic H-H bond formation pathways from monomeric Pt^{III}-H resulted extremely exergonic, independently of the proton source. However, neither heterolytic nor homolytic reactions account for the necessity of having a dimerization path. In case of the Pt-H...H-Pt coupling, the system would not suffer the important steric hindrance or

1.6.2.3 Rhodium based H₂ Production Catalysts

Rhodium catalysts are widely used in a variety of industrial processes such as hydrogenation of organic substrates, olefin hydrogenation and hydroformylation.¹¹⁸ This chemical activity is related with their ability to produce rhodium-hydride active species. However, these complexes were firstly used to photochemically reduce protons into molecular hydrogen at the end of the seventies. The Sauvage¹¹⁹ and Sutin¹²⁰ groups reported one of the first systems to photocatalyze the proton reduction reaction in pure aqueous media. The irradiation of a mixture of a rhodium complex ($[\text{Rh}^{\text{III}}(\text{bpy})_3]^{3+}$ (**52**) as catalyst, a photosensitizer ($[\text{Ru}^{\text{II}}(\text{bpy})_3]^{2+}$), EDTA as a sacrificial electron donor in acidic conditions ($\text{pH} < 5.5$), only a TON of 6 relative to **52** is reached (Figure 52). However, Sauvage *et al.* study demonstrated that rhodium complexes can act as H₂ evolving catalysts. On the basis of experimental data, they proposed the catalytic cycle depicted in Figure 52. The reaction starts with the visible light absorption by $[\text{Ru}^{\text{II}}(\text{bpy})_3]^{2+}$ to reach the excited state $[\text{Ru}^{\text{II}}(\text{bpy})_3]^{2+*}$. The oxidative quenching of $[\text{Ru}^{\text{II}}(\text{bpy})_3]^{2+*}$ by $[\text{Rh}^{\text{III}}(\text{bpy})_3]^{3+}$ forms the $[\text{Ru}^{\text{III}}(\text{bpy})_3]^{3+}$ and $[\text{Rh}^{\text{II}}(\text{bpy})_3]^{2+}$ intermediates. The $[\text{Ru}^{\text{III}}(\text{bpy})_3]^{3+}$ is reduced by the EDTA or TEOA, recovering the initial form of the photosensitizer. Simultaneously, reduction of the $[\text{Rh}^{\text{II}}(\text{bpy})_3]^{2+}$ by the photosensitizer induce the dissociation of a bpy ligand and the formation of a distorted square planar $[\text{Rh}^{\text{I}}(\text{bpy})_2]^{2+}$ intermediate. $[\text{Rh}^{\text{I}}(\text{bpy})_2]^{2+}$ can then react with a hydronium cation to give the hydride complex $[\text{Rh}^{\text{III}}(\text{H})(\text{bpy})_2(\text{H}_2\text{O})]^{2+}$. The Rh^{I} and $\text{Rh}^{\text{III}}\text{-H}$ were experimentally detected by visible light irradiation studies.¹²¹ The water molecule can be also incorporated into the complex structure in the $[\text{Rh}^{\text{II}}(\text{bpy})_3]^{2+}$ stage. Finally, the $\text{Rh}^{\text{III}}\text{-H}$ active species may generate H₂ either by the reaction with another H_3O^+ , or by the coupling of two metal-hydride fragments. The H-H bond formation may take place following by bipyridine ligand coordination, recovering the initial Rh^{III} species for the heterolytic pathway, and the Rh^{II} species for the homolytic pathway. $[\text{Rh}^{\text{I}}(\text{bpy})_2]^{2+}$ species may be also generated through disproportionation of $[\text{Rh}^{\text{II}}(\text{bpy})_2]^{2+}$ or $[\text{Rh}^{\text{II}}(\text{bpy})_3]^{2+}$ species.¹²⁰

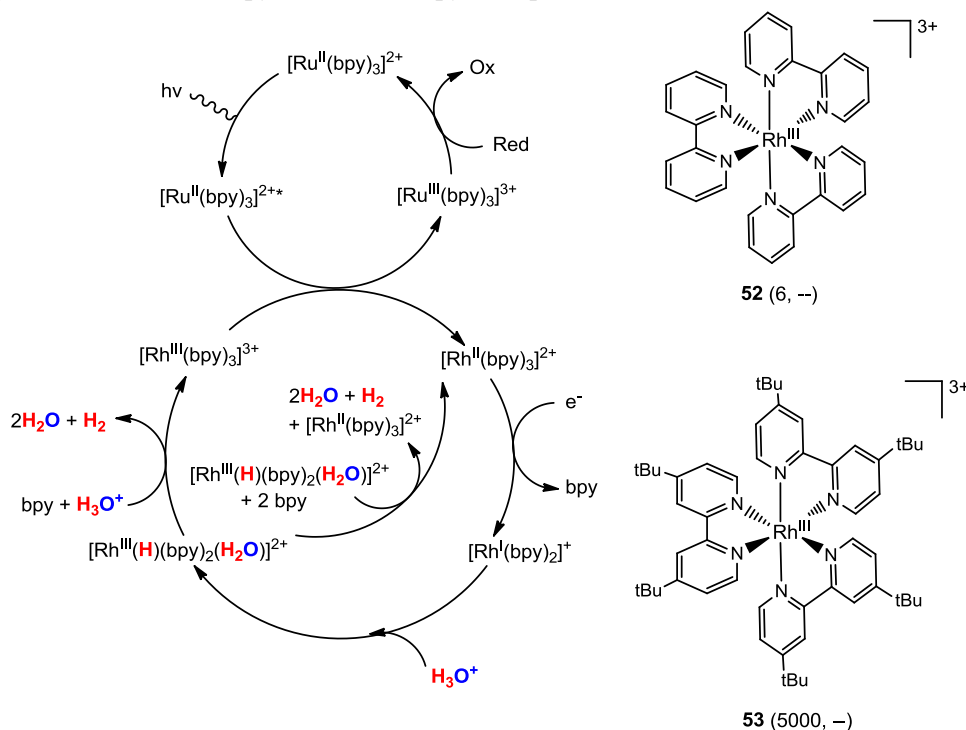


Figure 52: Left, proposed mechanism for H₂ generation by **52**. The label “Ox” means the oxidized form of the electron donor (EDTA or TEOA) and “Red” the reduced form. Right, molecular structures of complexes $[\text{Rh}^{\text{III}}(\text{bpy})_3]^{3+}$ (**52**) and $[\text{Rh}^{\text{III}}(\text{dtbbpy})_3]^{3+}$ (**53**). TON values are in parenthesis.

In 2008, the group of Bernhard investigated the catalytic performance of tris(bipyridyl) rhodium(III) complexes containing electron-donating (-tBu, -OMe) and electron-withdrawing (-F) groups in the bipyridine scaffold.¹²² After 22h irradiating a mixture of a cyclometalated iridium photosensitizer, the complex $[\text{Rh}^{\text{III}}(\text{dtbbpy})_3]^{3+}$ (**53**, Figure 52; dtbbpy = 4,4'-di-tert-butyl-2,2'-dipyridine) and the trimethylamine (TEA) electron donor at 460 nm in an 80 % THF-water solvent mixture, they obtained a TON over 5000. Electrochemical and photophysical studies suggested that the reduced form of the iridium photosensitizer may reduce the rhodium catalyst up to Rh^0 state. Then, after bpy ligand dissociation this species can be protonate to form $\text{Rh}^{\text{II}}\text{-H}$ active species. Finally, it was proposed that the H-H bond formation event may occur *via* a homolytic pathway or through the formation of a rhodium-dihydride species and the subsequent coupling of the hydride moieties.

Another interesting rhodium(III) complex is $[\text{Rh}^{\text{III}}(\text{dmbpy})_2\text{Cl}_2]^+$ (**54**, Figure 53; dmbpy = 4,4'-dimethyl-2,2'-bipyridine) with two *cis* labile positions. In 2013, Collomb and coworkers reported that **54** is an efficient photocatalyst for H_2 production in pure water, in combination with the $[\text{Ru}^{\text{II}}(\text{bpy})_3]^{2+}$ photosensitizer and ascorbic acid as an electron donor.¹²³ The visible light irradiation of the previous three-component system reaches up to 120 and 230 TONs respect to the rhodium catalyst with $[\text{Rh}^{\text{III}}(\text{dmbpy})_2\text{Cl}_2]^+ / [\text{Ru}^{\text{II}}(\text{bpy})_3]^{2+}$ ratios of 1:1 and 10:1, respectively, at the pH 4.0 imposed by a ascorbic (0.55 M)/ascorbate (0.55 M) buffer. Electrochemical data revealed that the irreversible $\text{Rh}^{\text{III}}/\text{Rh}^{\text{I}}$ two-electron reduction is coupled with the release of the chloride ligands, reaching distorted square planar Rh^{I} species. The use of ascorbic acid instead of EDTA or TEA allows to work at low pHs, favoring the formation of $\text{Rh}^{\text{III}}\text{-H}$ intermediates and the H_2 evolution pathways. As in the case previous case the reductive quenching of $[\text{Ru}^{\text{II}}(\text{bpy})_3]^{2+}$ excited state by the ascorbate ions leads to the formation of $[\text{Ru}^{\text{II}}(\text{bpy})_2(\text{bpy}\cdot^-)]^+$, which reduces the rhodium catalyst and the $\text{Rh}^{\text{III}}\text{-H}$ intermediate. The existence of the Rh^{I} and $\text{Rh}^{\text{III}}\text{-H}$ intermediates was confirmed by their electro-generation and spectroscopic characterization in CH_3CN solvent. When a ratio up to 500:1 was employed for $[\text{Ru}^{\text{II}}(\text{bpy})_3]^{2+} / [\text{Rh}^{\text{III}}(\text{dmbpy})_2\text{Cl}_2]^+$, the system gave a TON of 1010 and a TOF of 0.238 s^{-1} . A combination of photophysical and computational studies were performed to get insight into the mechanism of H_2 generation (Figure 53).¹²⁴ DFT(B3LYP) calculations confirm that the reaction starts with the reduction of the $[\text{Ru}^{\text{II}}(\text{bpy})_3]^{2+}$ triplet excited state to $[\text{Ru}^{\text{II}}(\text{bpy})_2(\text{bpy}\cdot^-)]^+$ by the ascorbate anion. Then, $[\text{Ru}^{\text{II}}(\text{bpy})_2(\text{bpy}\cdot^-)]^+$ is able to reduce the $[\text{Rh}^{\text{III}}(\text{dmbpy})_2\text{Cl}_2]^+$ catalyst to the distorted tetra-coordinated $[\text{Rh}^{\text{I}}(\text{dmbpy})_2]^+$ species, in agreement with the experimentally observed release of the chloride ligands. The following reaction of $[\text{Rh}^{\text{I}}(\text{dmbpy})_2]^+$ with protons forms $[\text{Rh}^{\text{III}}(\text{H})(\text{dmbpy})_2(\text{H}_2\text{O})]^{2+}$ hydride species, which have incorporated a water solvent molecule in the coordination sphere of the Rh center. This octahedral geometry may catalyze the H-H bond formation event following a heterolytic pathway between $[\text{Rh}^{\text{III}}(\text{H})(\text{dmbpy})_2(\text{H}_2\text{O})]^{2+}$ and H_3O^+ . In contrast, the homolytic pathway between two $[\text{Rh}^{\text{III}}(\text{H})(\text{dmbpy})_2(\text{H}_2\text{O})]^{2+}$ is thermodynamically banned. Finally, the initial complex **54** is recovered, with the reintroduction of chloride or aqua ligands into rhodium coordination sphere. Alternatively, the $\text{Rh}^{\text{III}}\text{-H}$ may be reduced to the square pyramidal $[\text{Rh}^{\text{II}}(\text{H})(\text{dmbpy})_2]^+$ by $[\text{Ru}^{\text{II}}(\text{bpy})_2(\text{bpy}\cdot^-)]^+$, and the subsequent heterolytic and homolytic H-H bond formation reactions are thermodynamically favored. Therefore, according to DFT, the high catalytic efficiency of **54** may be explained by the involvement of highly reactive $[\text{Rh}^{\text{II}}(\text{H})(\text{dmbpy})_2]^+$ species.

Binuclear rhodium complexes can also act as H_2 generation catalysts. In 2006, the group of Sakai investigated the catalytic activity of a the four-component system composed by the $[\text{Ru}^{\text{II}}(\text{bpy})_3]^{2+}$ photosensitizer, the electron donor EDTA, the electron relay methyl viologen (MVio^{2+}) and a binuclear rhodium complex quadruply bridged by carboxylate ligands (**55-57**, Figure 54). They obtained TON values of 4.0 and 4.5 for complexes **55** and **56**, respectively.¹²⁵ Absorption

spectroscopy, $^1\text{H-NMR}$, and ESI-TOF mass spectroscopy showed that the bridging carboxylate groups in the rhodium dimers remained intact during the photolysis experiments. This was indicative that the protonation reactions may occur at the axial positions of the dirhodium complexes. Experimental evidences indicate that the reaction may start with the oxidative quenching of the excited state of the photosensitizer by MVio^{2+} . The resulting viologen radical $\text{MVio}^{+\cdot}$ may reduce the $\text{Rh}_2^{\text{II,II}}$ dimers to the $\text{Rh}_2^{\text{II,I}}$ state. Then, the Rh^{I} accepts a proton to form $\text{Rh}^{\text{II}}\text{-Rh}^{\text{III}}\text{-H}$ species. However, DFT(B3LYP) calculations performed on complex **55** suggested that the evolution from $\text{Rh}_2^{\text{II,II}}$ to $\text{Rh}^{\text{II}}\text{-Rh}^{\text{III}}\text{-H}$ could occur through a PCET reaction, which was proposed to be the rate determining step (Figure 54). Finally, the H-H bond formation event could occur *via* another PCET on $\text{Rh}^{\text{II}}\text{-Rh}^{\text{III}}\text{-H}$ or following a homolytic coupling between two $\text{Rh}^{\text{III}}\text{-H}$ fragments. However, no experimental evidence of these PCET events was reported.

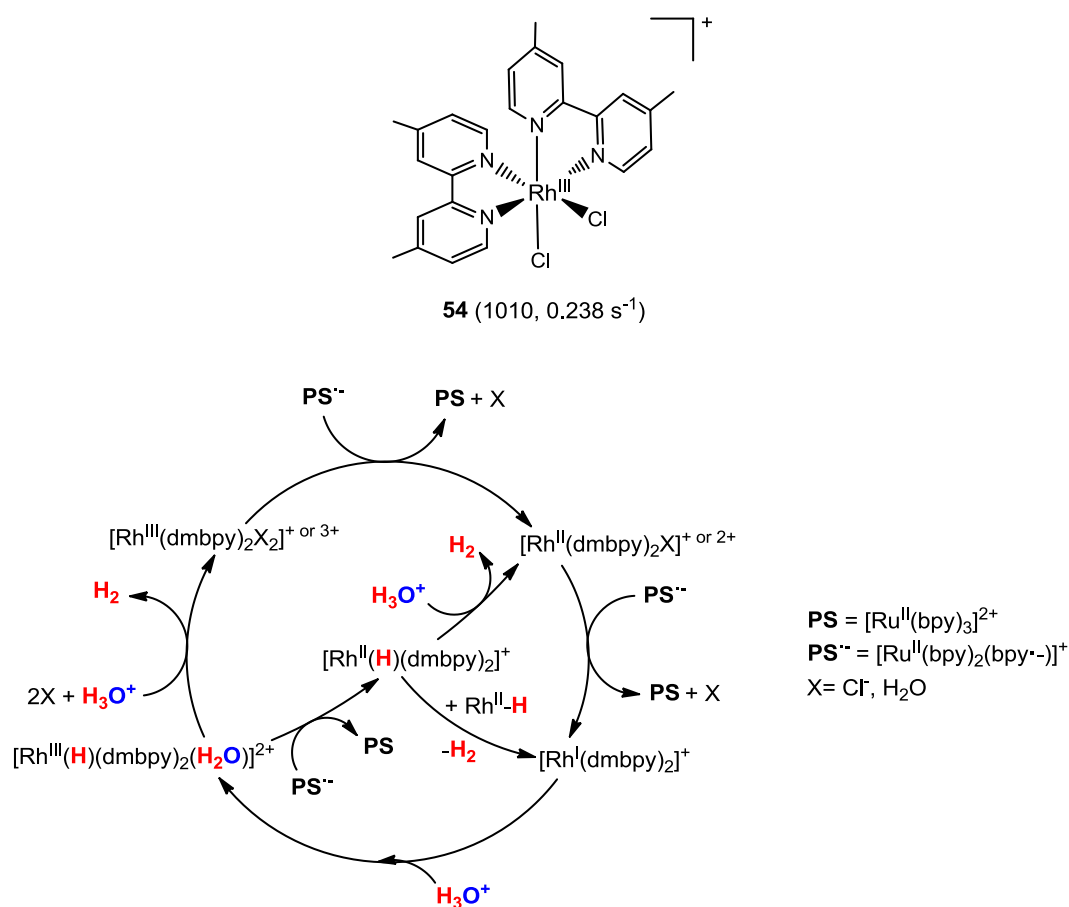


Figure 53: The DFT proposed mechanism for H₂ generation for $[\text{Rh}^{\text{III}}(\text{dmbpy})_2\text{Cl}_2]^+$ (**54**) complex. TON and TOF values are in parenthesis, respectively.

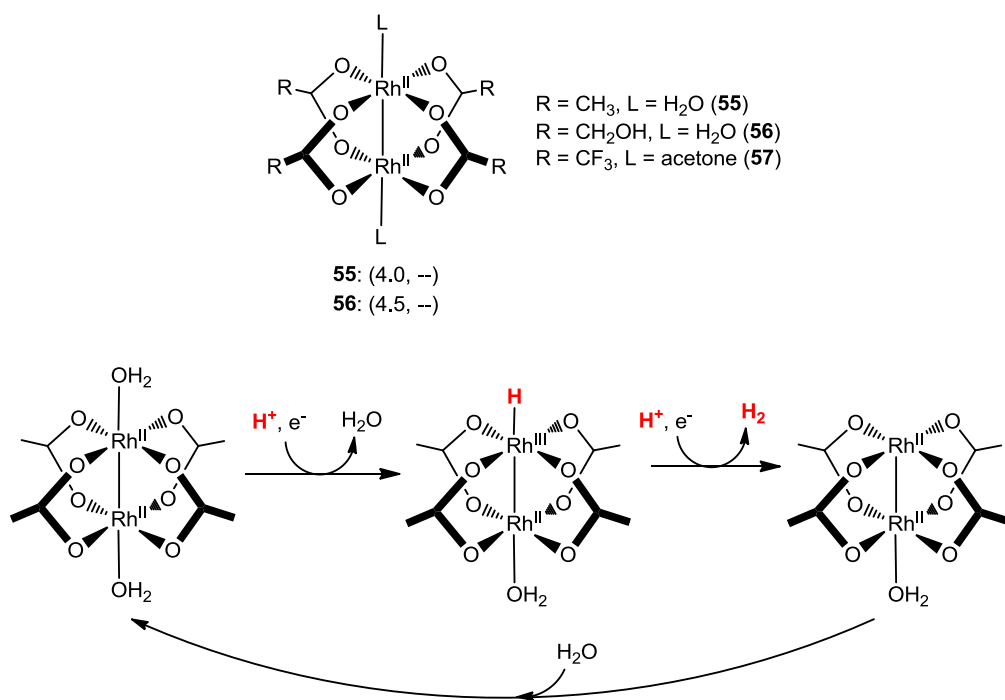


Figure 54: Metal-hydride and H-H bond formation steps through PCET reactions performed by a rhodium(II) dimer with quadruply bridged carboxylate ligands (**55**). TON values are in parenthesis.

1.6.3 First Row Transition Metal-based H_2 Production Catalysts

In the last decade, many efforts have been devoted to develop new mononuclear proton or water reduction catalysts based on earth-abundant and low cost transition metals such as Co, Ni, Mo and Cu. In this section, the mechanistic studies of some relevant proton and WRCs based on earth-abundant transition metals are summarized.

1.6.3.1 Cobalt based H_2 Production Catalysts

Fisher and Eisenberg reported in 1980 the first cobalt(II) complex based on a tetraazamacrocyclic ligand (**58**, Figure 55) that electrocatalyze the reduction of water and carbon dioxide.¹²⁶ The proton reduction reaction occurs at an applied potential of -1.26 V vs. SHE in a $\text{H}_2\text{O}/\text{CH}_3\text{CN}$ 2:1 (v/v) solvent mixture but also in pure water at -1.36 V vs. SHE, using a Hg electrode. Electrochemical measurements in the 2:1 water/acetonitrile mixture revealed a TOF value of 0.002 s^{-1} . The authors emphasized that a protic source was required for the production of CO and H_2 , suggesting that both products may arise from a common metal-hydride intermediate. However, no detailed mechanistic information was provided.

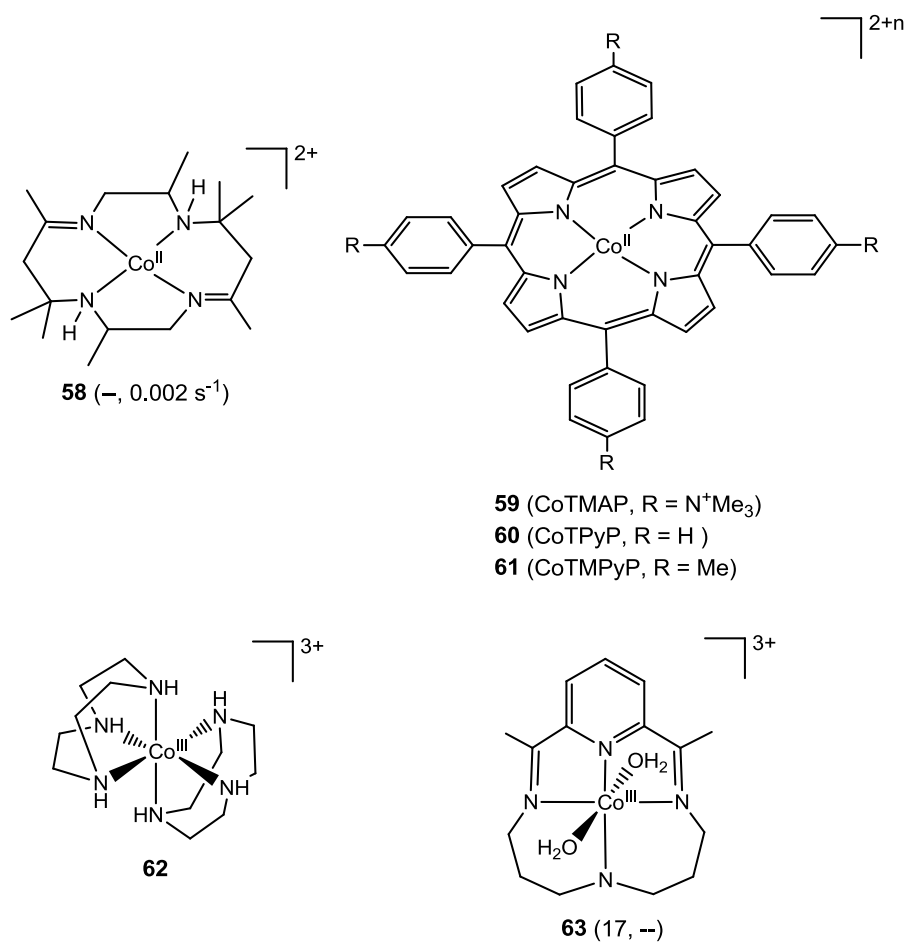


Figure 55: Molecular structures of the Co^{II} tetraazamacrocyclic (**58**), cobalt porphyrins (**59-61**), the bis(1,4,7-triazacyclodecane)cobalt(III) complex (**62**) and [Co^{III}(CR)(OH₂)₂]³⁺ (**63**). TON and TOF value are in parenthesis, respectively.

In 1985, Kellett and Spiro showed that cobalt(II) complexes based on water soluble porphyrins, such the CoTMAP (**59**, Figure 55; TMAP = *meso*-tetrakis(*N,N,N*-trimethylanilinium-4-yl)porphine), CoTPyP (**60**, Figure 8; TPyP = *meso*-tetrapyrro-4-ylporphine), and CoTMPyP (**61**, Figure 8; TMPyP = *meso*-tetrakis(*N*-methylpyridinium-4-yl)porphine) presented proton and water reduction activity.¹²⁷ The three cobalt systems produced H₂ in controlled potential electrolysis experiments on a Hg electrode at -0.71 V vs. SHE in 0.1 M trifluoroacetic acid (TFA). Cyclic voltammogram studies showed that the proton reduction also occurs after the Co^{II}/Co^I transformation in DMSO solutions with small amounts of water and in neutral and acidic aqueous buffered solutions. Spectrophotometry experiments conducted on **59** revealed that the Co^ITMAP reacts extremely fast with the water molecules (second-order rate constant > 10⁴ M⁻¹s⁻¹). With this data, the authors proposed the following mechanism for H₂ evolution: after the one electron reduction of the Co^{II} system, the resulting unstable Co^I species reacts with a water molecule or one proton to generate an intermediate which is represented by the resonance equilibrium [Co^{III} – H⁻ ↔ Co^{II} – H ↔ Co^I ... H⁺]. Finally, the resonance hybrid of the active species may produce H₂ following heterolytic or homolytic pathways.

Another azamacrocyclic catalyst for H₂ production is the six-coordinated bis(1,4,7-triazacyclodecane)cobalt(III) (**62**, Figure 55) reported by Nafady *et al.*¹²⁸ They showed that **62** can catalyze the proton reduction reaction at an onset potential of about -1.29 V vs SHE in aqueous

Britton–Robinson buffer solutions at pH 2–10 on a Hg electrode.¹²⁸ Cyclic voltammetry studies displayed two reduction waves, assigned to the $\text{Co}^{\text{III}}/\text{Co}^{\text{II}}$ and $\text{Co}^{\text{II}}/\text{Co}^{\text{I}}$ redox couples. The comparison between the electrochemical data and digital simulations of the cyclic voltammograms indicated that the reaction may proceed through the protonation of a Co^{I} intermediate to generate Co^{III} -hydride species. The generation of the metal-hydride requires the decoordination of one amine group but the authors did not clarify in which reaction step occurs. Finally, the digital simulations of the reaction kinetics point exclusively to a homolytic H–H bond formation pathway by Co^{III} -hydride species, discarding the heterolytic H–H bond formation pathway.

Relevant mechanistic data related with the electrochemical steps of the H_2 production reaction with Co catalysts was obtained by the group of Peters.¹²⁹ They established that the $[\text{Co}^{\text{III}}(\text{CR})(\text{OH}_2)_2]^{3+}$ complex (**63**, Figure 55) containing a pyridine donor catalyzes hydrogen evolution at -0.69 V vs SHE with a TON of 17 in a pH 2.2 phosphate buffer on a glassy carbon electrode. Interestingly, complex **63** presented a $\text{Co}^{\text{III}}/\text{Co}^{\text{II}}$ redox couple with a pH dependence consistent with a one-electron and one-proton reduction. On the other hand, the formal $\text{Co}^{\text{II}}/\text{Co}^{\text{I}}$ couple involves two-electrons and one-proton transfer. An electrochemical mechanism consistent with these pH dependences might start with the transformation of the Co^{III} system to a Co^{II} with a protonated amine. Then, the subsequent reduction of protonated Co^{II} species by two electrons may generate a Co^{II} -H intermediate. Finally, the protonation of the previous hydride may lead to the molecular hydrogen release.

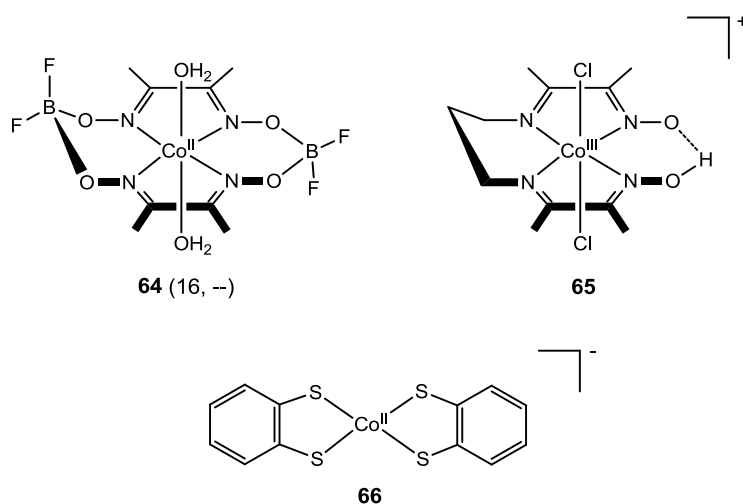


Figure 56: Molecular structures of cobaloximes $[\text{Co}^{\text{II}}(\text{dmgBF}_2)_2(\text{OH}_2)_2]$ (**64**) and $[\text{Co}^{\text{III}}\{(\text{DO})(\text{DOH})\text{pn}\}\text{Cl}_2]^+$ (**65**) and the Co bis-dithiolene complex (**66**). TON value is in parenthesis.

The bis(dimethylglyoximate) cobalt(II) complexes are another family of proton reduction catalysts that can operate under electrochemical and photochemical conditions in both, aqueous or organic media. The H_2 evolution activity of a cobalt oxime was first investigated by Espenson and Conolly in 1986.¹³⁰ They observed that the molecular hydrogen production by complex $[\text{Co}^{\text{II}}(\text{dmgBF}_2)_2(\text{OH}_2)_2]$ (**64**, Figure 56; dmgBF_2 = difluoroboryldimethylglyoxime) in water takes place when chromium chloride was used as an electron donor. In 2012, Peters and coworkers revealed that **64** can also electrocatalyze the proton reduction reaction in acidic water and controlled potential electrolysis at -0.69 V vs SHE in a pH 2.2 phosphate buffer displayed a TON of 16.¹²⁹ In order to obtain mechanistic data, the groups of Artero, Fontecave and Peters recorded cyclic voltammograms in different organic media, acids and introducing a variety of equatorial oxime substituents and axial ligands.¹³¹ This electrochemical data revealed that structural modifications of

the catalyst and the reaction conditions (i.e. applied potential and the pK_a of the acid used) may provide different mononuclear and binuclear hydrogen evolution pathways (Figure 57). The mechanistic knowledge was further refined by the theoretical studies reported independently by Hammes-Schiffer^{132,133} and Muckerman groups.¹³⁴ DFT calculations suggested that the most plausible reaction path for H_2 generation by cobaloximes involves the reduction of Co^{III} -H intermediate to Co^{II} -H species followed by protonation to generate H_2 .

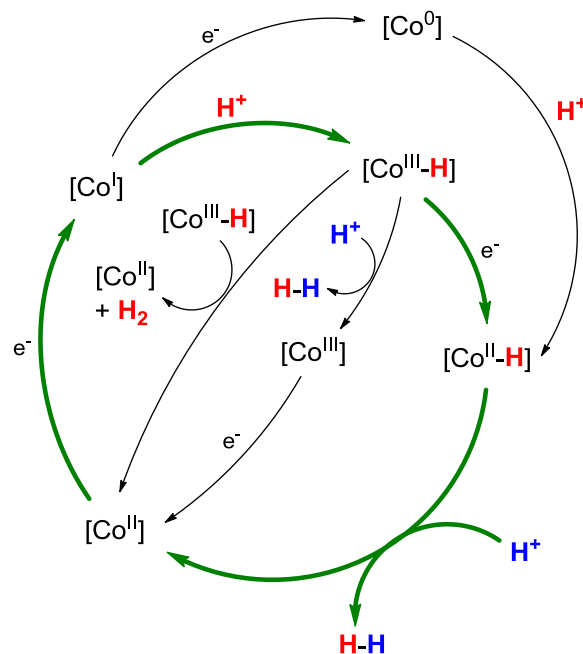


Figure 57: Proposed mononuclear and binuclear H_2 evolution pathways for cobaloxime catalysts. The green labeled arrows indicate the most energetically favored pathway according to DFT calculations.

Another class of cobaloxime systems based on a diimine-dioxime ligand was synthesized by Artero and Fontecave in 2009.¹³⁵ Among this series, the $[Co^{III}\{(DO)(DOH)pn\}Cl_2]^+$ complex (**65**, Figure 56; (DOH) (DOH)pn = N^2,N^2' -propanediylbis(2,3-butanedione-2-imine-3-oxime) presented a positive shift of the electrocatalytic potential for hydrogen evolution in organic solvents when stronger proton sources are employed, which was attributed to the protonation of the oxime bridge in the equatorial plane of the complex. This pointed to the involvement of PCET events in the H_2 generation mechanism. To corroborate this hypothesis, the group of Artero carried out a quantum mechanical study of the reaction mechanism triggered by different organic acids.¹³⁶ According to DFT(BP86/B3LYP) calculations, the first reaction step consist in one electron reduction of **65**, in conjunction with chloride ligands exchange by an acetonitrile molecule, leading to the generation of the $[Co^{II}(L)(MeCN)]^{2+}$ intermediate ($L = \{(DO)(DOH)pn\}$, Figure 58). Then, a sequential or concerted reduction and protonation on $[Co^{II}(L)(MeCN)]^{2+}$ is thermodynamically feasible, generating $[Co^I(LH)(MeCN)]^{2+}$ species with a protonated oxime moiety. Another PCET event can easily occur to form the $[Co^{II}(H)(LH)(MeCN)]^{2+}$ active species. At this point, $[Co^{II}(H)(LH)(MeCN)]^{2+}$ can follow a kinetically feasible but unconventional intramolecular H-H bond formation mechanism by the coupling between the protonated oxime moiety and the Co^{II} -H hydride group ($\Delta G^\ddagger = 22.0 \text{ kcal}\cdot\text{mol}^{-1}$). Finally, in the resulting Co^{II} - H_2 adduct, the molecular hydrogen can be displaced by an acetonitrile solvent molecule, closing the catalytic cycle. In

summary, this theoretical study unravels that the ligand may be involved not only in the redox but also in the chemical steps of the H₂ generation reaction. This role of the ligand was also proposed for the Co bis-dithiolene complex (**66**, Figure 56), in which the protonation of the sulfide moieties may favor the reduction and H-H bond formation events.¹³⁷

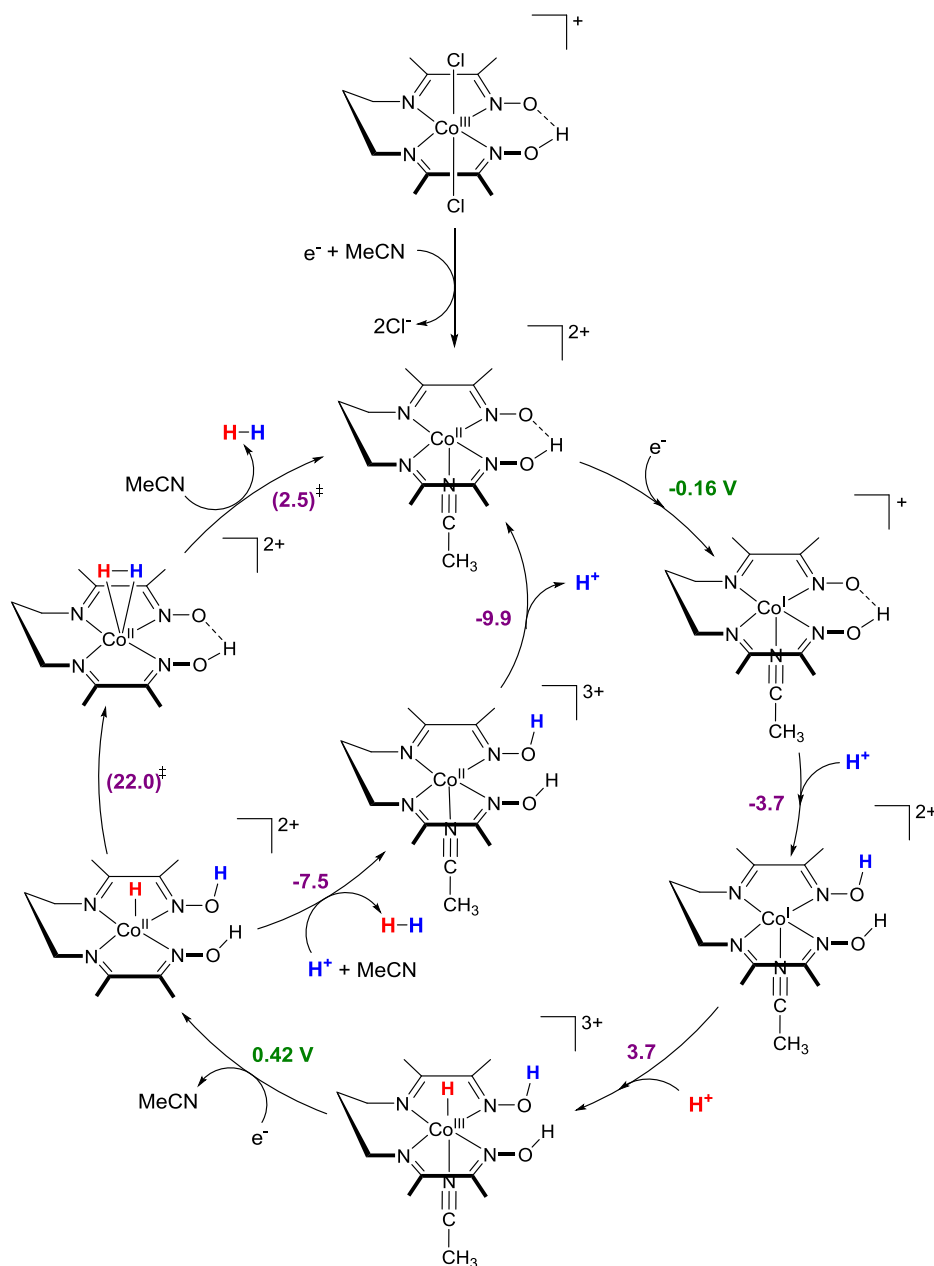


Figure 58: DFT(BP86) computed H₂ evolution catalytic cycle performed by cobaloxime **65** with the *p*-cyanoanilinium acid as proton source. Gibbs energies are in kcal·mol⁻¹. The reduction potentials were originally reported vs. the Fc⁺/Fc couple. Here in, an empirical correction of 675 mV was used to convert the potentials respect to the SHE electrode.

Alternatively to the azamacrocycle complexes, other H₂ production catalysts are based on polypyridyl ligands. In contrast with cobaloxime complexes, the polypyridyl systems are more stable in neutral and acidic aqueous solutions. However, the mechanistic details of the H₂ evolution reaction have been less studied. In 2011, Chang and coworkers reported a series of cobalt pentapyridine catalysts [Co^{II}(R-PY5Me₂)(OH₂)²⁺] (**67-69**, Figure 59) that were capable to reduce

water at pH = 7.¹³⁸ For **67**, controlled potential electrolysis at a potential of -1.30 V vs. SHE in a phosphate buffer on a mercury electrode showed H₂ evolution, with a relevant TON of 5.5·10⁴. The electronic structure of the cobalt catalyst was tuned introducing different groups in *para* position of the axial pyridine. Electron-withdrawing groups such CF₃ reduce the overpotential of the proton reduction reaction, since it favors the reduction to Co^I species, while the introduction of electron-donating substituents (i.e. NMe₂) provoke the inverse effect.

One of the most investigated cobalt polypyridyl catalyst from a mechanistic point of view is [Co^{II}(DPA-Bpy)(OH₂)]²⁺ (**70**, Figure 59a; DPA-Bpy = *N,N*-bis(2-pyridinylmethyl)-2,20-bipyridine-6-methanamine), reported by Zhao and Webster in 2012.¹³⁹ Cycle voltammogram studies revealed that **70** was capable to reduce water in pH 7 phosphate buffer, with the Co^{III}/Co^{II} and Co^{II}/Co^I redox couples falling before the catalytic onset potential of -1.2 V vs. SHE. Controlled potential electrolysis at -1.4 V vs. SHE on a mercury electrode display a TON > 3000. To shed some light into the mechanism of proton reduction by **70**, DFT(PBE) calculations were carried out. Several reaction paths for cobalt-hydride and H₂ generation were found thermodynamically feasible but the exact catalytic cycle remains unknown, since the kinetics aspects were not considered. The most important step into the elucidation of the reaction mechanism by **70** was conducted recently by Polyansky, Muckerman, Fujita and coworkers.¹⁴⁰ The electrochemical measurements, pulse radiolysis studies and DFT(B3LYP) calculations reveal that the Co^I intermediate is pentacoordinated, with a vacant position. However, DFT calculations also predicted the existence of a transient Co^I intermediate in which a pyridine moiety is decoordinated and replaced by a water molecule ([Co^I(κ⁴-L)(OH₂)]⁺, Figure 59b). The electrochemical and kinetic data are consistent with a rate determining step (RDS) which involves the slow decooordination of the aqua ligand in [Co^I(κ⁴-L)(OH₂)]⁺ and the structural rearrangement of the metal complex and the surrounding solvent prior to the Co^{III}-H formation.

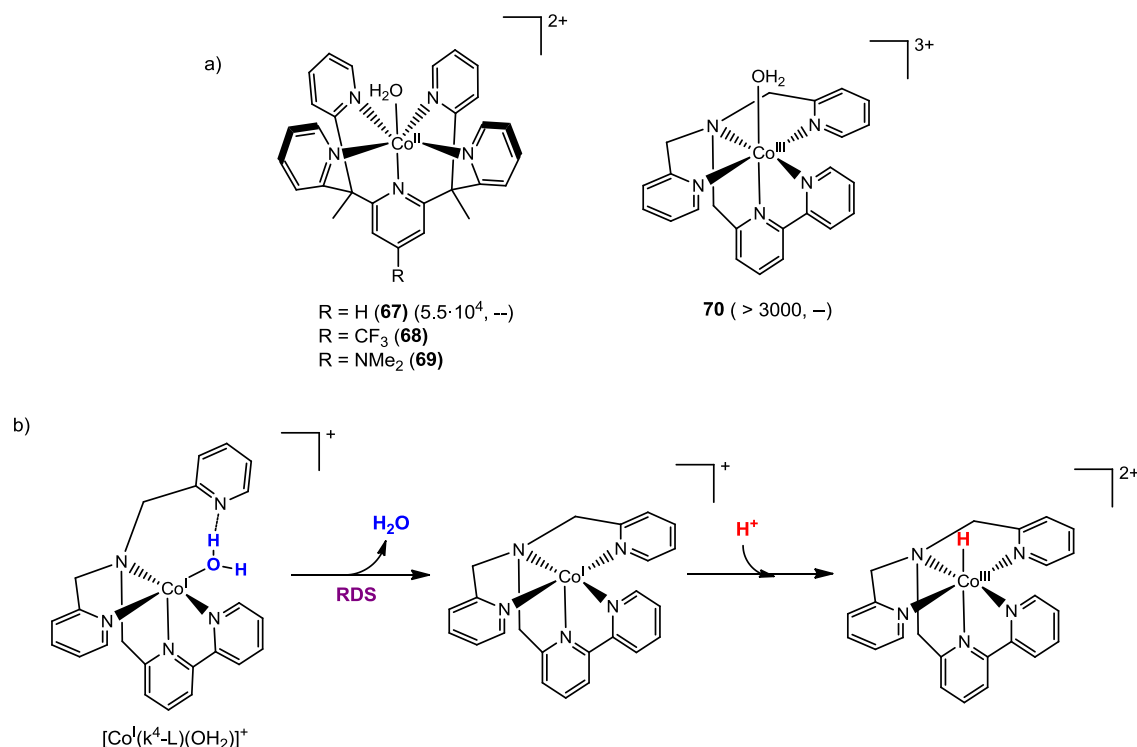


Figure 59: a) Molecular structures of [Co^{II}(R-PY5Me₂)(OH₂)]²⁺ (**67-69**) and [Co^{II}(DPA-Bpy)(OH₂)]²⁺ (**70**). TON values are in parenthesis. b) Proposed rate determining step proposed by **70**.

Lloret-Fillol *et al.* reported a new family of iron, nickel and cobalt complexes based on the aminopyridine pentadentate ligand 1,4-di(picolyl)-7-(*p*-toluenesulfonyl)-1,4,7-triazacyclononane (Py^{Ts}tacn), which presented different proton reduction activities depending of the reaction conditions (Figure 60).¹⁴¹ Electrochemical data revealed that the three complexes are capable to produce to H₂ in acetonitrile solvent, using trifluoroacetic acid (TFA) as a source of protons, with a TOF of 0.95 s⁻¹ for [Co^{II}(OTf)₂(Py^{Ts}tacn)]. However, only [Co^{II}(OTf)₂(Py^{Ts}tacn)] is active under photochemical conditions (under irradiation at 447 nm), when the solvent mixture CH₃CN/H₂O (3:7), the photosensitizer [Ir(ppy)₂(bpy)]PF₆ (**PSIr^{III}**, ppy = phenylpyridine) and the sacrificial electron donor Et₃N were employed. By analogy with the cobaloximes systems, the authors proposed that the Co^{III}-H intermediate generated after the one electron reduction of [Co^{II}(OTf)₂(Py^{Ts}tacn)] is the responsible of the H₂ evolution, although they didn't discard the formation of Co^{II}-H active species. On the basis of spectroelectrochemical data, the authors considered that the different chemical behavior of [Ni^{II}(OTf)₂(Py^{Ts}tacn)] and [Fe^{II}(OTf)₂(Py^{Ts}tacn)] may be related with the reduction potential required to reach the I oxidation state and the stability of the corresponding M^{III}-H species. However, the mechanistic details of the proton reduction catalytic cycle remain unclear. This family of complexes is a valuable platform to unravel the effect of the metal identity and the reaction conditions on the catalytic H₂ production. For this reason, the second part of this thesis focuses on the computational mechanistic study of the proton reduction reaction by these systems.

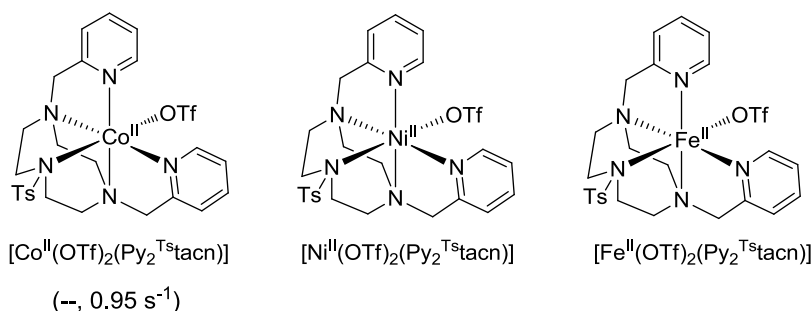


Figure 60: Molecular structures of [Co^{II}(OTf)₂(Py₂^{Ts}tacn)], [Ni^{II}(OTf)₂(Py₂^{Ts}tacn)] and [Fe^{II}(OTf)₂(Py₂^{Ts}tacn)] aminopyridine complexes. TOF value under electrochemical conditions is in parenthesis.

1.6.3.2 Nickel based H₂ Production Catalysts

In 1980, Fischer and Eisenberg also reported the first nickel complex capable to electrocatalytically reduce water and carbon dioxide to H₂ and CO, respectively.¹²⁶ The nickel(II) tetraazamacrocycle (**71**, Figure 61) behaves as a proton reduction catalyst at an applied potential of -1.46 V vs. SHE in a H₂O/CH₃CN 2:1 (v/v) solvent mixture, using a Hg electrode. Electrochemical measurements displayed a TOF value of about 0.0017 s⁻¹.

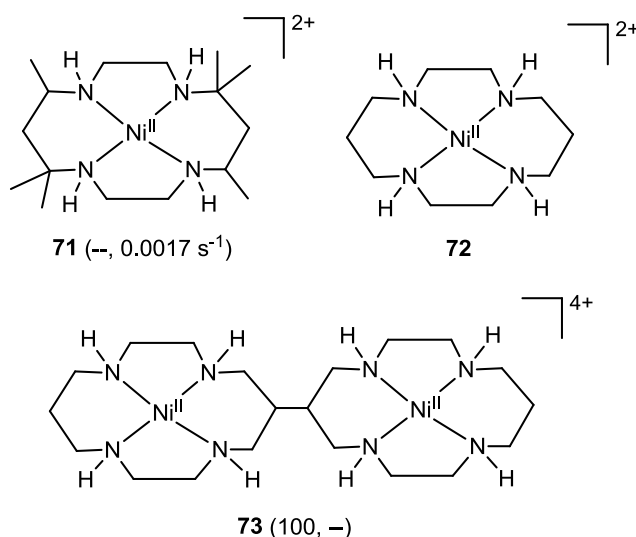


Figure 61: Molecular structures of the Ni^{II} tetraazamacrocyclic (**71**), $[\text{Ni}^{\text{II}}(\text{cyclam})]^{2+}$ (**72**) and $[\text{Ni}_2^{\text{II}}(\text{biscyclam})]^{4+}$ (**73**). TON and TOF values are in parenthesis, respectively.

Eight years later, Sauvage and coworkers investigated the electroreduction of water by the nickel complex $[\text{Ni}^{\text{II}}(\text{cyclam})]^{2+}$ (**72**, Figure 61; cyclam = 1,4,8,11-tetraazacyclotetradecane) and the bis-macrocyclic analog $[\text{Ni}_2^{\text{II}}(\text{biscyclam})]^{4+}$ (**73**, Figure 61).¹⁴² The two complexes were catalytically active when the reaction was performed in neutral water on a Hg electrode. Controlled potential electrolysis experiments at -1.26 V vs. SHE reveals that the dimer **73** is a more efficient H_2 production catalyst than the monomer **72**, with TONs up to 100. The enhancement of the catalytic activity of **73** was attributed to the cooperation between the two nickel centers. To rationalize this phenomenon, it was proposed that dihydride $[\text{Ni}_2^{\text{III}}(\text{H})_2(\text{biscyclam})]^{4+}$ active species might be responsible for the H-H bond formation. In contrast, for **72** it was postulated that the H_2 evolution occurs through a heterolytic pathway from $\text{Ni}^{\text{II}}\text{-H}$ species.

The most extensively studied nickel electrocatalysts for H_2 evolutions has been the family of $[\text{Ni}^{\text{II}}(\text{diphosphine})_2]^{2+}$ complexes developed by the group of Dubois.^{143,144,145,146} The research mainly focused on the evaluation of the factors that influence the thermodynamics of the hydride transfer event, which clearly have an impact on the energetic feasibility of the proton reduction reaction. In the last decades, their research specialized in the quest for structural motifs that may increase the proton reduction rate. In 2005, Dubois *et al.* discover that the complex $[\text{Ni}(\text{PNP})_2]^{2+}$ (**74**, Figure 62; PNP = $\text{Et}_2\text{PCH}_2\text{NMeCH}_2\text{PEt}_2$), which presents a pendant amine into the backbone of a diphosphine ligands, electrocatalyze the proton reduction reaction at a $\text{Ni}^{\text{II/I}}$ couple potential 600 mV more negative than the same for $[\text{Ni}^{\text{II}}(\text{depp})_2]^{2+}$ (depp = 1,2-bis(diethylphosphino)propane), which lack a pendant amine.¹⁴⁷ These significant change in the potential was attributed to the coupling of the electron and proton transfer events, since the pendant amine facilitates the proton exchange between the solution and the active metal site and avoids a significant reorganization of the coordination sphere of the metal complex.

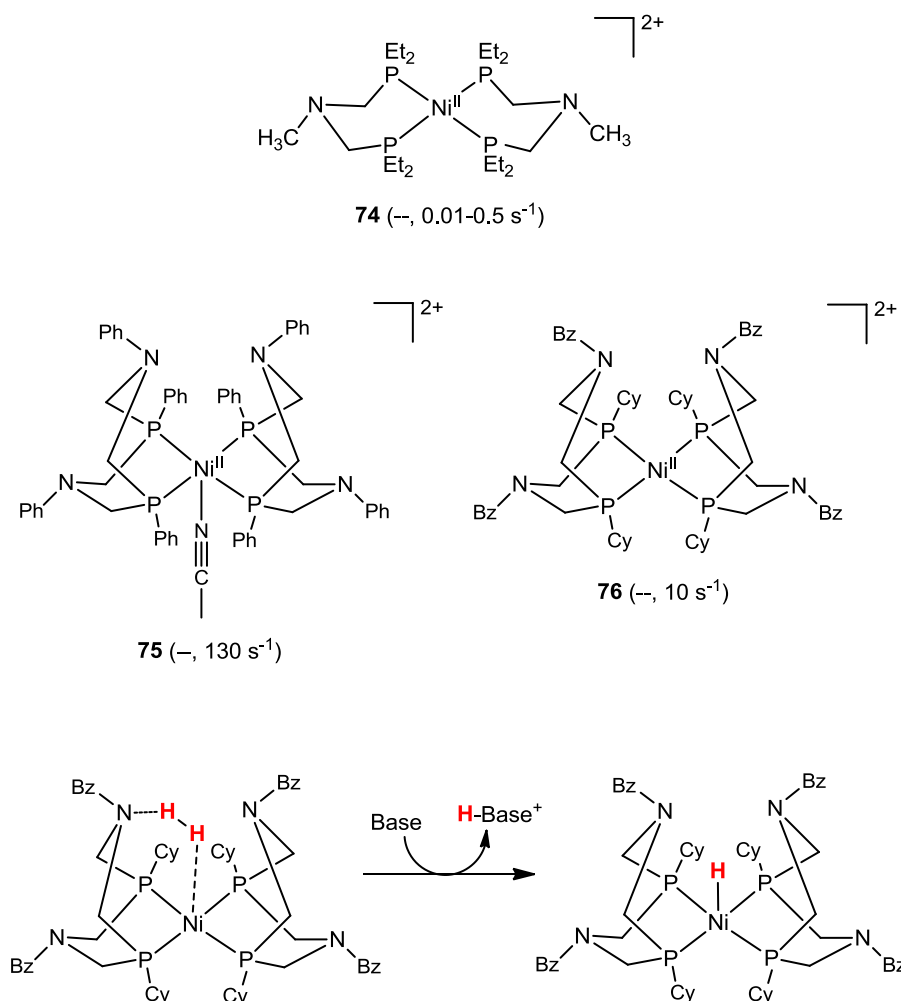


Figure 62: Above, molecular structures of $[\text{Ni}(\text{PNP})_2]^{2+}$ (**74**), $[\text{Ni}^{\text{II}}(\text{P}^{\text{Ph}}_2\text{N}^{\text{Ph}}_2)_2(\text{NCCH}_3)]^{2+}$ (**75**) and $[\text{Ni}^{\text{II}}(\text{P}^{\text{Cy}}_2\text{N}^{\text{Bz}}_2)_2]^{2+}$ (**76**). TOF values are in parenthesis. Below, schematic representation of the Ni-H₂ adduct derived from **76** and its conversion into the Ni-H intermediate.

The PNP ligand has to evolve from a chair to a boat conformational isomer to approach the pendant group to the metal center. One strategy to force the boat conformation is the employment of cyclic diphosphine ligands. Dubois and coworkers reported the synthesis and characterization of $[\text{Ni}^{\text{II}}(\text{P}^{\text{Ph}}_2\text{N}^{\text{Ph}}_2)_2(\text{NCCH}_3)]^{2+}$ (**75**, Figure 62; $\text{P}^{\text{Ph}}_2\text{N}^{\text{Ph}}_2 = 1,3,5,7\text{-tetraphenyl-1,5-diaza-3,7-diphosphacyclooctane}$) and $[\text{Ni}^{\text{II}}(\text{P}^{\text{Cy}}_2\text{N}^{\text{Bz}}_2)_2]^{2+}$ (**76**, Figure 62) complexes based on cyclic diphosphine ligands.¹⁴⁵ NMR and UV-Vis spectroscopic studies, in conjunction with the addition of external bases such as TEA or anisidine and molecular hydrogen gas, allowed the authors to detect the formation of a Ni-H₂ adduct and monohydride nickel species. In the former intermediate, the pendant base and the Ni center stabilize the H₂ molecule and the addition of a base generates a hydride moiety on the nickel center (Figure 62). It was also corroborated that the hydrogen activation/generation is a reversible process. Electrochemical data in acetonitrile solutions using a triflic acid (HOTf)/dimethylformamide (DMF) mixture as a protons source and a glassy carbon working electrode revealed that both complexes can be reduce to the Ni^I state prior to the H₂ evolution. Moreover, it was confirmed that the extremely acid character of the protonated pendant amines makes the system rapidly react with the Ni-H moiety to produce H₂. Kinetic studies on **76** indicated that the rate determining step corresponds to the H₂ activation in the hydrogen oxidation reaction. The TOF values for **75** and **76** were 130 s⁻¹ and 10 s⁻¹, respectively, being significantly

higher than the $0.01\text{--}0.5\text{ s}^{-1}$ obtained from **74**. Therefore, this study suggests that the pendant amine groups decrease the activation barrier for the H-H bond cleavage or formation.

The $[\text{Ni}(\text{P}^{\text{R}}_2\text{N}^{\text{R}'}_2)_2]^{2+}$ based electrocatalysts have been studied by means of DFT calculations to shed some light on the mechanism of the reversible H_2 oxidation/production reactions, taking into account also the relative energies of the boat and chair configurations.^{146,147,148} The molecular hydrogen generation pathway starts with the reduction of the initial Ni^{II} complex to generate Ni^{I} species (Figure 63). The reduction process triggers a conformational change of one $\text{P}^{\text{R}}_2\text{N}^{\text{R}'}_2$ ligand, which is considered that activates the catalyst. Then, one $\text{P}^{\text{R}}_2\text{N}^{\text{R}'}_2$ ligand is protonated and the generated N-H moiety is stabilized by the Ni^{I} center. Subsequent one electron reduction favors the proton transfer from the pendant amine group to the nickel atom, forming a $\text{Ni}^{\text{II}}\text{-H}$ intermediate. The pendant amine group close to the hydride ligand is again protonated and the coupling between the two hydrogen moieties leads to the formation of a $\text{Ni}\text{-H}_2$ adduct. Finally, the molecular hydrogen release takes place, closing the catalytic cycle. In general, the global reaction proceeds downhill to H_2 generation but the thermodynamics will be marked by the strength of the employed acid. DFT calculations also indicate that proton and electron transfer reaction may occur through PCET events.¹⁴⁹

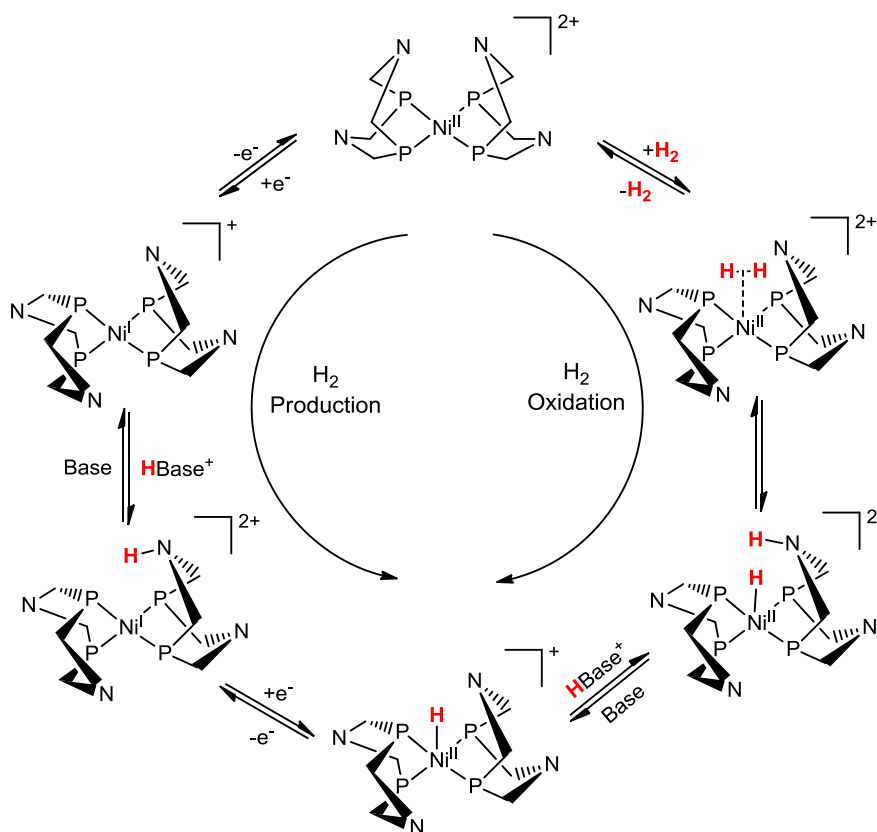


Figure 63: Catalytic cycle for H_2 oxidation and production by the $[\text{Ni}(\text{P}^{\text{R}}_2\text{N}^{\text{R}'}_2)_2]^{2+}$ family of catalyst.

It has been observed experimentally that the addition of water in organic solvents increases significantly the proton reduction rate. Kilgore and coworkers reported that the TOF value for the H_2 evolution catalyst $[\text{Ni}^{\text{II}}(\text{P}^{\text{Ph}}_2\text{N}^{\text{R}}_2)]^{2+}$ (**77**, Figure 64; $\text{R} = \text{C}_6\text{H}_4\text{CH}_2\text{P}(\text{O})(\text{OEt})_2$) increases from 500 s^{-1} in dry acetonitrile solvent to 1850 s^{-1} in the presence of 0.2 M water.¹⁵⁰ Helm *et al.* also observed for the $[\text{Ni}^{\text{II}}(\text{P}^{\text{Ph}}_2\text{N}^{\text{Ph}}_2)]^{2+}$ catalyst (**78**, Figure 64) an impressive increase of the TOF from 33000 s^{-1} to 106000 s^{-1} in acetonitrile when 1.2 M H_2O was employed.¹⁵¹ The group of Bullock performed

hybrid QM/MM calculations to understand the origin of this phenomena.¹⁵² They revealed that the water molecules cannot accelerate the H-H bond formation event. Instead, it was suggested that water may facilitate the rate determining proton delivery events.

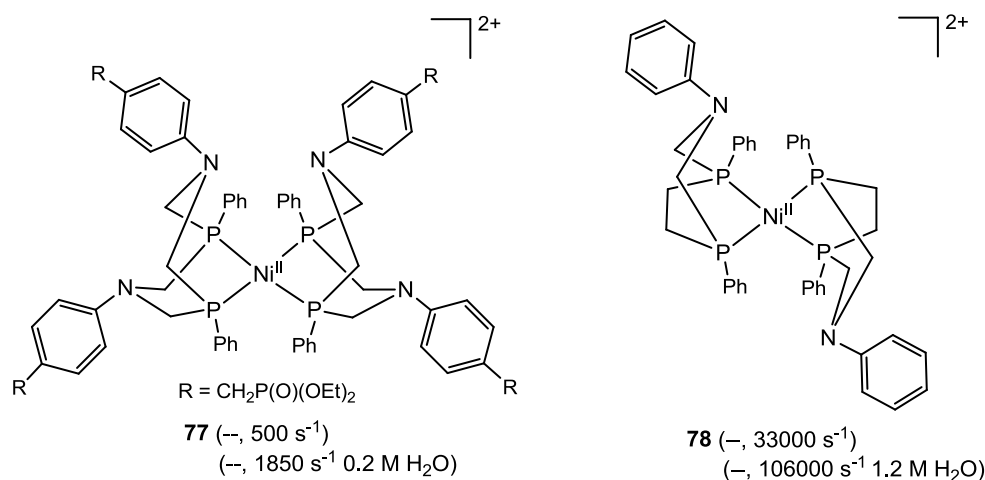


Figure 64: Molecular structures of $[\text{Ni}^{\text{II}}(\text{P}^{\text{Ph}}_2\text{N}^{\text{R}}_2)_2]^{2+}$ (**77**) and $[\text{Ni}^{\text{II}}(\text{P}^{\text{Ph}}_2\text{N}^{\text{Ph}})_2]^{2+}$ (**78**). TOF values are in parenthesis.

Another strategy to reduce the overpotential for H_2 production consists in the introduction of redox non-innocent moieties into the ligand framework. For example, in 2012 the group of Crabtree, Batista and Brudvig reported a Ni^{II} complex based on a pyridinediimine pincer ligand (**79**, Figure 65) that reduces protons in aqueous and organic acidic media.¹⁵³ Bulk electrolysis experiments demonstrated that complex **79** can reduce water at a potential of -1.1 V vs. NHE on a vitreous carbon electrode at $\text{pH} = 1$ (0.1 M KCl/HCl solution). Interestingly, cyclic voltammetry studies in acidic acetonitrile showed a reduction wave just above zero V, which on the basis of EPR data was assigned to a ligand-centered reduction. The measured voltammetric rate of hydrogen formation was 105 s^{-1} . On the basis of the previous data and quantum mechanical studies, the authors propose the H_2 production mechanism illustrated in Figure 64. DFT(B3LYP) calculations indicate that in water complex **35** is only a precatalyst and the catalytic cycle begins with a square planar Ni^{II} aqua complex. In the first step, the pyridinediimine ligand is reduced instead of the nickel center (-1.16 V vs. NHE). The spin density analysis revealed that the reduced system is best represented as a $\text{Ni}^{\text{II}}\text{-pyr}^\bullet$ radical, in which an unpaired electron is delocalized in the pyridine ring. Then, the system follows a PCET reaction to generate the $\text{Ni}^{\text{II}}\text{-H}$ active species (-0.97 V vs. NHE at $\text{pH} = 0$). The subsequent H-H bond formation proceeds *via* a heterolytic pathway until the formation of a $\text{Ni}^{\text{II}}\text{-H}_2$ adduct with a free energy cost of $9.0 \text{ kcal}\cdot\text{mol}^{-1}$. Finally, the displacement of the molecular hydrogen by a water molecule is an exergonic process ($\Delta G = 19.8 \text{ kcal}\cdot\text{mol}^{-1}$), leading to the recovery of the initial Ni^{II} aqua complex. Although the proposed catalytic cycle is thermodynamically feasible, the kinetics of the hydride and hydrogen generation was not considered.

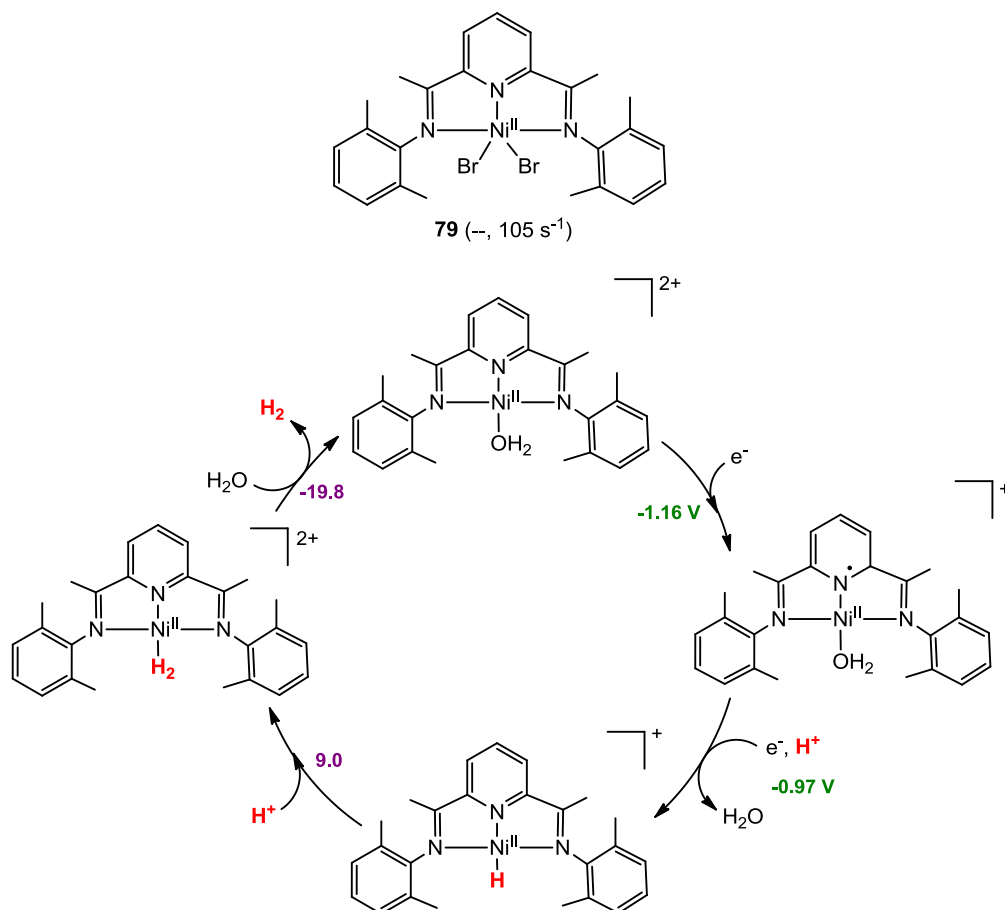


Figure 65: DFT proposed mechanism for H₂ generation for **79**. TOF value is in parenthesis. Gibbs energies are in kcal·mol⁻¹. The reduction potentials are relative to the NHE electrode at pH = 0.

1.6.3.3 Molybdenum based H₂ Production Catalysts

In 2010, Christopher Chang *et al.* reported the first molybdenum(IV)-oxo electrocatalyst for H₂ production based on a pentadentate polypyridyl ligand [(PY5Me₂)Mo^{IV}(O)]²⁺ (**80**, Figure 66; PY5Me₂ = 2,6-bis(1,1-bis(2-pyridyl)ethyl)-pyridine), in which the oxo moiety acts as a reductive site.¹⁵⁴ Complex **80** can catalyze the water reduction reaction at a potential of -1.4 V vs. SHE using a Hg electrode in a pH 7 buffered aqueous solution, showing minimum TOF and TON values of 2.4 s⁻¹ and 6.1·10⁵, respectively. Interestingly, **80** also operate in seawater keeping a similar activity. This system can reduce the protons derived from the acetic acid to hydrogen in an acetonitrile solution on a glassy carbon electrode under diffusion-limited conditions.¹⁵⁵ Moreover, cyclic voltammetry experiments showed that three electron reductions of the Mo^{IV}-oxo are required for proton reduction in both water and organic solvents. On the basis of this data, the group of C. Chang performed a DFT(BP86) study to investigate the mechanism for the electrocatalytic generation of H₂ from water (Figure 66).¹⁵⁶ Quantum mechanical computations indicate that the first reduction step involves a PCET reaction from [(PY5Me₂)Mo^{IV}(O)]²⁺ to [(PY5Me₂)Mo^{III}(OH)]²⁺. The computed reduction potential of 0.48 V vs. SHE is in agreement with the experimentally measured 0.55 V. Then, a second PCET event connects the [(PY5Me₂)Mo^{III}(OH)]²⁺ intermediate with [(PY5Me₂)Mo^{II}(OH₂)]²⁺ (0.47 V). The predicted third one-electron reduction leads to the generation of formal [(PY5Me₂)Mo^I(OH₂)]⁺ species with a potential of 0.77 V, which is consistent with the 1.1 V measured for the experimental onset potential. The Localized Orbital Bonding Analysis (LOBA) of the previous structure showed that the extra electron is partially delocalized on the axial pyridine

ligand, being the electronic structure best represented as $[\cdot(\text{PY5Me}_2)\text{Mo}^{\text{II}}(\text{OH}_2)]^+$. The reductive cleavage of the aqua ligand forms the $[(\text{PY5Me}_2)\text{Mo}^{\text{III}}(\text{H})(\text{OH})]^+$ active species, in which the OH group is in *cis* relative position respect to the hydride ligand. Then, the lowest in energy H-H bond formation pathway involves a solvent water molecule acting as a proton shuttle, promoting the proton transfer between the OH ligand and the hydride. However, the computed free energy barrier ($25.1 \text{ kcal}\cdot\text{mol}^{-1}$) is still far from the $16.9 \text{ kcal}\cdot\text{mol}^{-1}$ derived with the TOF value. Finally, the oxo group on the resulting $[(\text{PY5Me}_2)\text{Mo}^{\text{III}}(\text{O})]^+$ species is protonated, restarting the catalytic cycle.

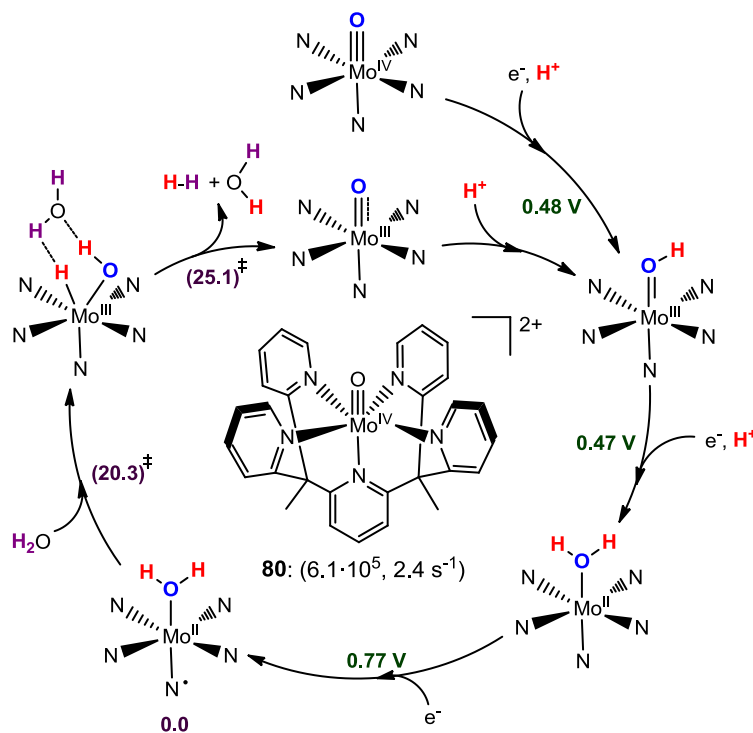


Figure 66: Molecular structure of complex $[(\text{PY5Me}_2)\text{Mo}^{\text{IV}}(\text{O})]^{2+}$ (**80**) and DFT proposed mechanism for H₂ production. TON and TOF values are in parenthesis, respectively. Gibbs energy barriers are in $\text{kcal}\cdot\text{mol}^{-1}$. Redox potentials respect to the SHE electrode.

The molybdenum based analogous of the Co bis-dithiolene complex, $[\text{Mo}^{\text{IV}}(\text{bdt})_2(t\text{-BuNC})_2]$ (**81**, Figure 67; bdt = bis(dithiolene), *t*-BuNC = *t*-Butyl isocyanide), was synthesized and characterized by Eisenberg and co-workers.¹⁵⁷ The photochemical proton reduction activity of catalyst **81** was evaluated in the presence of $[\text{Ru}^{\text{II}}(\text{bpy})_3]^{2+}$, ascorbic acid, and visible light in a $\text{CH}_3\text{CN}/\text{H}_2\text{O}$ solvent mixture. Electrochemical data in acetonitrile revealed that the system follows two sequential one-electron reductions before the H₂ is catalytically generated. The two previous redox events were assigned to the $\text{Mo}^{\text{IV}}/\text{Mo}^{\text{III}}$ (-0.79 V vs. SCE) and $\text{Mo}^{\text{III}}/\text{Mo}^{\text{II}}$ (-1.38 V vs. SCE) couples. Kinetic studies showed that **81** achieve a TON value of 520. The ¹H-NMR peaks corresponding to the free *t*-BuNC ligands were observed after the two reduction reactions, indicating that the *t*-BuNC ligands dissociate during the redox events. After protonation of $[\text{Mo}^{\text{II}}(\text{bdt})_2]^{2-}$, a new intermediate was detected by a UV-Vis spectroscopy analysis, possibly the neutral $[\text{Mo}^{\text{IV}}(\text{bdt})_2]$ species generated after the H₂ evolution. According to all this data, a mechanism was proposed in which the $[\text{Mo}^{\text{IV}}(\text{bdt})_2(\text{H})]^-$ active species catalyze the H-H bond formation event through a heterolytic pathway (Figure 67). However, the authors do not discard the possible protonation of the sulfur atoms, instead of the metal center, and the involvement of the S-H and Mo-H fragments in the H-H bond formation event. Then, the resulting $[\text{Mo}^{\text{IV}}(\text{bdt})_2]$ species are doubly reduced and protonated to recover the $[\text{Mo}^{\text{IV}}(\text{bdt})_2(\text{H})]^-$ intermediate, closing the catalytic cycle.

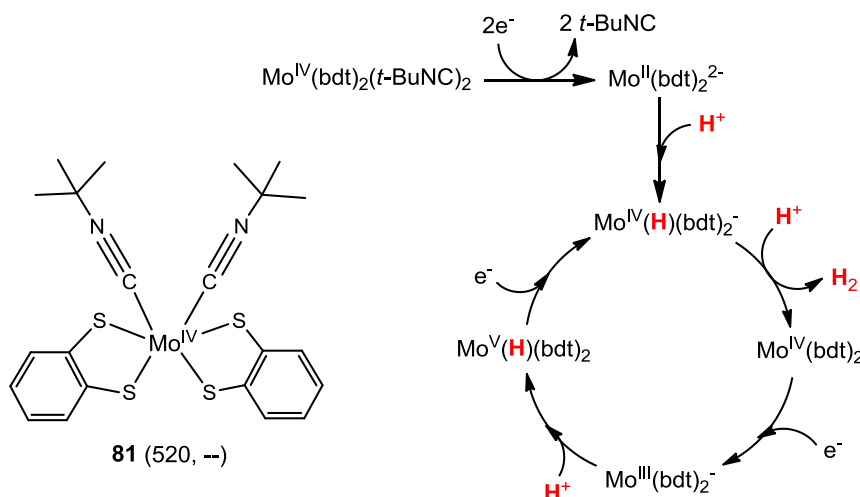


Figure 67: Left, molecular structure of [Mo^{IV}(bdt)₂(t-BuNC)₂] (**81**). Right, proposed mechanism for H₂ production. TON value is in parenthesis.

Another molybdenum bis-dithiolene catalyst for molecular hydrogen production, [Mo^{IV}(O)(qpdt)₂]²⁻ (**82**, Figure 68; qpdt = quinoxaline–pyran-fused dithiolene) was reported by Fontecave and coworkers in 2015.¹⁵⁸ The synthesis of **82** was inspired by the structure and constitution of the molybdopterin ligands present in the active site of many Mo and W enzymes. Complex **82** was characterized by X-ray diffraction, UV-Vis, IR, ¹H-NMR spectroscopy and ESI-MS spectrometry experiments. First, the catalytic activity of **82** was evaluated under reaction conditions comparable to those used for **81**. The monitoring of the H₂ production during the photochemical reduction of protons shows a remarkable initial TOF of 0.056 s⁻¹ and a TON of 500. Cyclic voltammogram studies in acetonitrile display a reversible transition at -0.19 V vs. Ag/AgCl/KCl-saturated electrode, assigned to the Mo^{IV}/Mo^V couple, and one irreversible transition attributed to the dithiolene ligand oxidation (0.62 V vs. Ag/AgCl/KCl-saturated electrode). Interestingly, when TFA is added, two new catalytic waves appeared: one corresponding to the potential onset (-0.55 V) and another associated with the Mo^{IV}/Mo^{III} couple (-0.75 V), which shifts to more positive potentials as the acid concentration increases. A quantitative analysis of the electrochemical data gave a TOF value of 1030 s⁻¹ at -1.3 V vs. Ag/AgCl using 0.1M of TFA. DFT(B3LYP) calculation were also conducted to explore the H₂ evolution reaction pathways (Figure 68). In the first step, the protonation of a nitrogen atom of one of the qpdt ligands is thermodynamically more favored than the protonation of the oxo ligand (-27.3 kcal·mol⁻¹ and +12.6 kcal·mol⁻¹ respectively). The protonation of the ligand makes exergonic the subsequent one electron reduction (-16.5 kcal·mol⁻¹ vs. 5.3 kcal·mol⁻¹) and then the oxo group is protonated to reach the [Mo^{III}(OH)(H-qpdt)(qpdt)]⁻ intermediate. The previous reactions may occur sequential or in a concerted way. Further reduction and protonation generate [Mo^{IV}(OH)(H)(H-qpdt)(qpdt)]⁻ active species. Finally, an intramolecular H-H bond formation occurs between the hydride and OH ligands leading to the H₂ (ΔG[‡] = 20.4 kcal·mol⁻¹). The DFT calculations also revealed that, under photochemical conditions, the electron transfer between the excited state [Ru^{II}(bpy)₃]^{2+*} and **82** occur through the π-stacking of the bpy and the qpdt ligands.

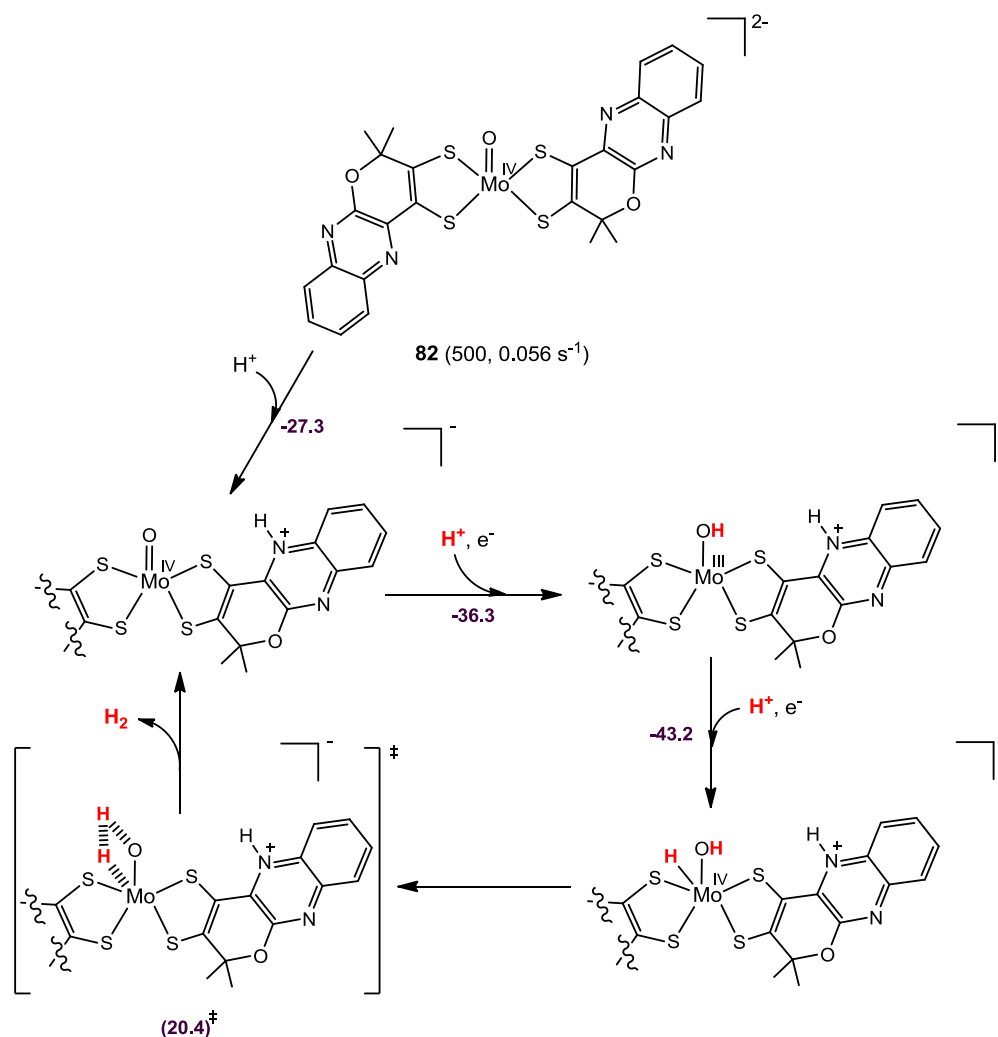


Figure 68: DFT computed mechanism for H₂ production by [Mo^{IV}(O)(qpdt)₂]²⁻ (**82**). TON and TOF values are in parenthesis, respectively. Gibbs energies are in kcal·mol⁻¹.

1.6.3.4 Copper based H₂ Production Catalysts

Few copper hydrogen evolving catalysts have been reported. In 2014, Zhan and coworkers showed that copper complex [Cu(opba)]²⁻ (**83**, Figure 69; opba = *o*-phenylenebis(oxamato)) is a robust electrocatalyst for water oxidation and reduction reactions in pure water,¹⁵⁹ reaching a TOF of 0.37 s⁻¹ for H₂ evolution at neutral pH with an overpotential of 788 mV. The cyclic voltammogram of an aqueous solution of **83** showed two redox waves attributed to the Cu^{II}/Cu^I and Cu^{III}/Cu^{II} redox couples. On the basis of this data and the literature precedents, the authors proposed a catalytic cycle in which Cu^{III}-H species are responsible of the H-H bond formation. The Zhan's group also reported two dinuclear copper catalysts for water reduction, [Cu(Me₂oxpn)Cu(OH)₂] (**84**, Figure 69; Me₂oxpn = N,N'-bis(2,2'-dimethyl-3-aminopropyl)oxamido) and [Cu(oxpn)Cu(OH)₂] (**85**, Figure 69; oxpn = N,N'-bis(3-aminopropyl)oxamido), which can operate under similar reaction conditions (Figure 69).^{160,161} For the latter complexes, it was suggested that the H₂ generation proceeds through the coupling of two Cu^{III}-H moieties. However, no detailed mechanistic analysis has been conducted to validate the formation of these copper-hydride active species.

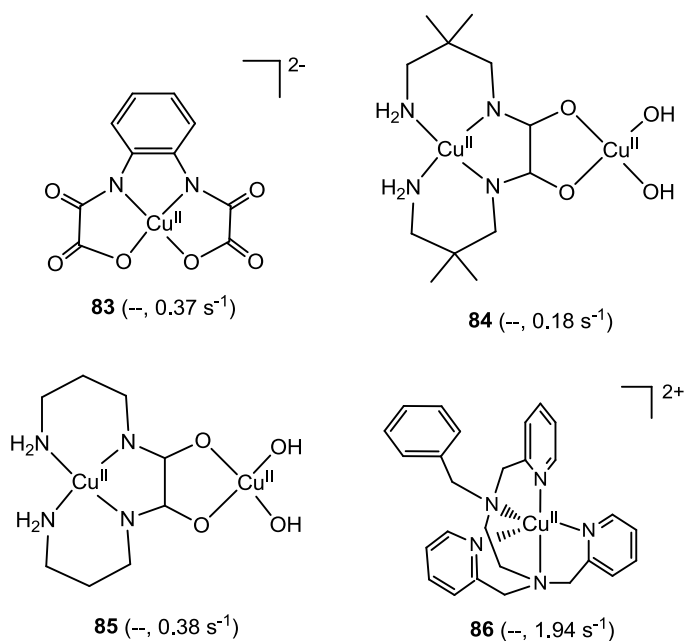


Figure 69: Molecular structures of copper complexes $[\text{Cu}(\text{opba})]^{2-}$ (**83**), $[\text{Cu}(\text{Me}_2\text{oxpn})\text{Cu}(\text{OH})_2]$ (**84**) and $[\text{Cu}(\text{oxpn})\text{Cu}(\text{OH})_2]$ (**85**). TOF values are in parenthesis.

In contrast with the previous copper systems, valuable mechanistic data has been obtained from the first polypyridil mononuclear copper complex $[\text{Cu}^{\text{II}}(\text{bztpen})]^{2+}$ (**86**, Figure 69; bztpen = *N*-benzyl-*N,N',N'*-tris(pyridine-2-ylmethyl)ethylenediamine) reported by Wang and co-workers.¹⁶² Complex **86** is a very efficient water reduction electrocatalyst in a phosphate buffer at pH 2.5 with an onset overpotential of 420 mV. Differential pulse voltammetry studies of **86** showed a pH-dependent reversible peak at -0.03 V vs. SHE , which was assigned to the $\text{Cu}^{\text{II}}/\text{Cu}^{\text{I}}$ redox couple. The catalytic peak corresponding to the water reduction reaction appeared at -0.82 V vs. SHE , also involving a PCET event. Potential electrolysis experiments at an applied potential of -0.9 V using a glassy carbon electrode showed a hydrogen-generation rate constant was higher than 10000 s^{-1} . UV-Vis and NMR data suggest that the pyridine moieties may get protonated during the catalysis. Taking into account all this data, Siegbahn, Sun and co-workers performed quantum mechanical study to unravel how the redox processes and the H-H bond formation occurs.¹⁶³ DFT(B3LYP) calculations indicate that the first PCET event involves the protonation of a pyridine moiety to form Cu^{I} pyridinium species instead of a $\text{Cu}^{\text{III}}\text{-H}$ intermediate (Figure 70). Then, a second metal centered PCET leads to generation of a $\text{Cu}^{\text{II}}\text{-H}$ intermediate. Finally, the coupling between the Cu-H and pyridinium moieties leads to the H_2 formation. The H-H bond formation energy barrier at an applied potential of -0.90 V vs. SHE ($\Delta G^\ddagger = 10.9 \text{ kcal}\cdot\text{mol}^{-1}$) is in agreement with the magnitude of the hydrogen-generation rate constant. Therefore, the theoretical data indicates that pyridine groups may function as proton shuttles, avoiding the formation of highly energetic $\text{Cu}^{\text{III}}\text{-H}$ active species and lowering the energy barrier for the H_2 evolution.

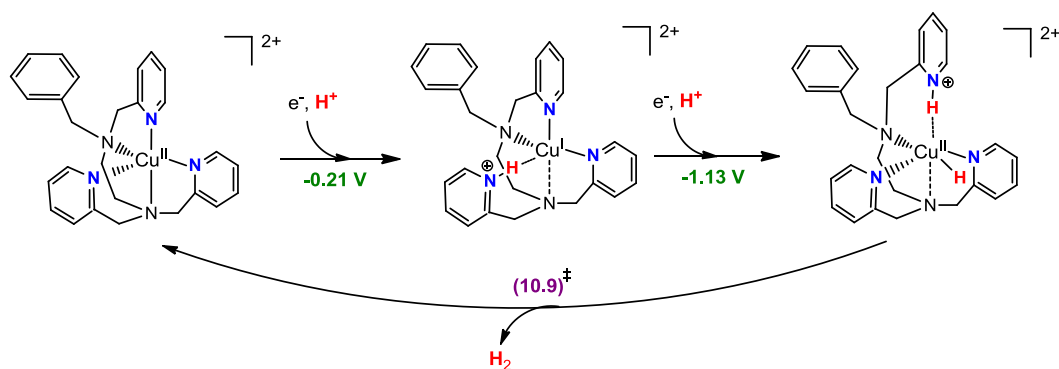


Figure 70: DFT computed H_2 production mechanism for complex **86**. The Gibbs energy barrier is given in $\text{kcal}\cdot\text{mol}^{-1}$.

To conclude, the combination of computational and experimental studies on several metal proton reduction catalysts has revealed the identity of the active species and the possible involvement of the catalyst's ligand platform in the process. However, in contrast with the WO field, only few mechanistic data about the fundamental steps is provided. Surprisingly, for the most studied cobaloximes systems, almost all the available computational data exclusively focus on the thermodynamics of all the possible proton reduction pathways without any reference to the kinetics aspects. Furthermore, for cobalt aminopyridine systems there is almost no mechanistic information. Although it is considered that the relative probability of the different reaction pathways may depend of the reaction conditions, no study has been conducted to model these effects.

It is essential to cover the lack of mechanistic data to rationally design more efficient proton reduction catalysts. Therefore, to address this goal, the second part of this thesis focuses on the computational analysis of the proton reduction activity of a family of cobalt, nickel and iron aminopyridine complexes. The effect of the ligand, metal and solvent on the H_2 generation is unraveled in chapter 9. Finally, the kinetic and thermodynamic aspects of the electro- and photochemical proton reduction catalytic cycles are explored in chapters 10 and 11.

CHAPTER 2:

THEORETICAL METHODOLOGY

2. THEORETICAL METHODOLOGY

2.1 Basics of quantum mechanics

Quantum chemistry is a branch of the theoretical chemistry field which is founded on the postulates of quantum mechanics. It aims to rationalize the behavior of chemical compounds at atomic and molecular scale by using computational tools. Modelling the molecular electronic and nuclear structure of the systems under study, it is possible to calculate a great variety of molecular properties (electronic energy, thermodynamic effects, vibrational frequencies, charge distribution, etc.) in their ground or excited states, to understand the inter- and intramolecular interactions that lead to the bonding between atoms and to elucidate the chemical reaction mechanisms in gas phase or in solution.¹⁶⁴

In quantum mechanics, the wave function describes the quantum state of an isolated system of particles. The wave function is determined by solving the Schrödinger equation, which is the analog of Newton's second law for a quantum system. To calculate the stationary properties of an atom or molecule, it is necessary to solve the time independent non-relativistic Schrödinger equation (Eq .4):¹⁶⁵

$$\hat{H}\Psi(r, R) = E\Psi(r, R) \quad (4)$$

where $\Psi(r, R)$ is the wave function of the system which depends on the electronic (r) and nuclear (R) coordinates, \hat{H} is the Hamilton operator containing the kinetic and potential energies of the system and E is the total energy obtained as an eigenvalue of the Hamiltonian. The molecular Hamiltonian within the non-relativistic approximation can be written as:

$$\hat{H} = T_N + V_{NN} + T_e + V_{ee} + V_{Ne} \quad (5)$$

where T_N is the nuclear kinetic energy, V_{NN} means the nucleus-nucleus repulsion interaction, T_e is the electron kinetic energy, V_{ee} is the electron-electron repulsion interaction and V_{Ne} is the attraction between nucleus and electrons. The previous kinetic and potential operators can be expressed as:

$$T_N = \sum_{a=1}^N -\frac{1}{2M_a} \nabla_a^2, \quad V_{NN} = \sum_{a=1}^N \sum_{b>a}^N \frac{Z_a Z_b}{R_{ab}}, \quad T_e = \sum_{i=1}^n -\frac{1}{2} \nabla_i^2, \quad V_{ee} = \sum_{i=1}^n \sum_{i>j}^n \frac{1}{r_{ij}}, \quad V_{Ne} = \sum_{i=1}^n \sum_{a=1}^N -\frac{Z_a}{r_{ia}}$$

where M_a and Z_a are respectively the mass and charge of the nucleus a , R_{ab} is the distance between the nuclei a and b , r_{ij} is the distance between the electrons i and j , r_{ai} is the distance between the nucleus a and the electron i , N and n are the number of nuclei and electrons of the molecule, respectively. Many approximations are used to solve the non-relativistic Schrödinger equation, being the Born-Oppenheimer approximation of capital importance in quantum chemistry. This approximation assumes that the motion of the heavy nuclei is much slower than that of light electron. Therefore, the electron-nuclei coupling can be neglected and then the electronic part of the Schrödinger equation only depends parametrically on the nuclear coordinates. Hence, the nuclei are considered to move on the potential energy surface obtained by solving the electronic Schrödinger equation.

2.2 *Ab initio* methods

Solving the time-independent Schrödinger equation with the Born-Oppenheimer approximation is still too complicated, since the instantaneous interactions between all the electrons have to be

considered. To study polyatomic molecular systems, other mathematical approximations must be employed. When these techniques have no empirical parameters are called *ab initio* methods. One example is the *Hartree-Fock* (HF) method,¹⁶⁵ in which the electrons are assumed to move independently under the mean Coulomb potential field generated by the remaining electrons. In this theory, the global electronic wave function of the system is given by the antisymmetric product of spin-orbital one-electron wave functions, leading to the construction of a Slater determinant.

In the spin unrestricted formalism, the HF equation of a n electron system can be written as set of n equations of the form:

$$F_i \varphi_i = \varepsilon_i \varphi_i \quad (6)$$

where φ_i is a HF molecular orbital, F_i is the Fock operator of the i^{th} electron and ε_i means the energy of the HF orbital. The Fock operator F_i is defined as:

$$F_i = -\frac{1}{2} \nabla_i^2 - \sum_{a=1}^N \frac{Z_a}{r_{ia}} + \sum_{j=1}^n (J_j - K_j) \quad (7)$$

where the first two terms of Eq. 7 denote the single electron kinetic and electron-nuclei potential energies, respectively. The last terms J_j and K_j are the Coulomb and exchange operators, respectively. The Roothan-Hall equation allow the computation of the molecular HF wave function, expanding the molecular orbitals as a linear combination of atomic orbitals (*LCAO*) and finding the value of the coefficients which leads to the lowest electronic energy. The coefficients are computed following an iterative procedure until energy converges, in the so called *self-consistent field (SCF)* procedure.

The main limitation of Hartree-Fock theory is that the single-determinant approximation only takes into account the correlation between electrons with the same spin (*exchange correlation*), but not for electrons with different spin (*Coulomb correlation*). This leads to a total electronic energy different from the exact solution of the Schrödinger equation. To solve this deficiency, more accurate methods based on the HF formalism have been developed, known as *post-SCF* or *post-Hartree-Fock* methods, to include the correlation effects and improve the results. Some examples are the Møller-Plesset Perturbation theory (MPn),¹⁶⁶ the Configuration Interaction method (CI),¹⁶⁷ the Multi-Configuration Self-Consistent Field approach (MCSCF)¹⁶⁸ or the Coupled Cluster theory (CC).¹⁶⁹

The post-SCF methods are computationally too expensive for systems with a large number of atoms, limiting their applications, especially in biological and transition-metal chemistry. However, an optimal balance between computational cost and accuracy can be achieved through the *Density Functional Theory (DFT)*, which presents a computational cost similar to that of HF method but including all the correlation effects.

2.3 Density Functional Theory (DFT)

2.3.1 DFT foundations

Thomas, Fermi and Dirac contributed in the development of the first model to describe the properties of a system with the electron density.¹⁷⁰ The Thomas-Fermi-Dirac model is considered the root of the modern Density Functional Theory (DFT) method.¹⁷¹ In DFT, which is based on the theorems by Hohenberg and Kohn,¹⁷² the electronic energy of the ground state is totally determined by the

electron density and the properties of a many-electron system can be determined by using functionals of spatial electron probability density ($\rho(\mathbf{r})$). This is more attractive than a polyelectronic wave function because $\rho(\mathbf{r})$ only depends on three spatial coordinates (x, y, z), while the latter depends on $3n$ variables ($4n$ taking into account the spin), where n is the number of electrons. Thus, DFT approach reduces the computational cost with respect to *ab initio* methods.

The theorems upon which modern DFT methodology has been built were formulated by Hohenberg and Kohn in 1964. They demonstrate that:

-First Theorem: The properties (observables) of the non-degenerate ground state of a chemical system are functionals of the electron density and can be calculated based on the electron density of the ground state.

-Second Theorem: The energy obtained as a function of the exact electron density, is the exact energy of the system and any other density will give a higher energy. According to the variational principle, we can obtain the exact electron density $\rho(\mathbf{r})_{\text{exact}}$ of the system by finding the minimum of the energy functional $E[\rho(\mathbf{r})]$.

$$E[\rho] \geq E[\rho_{\text{exact}}] = E_{\text{min}} \quad (8)$$

This theorem is only satisfied if $\rho(r) \geq 0$, and its integral extended to the whole space is equal to the number of electrons of the system (n).

The previous two theorems allow expressing the total energy of the ground state as a density functional of the electron density, with the following components:

$$E[\rho] = T_e[\rho] + V_{\text{ext}}[\rho] + V_{ee}[\rho] \quad (9)$$

where $T_e[\rho]$ is the kinetic energy of the electrons, $V_{\text{ext}}[\rho]$ the external potential functional which the system is embedded (for example, from the nucleus) and $V_{ee}[\rho]$ is the electronic repulsion potential.

Hohenberg and Kohn combined all the functionals that do not depend on the external potential, $v(r)$, into one called the Hohenberg-Kohn functional ($F_{HK}[\rho]$):

$$E[\rho] = F_{HK}[\rho] + V_{\text{ext}}[\rho] = F_{HK}[\rho] + \int \rho(r)v(r)dr \quad (10)$$

$F_{HK}[\rho]$ operates only on the density and is universal, i.e. can be applied to any chemical system because it does not depend on $v(r)$. Unfortunately, the Hohenberg-Kohn theorems only confirm that such a functional exist and describe nothing about the exact form of the functional dependence of energy on the density.

The Hohenberg-Kohn functional is unknown. Therefore, the next step in the development of DFT came with the derivation of approximate equations from which the electron density and the electronic energy could be obtained. A key step towards this goal occurred in 1965, when Kohn and Sham devised a practical method to calculate ρ and $E[\rho]$.¹⁷³ They consider a fictitious reference system of non-interacting electrons with the same electron density as the real system, moving in a local effective external potential, called the *Kohn-Sham potential* ($v_{\text{eff}}(\mathbf{r})$). Then, as Kohn and Sham

show, the exact ground state electronic energy E of a system of n interacting electrons can be written as:

$$E[\rho] = -\frac{\hbar^2}{2m_e} \sum_{i=1}^n \int \psi_i^*(\mathbf{r}_1) \nabla_1^2 \psi_i(\mathbf{r}_1) d\mathbf{r}_1 - \sum_{I=1}^N \int \frac{Z_I e^2}{4\pi\epsilon_0 r_{I1}} \rho(\mathbf{r}_1) d\mathbf{r}_1 + \frac{1}{2} \int \frac{\rho(\mathbf{r}_1)\rho(\mathbf{r}_2)e^2}{4\pi\epsilon_0 r_{12}} d\mathbf{r}_1 d\mathbf{r}_2 + E_{xc}[\rho] \quad (11)$$

where the first term in Eq. 11 represent the kinetic electronic energy of the system of non-interacting electrons; the second is the electron-nucleus attraction; the third term represents the Coulomb repulsion between the total electronic charge distribution at \mathbf{r}_1 and \mathbf{r}_2 ; the last term is the exchange-correlation energy (E_{xc}), which take into account all nonclassical interaction between electrons and the difference between the exact kinetic energy of the real system and the kinetic energy of the system formed by non-interacting electrons. E_{xc} can be expressed as:

$$E_{xc}[\rho] = T[\rho] - \frac{\hbar^2}{2m_e} \sum_{i=1}^n \int \psi_i^*(\mathbf{r}_1) \nabla_1^2 \psi_i(\mathbf{r}_1) d\mathbf{r}_1 + V_{ee}[\rho] - \frac{1}{2} \int \frac{\rho(\mathbf{r}_1)\rho(\mathbf{r}_2)e^2}{4\pi\epsilon_0 r_{12}} d\mathbf{r}_1 d\mathbf{r}_2 \quad (12)$$

where $T[\rho]$ and $V_{ee}[\rho]$ are the exact kinetic and electron-electron interaction energies, respectively. KS equations can be derived by applying the variational principle to the electronic energy $E[\rho]$, and have the form:

$$\left\{ -\frac{\hbar^2}{2m_e} \nabla_1^2 + v_{eff}(\mathbf{r}_1) \right\} \psi_i(\mathbf{r}_1) = \epsilon_i \psi_i(\mathbf{r}_1) \quad (13)$$

where:

$$v_{eff}(r_1) = \sum_{I=1}^N \frac{Z_I e^2}{4\pi\epsilon_0 r_{I1}} + \int \frac{\rho(\mathbf{r}_2)e^2}{4\pi\epsilon_0 r_{12}} d\mathbf{r}_2 + V_{xc}(\mathbf{r}_1) \quad (14)$$

ϵ_i are the KS orbital energies and V_{xc} the exchange-correlation potential, which is a functional derivative of the exchange-correlation energy:

$$V_{xc}[\rho] = \frac{\delta E_{xc}[\rho]}{\delta \rho} \quad (15)$$

The KS equations are solved in a self-consistent fashion like in Hartree-Fock method.

V_{xc} can be obtained from E_{xc} . However, the E_{xc} is the only unknown energetic term and a lot of approximate forms are used. The nature of this approximation is the origin of the different DFT functionals. The local density approximation (LDA) was the first envisaged E_{xc} term,¹⁷⁴ which only depends on the electron density of the system under study at each point of the space. The LDA method is still used in the solid state physics. The next step was the introduction of the first derivative of the density in the so called Generalized Gradient Approximation (GGA).¹⁷⁵ The later approximation gives better chemical accuracy than LDA. Actually, the most used approximation is the hybrid DFT method, in which the exchange-correlation functional includes a fraction of the Hartree-Fock exchange. The B3LYP functional, which is a hybrid functional, has become the most popular hybrid DFT method.¹⁷⁶

2.3.2 Efficiency and applications

Currently, the DFT calculations are enough accurate and speedy for application in the study of reaction mechanisms. It can be used to do calculations in molecules of 100 or more atoms in significantly less time than post-HF methods. Furthermore, DFT results frequently agree more closely with experiment data than HF calculations for most of the chemical systems. For the particular case of the molecules involving *d*-block metals, whereas HF leads to unreliable results, DFT hybrid methods often successfully reproduce the experimental data. Therefore, it is not surprising that DFT calculations have been applied to a wide range of chemical reactions, organic and inorganic, and it has also allowed the study of catalytic processes involving organometallic and enzymatic catalytic systems.^{177,178}

The accuracy of the most popular B3LYP method has been estimated using several benchmark tests, for example the extended G3 set (376 entries). Including only the 301 entries that are most relevant when only a few bonds are formed or broken, the B3LYP functional has an average error of 3.3 kcal·mol.¹⁷⁹ Indeed, this error is reduced if the energy comparison is done between differences of reactions energies and transition state barriers among similar structures.

There is a strong agreement between the distances and angles calculated with DFT and experimental methods. For instance, hybrid functionals like B3LYP and B3WP91, give rise to deviations of ± 0.02 Å in terms of bond distances and $\pm 1^\circ$ for angles in the main group elements. In comparison, the HF calculations tend to give bond distances too short and reproduce with difficulty the multiple bonds (because they do not take into account the correlation energy), while the MP2 method approximates the experimental results but overestimates the bond distances.

The deviations increase in the calculated bond distances between transition metal atoms and the coordinated ligand. In the best cases (hybrid functionals and closed shell complexes) the deviations lie around ± 0.05 Å for bond distances. With HF methods deviation increased to ± 0.1 Å while the MP2 gives values comparable to the best DFT functionals, but it depends on the electronic system.

The B3LYP has been previously used by our group in the study of water oxidation and reduction reactions to support some mechanistic proposals, with satisfactory results.^{69,141} Therefore, most of the computational studies about water oxidation and proton reduction reactions presented in this thesis are based on this functional. The solvation (SMD model)¹⁸⁰ and dispersion (Grimme-D₂/D₃ corrections)¹⁸¹ effects were introduced on the geometry optimizations and single point calculations to obtain a more reliable description of the chemical systems under catalytic conditions. The data obtained from DFT studies has been used to compute the necessary thermodynamic and kinetic parameters to predict the reactivity trends of the systems under study. The methodology employed is summarized in the following paragraphs.

2.4. pK_a calculations

The standard free energy dissociation (ΔG°) of an acid (HA) to form its conjugate base (A⁻) in solution may be defined as:

$$\Delta G_s^\circ = G(A_s^-) + G(H_s^+) - G(AH_s) \quad (16)$$

where $G(AH_s)$, $G(A_s^-)$ and $G(H_s^+)$ are standard free energies of the acid, its conjugate base and the proton in solution, respectively. The solvation energy of a proton ($\Delta G_{\text{solv}}^{H^+}$) cannot be computed through an implicit model of the solvent, since the dielectric environment does not describe the

strong hydrogen bonding interactions that establish the proton within polar solvents. Therefore, $G(\text{H}_s^+)$ is calculated as follows:

$$G(\text{H}_s^+) = G(\text{H}_{\text{gas}}^+) + \Delta G_{\text{solv}}^{\text{H}^+} + \Delta G^{o/*} \quad (17)$$

where $\Delta G_{\text{solv}}^{\text{H}^+}$ is taken from the experimental solvation free energy in a given solvent ($\Delta G_{\text{solv}}^{\text{H}^+}(\text{in water}) = -265.9 \text{ kcal} \cdot \text{mol}^{-1}$; $\Delta G_{\text{solv}}^{\text{H}^+}(\text{in acetonitrile}) = -260.2 \text{ kcal} \cdot \text{mol}^{-1}$), and the gas-phase free energy $G(\text{H}_{\text{gas}}^+)$ is computed from the translational partition function ($-6.3 \text{ kcal} \cdot \text{mol}^{-1}$).¹⁸² $\Delta G^{o/*}$ is the free energy change associated with the conversion from a standard state of 1 M in the solvent phase and 1 atm in gas phase, to the desired concentration in both phases.

ΔG^* values are derived from the following expression:

$$\Delta G^{o/*} = RT \ln(24.4 * c) \quad (18)$$

where R is the universal gas constant ($1.987 \text{ cal} \cdot \text{mol}^{-1} \cdot \text{K}^{-1}$), T is the temperature in Kelvin and c the concentration in $\text{mol} \cdot \text{L}^{-1}$. Its value at 1 M concentration and 298.15 K is $1.89 \text{ kcal} \cdot \text{mol}^{-1}$.¹⁸³ In this thesis, the $\Delta G^{o/*}$ parameter is also employed to adjust the concentration of all the species involved in the reactions under study, including the solvent concentration.

Taking into account the previous equations, the pK_a of an acid HA in solution is computed as:

$$\text{pK}_a = \frac{\Delta G_s^o}{RT \ln(10)} \quad (19)$$

The B3LYP calculation of pK_a values may lead in the worst case an error of 3 pK_a units.

2.5. Thermodynamics and kinetics of redox reactions

In many chemical reactions, especially in biochemical processes, one electron is transferred from one reactant to another.¹⁸² If the coupling between reactants is strong enough, for example, two metal complexes connected through a ligand bridging group, an inner-sphere electron transfer may occur. In contrast, when no direct bonding exists between the donor and acceptor species, an outer-sphere electron transfer reaction takes place and the electron tunnels from one species to the other through the solvent. In this thesis, the two electron transfer channels have been considered.

For outer-sphere one electron transfer reactions, the standard redox potentials relative to a reference electrode is calculated by:

$$E^o = -\frac{\Delta G^o - \Delta G_{\text{ref}}}{F} \quad (20)$$

where ΔG^o is the standard free energy change associated with the reduction reaction, F is the Faraday constant ($23.061 \text{ kcal} \cdot \text{mol}^{-1}$) and ΔG_{ref} is the free energy change associated with the complementary oxidation/reduction reaction suffered by the reference electrode. At experimental conditions, the measured redox potentials are related to E^o (standard conditions, $\text{pH} = 0$) through the Nernst equation:

$$E = E^o - 0.059 * \text{pH} \quad (21)$$

Taking into account the B3LYP mean error for the energy, the computed redox potentials may lead to an average error around 200 mV.

The kinetics of outer sphere electron transfer reactions in homogeneous phase are approximately accounted by the Marcus theory.¹⁸⁴ According to this, the energy barrier of an electron transfer reaction depends on its thermodynamics (ΔG^*) and the total reorganization energy (λ_t) of the system involved in the redox reaction. The free energy barrier for an electron transfer is approximated with the following expression:

$$\Delta G^\ddagger = \frac{(\Delta G^* + \lambda_t)^2}{4\lambda_t} \quad (22)$$

where the total reorganization energy λ_t can be expressed as the sum of the inner (λ_{int}) and outer (λ_{out}) reorganization energies. The λ_{int} quantifies the structural changes within the electron donor and acceptor, while λ_{out} is related with the solvent reorientation around the species involved in the redox event.

The inner reorganization energy was determined with the Klimkans and Larsson formula:¹⁸⁵

$$\lambda_{int} = \frac{E_{Ox}(X_e^{Red}) - E_{Ox}(X_e^{Ox}) + E_{Red}(X_e^{Ox}) - E_{Red}(X_e^{Red})}{2} \quad (23)$$

where X_e^{Red} and X_e^{Ox} are the optimized geometries of the reduced and oxidized species, respectively, and E_{Red} and E_{Ox} are the electronic potential energies for the redox species. The outer reorganization energy¹⁸⁴ has been calculated assuming that reactants behave as conducting spheres:

$$\lambda_{out} = e^2 \left(\frac{1}{\epsilon_{op}} - \frac{1}{\epsilon_s} \right) \left(\frac{1}{2r_1} + \frac{1}{2r_2} - \frac{1}{r_1 + r_2} \right) \quad (24)$$

where ϵ_{op} and ϵ_s are the optical and the static dielectric constants of the solvent. The r_1 and r_2 are respectively the mean radii of the donor and the acceptor in Å, obtained from the molecular volume (keyword “volume” in Gaussian09) and assuming a spherical shape.

Some redox reactions are coupled with proton transfer events. The structural changes of the reactants when a proton and electron transfer takes place can be accounted by defining a reorganization energy (E_{reor}) parameter. This parameter can be used to qualitatively estimate the magnitude of the proton transfer barriers. The E_{reor} was determined with a modified Klimkans and Larsson based formula^{140,185} originally derived for electron transfer processes:

$$E_{reor} = \frac{E_{No_Prot}(X_e^{Prot}) - E_{No_prot}(X_e^{No_prot}) + E_{Prot}(X_e^{No_Prot}) - E_{Prot}(X_e^{Prot})}{2} \quad (25)$$

where X_e^{Prot} and $X_e^{No_Prot}$ are the equilibrium geometries of the protonated and no protonated species, respectively, and E_{Prot} and E_{No_Prot} are the corresponding electronic energies in different protonation states.

2.6. Broken spin symmetry methodology

In DFT, the wavefunction of the system is represented by a single Slater determinant constructed with the Kohn-Sham orbitals. Instead, the wavefunction of several compounds based on first row transition metals present a strong multireference character and their electronic structure is not well described by a single determinant. In such cases, DFT is not directly applicable¹⁸⁶ and a more accurate method, i.e, CASSCF/CASPT2, may be desirable. However, the computational cost of multireference and post-HF methods is usually huge to be used routinely in mechanistic studies of catalytic reactions. To solve this deficiency in a simple manner, the broken spin symmetry (BS) DFT approach can be adopted: In standard Kohn-Sham DFT, the single determinant representation of the wavefunction provokes an important mixing of spin states that translates into an increase of the total square spin angular momentum expected value ($\langle S^2 \rangle$) respect to the ideal one. The spin-purified energy for a selected spin state can be computed using the following equations:¹⁸⁷

$$E_{\langle S^2 \rangle_{corr}} = \frac{E_{cont} - a * E_{(S+1)}}{1 - a} \quad (26)$$

$$a = \frac{\langle S^2_{cont} \rangle - S * (S + 1)}{\langle S^2_{(S+1)} \rangle - S * (S + 1)}$$

where $E_{\langle S^2 \rangle_{corr}}$ is the spin corrected electronic energy, E_{cont} and $\langle S^2_{cont} \rangle$ are the energy and total square spin angular momentum respectively, obtained from the computational level employed for geometry optimizations and the $E_{(S+1)}$ and $\langle S^2_{(S+1)} \rangle$ are the energy and total square spin angular momentum of the afterward unpaired spin state (S+1), respectively, computed at the same computational level and molecular geometry. The broken symmetry approach has been proven effective for the prediction of spin state energy splitting in metal coordination complexes.¹⁸⁸⁻¹⁹⁰

CHAPTER 3:

MAIN OBJECTIVES

3. MAIN OBJECTIVES

The development of water splitting devices requires the use of efficient catalysts capable to overcome the high energetic cost of the WO reaction. In addition, the catalysts in the oxidative and reductive sites would be based on earth abundant metals, compatible under catalytic conditions and work in a cooperative manner to obtain the best catalytic performance with the lowest cost. The economically viable large-scale production of the promising H₂ fuel by an artificial photosynthetic system may be achieved if the mechanistic details of the multiple electron and proton transfer events, as well as the electronic and geometric features that lead to the O-O and H-H bond formation, are known. The quest for a comprehensive atomic picture of the water splitting reaction can benefit of computational simulations, since the tools provided by theoretical chemistry allow the access to intermediates that cannot be detected by experimental techniques. Toward this end, this thesis focuses in the computational study of the water oxidation and proton reduction reactions by catalysts based on first transition metals.

The present dissertation has eight objectives, which can be summarized in two general goals.

- 1) The first general goal is the computational insight into the mechanism of the water oxidation catalytic cycle performed by a family of non-heme iron WOCs (**Figure 71**). To achieve this goal, we proposed the following objectives:
 - 1.1 First, the energetic accessibility of the proposed Fe^V=O active species from Fe^{IV}=O intermediates for the **1**, **2**, **3** and **4** iron complexes will be studied by calculation of the redox potentials and pK_a values (Chapter 4).
 - 1.2 Likewise, a DFT study of the O-O bond formation event, starting from the iron-oxo in oxidation state V, will be performed for iron water oxidation active complexes **1** and **2**, and the inactive complexes **3** and **4** (Chapter 4). The study will permit to unravel the effect of the ligand coordination number and mode on the WO activity of the previous iron complexes. This data will shed light on the factors that govern the progress of the WO reaction. The possible involvement of **1** Fe^{IV}=O species in the O-O bond formation mechanism will be also considered (Chapter 5).
 - 1.3 Then, the discovered key factors that determine the energetic feasibility of the WO reaction will be used to *in silico* design new WO complexes. It will be explored the possibility of using pentadentate anionic ligands. This study will permit to understand how the metal-ligand cooperation benefits the WO catalysis (Chapter 6).
 - 1.4 The generation, structure and WO activity of the recently detected Fe^{IV}-O-Ce^{IV} intermediate from **1- α** will be explored. This work will focus on the mechanistic implications of the sacrificial oxidant (CAN) involvement in the O-O bond formation event. The divergent WO activity of topological isomers **1- α** and **1- β** will be also investigated (Chapter 7).
 - 1.5 Finally, the capacity of **1- α** Fe^V=O species to oxidize molecular hydrogen will be elucidated and their convenience in the construction of water splitting devices discussed (Chapter 8).

All this knowledge will permit to design new and improved WOCs based on iron, as well as the application of this kind of catalyst for the activation of other small molecules.

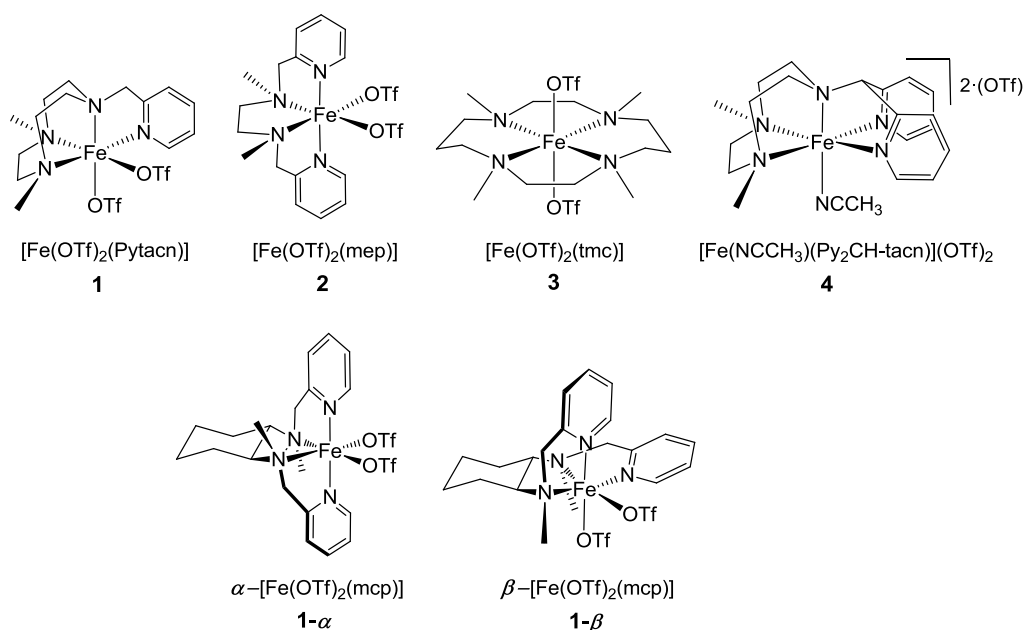


Figure 71: Selected iron complexes for study the WO mechanism.

2) The second general goal is the computational study of the proton/water reduction reaction by aminopyridine metal complexes $[\text{M}(\text{Py}_2^{\text{Ts}}\text{tacn})(\text{OTf})]$ ($\text{M} = \text{Co}, \text{Ni}, \text{Fe}$) (**Figure 72**). To achieve this second goal, the following objectives were proposed:

- 2.1 The redox potentials and pK_a values connecting the 1Co^{II} , 1Ni^{II} and 1Fe^{II} *N*-pentadentate complexes with M^{I} and $\text{M}^{\text{III}}\text{-H}$ ($\text{M} = \text{Co}, \text{Ni}, \text{Fe}$) intermediates will be computed. The preference of water and acetonitrile solvent molecules to occupy the sixth vacant coordination site of the metal complexes and their influence on the reactivity will be examined ([Chapter 9](#)). This study will reveal the origin of the different reactivity patterns exhibited by 1M^{II} complexes.
- 2.2 Elucidation of the proton reduction mechanism under electrochemical conditions (acetonitrile solvent and trifluoroacetic acid as a source of protons) performed by 1Co^{II} . The minimum energy reaction pathways and the mechanistic role of the pyridine arm in the $\text{Py}_2^{\text{Ts}}\text{tacn}$ ligand will be explored ([Chapter 10](#)).
- 2.3 Elucidation of the proton reduction mechanism under photochemical conditions (water/acetonitrile solvent mixture, the $[\text{Ir}(\text{ppy})_2(\text{bpy})](\text{PF}_6)$ photosensitizer, Et_3N as a sacrificial reductor and $\text{pH} = 12$) performed by 1Co^{II} and the electronic structure analysis of the cobalt-hydride active species. The origin of reactive protons in basic media will be investigated ([Chapter 11](#)).

The computational elucidation of the effect of reaction conditions (i.e solvent mixture, protons source, etc.) and the metal identity on the electronic structure of an aminopyridine complex will open a new way for the design of more efficient proton reduction catalysts.

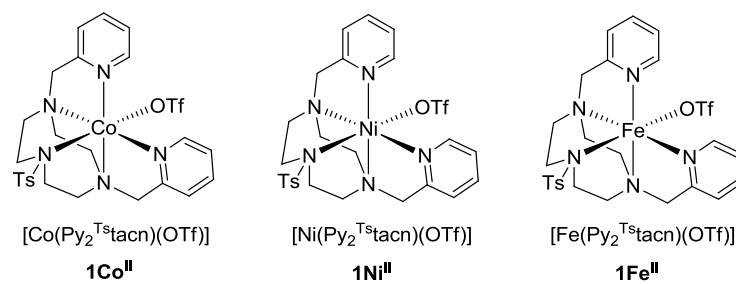


Figure 72: Selected aminopyridine complexes for study the proton reduction mechanism.

CHAPTER 4:

UNRAVELLING THE MECHANISM OF WATER OXIDATION CATALYZED BY NON-HEME IRON COMPLEXES^a

^a This chapter is based on the publication: Acuña-Parés, F.; Codolà, Z.; Costas, M.; Luis, J.M.; Lloret-Fillol, J. *Chem. Eur. J.* **2014**, *20*, 5696.

4. Unravelling the Mechanism of Water Oxidation Catalyzed by Non-heme Iron Complexes

In this chapter, density functional theory is employed to: 1) propose a viable catalytic cycle consistent with our experimental results for the mechanism of chemically driven (Ce^{IV}) O_2 generation from water mediated by non-heme iron complexes; and 2) to unravel the role of the ligand on the non-heme iron catalyst in the water oxidation reaction activity. To this end, the key features of the water oxidation catalytic cycle for the highly active complexes $[\text{Fe}(\text{OTf})_2(\text{Pytacn})]$ (Pytacn: 1-(2'-pyridylmethyl)-4,7-dimethyl-1,4,7-triazacyclononane; OTf: CF_3SO_3^-) (**1**) and $[\text{Fe}(\text{OTf})_2(\text{mep})]$ (mep: *N,N'*-bis(2-pyridylmethyl)-*N,N'*-dimethyl ethane-1,2-diamine) (**2**) as well as for the catalytically inactive $[\text{Fe}(\text{OTf})_2(\text{tmc})]$ (tmc: *N,N',N'',N'''*-tetramethylcyclam) (**3**) and $[\text{Fe}(\text{NCCH}_3)(^{\text{Me}}\text{Py}_2\text{CH-tacn})](\text{OTf})_2$ ($^{\text{Me}}\text{Py}_2\text{CH-tacn}$: *N*-(dipyridin-2-yl)methyl)-*N',N''*-dimethyl-1,4,7-triazacyclononane) (**4**) have been analyzed.

4.1. State-of-the-art

Lloret-Fillol *et al.*⁶⁸ reported a family of iron catalysts for water oxidation, which yield the one of the highest turnover number described so far for any homogeneous WOC based on a first row transition metal. These catalysts contain readily available and modular tetradentate nitrogen ligands (Figure 73). Moreover, the accessibility to broad array of nitrogen-based ligands allowed them to extract preliminary data of the scope, efficiency and mechanistic information of the corresponding iron complexes in catalytic water oxidation reactions.

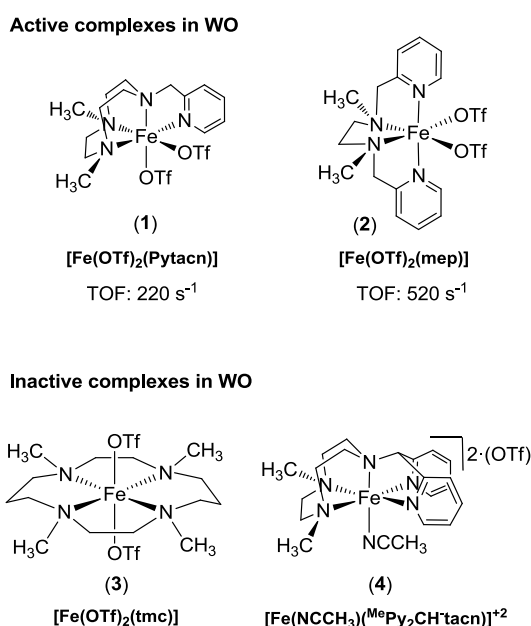


Figure 73: Schematic diagram of iron complexes $[\text{Fe}(\text{OTf})_2(\text{L}^{\text{N}4})]$ and $[\text{Fe}(\text{NCCH}_3)(\text{L}^{\text{N}5})](\text{OTf})_2$ used in this study. OTf stands for CF_3SO_3^- anion.

It was found that iron complexes with tetradentate nitrogen-based ligands that leave two available *cis*-positions were effective WO catalysts (up to 82 TON = $n(\text{O}_2)/n(\text{Cat})$), 145 TON and 360 TON when $[\text{Fe}(\text{OTf})_2(\text{Pytacn})]$ (Pytacn = 1-(2'-pyridylmethyl)-4,7-dimethyl-1,4,7-triazacyclononane and OTf for CF_3SO_3^-) (**1**), $[\text{Fe}(\text{OTf})_2(\text{mep})]$ (mep = *N,N'*-bis(2-pyridylmethyl)-*N,N''*-dimethyl-1,2-diaminoethane) (**2**) and $[\text{Fe}(\text{OTf})_2(\text{mcp})]$ (mcp = *N,N'*-bis(2-pyridylmethyl)-1,2-

diaminocyclohexane) were used as catalysts, respectively, and $[\text{Ce}^{\text{IV}}(\text{NO}_3)_6](\text{NH}_4)_2$ (CAN) as a oxidant).⁶⁸ On the contrary, iron complexes $[\text{Fe}(\text{OTf})_2(\text{tmc})]$ (**3**) ($\text{tmc} = N,N',N'',N'''$ -tetramethylcyclam), with tetradentate nitrogen ligands that leave two available *trans*-positions, and $[\text{Fe}(\text{NCCH}_3)(^{\text{Me}}\text{Py}_2\text{CH-tacn})](\text{OTf})_2$ (**4**) ($^{\text{Me}}\text{Py}_2\text{CH-tacn} = N$ -(dipyridin-2-yl)methyl)- N',N'' -dimethyl-1,4,7-triazacyclononane), with pentadentate nitrogen ligands, were ineffective WO catalysts (Figure 1). Furthermore, Costas *et al.*¹⁹¹ have recently observed that complexes like **1** and **2**, with *cis*-labile binding sites, were catalytically active in stereospecific hydroxylation of alkanes and *cis*-dihydroxylation of olefins using water as a source of oxygen and CAN as oxidant. When H_2O_2 is used as oxidant instead of Ce^{IV} , the same selectivity patterns are obtained, which suggests that Ce^{IV} is not directly involve in the substrate oxidation. Otherwise, under the same catalytic conditions **3** and **4** do not produce any oxidation of *cis*-decaline and *cis*-2-octene. Indeed, C-H and C=C oxidation as well as WO, appear to all require iron complexes containing a tetradentate ligand that leaves two available *cis* sites. Therefore, this obvious correlation strongly suggests the involvement of common iron intermediates mediating substrate oxidation in both catalytic pathways.

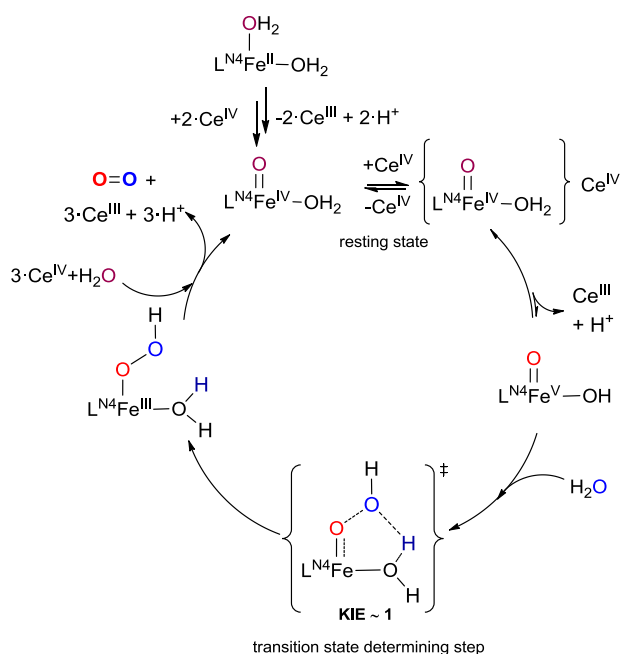


Figure 74: Proposed catalytic cycle for water oxidation reaction by iron complexes based on tetradentate nitrogen ligands with *cis*-labile positions ($\text{L}^{\text{N}4}$).

Towards the aim to understand the basic principles of the reaction of water oxidation with this type of complexes we started a study of the reaction mechanism. Our preliminary mechanistic investigations with $[\text{Fe}(\text{OTf})_2(\text{Pytacn})]$ (**1**) showed that the reaction rate exhibits a first-order dependence with respect to the concentration of both the metal complexes and cerium ammonium nitrate (CAN) at low concentration of oxidant.⁶⁹ This result suggests that the WOC is single site and excludes the possibility of a direct coupling (DC) mechanism. High valent $\text{Fe}^{\text{IV}}=\text{O}$ species were spectroscopically detected and identified as the resting state under these catalytically relevant conditions, and also as competent intermediates in the formation of a highly electrophilic $\text{Fe}^{\text{V}}=\text{O}$ complex, which performs the O-O bond-formation event. Under the catalytic conditions, the TOF determining transition state (TDTS)¹⁹² for WO is proposed to correspond to an attack of a water molecule to a highly electrophilic $\text{Fe}^{\text{V}}(\text{O})$ complex.

Our previous mechanistic studies provide no answer on the standing problem of the different reactivity observed among the iron complexes. But it is an ideal starting point to unravel the questions of why iron complexes with two *cis*-labile coordination sites are active in WO, whereas those with two *trans*-labile coordination sites or pentadentate nitrogen ligands are ineffective in WO. In the present chapter, we decoded these striking differences among isomers (*trans*- vs. *cis*-) and coordination index (tetradentate vs. pentadentate) and provide clarification in some fundamental operational principles of the WO, as well as useful hints to pursue in the future design of more effective water oxidation catalysts.

Specifically, herein we present a density functional theory (DFT) study of the O-O bond formation mechanism for catalytically active complexes **1** and **2**, and for the non-active complexes **3** and **4**. We evaluate theoretically the redox and acid-base processes connecting $\text{Fe}^{\text{IV}}(\text{O})(\text{OH}_2)$ and $\text{Fe}^{\text{V}}(\text{O})(\text{OH})$ for complexes **1**, **2**, **3** and **4**. This is indeed the first step of the proposed catalytic WO cycle. Then, we modelled the following step computing the Gibbs free-energy profile for the O-O bond-formation event starting from the iron-oxo in oxidation state V ($\text{Fe}^{\text{V}}(\text{O})(\text{OH})$) for the four catalysts. For **1**, the WO catalytic cycle is completed with a DFT study of the steps that connect $\text{Fe}^{\text{III}}(\text{OOH})(\text{OH}_2)$ and $\text{Fe}^{\text{IV}}(\text{O})(\text{OH}_2)$ species, closing the catalytic cycle. Finally, we discuss the Gibbs free-energy profile for the complete cycle. The first two steps of the catalytic cycle are the most energetic demanding and therefore the ones for which the four catalysts were studied. Overall, the analysis described herein provides valuable design principles to rationally develop highly active WOCs.

4.2. Results and Discussion

In this computational study, density functional theory (DFT) was chosen as a compromise between accuracy and computing time. The computational study was carried out using the Gaussian09 software,¹⁹³ with the B3LYP hybrid exchange-correlation functional.¹⁷⁶ Optimizations were performed with the 6-31G* 6d basis set for all atoms and including the effect of water solvent through the polarizable continuum model of Truhlar and co-workers (SMD).¹⁸⁰ We have checked that taking into account solvent effects in the optimization was essential to reproduce the experimental data.⁶⁹ The energies were further refined by single-point calculations with the cc-pVTZ dunning basis set for all atoms ($E_{\text{cc-pVTZ}}$). All calculations employed the spin-unrestricted formalism and spin-contaminated energies were systematically corrected using Eq. 25. Additionally, dispersion effects neglected in B3LYP, could give significant contributions and therefore in this study we correct them by adding the simple DFT-D₂ correction of Grimme (E_{disp}).¹⁸¹

Gibbs energy corrections at 298.15 K were obtained from solvent phase frequency calculations at B3LYP/6-31G* level (G_{corr}). Cramer, Truhlar, and coworkers recently recommended the calculation of Gibbs energy corrections in solvent phase for cases in which there are important differences between liquid- and gas-phase structures or when even stationary points in solution do not exist in the gas phase,¹⁹⁴ which indeed occurs in our proposed WO mechanism.⁶⁹ The solvent effects were computed at the same level by performing gas phase and solvent phase calculations and taking the difference of the resulting energies (G_{solv}). Indeed, it is well known that for reactions carried out in water the solvent usually has a large effect on the reactivity.^{27,62,67,195-197} All calculated solvation free-energies use a standard state of an ideal gas at a gas-phase concentration of 1 mol L⁻¹ dissolving as an ideal dilute solution at a liquid-phase concentration of 1 mol L⁻¹, but for water itself a 55.6 M standard state was employed. Thus, as it has been indicated by Cramer *et. al.*,¹⁸³ we calculated the free-energy change associated with moving from a standard-state gas-phase pressure

of 1 atm to a standard-state gas-phase concentration of 1 M (55.6 M for water), $\Delta G^{o/*}$. The value of $\Delta G^{o/*}$ at 298 K is 1.9 kcal·mol⁻¹ for 1 M standard state solutes and 4.3 kcal·mol⁻¹ for 55.6 M standard-state water. The total Gibbs free energy (G) was obtained by adding the previous corrections to the spin corrected electronic energy $E_{\text{spin corr.}}$:

$$G = E_{\text{spin corr.}} + E_{\text{disp}} + G_{\text{corr.}} + G_{\text{solv.}} + \Delta G^{o/*} \quad (27)$$

All energies given in this chapter are referred to Gibbs energies G , unless otherwise noted. Since the lowest energy spin state for transition-metal complexes is not obvious, at least two spin states for each species were calculated and the respective geometries were optimized. The nature of the stationary points was established by frequency calculations in solvent-phase, where minima have no imaginary frequencies and transition states have one and only one. Finally, the connectivity of all transition states was confirmed by relaxing the transition state geometries towards both the reactants and the products through intrinsic reaction coordinate (IRC) calculations.

The methodology used herein, B3LYP-D₂/cc-pVTZ//B3LYP/6-31G* including solvent (SMD) and Gibbs corrections, has been previously benchmarked and shown notable experimental agreement.^{198,199} Although the use of more accurate theoretical methods (CASSCF/CASPT2) may be desirable for a better description of the electronic structure, the excellent agreement between theoretical and experimental data (see below) indicates that this approach leads to a good compromise between accuracy and computational cost. The minimum energy spin-crossing points (MECPs) between potential energy surfaces of different spin states is not likely to have a relevant role on the determination of the total Gibbs energy barriers. Consequently, we have assumed that the spin-crossing as instantaneous and therefore the MECPs have not been computed.

Standard one electron reduction potentials and PCET events were calculated using Eq. 20-21 at pH 1, relative to the standard hydrogen electrode (SHE), The employed free-energy change associated with the reduction of a proton in the SHE (ΔG_{SHE}^o) is -4.28 eV.²⁰⁰ Some oxidation events are characterized by proton-coupled electron transfer (PCET), in which electron transfer and proton transfer to the solvent occur simultaneously.

Labels **I**, **II**, **III**, **IV** and **TS** are used as short nomenclature of the successive intermediates and transition states involved in the O-O bond-formation event by complexes **1**, **2**, **3** and **4**, respectively, and **Fe^{IV}=O** for the resting state. Besides, subscripts **d**, **q**, **t**, **quint** and **sext** are used to specify the doublet, quadruplet, triplet, quintuplet and sextuplet spin state of the metal center in the previous structures, and the **·H₂O** label is related to the number of water molecules composing the first solvation shell. Finally, the labels **-OH₂** and **-OH** are used when an aqua or hydroxo ligand are present in the *trans* relative position to the oxo group for complex **3** (see Supporting Information of ref. 201).

Spectroscopic monitoring of catalytic water oxidation reactions mediated by **1** showed that $[\text{Fe}^{\text{IV}}(\text{O})(\text{OH}_2)(\text{Pytacn})]^{2+}$ can be best described as the resting state of the catalytic cycle.⁴⁶ Indeed, $[\text{Fe}^{\text{IV}}(\text{O})(\text{OH}_2)(\text{Pytacn})]^{2+}$ (**1Fe^{IV}=O**) is generated in water by reaction of **1** with 2.8 equivalents of cerium ammonium nitrate (CAN) at pH 1, and has a long half-life (around 2.4 hours). Furthermore, no oxygen was detected during its eventual decay. In contrast, significant amounts of O₂ were generated at relatively fast rates when an excess of CAN was added to a previously generated $[\text{Fe}^{\text{IV}}(\text{O})(\text{OH}_2)(\text{Pytacn})]^{2+}$ solution. This strongly suggests that the formation of the O-O bond may take place through a higher oxidation state of the iron centre such as in $[\text{Fe}^{\text{V}}(\text{O})(\text{OH}_2)(\text{Pytacn})]^{3+}$ or $[\text{Fe}^{\text{V}}(\text{O})(\text{OH})(\text{Pytacn})]^{2+}$ species.

As a first step to unravel the WO mechanism catalysed by **1-4**, we evaluated the pK_a and reduction potential for the different hydroxo/water acid-base and $Fe^{IV/V}$ redox couple respective transformations. This analysis allowed us to determine which dominant species are in solution under the catalytic conditions. Before evaluating these thermodynamic parameters, we had examined the relative energies of all possible spin multiplicities for the iron species in oxidation states IV/V, to identify the ground spin state in each case (See Table S1, see Supporting Information ref. 201). For $Fe^{IV}(O)(OH_2)$ complexes **1** and **2** the decoordination of a water molecule *cis* to the oxo group is endergonic ($[Fe^{IV}(O)(OH_2)(Pytacn)]^{2+}$: $\Delta G = 0.6 \text{ kcal}\cdot\text{mol}^{-1}$; $[Fe^{IV}(O)(OH_2)(mep)]^{2+}$: $\Delta G = 1.1 \text{ kcal}\cdot\text{mol}^{-1}$). On the contrary, for complex **3** the free energy associated with decoordination of the aqua ligand in $[Fe^{IV}(O)(OH_2)(tmc)]^{2+}$ ($\Delta G = -2.0 \text{ kcal}\cdot\text{mol}^{-1}$) clearly indicates that the most stable configuration presents an open vacant site *trans* to the oxo group. Indeed, the pK_a value of $[Fe^{IV}(O)(OH_2)(tmc)]^{2+}$ species is 10.4, therefore this intermediate under catalytic conditions cannot evolve to the hexacoordinate complex $[Fe^{IV}(O)(OH)(tmc)]^{2+}$ in which hydroxide ligand strongly bind the Fe^{IV} center. Thus, for **3** and also for pentadentate complex **4**, which has a unique coordination position not occupied by the ligand, only the $Fe^{IV/V}$ redox couple was calculated.

A summary of the results can be found in Table 1. The effect of the first solvation shell of H_2O molecules was explored asserting that the inclusion of one explicit water molecule was enough to obtain reliable standard redox potential values (Table S2, see Supporting information). The pK_a values for $[Fe^{IV}(O)(OH_2)L^{N4}]^{2+}$ ($L^{N4} = Pytacn$ and *mep*) indicate that their deprotonation may be achieved at accessible pH values (ca. 6) in water, although at pH = 1 (i.e. catalytic conditions) the deprotonation is negligible. As expected, the species $[Fe^V(O)(OH_2)L^{N4}]^{3+}$ is far more acidic than $[Fe^{IV}(O)(OH_2)L^{N4}]^{2+}$. But more interestingly, in complexes **1** and **2** the pK_a for $[Fe^V(O)(OH_2)L^{N4}]^{3+}$ are largely negative (-4.7 and -6.8, respectively).

Table 1: Redox potentials E° , $E_{1/2}(\text{PCET})$ and pK_a values of the thermodynamic cycle involving Fe^{IV}/Fe^V transformations.^a

Complexes	pK_{a1}^b	pK_{a2}^b	$E_1^\circ{}^c$	$E_2^\circ{}^c$	$E_3^\circ{}^c$
1	7.3	-4.7	2.04	1.33	1.70 ^d
2	6.3	-6.8	2.19	1.42	1.73 ^d
3	-	-	2.07 ^e	-	-
4	-	-	2.17 ^e	-	-

[a] All values were calculated using the ground-state energy of the complexes with one water molecule H bonded to oxygen moieties. [b] Values have been calculated at $T = 298.15 \text{ K}$ and atmospheric pressure. [c] Values correspond to the standard redox potentials relative to SHE electrode and $E_{1/2}(\text{PCET})$ values are the proton coupled electron transfer redox potentials at pH 1. [d] Values correspond to the $Fe^{IV}(O)(OH_2)/Fe^V(O)(OH)$ redox couple. [e] Values correspond to the $Fe^{IV}(O)/Fe^V(O)$ redox couple.

Under the catalytic conditions the Fe^V species may be formed if the redox potential of the Fe^{IV}/Fe^V process allows its oxidation by Ce^{IV} . The Ce^{IV}/Ce^{III} half reaction has a reduction potential of 1.72 V at pH 1,^{67,202} compared to normal hydrogen electrode (NHE). In the catalytic experiments

and kinetic studies a large excess of Ce^{IV} with respect to Ce^{III} is always present. Usually, more than the 85% of the initial cerium stays as Ce^{IV} at the end of the reaction. Next, we can estimate that the effective redox potential for the $\text{Ce}^{\text{IV}}/\text{Ce}^{\text{III}}$ couple under experimental conditions ($\text{pH} = 1$), taking into consideration the Nernst equation, ranges between 1.60 V and 1.75 V. Thus, the amount of Fe^{V} in solution will be determined by the oxidation potential of the complex $[\text{Fe}^{\text{IV}}(\text{O})(\text{OH}_2)(\text{Pytacn})]^{2+}$ and the effective oxidation potential of the Ce^{IV} according to the Nernst equation. The oxidation redox potentials of $[\text{Fe}^{\text{IV}}(\text{O})(\text{OH}_2)(\text{Pytacn})]^{2+}$ and $[\text{Fe}^{\text{IV}}(\text{O})(\text{OH}_2)(\text{mep})]^{2+}$ corresponding to simple $1e^-$ oxidation have remarkable high values (2.04 V and 2.19 V respectively), far from that attainable with Ce^{IV} under our experimental conditions (Table 1). However, corresponding Fe^{V} species ($[\text{Fe}^{\text{V}}(\text{O})(\text{OH})(\text{L}^{\text{N}4})]^{2+}$ ($\text{L}^{\text{N}4} = \text{Pytacn}, \text{mep}$) may still evolve from $[\text{Fe}^{\text{IV}}(\text{O})(\text{OH}_2)(\text{L}^{\text{N}4})]^{2+}$ through a proton coupled electron transfer, because in this case the PCET oxidation potentials for $[\text{Fe}^{\text{IV}}(\text{O})(\text{OH}_2)(\text{Pytacn})]^{2+}$ and $[\text{Fe}^{\text{IV}}(\text{O})(\text{OH}_2)(\text{mep})]^{2+}$ are 1.70 V and 1.73 V, respectively. On the contrary, the redox potential for the direct oxidation of $[\text{Fe}^{\text{IV}}(\text{O})(\text{tmc})]^{2+}$ and $[\text{Fe}^{\text{IV}}(\text{O})(\text{MePy}_2\text{CH-tacn})]^{2+}$ are 2.07 V and 2.17 V, respectively, which are clearly too demanding to be reached under catalytic conditions.

4.2.1 O-O bond formation reaction pathway

As explained above, $[\text{Fe}^{\text{IV}}(\text{O})(\text{OH}_2)\text{L}^{\text{N}4}]^{2+}$ is not involved in the O-O bond formation and the redox potentials are indicative of the accessibility of Fe^{V} species for complexes **1** and **2**. On the bases of the computed pK_a values it could be deduced that $[\text{Fe}^{\text{V}}(\text{O})(\text{OH})\text{L}^{\text{N}4}]^{2+}$ are accessible species in catalytic conditions. Then, we examined the attack of a water molecule to $[\text{Fe}^{\text{V}}(\text{O})(\text{OH})\text{L}^{\text{N}4}]^{2+}$ species for **1** and **2**. Additionally for comparison reasons, the O-O bond-formation mechanism has been also studied for complexes **3** and **4** (Figures 75, 76, 77, 78 and 79).

4.2.1.1 O-O bond formation for cis-site complexes **1** and **2**

The O-O bond-formation mechanism operating for complex **1** has been previously described,⁶⁹ but herein we further refine the energy values with the introduction of dispersion corrections through the D₂-Grimme. As in the previous publication, we considered that in $[\text{Fe}^{\text{V}}(\text{O})(\text{OH})\text{L}^{\text{N}4}]^{2+}$ the hydroxide ligand, *cis* to the oxo group, may act as a base in the WO process, activating the water molecule and aiding in the O-O bond formation. The effect of an internal base on the performance of the O-O bond formation event has been previously described in the case of iridium complexes.^{37-38b}

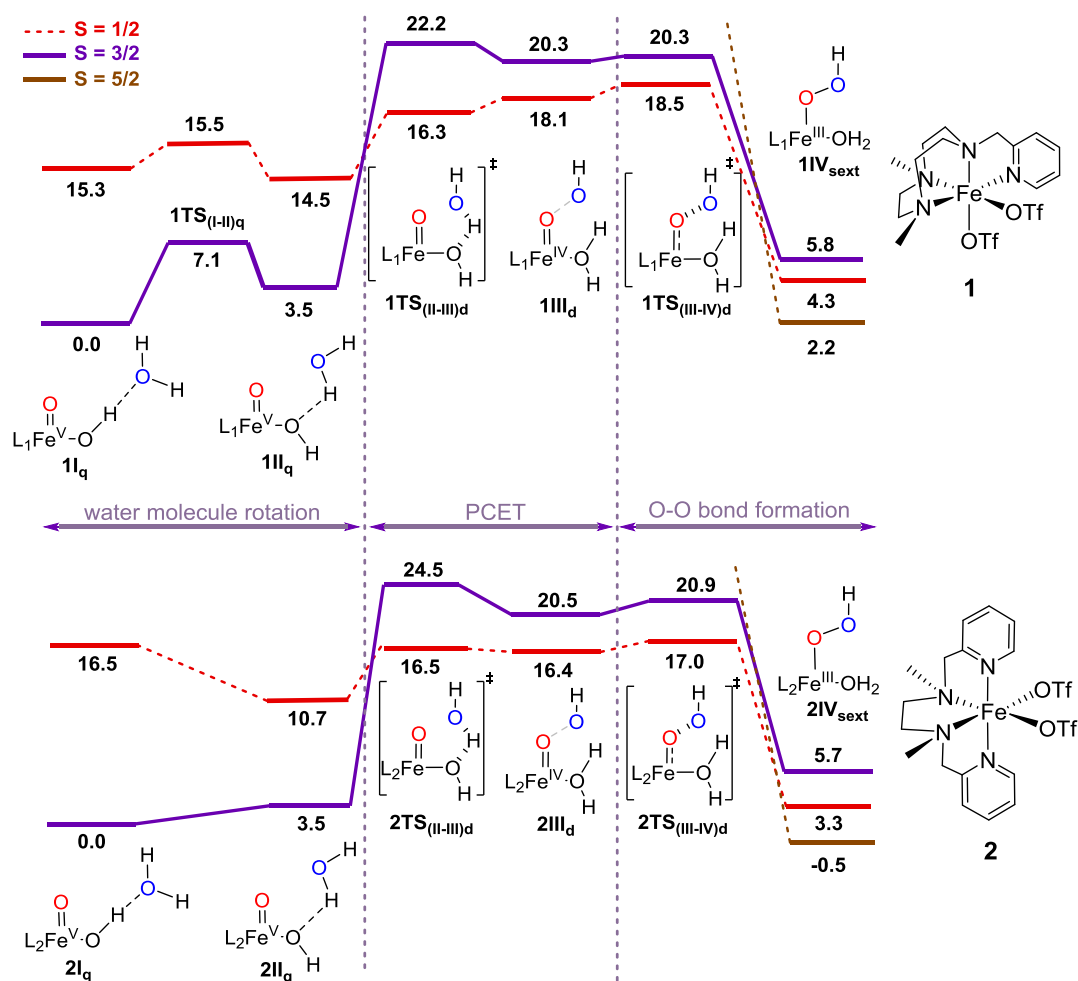
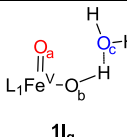
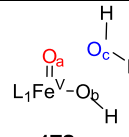
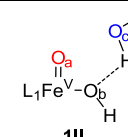
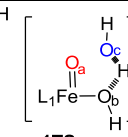
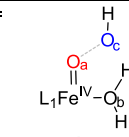
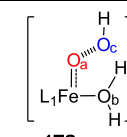
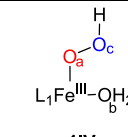


Figure 75: Energy profile for O-O bond formation with complexes **1** and **2**. Values indicate solvent state Gibbs energies corrected with a D2-Grimme dispersion model ($\text{kcal}\cdot\text{mol}^{-1}$). The subscripts d and q represent spin states of $S = 1/2$ and $S = 3/2$, respectively. The ground state $S = 5/2$ Fe^{III} hydroperoxo intermediate energies are also included.

Table 2: Mulliken atomic spin populations, Fe-O_a and O_a-O_c bond distances for key species involved in the O-O bond formation mechanism for complex **1**.

							
$\rho(\text{Fe})^{\text{a}}$	2.10	2.33	2.11	1.61	1.48	1.41	4.26
$\rho(\text{O}_a)^{\text{a}}$	0.79	0.77	0.86	0.04	0.30	0.30	0.23
$\rho(\text{O}_b)^{\text{a}}$	0.22	0.05	0.18	-0.02	-0.01	-0.01	0.06
$\rho(\text{O}_c)^{\text{a}}$	0.01	0.01	0.01	-0.53	-0.67	-0.61	0.03
$d(\text{Fe}-\text{O}_a)^{\text{b}}$	1.64	1.66	1.64	1.65	1.64	1.65	1.85
$d(\text{O}_a-\text{O}_c)^{\text{b}}$	2.91	2.87	3.23	2.06	2.04	1.95	1.94

[a] All values are calculated at the B3LYP(SMD)/6-31G* level in water as solvent. [b] Bond distances in Å.

The Gibbs free reaction profiles for the O-O bond-formation mechanism for complexes **1** and **2** are shown in Figure 75. The high oxidation state complex $[\text{Fe}^{\text{V}}(\text{O})(\text{OH})\text{L}^{\text{N}4}]^{2+}$ and the hydroperoxo iron complex $[\text{Fe}^{\text{III}}(\text{OOH})(\text{OH}_2)\text{L}^{\text{N}4}]^{2+}$ (IV_{sext} , subscript sext represent spin state of $S = 5/2$) are

connected thought a stepwise mechanism that formally involves three different types of transitions states (TS), $\text{TS}_{(\text{I-II})q}$, $\text{TS}_{(\text{II-III})d}$ and $\text{TS}_{(\text{III-IV})d}$ (subscripts d and q represent spin states $S = 1/2$ and $S = 3/2$, respectively) through two intermediates II_q and III_d . The transformation of I_q to IV_{sext} is in both *cis*-site complexes thermoneutral (i.e. $\Delta G = 2.2 \text{ kcal}\cdot\text{mol}^{-1}$ and $\Delta G = -0.5 \text{ kcal}\cdot\text{mol}^{-1}$ for **1** and **2**, respectively). The starting II_q and 2II_q complexes include the interaction of $[\text{Fe}^{\text{V}}(\text{O})(\text{OH})\text{L}^{\text{N4}}]^{2+}$ with a water molecule through a hydrogen bond between the H of the hydroxyl ligand and the oxygen of the water molecule. The first TS towards the O-O bond formation, which is the lowest in energy ($\text{1TS}_{(\text{I-II})q}$: $\Delta G^\ddagger = 7.1 \text{ kcal}\cdot\text{mol}^{-1}$ versus I_q ; Figure S1, see Supporting Information of ref. 201) involves only the rotation of the water molecule leading to II_q , in which the hydrogen bond comprises the H of the water molecule and the O of the hydroxyl ligand (Figure 75). At this point the water molecule is located in a suitable disposition to react with the iron oxo unit.

The population analysis of the reactant species III_q reveals significant spin density located on the oxo ligand ($\rho(\text{O}_a) = 0.77$) and about two unpaired electrons on the iron atom ($\rho(\text{Fe}) = 2.33$; Table 2). This electronic structure has been previously associated to a high spin $\text{Fe}^{\text{V}}=\text{O}$ moiety, in which one electron is mainly localized on the iron center and the other two unpaired electrons occupy two degenerate π^* FeO orbitals.⁷⁷ The positive spin density at the oxo group could be also involved with the existence of an oxyl intermediate ($\text{Fe}^{\text{IV}}-\text{O}^\cdot$). However, the short Fe-O bond distance (1.63 Å) of $[\text{Fe}^{\text{V}}(\text{O})(\text{OH})(\text{Pytacn})]^{2+}$ complex, very similar to $\text{Fe}^{\text{IV}}=\text{O}$ bond (1.64 Å), corresponds to the existence of a double bond between the iron and the oxo group. The $\text{Fe}^{\text{IV}}-\text{O}^\cdot$ electronic state should have a longer Fe-O bond distance. Therefore, the $\text{Fe}^{\text{V}}=\text{O}$ model can be envisaged as valid description for the electronic structure of the $[\text{Fe}^{\text{V}}(\text{O})(\text{OH})(\text{Pytacn})]^{2+}$ complex.

After a spin-crossing the second TS is found, ($\text{1TS}_{(\text{II-III})d}$: $\Delta G^\ddagger = 16.3 \text{ kcal}\cdot\text{mol}^{-1}$ and $\text{2TS}_{(\text{II-III})d}$: $\Delta G^\ddagger = 16.5 \text{ kcal}\cdot\text{mol}^{-1}$; Figure S2, see Supporting information of ref. 201) and involves a PCET from the water molecule yielding a high energy III_d intermediate (III_d : $\Delta G^\ddagger = 18.1 \text{ kcal}\cdot\text{mol}^{-1}$ and 2III_d : $\Delta G^\ddagger = 16.4 \text{ kcal}\cdot\text{mol}^{-1}$; IRC depicted in Figures S3 and S4, see Supporting information of ref. 201).²⁰³ The spin-forbidden transition between the quartet and the doublet state should be favored by the large spin-orbit coupling at the iron center, and it has been previously reported for the O-O bond cleavage mechanism of $[\text{Fe}^{\text{III}}(\text{OOH})(\text{H}_2\text{O})(\text{TPA})]^{2+}$, TPA = tris-(2-methylpyridil)amine.²⁰⁴ In III_d the proton has been completely transferred forming a second water molecule. Interestingly, the Mulliken population spin density analysis of the $\{\text{Fe}(\text{O})(\text{OH}_2)\}$ moiety of III_d shows a value around 2 for the fragment (Table 2). This analysis implies a description of the iron center as $S = 1$ and an oxidation state of IV. A closer look at the spin density on the iron center ($\rho(\text{Fe}) = 1.48$) and the oxygen atom belonging to the water molecule ($\rho(\text{O}_c) = -0.67$) clearly shows that there is an antiferromagnetic coupling between the $\{\text{Fe}(\text{O})(\text{OH}_2)\}$ and the O_cH fragments. This could be explained by an electron transfer from the former water molecule to the $\{\text{Fe}(\text{O})(\text{OH}_2)\}$ moiety leading to a formal Fe^{IV} center.

The intermediate III_d connects with the hydroperoxo Fe^{III} complex IV_d via $\text{TS}_{(\text{III-IV})d}$ in which the O-O bond is formed ($\text{1TS}_{(\text{III-IV})d}$: $\Delta G^\ddagger = 18.5 \text{ kcal}\cdot\text{mol}^{-1}$ and $\text{2TS}_{(\text{III-IV})d}$: $\Delta G^\ddagger = 17.0 \text{ kcal}\cdot\text{mol}^{-1}$, Figure S5, see Supporting Information of ref. 201). For both catalysts, the $\text{TS}_{(\text{III-IV})d}$ is slightly but significantly higher in energy than $\text{TS}_{(\text{II-III})d}$, and then constitutes the TDTS (Figure 75). Overall in both systems, the energy profile from $\text{TS}_{(\text{II-III})d}$ to $\text{TS}_{(\text{III-IV})d}$ is quite flat, which suggests that rather than a two-step mechanism, the reaction may be also viewed to take place through a highly asynchronous concerted process. Indeed, subtle geometrical changes on complex **1** may lead to significant changes on the potential energy surface of the reaction, modifying the degree of asynchronicity of the O-O bond formation event (Figure S10 and S11, see Supporting Information of ref. 201).

It is known that the B3LYP functional over-stabilizes the high spin states over the lower ones. Even so, intermediates involving $\text{TS}_{(\text{II-III})} \rightarrow \text{IV}$ in $S = 3/2$ spin state are slightly higher in energy than the corresponding in $S = 1/2$. The $S = 5/2$ spin state energy profile was also explored and the energy barriers ($\Delta G^\ddagger > 30 \text{ kcal}\cdot\text{mol}^{-1}$) are clearly too high in energy to be directly involved in the reaction pathway. Therefore, the $S = 1/2$ spin state is preferred for the O-O bond formation. Nevertheless, the $S = 5/2$ spin state was found to be the ground state for the hydroperoxo Fe^{III} complexes (IV_{sext}). Although free energy differences between $\text{TS}_{(\text{II-III})\text{d}}$ and $\text{TS}_{(\text{III-IV})\text{d}}$ are below the average error of our theoretical approach, they have clear connections with the experimental kinetic studies.^{68,69} First, the calculated KIE for O-O bond formation $1\text{TS}_{(\text{III-IV})\text{d}}$ is 0.98, in excellent agreement with the experimental KIE = 1 value obtained at high oxidant (CAN) concentration. The TOF-determining transition state $2\text{TS}_{(\text{III-IV})\text{d}}$, with the proton completely transferred, is also consistent with the inexistence of experimental KIE for complex **2**. Moreover, the energy for the TDTS is lower for **2** than for **1**, reproducing the experimentally observed reactivity trend.

While complex **2** is C_2 symmetric, complex **1** has two possible tautomeric forms related by the exchange of the *cis*-(O)(OH) groups. Both isomers could be involved in the WO reaction and were consequently explored. The previous discussed form of **1** has the oxo moiety perpendicular to the pyridine ring (**1**), while the other tautomer presents a parallel oxo respect to the pyridine group (**1b**). Taking into consideration that complexes **1** and **1b** have a very similar DFT free energy ($\Delta G = 0.2 \text{ kcal}\cdot\text{mol}^{-1}$) and previous studies showed that this isomerization have associated low energy barriers²⁰⁵ both isomers could exist in solution. The free energy profiles for both tautomers are very similar (See Figure S10 and S11 and Table S3, see Supporting Information of ref. 201) but, from a computational point of view, the reaction could evolve through two possible mechanisms with different degrees of asynchronicity in the O-O bond formation event. Free energy profile of **1b** suggests a larger deuterium KIE than the experimentally observed, since the TDTS is determined by a proton transfer TS. Instead, there is an excellent agreement between the experimental KIE and DFT KIE obtained from **1** free energy profile (see discussion above). Therefore, the two-step mechanism must to be considered for complexes **1** and **2** since it reproduces the kinetic data. Thus, we selected tautomer **1** for the full catalytic cycle study.

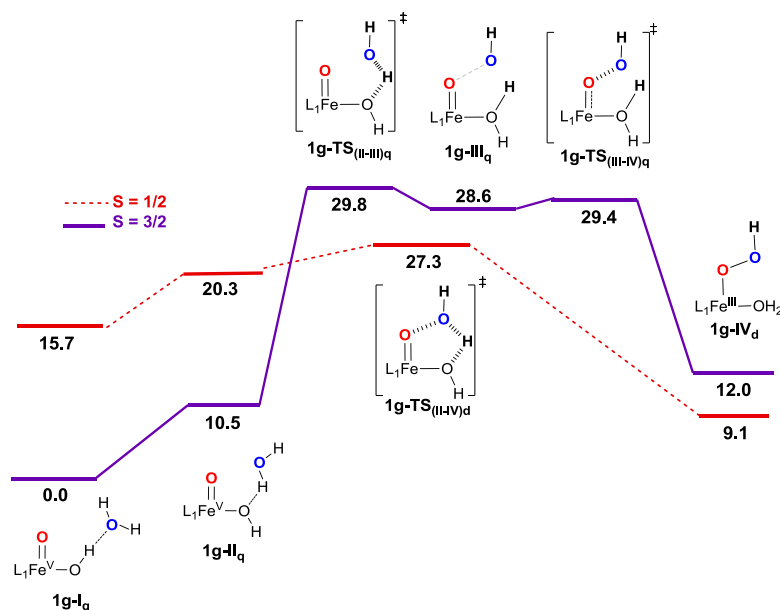


Figure 76: Doublet and quadruplet spin state surfaces of complex **1** in gas phase. Values indicate Gibbs energies corrected with a D2-Grimme dispersion model ($\text{kcal}\cdot\text{mol}^{-1}$). The subscripts d and q represent spin states of $S = 1/2$ and $S = 3/2$, respectively. L_1 is the Pytacn ligand.

Finally, to rationalize the effect of the implicit water solvent on the asynchronous behavior of the O-O bond formation reaction, the mechanism on complex **1** was also explored in gas phase (Figure 76). The spin state energy surfaces found by DFT calculations show that the Fe^V-water complex (**1g-I_d**) and the hydroperoxo iron product (**1g-IV_d**; $\Delta G = 9.1 \text{ kcal}\cdot\text{mol}^{-1}$) are connected through a synchronous mechanism that involves an energetically unreachable concerted transition state **1g-TS_{(II-IV)_d}** ($\Delta G^\ddagger = 27.3 \text{ kcal}\cdot\text{mol}^{-1}$), in which the proton transfer to the hydroxo ligand and the O-O bond formation occurs simultaneously. In contrast, in the quadruplet spin state surface the reaction follows the previously observed stepwise mechanism with two different transition states **1g-TS_{(II-III)_q}** and **1g-TS_{(III-IV)_q}**. The comparison between the solvent and gas phase free energy profiles reveal that the introduction of the solvent effects favors the decoupling between the PCET and the O-O bond formation transition states, stabilizing the [Fe^{IV}(O)(OH₂)]-radical OH intermediate (labeled as **III_d**, see above) and leading to a different description of the reaction. Therefore, the stepwise or concerted character of the O-O bond formation may be affected also by the electrostatic perturbations imposed by the dielectric medium on the electronic structure of the iron complex.

4.2.1.2 *cis*-OH ligand-assisted- versus external-water attack in the Fe^V=O mechanism

The hydroxyl ligand in complexes **1** and **2** can act as an internal base by pulling the proton of the water molecule and thus favor the nucleophilic attack of the water molecule to the Fe^V=O fragment. This was confirmed by studying the O-O bond formation mechanism in the case of an external nucleophilic attack of a water molecule to the electrophilic Fe^V=O group (see Supporting Information ref. 201, Figure S6). In the external-water attack mechanism by the most stable isomer **1b**, the proton transfer is assisted by a cluster of three water molecules instead of the *cis*-OH ligand. For complex **1**, this mechanism exhibits an increase of $7.4 \text{ kcal}\cdot\text{mol}^{-1}$ in the free energy barrier with respect to *cis*-OH ligand-assisted water-attack barrier, while for **1b** exhibits an increase of $8.7 \text{ kcal}\cdot\text{mol}^{-1}$ (Figure 77). In addition, as expected the formation of the [Fe^{III}(OOH)(OH)(Pytacn)]⁺ intermediate becomes also much more endergonic ($\Delta G = 11.2 \text{ kcal}\cdot\text{mol}^{-1}$) than in the *cis*-OH ligand-assisted mechanism found for **1** or **2**. Therefore, the Brønsted base activity together with the appropriate geometrical *cis* disposition of the hydroxyl group with respect to the oxo ligand moiety in complex **1** suppose a notorious energy reduction cost for the O-O bond-formation step.

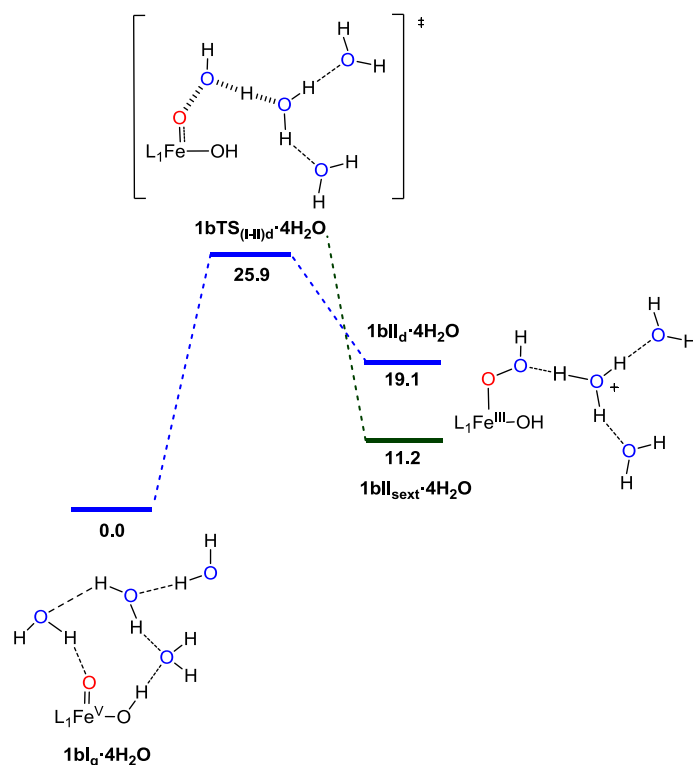


Figure 77: Free energy profile of O-O bond formation event for complex **1b** in solvent phase when the proton transfer is assisted by an external cluster of three water molecule. Values indicate Gibbs energies ($\text{kcal}\cdot\text{mol}^{-1}$). L_1 represents the Pytacn ligand.

4.2.1.3 O-O bond formation mechanism for complex **3**

Despite that the oxidations of $[\text{Fe}^{\text{IV}}(\text{O})(\text{tmc})]^{2+}$ and $[\text{Fe}^{\text{IV}}(\text{O})(^{\text{Me}}\text{Py}_2\text{CH-tacn})]^{2+}$ to their corresponding Fe^{V} species have excessively high DFT redox potentials (2.07 V ad 2.17 V, respectively), we analyzed the O-O bond-formation mechanism in these putative Fe^{V} complexes (**3** and **4**). Different circumstances have to be considered to explore the capacity of complex **3** in the O-O bond formation. First, the two labile sites are located *trans* to each other. In addition, the most stable $\text{Fe}^{\text{V}}(\text{O})$ species in catalytic conditions is the oxo-complex $[\text{Fe}^{\text{V}}(\text{O})(\text{tmc})]^{3+}$ with an open vacant site. In contrast to complexes **1** and **2**, the complex **3** has no anionic group that could act as a base and therefore the benefit from the presence of an internal base assisting the attack of the water molecule to the oxo group is not present. Therefore, in order to compare **3** with **1** and **2** under the closest conditions, at least three more solvent water molecules have to be considered in assisting the proton transfer step.^{27,62,196-197} Therefore, a cluster of three water molecules were explicitly introduced for suitable solvation of the generated proton in the reaction. Furthermore, we also evaluated the feasibility of the O-O bond formation step for $[\text{Fe}^{\text{V}}(\text{O})(\text{tmc})(\text{L})]^{3+}$ (L stands for none, H_2O and OH ligands *trans* to the oxo group) species considering in addition the role of the water in *trans* to the oxo group.

The Gibbs free energy profile for the O-O bond formation reaction of complex **3** for $S = 1/2$ and $3/2$ spin states is presented in Figure 78. The $\text{Fe}^{\text{V}}(\text{O})$ complex **3I**· $4\text{H}_2\text{O}$ present the $S = 3/2$ spin state as the most stable, although $S = 1/2$ can be energetically accessible and should to be considered as well. **3I**_q· $4\text{H}_2\text{O}$, presents hydrogen bonds between the four water molecules (Figure 78). All attempts directed to obtain the two step mechanism reaction pathway as in complexes **1** and **2** fail, which is in agreement with a previous study done by the groups of Morokuma, Que and co-

workers.²⁰⁶ For $S = 1/2$, $3/2$ and $5/2$ spin states, we found a single transition state for the formation of the hydroperoxo iron complex $3\text{III}\cdot 4\text{H}_2\text{O}$ from the 3II ($\text{Fe}^{\text{V}}=\text{O}$) species. The energy surface $S = 1/2$ presents a slightly lower energy transition state ($3\text{TTS}_{(\text{II-III})\text{d}}\cdot 4\text{H}_2\text{O}$, $\Delta G^\ddagger = 17.9 \text{ kcal}\cdot\text{mol}^{-1}$; Figure S7, see Supporting Information of ref. 201) than the $S = 3/2$ energy surface ($3\text{TTS}_{(\text{II-III})\text{q}}\cdot 4\text{H}_2\text{O}$, $\Delta G^\ddagger = 19.0 \text{ kcal}\cdot\text{mol}^{-1}$), although the starting product 3I_d is $14.5 \text{ kcal}\cdot\text{mol}^{-1}$ higher in energy than 3I_q . The $S = 5/2$ TS, $3\text{TTS}_{(\text{II-III})\text{sext}}\cdot 4\text{H}_2\text{O}$, is too high in energy to play a role in the reactivity. $S = 1/2$ and $S = 3/2$ O-O bond-formation pathways are equivalent. First, the water cluster moves and disposes in such a way that facilitates the interaction between the O atom of the nucleophilic water molecule and the oxo group to form the O-O bond.

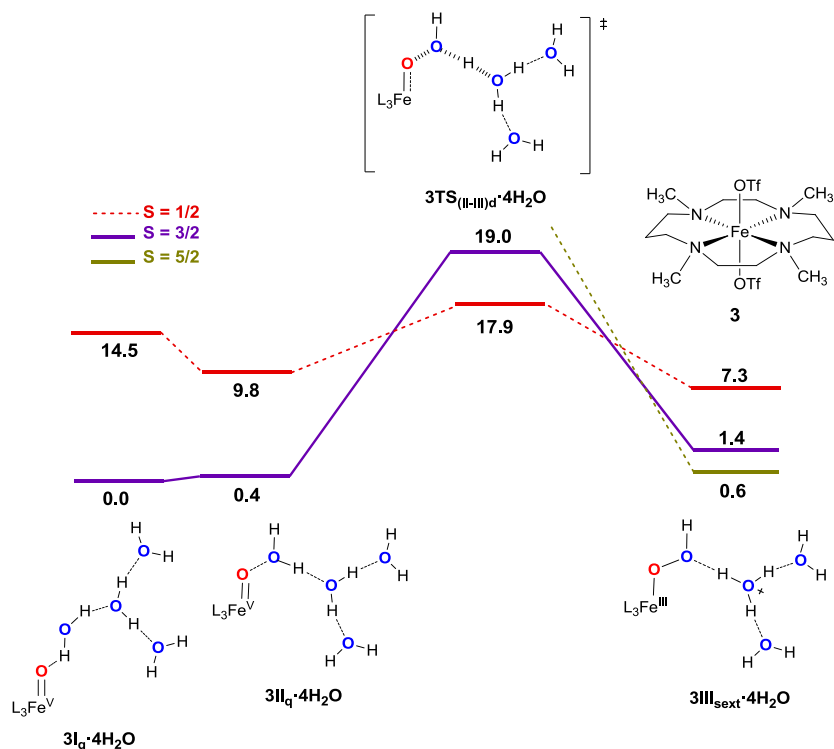


Figure 78: Solvent phase mechanisms for the assisted O-O bond formation performed by $[\text{Fe}^{\text{V}}(\text{O})(\text{tmc})]^{3+}$ species, generated from complex **3**. Values indicate Gibbs energies ($\text{kcal}\cdot\text{mol}^{-1}$). L_3 represents the tmc ligand. The ground state $S = 5/2$ Fe^{III} hydroperoxo intermediate is also included.

molecule to the $\text{Fe}^{\text{V}}=\text{O}$ center. Thus, the proton transfer is also for **4** modelled with four explicit water molecules. The corresponding Gibbs free-energy profile is showed in Figure 79.

Optimization of the $[\text{Fe}^{\text{V}}(\text{O})(^{\text{Me}}\text{Py}_2\text{CH-tacn})]^{2+}$ species in the presence of four water molecules yields a distorted octahedral iron complex, **4I**·**4H₂O**. In contrast with **3I**·**4H₂O**, the oxo moiety of the most stable Fe^{V} conformer **4I**·**4H₂O** interacts with a tetrahedral cluster of water molecules. Reaction is initiated by water molecule reorientation. A water molecule H-bonded to the oxo ligand disposes in such a way that the oxygen atoms of the oxo ligand and of the water molecule are located in an ideal spatial disposition to form the O-O bond (**4II_d**·**4H₂O**: $\Delta G = 1.1 \text{ kcal}\cdot\text{mol}^{-1}$). The energy profile connects the reactant complex **4II_d**·**4H₂O** with the Fe^{III} hydroperoxo complex **4III_{sext}**·**4H₂O** ($\Delta G = -8.4 \text{ kcal mol}^{-1}$) through transition state **4TS_{(II-III_d)}}**·**4H₂O** ($\Delta G^\ddagger = 4.0 \text{ kcal}\cdot\text{mol}^{-1}$; Figure S8, see Supporting Information of ref. 201), which involves a concerted O-O bond formation and proton transfer (Figure 79). Interestingly, the Gibbs energy for the O-O bond formation is much smaller than the one obtained for the previous complexes. This low energy barrier is also reproduced when the energy profile is evaluated with only two water molecules (Figure S15, see Supporting Information of ref. 201).

The low energy barrier associated to O-O bond formation suggests that an external attack of a water molecule would be favorable if complex **4** could access the $\text{Fe}^{\text{V}}(\text{O})$ oxidation state. Therefore, in the absence of an anion in the coordination sphere of the complex, the pentadentate ligand is unable to stabilize the high oxidation state of the iron atom, but this coordination environment simultaneously makes the $\text{Fe}^{\text{V}}(\text{O})$ moiety highly reactive towards O-O bond formation. In conclusion, the computational analyses indicate that an efficient iron WOC should present an energetic balance between the redox potential connecting the Fe^{V} and Fe^{IV} species, and the reactivity of the $\text{Fe}^{\text{V}}(\text{O})$ state in the O-O bond-formation reaction.

4.2.2 Reaction pathway for O_2 generation from the Fe^{III} -OOH species

To explore the last part of the WO catalytic cycle, we studied the molecular oxygen release path for complex **1**. A viable reaction pathway from $\text{Fe}^{\text{III}}(\text{OOH})$ to $\text{Fe}^{\text{IV}}(\text{O})(\text{OH}_2)$ and the formation of O_2 is illustrated in Figure 80a. Starting from the hydroperoxo Fe^{III} complex $[\text{Fe}^{\text{III}}(\text{OOH})(\text{OH}_2)(\text{Pytacn})]^{2+}$ **1IV_{sext}**, it is found that a subsequent PCET step generates $[\text{Fe}^{\text{III}}(\text{OO}\cdot)(\text{OH}_2)(\text{Pytacn})]^{2+}$ **1V_t** (subscript t represents the lowest energy triplet spin state) through a moderate potential of 1.11 V, which could be readily attainable by the Ce^{IV} oxidant, present in large excess. The analysis of spin density on the iron centre ($\rho(\text{Fe}) \approx 1$) and on the oxygen atoms of the former hydroperoxo group ($\rho(\text{O}_a) \approx \rho(\text{O}_b) \approx 0.5$), as well as the topology of the spin density distribution (Figure 80b) and the O-O bond distance, suggest that **1V_t** is better described as a superoxide $[\text{Fe}^{\text{III}}(\text{OO}\cdot)(\text{OH}_2)(\text{Pytacn})]^{2+}$ rather than a high valent peroxide $[\text{Fe}^{\text{IV}}(\text{O}_2)(\text{OH}_2)(\text{Pytacn})]^{2+}$. From this intermediate, the species **1V_t** can evolve through a subsequent oxidation step to form **1VI_q** species at a low potential, 0.81 V, in which the O_2 molecule is already formed, with $\rho(\text{O}_a) \approx \rho(\text{O}_b) \approx 1$. Again, oxidation occurs at the O_2 moiety rather than at the metal center. Finally, the last intermediate can undergo a O_2 displacement by a water molecule with an associated free energy of $-11.4 \text{ kcal}\cdot\text{mol}^{-1}$, leading to $[\text{Fe}^{\text{III}}(\text{OH}_2)_2(\text{Pytacn})]^{3+}$, **1VII_d** and eliminating O_2 . Complex **1VII_d** can be rapidly oxidized and deprotonated to yield $[\text{Fe}^{\text{IV}}(\text{O})(\text{OH}_2)(\text{Pytacn})]^{2+}$ at a potential of 1.56 V, completing the 4-electron catalytic cycle.

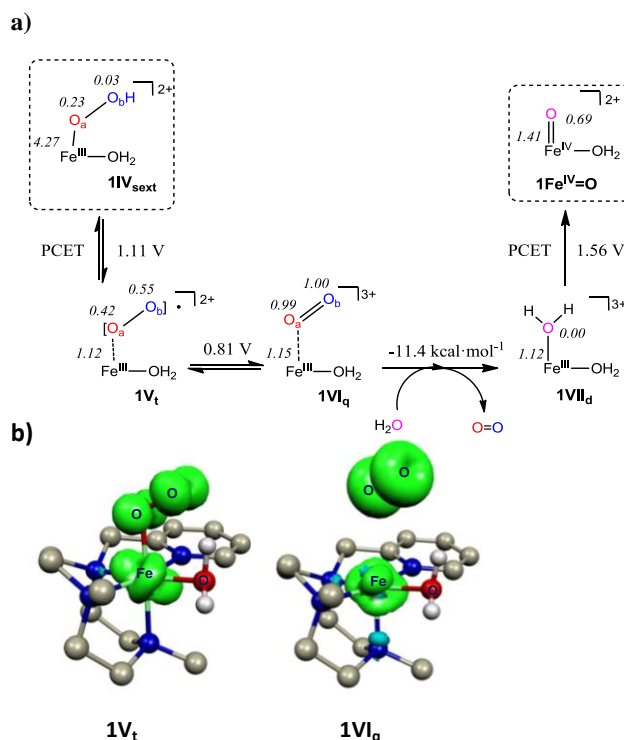


Figure 80: a) Viable O_2 generation mechanism from the $\text{Fe}^{\text{III}}(\text{OOH})$ to $\text{Fe}^{\text{IV}}(\text{O})$. Values shown in the figure indicate the Mulliken spin densities for selected atoms. All redox potentials have been calculated at $\text{pH} = 1$. b) Comparison of spin densities contours (iso-value of 0.01) of $\mathbf{1V}_t$ (left) and $\mathbf{1VI}_q$ (right) species.

Another thermodynamically feasible reaction pathway for O_2 generation was explored starting from the $\mathbf{1V}_t$ intermediate (Figure 81). By analogy with the mechanism of water oxidation proposed for ruthenium polypyridyl complexes,^{6,37} the reaction may proceed first with a water nucleophilic attack on $[\text{Fe}^{\text{III}}(\text{OO}\cdot)(\text{OH}_2)(\text{Pytacn})]^{2+}$ to generate a $[\text{Fe}^{\text{II}}(\text{OH}_2)_2(\text{Pytacn})]^{2+}$ intermediate ($\mathbf{1VIII}_{\text{quint}}$) and the molecular oxygen product ($\Delta G = -16.7 \text{ kcal}\cdot\text{mol}^{-1}$). In this reaction step, the superoxide moiety is oxidized to O_2 while the metal center reduced by one electron. Then, the intermediate $\mathbf{1VIII}_{\text{quint}}$ can be easily oxidized and deprotonated to yield $[\text{Fe}^{\text{III}}(\text{OH})(\text{OH}_2)(\text{Pytacn})]^{2+}$ species ($\mathbf{1IX}_{\text{sext}}$) at a potential of 0.80 V. Finally, $[\text{Fe}^{\text{IV}}(\text{O})(\text{OH}_2)(\text{Pytacn})]^{2+}$ species can be derived from $\mathbf{1IX}_{\text{sext}}$ by applying a substantial potential of 1.67 V. The two presented mechanistic proposals to close the catalytic cycle are thermodynamically feasible. To determine which of the two mechanism is kinetically most favorable is required the computation of the energy barriers for the O_2 displacement and PCET events. However, taking into account that the latter mechanism present the highest redox potential to achieve the $\mathbf{1Fe}^{\text{IV}}=\text{O}$ species, we have consider the former to complete the WO catalytic cycle.

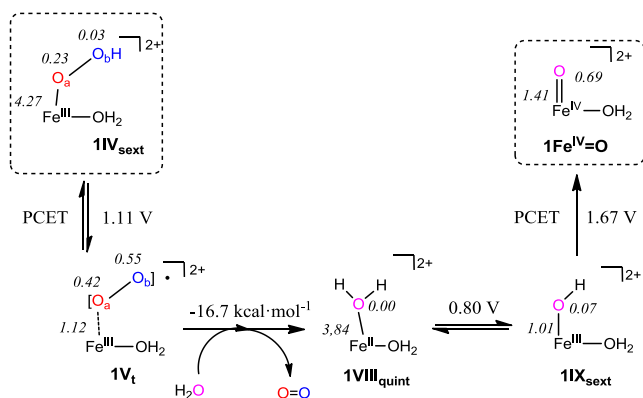


Figure 81: Second viable mechanistic proposal for the evolution from $\text{Fe}^{\text{III}}(\text{OOH})$ to $\text{Fe}^{\text{IV}}(\text{O})$ species. Values shown in the figure indicate the Mulliken spin densities for selected atoms. All redox potentials have been calculated at $\text{pH} = 1$.

4.2.3 Global catalytic cycle

In Figure 82, a complete WO catalytic cycle for complex **1** is presented, and in Figure 83 the corresponding Gibbs free energy profile is also shown, constructed taking into account the experimental driving force introduced by the Ce^{IV} . As previously noted, under catalytic conditions the large excess of Ce^{IV} produces an effective redox potential between 1.60 V and 1.75 V. Taking this in consideration, in the theoretical evaluation of the free energy profile of the complete cycle we set the $\text{Ce}^{\text{IV}}/\text{Ce}^{\text{III}}$ redox value to 1.72 V. As expected, one complete cycle is clearly exergonic ($-46.5 \text{ kcal}\cdot\text{mol}^{-1}$) and the energetically most demanding step is the O-O bond formation event.²⁰⁷ Besides, **II_q** can be reached with CAN and it is isoenergetic with the resting state **1Fe^{IV}=O·H₂O**. The value of the free energy activation barrier for the full catalytic cycle ($\Delta G^\ddagger = 18.9 \text{ kcal}\cdot\text{mol}^{-1}$ with respect to the resting state) is in agreement with the experimentally observed reactivity. The last part of the catalytic cycle, the evolution from **1IV_{sext}** to $[\text{Fe}^{\text{IV}}(\text{O})(\text{OH}_2)(\text{Pytacn})]^{2+}$, is spontaneous when using CAN as oxidant, recovering the resting state of the catalytic cycle (see Supporting Information of ref. 201, Figure S16 for the tautomer **1b** computed WO catalytic cycle).

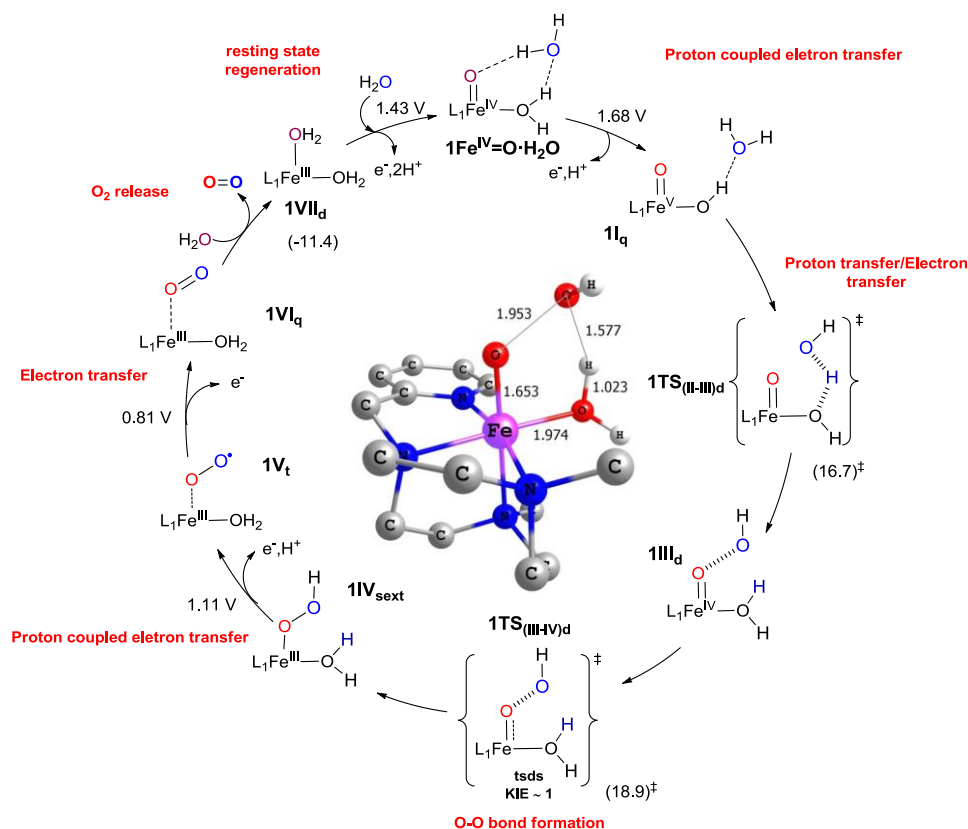


Figure 82: Computed WO catalytic cycle catalyzed by **1**. Inset: the optimized geometry for the $1\text{TS}_{(\text{III-IV})\text{d}}$ with the most relevant bond distances (\AA). Values represent redox potentials (V) and those in parenthesis report the free energies ($\text{kcal}\cdot\text{mol}^{-1}$).

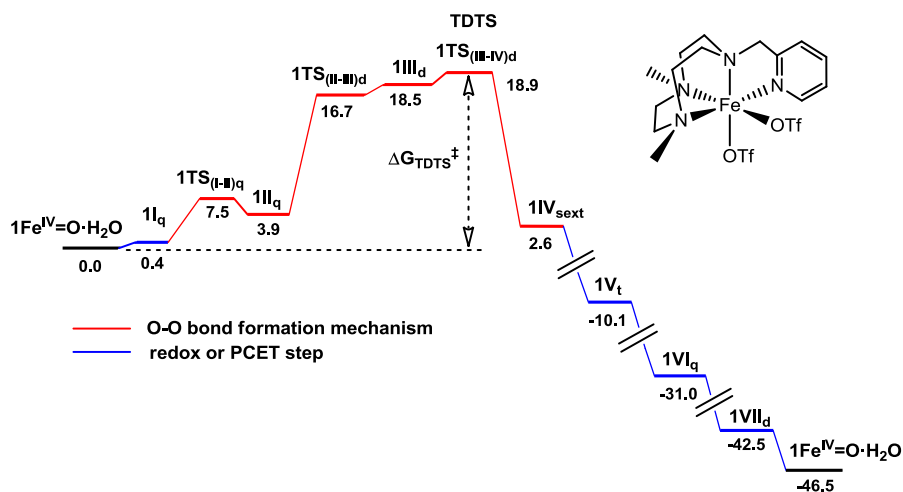


Figure 83: Free energy profile ($\text{kcal}\cdot\text{mol}^{-1}$) for water oxidation reaction by catalyst **1**. The H_2O and O_2 molecules necessary to ensure the correct energetic balance in all the steps of the catalytic cycle are included in the calculation, but are omitted in the Figure for clarity.

To provide additional confidence in our calculations, the theoretical values of the activation parameters (ΔH^\ddagger , ΔS^\ddagger and ΔG^\ddagger) at room temperature for complex **1** were compared with those determined experimentally through an Eyring equation (Table 3 and the Supporting Information of

ref. 201, Figure S17). We notice that the computationally determined values are in good agreement with the experimental activation parameters. It is important to remark that all three activation parameters ΔH^\ddagger , ΔS^\ddagger and ΔG^\ddagger are close to the experimental estimated deviation for those parameters.

Table 3: Theoretical and experimental values of the activation parameters (ΔH^\ddagger , ΔS^\ddagger and ΔG^\ddagger) for iron complex **1**.

	ΔH^\ddagger (kcal·mol ⁻¹)	ΔS^\ddagger (cal·mol ⁻¹ ·K ⁻¹)	ΔG^\ddagger (kcal·mol ⁻¹)
Theor. (Fe ^{IV}) ^a	15.2	-12.4 ^b	18.9
Exp. ^c	12.6 ± 2.0	-16.8 ± 6.9	17.6 ± 1.6

[a] Activation parameters evaluated taking **1**Fe^{IV}=O·H₂O as reference. The ΔH^\ddagger was derived from ΔG^\ddagger and ΔS^\ddagger obtained in the TDTS. [b] ΔS^\ddagger value was computed at the B3LYP(SMD)/6-31G* level, including three interacting explicit solvent water/hydronium molecules in the entropy balances. [c] Experimental activation parameters for complex **1** were obtained from Eyring analysis of k_{obs} values determined from initial rates of Ce^{IV} consumption.

In this chapter, the mechanism of water oxidation by non-heme iron complexes containing N-tetradentate ligands is elucidated. The proposed mechanism provides an explanation for the effect of ligand coordination number and mode in the water oxidation mechanism. The Fe^{IV} to Fe^V oxidation reaction and the O-O bond-formation event are the key features to define the capacity of a nonheme iron complex based on polydentate nitrogen-based ligands to oxidize the water molecule.

The results indicate that [Fe^V(O)(OH)L^{N4}]²⁺ species are easily accessible by iron catalysts **1** and **2** from [Fe^{IV}(O)(OH₂)L^{N4}]²⁺ compounds (1.70 V and 1.73 V respectively), and they constitute the active species responsible for the O-O bond formation reaction. Both **1** and **2** contain tetradentate ligands that leave two *cis*-labile sites, occupied by a hydroxyl and a terminal oxo ligands *cis* to each other. On the contrary, iron complexes **3** and **4** need higher oxidation potentials to reach the Fe^V oxidation state (2.07 V and 2.17 V, respectively). Therefore, the incorporation of the water molecule in *cis* position enables a proton coupled electron transfer (PCET) mechanism, characterized by a substantially smaller oxidation potential, leading access to the Fe^V(O) when using Ce^{IV} as oxidant. The O-O bond-formation mechanism for **1** and **2** is kinetically favorable in both cases. Remarkably, theoretical activation parameters for the water oxidation with **1** agree nicely with the experimental results.

The comparison between **1** and **2** with **3** and **4** suggests that the lack of a *cis*-internal base impose that the proton transfer that occurs concomitantly to O-O bond formation needs to take place with aid of the bulk solvent. Finally, complexes **3** and **4** cannot access the reactive Fe^V(O) state, but in the hypothetical case that they could be formed, such intermediates will be highly reactive and will present a very low energy barrier for reacting with H₂O. The later high reactivity could be explained by considering that the Fe^V(O) state is not stabilized by a negatively charged *cis*-ligand and therefore is much more reactive.

Based on these results, a strategy to design more efficient iron WOCs must consider both the optimization of the redox potential value for the Fe^{IV}/Fe^V PCET step, which will also have a direct translation in the overpotential needed for the WO to proceed, and the energy barrier of the O-O bond-formation step. The modulation of these two parameters envisions *in silico*-design of new water oxidation catalysts for higher efficiencies. For instance, this goal could be achieved by the introduction of anionic groups at the ligand *cis* to oxo-group, which may facilitated both the PCET from Fe(IV) to Fe(V) and the attack of the water molecule. The nature of the negatively charged *cis* group and the chelating ligand can allow modulation of the accessibility and the reactivity of the

$\text{Fe}^{\text{V}}=\text{O}$ species, since the anionic fragment would stabilize the high iron oxidation state, lowering the required oxidation potential, and would also act as an internal Brønsted base to assist the proton transfer from a solvent water molecule. Once the negative charge is neutralized, the $\text{Fe}^{\text{V}}=\text{O}$ would become more reactive reducing the energy barrier for O-O bond formation.

Finally, in the specific case of **1** we have computed the full mechanism of the WO catalytic cycle. The free energy profile confirms that: 1) The resting state is the $[\text{Fe}^{\text{IV}}(\text{O})(\text{OH}_2)(\text{Pytacn})]^{2+}$; 2) The TDTS of the cycle is given by the O-O bond formation; and 3) the oxidation step that requires the highest redox potential is the oxidation of $[\text{Fe}^{\text{IV}}(\text{O})(\text{OH}_2)(\text{Pytacn})]^{2+}$ to $[\text{Fe}^{\text{V}}(\text{O})(\text{OH})(\text{Pytacn})]^{2+}$.

CHAPTER 5:

THEORETICAL STUDY OF THE WATER OXIDATION MECHANISM WITH NON-HEME Fe(PYTACN) IRON COMPLEXES: EVIDENCE THAT THE Fe^{IV}(O)(PYTACN) SPECIES CANNOT REACT WITH THE WATER MOLECULE TO FORM THE O-O BOND^a

^a This chapter is based on the publication: Acuña-Parés, F.; Costas, M.; Luis, J.M.; Lloret-Fillol, J. *Inorg. Chem.* **2014**, *53*, 5474.

5. Theoretical Study of the Water Oxidation Mechanism with Non-heme Fe(Pytacn) Iron Complexes. Evidence that the Fe^{IV}(O)(Pytacn) Species Cannot React with the Water Molecule to Form the O-O Bond

Recent studies have shown that non-heme iron complexes [Fe(L^{N4})X₂], where L^{N4} stands for a tetradentate nitrogen based aminopyridine ligand (L^{N4} = Pytacn, mcp or mep, Pytacn = 1-(2-pyridylmethyl)-4,7-dimethyl-1,4,7-triazacyclononane, mcp = *N,N'*-dimethyl-*N,N'*-bis(2-pyridylmethyl)-cyclohexane-*trans*-1,2-diamine, mep = *N,N'*-dimethyl-*N,N'*-bis(2-pyridylmethyl) ethylenediamine), and X are monodentate ligands (X = Cl, CH₃CN, CF₃SO₃⁻ or H₂O), catalyze the oxidation of water using cerium(IV) ammonium nitrate (CAN) as oxidant. Spectroscopic monitoring of catalytic water oxidation with complex [Fe(CF₃SO₃)₂(Pytacn)] established [Fe^{IV}(O)(OH₂)(Pytacn)]²⁺ as an intermediate along the catalytic pathway, raising the question if these high valent species could be directly responsible for the O-O bond formation event. Herein, this question is addressed by a computational analysis of the thermodynamic and kinetic parameters associated with the reaction of non-heme iron complexes [Fe^{IV}(O)(OH)(Pytacn)]⁺, [Fe^{IV}(O)(OH₂)(Pytacn)]²⁺ and [Fe^{IV}(OH)(OH)(Pytacn)]²⁺ with water. Two different mechanism have been studied for [Fe^{IV}(O)(OH)(Pytacn)]⁺; the nucleophilic water attack assisted by the hydroxyl group as internal base, which is the lowest energy path, and the external nucleophilic water attack. For [Fe^{IV}(OH)(OH)(Pytacn)]²⁺, only the attack assisted by the internal base has been studied, while in the case of [Fe^{IV}(O)(OH₂)(Pytacn)]²⁺, the only viable mechanism is the external nucleophilic water attack.

5.1. State-of-the-art

We have previously described that, by using cerium ammonium nitrate (CAN) as a sacrificial oxidant, iron catalysts with neutral tetradentate ligands and two available positions in *cis* are effective in the WO reaction in acidic conditions (pH = 1).^{68,69} On contrary, neutral tetradentate ligands with *trans*-labile sites or pentadentate ligands are inactive. Spectroscopic monitoring showed that the initial Fe^{II} complexes are immediately oxidized by the addition of a slight excess of Ce^{IV} (3 equivalents at pH 1) to quantitatively form the resting state [Fe^{IV}(O)(OH₂)(L^{N4})]²⁺ (L^{N4} stands for i.e. Pytacn, mcp and mep, among others). Under these conditions, these intermediates were found relatively stable, with a half-life time between 20 to 200 min. Moreover, no O₂ was detected after the decay of these intermediates. At low concentrations of CAN, the reaction rate present a first order dependence respect to the concentration of both the metal and the sacrificial oxidant. This result excludes the possibility of a direct coupling mechanism between two Fe^{IV}=O moieties to form the O-O bond and the WO reaction can be expected as single site. Therefore, the [Fe^{IV}(O)(OH₂)(L^{N4})]²⁺ species could not be responsible for the O-O bond formation. Instead, O₂ formation was detected when an excess of CAN was added to a solution of [Fe^{IV}(O)(OH₂)(L^{N4})]²⁺, which suggests that the formation of the O-O bond requires a higher oxidation state of the iron center, [Fe^V(O)(OH)(L^{N4})]²⁺ species. In chapter 4, DFT calculations supported the accessibility of [Fe^V(O)(OH)(Pytacn)]²⁺ species under catalytic conditions. Furthermore, the free energy barrier for the O-O bond formation mechanism involving the nucleophilic water molecule attack to a highly electrophilic [Fe^V(O)(OH)(Pytacn)]²⁺ was 18.5 kcal·mol⁻¹, in very good agreement with the experimental value (ΔG[‡]_(exp.) = 17.6 kcal·mol⁻¹).²⁰¹ Nevertheless, there is a lack of information about the kinetics of the O-O bond formation reaction from non-heme Fe^{IV}(O) species, which is the matter herein.

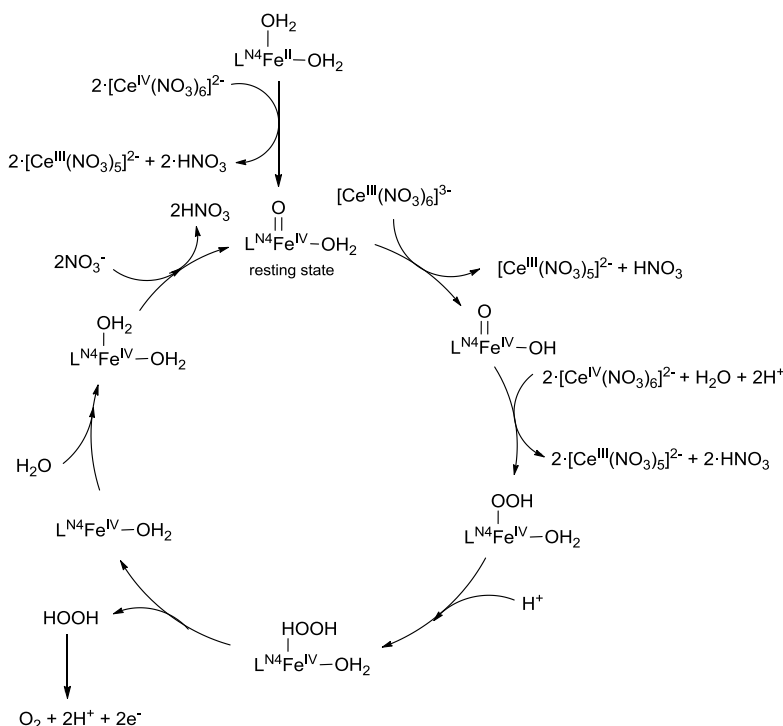


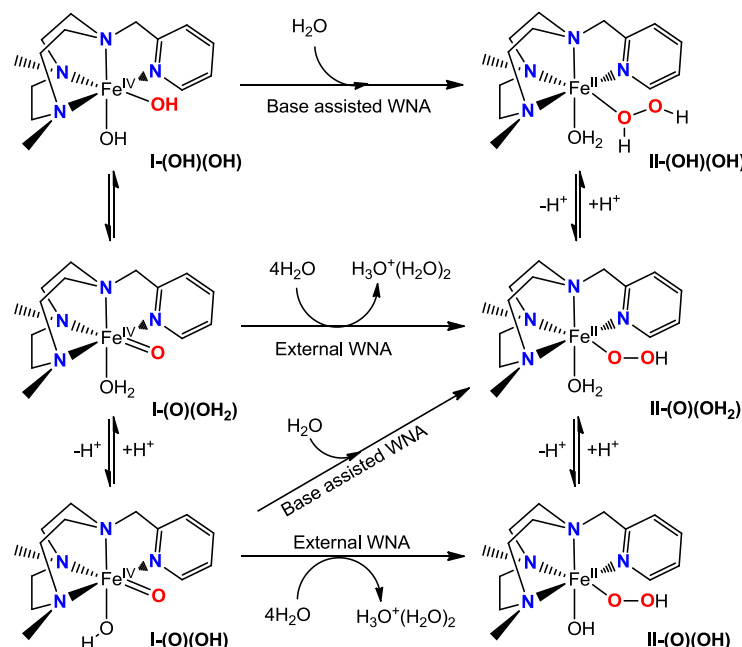
Figure 84: Theoretical proposal by Kasapbasi and co-workers which occurs exclusively at Fe^{IV} oxidation state.²⁰⁸

Closely related to our work, Kasapbasi *et al.* recently reported a theoretical study proposing a WO catalytic cycle accomplished by non-heme iron catalyst **1** on the basis of DFT calculations.²⁰⁸ The authors suggest that all the species involved in the catalytic cycle have the same oxidation state (Fe^{IV}), and that the species driving the O-O bond formation event is the $[\text{Fe}^{\text{IV}}(\text{O})(\text{OH})(\text{Pytacn})]^+$ intermediate, which is formed *via* deprotonation of the resting state $[\text{Fe}^{\text{IV}}(\text{O})(\text{OH}_2)(\text{Pytacn})]^{2+}$ (Figure 84). The nitrate anions present in the coordination sphere of the Ce^{IV} cation are proposed to act as a base that deprotonate the resting state $[\text{Fe}^{\text{IV}}(\text{O})(\text{OH}_2)(\text{Pytacn})]^{2+}$.

Taking the proposal by Kasapbasi into consideration, in this chapter we sought to investigate by computational methods the competence of the spectroscopically detected $[\text{Fe}^{\text{IV}}(\text{O})(\text{OH}_2)(\text{Pytacn})]^{2+}$, its isomeric form $[\text{Fe}^{\text{IV}}(\text{OH})(\text{OH})(\text{Pytacn})]^{2+}$ and its conjugated base $[\text{Fe}^{\text{IV}}(\text{O})(\text{OH})(\text{Pytacn})]^+$ to perform the O-O bond formation event (Scheme 1). We have also analyzed in which conditions the WO catalytic cycle proposed by Kasapbasi *et al* could be viable. Finally, we have investigated the energetic accessibility of $\text{Fe}^{\text{V}}(\text{O})$ and $\text{Fe}^{\text{VI}}(\text{O})$ intermediates under catalytic conditions and their role as possible catalytic active species in WO reaction. Key to our study is the inclusion of explicit water molecules in the computed mechanism, as well as enthalpic and entropic corrections, which are particularly important in the estimation of the computed pK_a of the nitrate anions.

There is also the possibility that binuclear Fe^{IV} species might participate in the O-O bond formation event. For instance, Que and coworkers presented the first non-heme diiron(IV) complex with the capacity to oxidize water through formation of hydroxyl radicals *via* a hydrogen abstraction reaction.⁷⁴ In addition, Ray and coworkers has shown that a hexanuclear iron complex supported on a stannoxane core can undergo a facile O-O bond formation between two $\text{Fe}^{\text{IV}}=\text{O}$ moieties, revealing the viability of a DC mechanism.²⁰⁹ Moreover, the conversion of a bis-TPA peroxodiiron(III) complex to oxodiiron(IV) species *via* reversible O-O bond rupture was observed by the Kodera and

coworkers.²¹⁰ Sakai and coworkers also show that the WO reaction rate for complex μ -O- μ -(SO₄)-[(TPA)Fe]₂(HSO₄)₂ increases with the decreasing of the pH, consistent with an equilibria between mononuclear and binuclear Fe^{III/IV} species.²¹¹ However, kinetic studies on complex **1** revealed a first order dependence respect to the concentration of both iron complex and sacrificial oxidant, excluding for complex **1** the O₂ evolution through a bimetallic reaction pathway.



Scheme 3: Studied O-O bond formation pathways involving Fe^{IV} species. The microsolvation of the iron complex was modeled by three explicit water molecules. WNA stands for Water Nucleophilic Attack.

5.2. Results and discussion

All structure optimizations were performed at DFT(B3LYP)¹⁷⁶ level with the 6-31G* basis set for all atoms and taking into account the solvent effects and the dispersion corrections. All the calculations were done using Gaussian09 software.¹⁹³ Spin unrestricted B3LYP calculations were performed on all possible conformers and all corresponding spin states for the iron metal center were taken into account to locate the ground state. The nature of the stationary points was confirmed by frequency calculations in aqueous phase, where minima have no imaginary frequencies and transition states have only one. The connectivity between minimums and transition states was confirmed through intrinsic reaction coordinate (IRC) calculations. The energies were further refined by single-point calculations with the cc-pVTZ dunning basis set for all atoms (E_{cc-pVTZ}). The London dispersion effects were introduced with the B3LYP-D₂ Grimme correction (E_{disp})¹⁸⁰ and free energy corrections (G_{corr}), which include the enthalpic and entropic terms, were determined from gas phase frequency calculations at B3LYP/6-31G* level on aqueous phase structures. The solvent effect of aqueous medium was taken into account through the SMD polarizable continuum model (G_{solv}).¹⁸¹ All calculated solvation free energies of the solute molecules were set to a standard state of an ideal gas at a gas-phase concentration of 1 mol·L⁻¹ that is dissolved as an ideal dilute solution at a liquid-phase concentration of 1 mol·L⁻¹. For the explicit solvent water molecules, a 55.6 M standard state was employed. Thus, as has been indicated by Cramer *et. al.*,¹⁸³ we calculated the free energy associated with the phase change from a standard-state gas-phase pressure of 1 atm to a standard-state gas-

phase concentration of 1 M (55.6 M), $\Delta G^{0/*}$. The value of $\Delta G^{0/*}$ at 298 K is 1.9 kcal·mol⁻¹ for 1 M standard state solutes and 4.3 kcal·mol⁻¹ for 55.6 M standard state explicit water molecules. Then, the total Gibbs free energies (G) were given by:

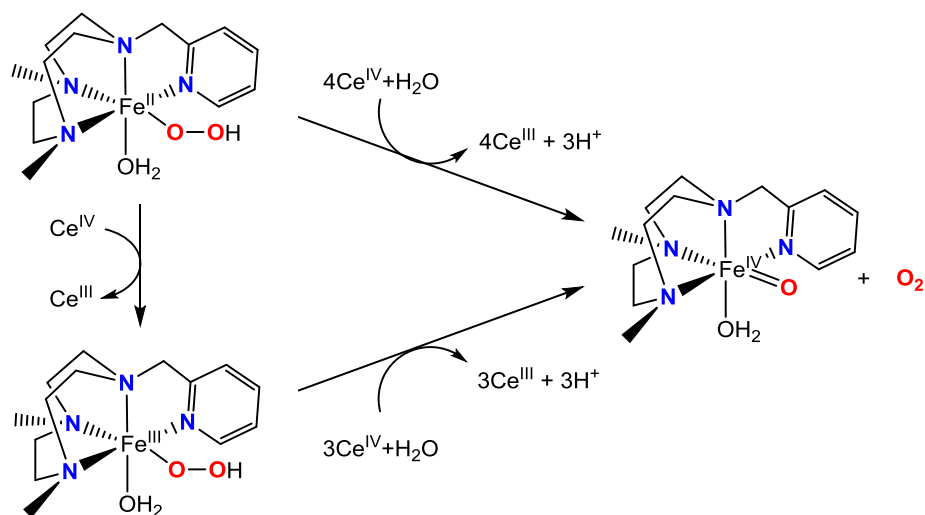
$$G = E_{cc-pVTZ} + E_{disp} + G_{corr.} + G_{solv} + \Delta G^{0/*} \quad (28)$$

The standard reduction potentials were computed with Eq. 20-21 at pH 1, relative to the SHE ($\Delta G_{SHE}^0 = -4.28$ eV).²⁰⁰

Labels **I-(O)**, **TS-(O)**, **II-(O)** or **III-(O)** were used as short nomenclature of reactants, transition states, intermediates and products involved in the O-O bond formation event by complex **1**. These labels **a** and **b** refer to the two *cis*-tautomeric forms of complex **1**. In the tautomer **a**, the Fe=O moiety is in *trans* relative position to one of the Me-substituted amines. Subscripts **s**, **t**, **qt** and **sept** are used to specify the singlet, triplet, quintuplet and septuplet spin state of the metal center, and the **H₂O** and **OH** labels are related to the nature of the *cis* ligand respect the oxo group. Finally, the subscript **int** is used when the *cis* ligand to the oxo group acts as an internal Brønsted base.

5.2.1 O-O bond formation mechanism through [Fe^{IV}(O)(OH₂)(Pytacn)]²⁺

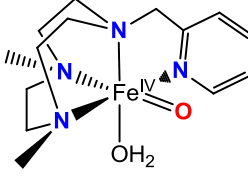
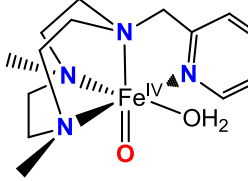
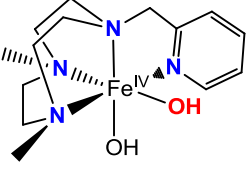
UV-Vis, ¹H-NMR spectroscopy and electrospray ionization mass spectrometry (ESI-MS) show that oxo-aqua Fe^{IV} species [Fe^{IV}(O)(OH₂)(Pytacn)]²⁺ are formed when 3 equiv. of CAN are added to a water solution of complex **1**. This species have long half-lives (> 90 min) and no oxygen evolution was observed during their decay.^{68,69} These experimental observations suggest that while these species are intermediates in the WO mechanism, by itself cannot produce O₂. Instead, experimentally is found that [Fe^{IV}(O)(OH₂)(Pytacn)]²⁺ needs to react with an excess of Ce^{IV} (2-3 equiv.) for O₂ to be detected. However, still it is possible to define a hypothetical scenario where the O-O bond is formed (See scheme 3) but instead of O₂ release the formation of H₂O₂ is produced. For instance, the nucleophilic attack of a water molecule to [Fe^{IV}(O)(OH₂)(Pytacn)]²⁺ would produce the formation of the O-O bond and the Fe^{II}OOH intermediate (Scheme 3). Finally, the oxidation of Fe^{II}OOH could produce O₂ and regenerate the resting state [Fe^{IV}(O)(OH₂)(Pytacn)]²⁺ (Scheme 4) or their protonation could produce H₂O₂. Indeed, this process could in some extend be operative. In this regard, we present herein DFT calculations studies to provide an estimation of the energy barrier for the reaction O-O bond formation, and to address the viability of the process.

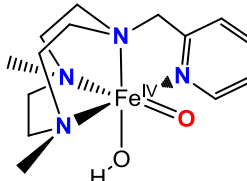
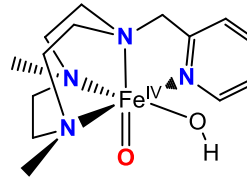


Scheme 4: O_2 evolution and regeneration of the $[\text{Fe}^{\text{IV}}(\text{O})(\text{OH}_2)(\text{Pytacn})]^{2+}$ resting state through hydroperoxo intermediates.

Water nucleophilic attack (WNA) over the terminal oxo of $[\text{Fe}^{\text{IV}}(\text{O})(\text{OH}_2)(\text{Pytacn})]^{2+}$ results in formation of the O-O bond, forming a $[\text{Fe}^{\text{III}}(\text{OOH})(\text{OH}_2)(\text{Pytacn})]^+$ species and releasing a proton. Attempts to model the mechanism including only two water molecules failed. This is due to the poor description of the strong hydrogen bonds between the formed hydronium ion and the solvent water molecules given by the polarizable continuum model. Therefore, the two water molecules that form the first solvation shell of the hydronium ion have to be included as explicit water molecules to reproduce accurately such key hydrogen bonds during the O-O bond formation event. In the same line, we highlight that previous theoretical studies^{27,67,196,197} in related systems have shown that the consideration of the explicit water molecules forming the first solvation shell has a large influence in the energy of the O-O bond formation event.

Table 4: Spin states relative free energies (kcal·mol⁻¹) of the Fe^{IV} intermediates for complex **1** in the two *cis*-tautomers **a** and **b**.

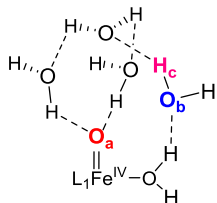
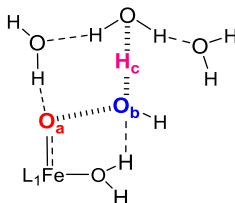
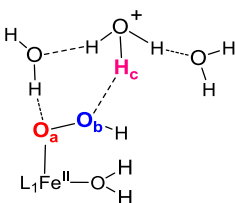
			
	1a-(O)(OH₂)	1b-(O)(OH₂)	1-(OH)(OH)
S = 0	10.8 (35.9)	10.0 (29.5)	21.8
S = 1	0.9 (2.2)	0.2 (2.4)	0.2
S = 2	0.0 ^a (0.0) ^b	2.9 (4.9)	3.5

		
	1a-(O)(OH)	1b-(O)(OH)
S = 0	30.5 (22.1)	29.5 (28.5)
S = 1	3.1 (2.0)	1.3 (0.6)
S = 2	0.0 ^a (0.0) ^b	1.5 (3.2)

[a] Free energies respect to the most stable structure. [b] In parenthesis, the free energy differences taking into account one solvent explicit water molecule.

Before exploring the O-O bond formation mechanism, we examined the relative energies of all different spin states for the iron IV species in the two possible *cis*-tautomers **a** and **b**. We also studied the influence of a solvent explicit water molecule in the spin splitting, to properly characterize the ground state and the most stable geometry for each Fe^{IV} species (see Table 4). The optimization of [Fe^{IV}(O)(OH₂)(Pytacn)]²⁺ with four explicit water molecules yields **1a-(O)(OH₂)** in the S = 2 ground state, with Fe-O_a and O_a-O_b bond lengths of 1.640 Å and 3.232 Å, respectively (Table 5).²¹² The difference between S = 2 and S = 1 states is only ΔG = 0.2 kcal·mol⁻¹, which falls into the mean error of the used DFT methodology. On the other hand, the S = 0 state is 10.3 kcal·mol⁻¹ higher in energy than the spin state S = 2 and it is clearly not significant in the energy reaction path. Consequently, S = 1 spin state should be carefully considered for the evaluation of the barrier of O-O bond formation. The most stable structure for the tautomer **1b-(O)(OH₂)**, which has a S = 1, is 2.4 kcal·mol⁻¹ higher in energy than the ground state S = 2 **1a-(O)(OH₂)** when one explicit water molecule is considered (see Table 4). The free energy profile calculated for the O-O bond formation mechanism starting from **1a-(O)(OH₂)** is summarized in the Figure 85.

Table 5: Selected Mulliken spin densities and bond distances for the stationary points obtained in the formation of the O-O bond by an external water nucleophilic attack to the $S = 2$ $[\text{Fe}^{\text{IV}}(\text{O})(\text{OH}_2)(\text{Pytacn})]^{2+}$ complex.

			
	Ia_{qt}-(O)(OH₂)	TSa_{qt}-(O)(OH₂)	IIa_{qt}-(O)(OH₂)
$\rho(\text{Fe})$	3.31	3.38	3.82
$\rho(\text{O}_a)$	0.47	0.15	0.04
$\rho(\text{O}_b)$	0.00	0.36	0.00
$d(\text{Fe}-\text{O}_a)^b$	1.640	1.833	2.018
$d(\text{O}_a-\text{O}_b)^b$	3.232	1.753	1.495
$d(\text{O}_b-\text{H}_c)^b$	0.998	1.555	1.619

[a] L_1 stands for the Pytacn ligand. [b] Bond lengths are given in Å.

As Figure 85 shows, the O-O bond formation step from $[\text{Fe}^{\text{IV}}(\text{O})(\text{OH}_2)(\text{Pytacn})]^{2+} \cdot 4\text{H}_2\text{O}$ (**Ia-(O)(OH₂)**) to yield $[\text{Fe}^{\text{II}}(\text{OOH})(\text{OH}_2)(\text{Pytacn})]^+ \cdot \text{H}_3\text{O}^+(\text{H}_2\text{O})_2$ (**IIa-(O)(OH₂)**) are connected through a concerted transition state (**TSa-OH₂**) for all studied spin states. The transition state lowest in energy was found to be the $S = 1$ **TSa_r-(O)(OH₂)**, which lie at $52.0 \text{ kcal}\cdot\text{mol}^{-1}$ over $S = 2$ $[\text{Fe}^{\text{IV}}(\text{O})(\text{OH}_2)(\text{Pytacn})]^{2+} \cdot 4\text{H}_2\text{O}$ (see Figure SI.1 of ref. 213 for geometries in the $S = 0$ and $S = 1$ spin states). However, after a spin crossing, the reaction evolves to the spin state most stable $S = 2$ Fe^{II} hydroperoxo product, **IIa_{qt}-(O)(OH₂)**, which was found 10.5 and $15.7 \text{ kcal}\cdot\text{mol}^{-1}$ lower in energy than the $S = 1$ and $S = 0$ products, respectively (see Figure 85). Taking these results in consideration, the O-O bond formation pathway is not feasible through $[\text{Fe}^{\text{IV}}(\text{O})(\text{OH}_2)(\text{Pytacn})]^{2+}$. This result is indeed in complete agreement with the experimental observation that $[\text{Fe}^{\text{IV}}(\text{O})(\text{OH}_2)(\text{Pytacn})]^{2+}$ in water does not evolve to produce molecular oxygen. Nevertheless, we noted that the inverse reaction $S = 2$ path from Fe^{II} to Fe^{IV} species presents a very low energy barrier of $17.0 \text{ kcal}\cdot\text{mol}^{-1}$, suggesting that the non-heme $\text{Fe}^{\text{IV}}=\text{O}$ species could be generated by direct reaction of Fe^{II} and H_2O_2 in water. This reaction actually finds precedent in some bioinspired synthetic complexes with related nitrogen based ligands,²¹⁴ and is also reminiscent with the O-O breakage mechanism operating in non-heme dependent oxygenases.²¹⁵

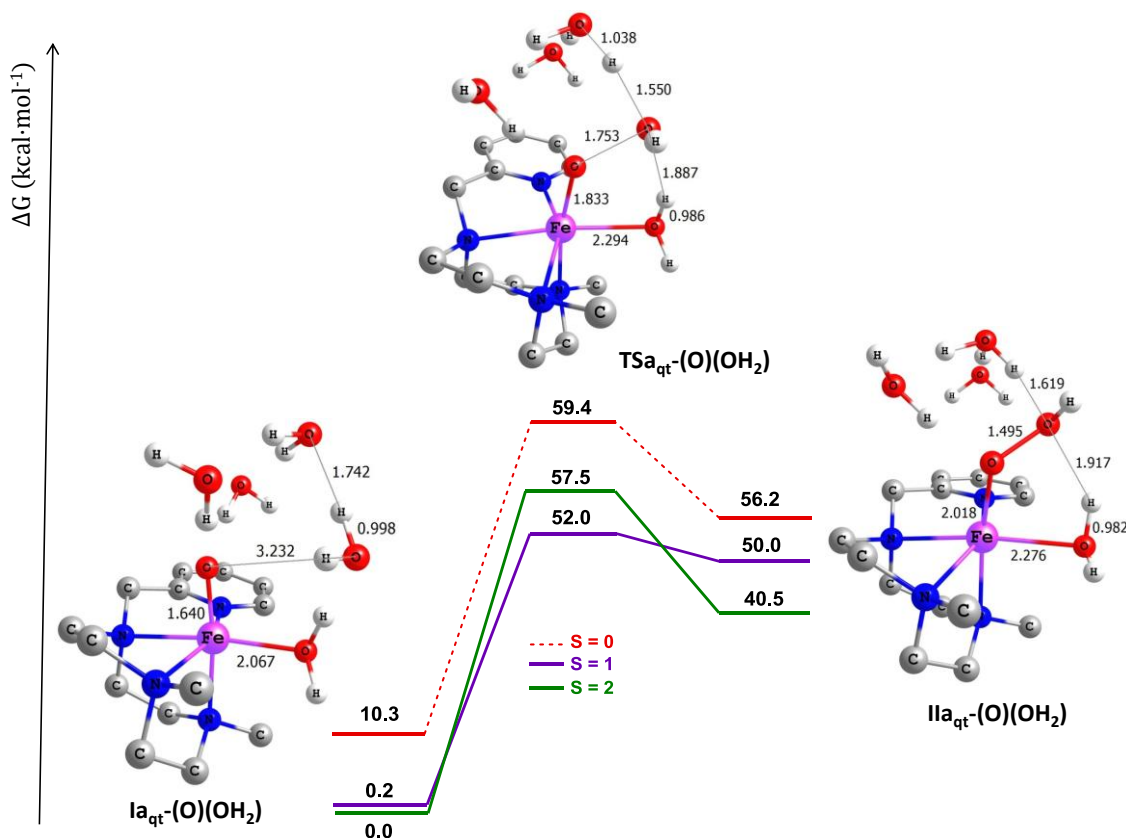


Figure 85: O-O bond formation profiles found for the **a** tautomer of $[\text{Fe}^{\text{IV}}(\text{O})(\text{OH}_2)(\text{Pytacn})]^{2+} \cdot 4\text{H}_2\text{O}$ for the S = 0, 1 and 2 spin states. Gibbs energy values are given in kcal·mol⁻¹. Figures inserted correspond to the S = 2 spin state, where selected bond distances (Å) are presented.

5.2.2 O-O bond formation mechanism through $[\text{Fe}^{\text{IV}}(\text{O})(\text{OH})(\text{Pytacn})]^+$

pK_a value of 10 of the water ligand in $[\text{Fe}^{\text{IV}}(\text{O})(\text{OH}_2)(\text{Pytacn})]^{2+}$ indicates that the oxo-aqua complex is the stable species under catalytic conditions (pH = 1). To obtain a consistent pK_a value we have studied the effect of increasing the number of explicit solvent water molecules, obtaining a pK_a convergence value close to 10 (see Supp. Info. of ref. 213, Table SI.1). At the catalytic pH value of 1, the Gibbs energy of $[\text{Fe}^{\text{IV}}(\text{O})(\text{OH})(\text{Pytacn})]^+$ is 12.0 kcal·mol⁻¹ higher than $[\text{Fe}^{\text{IV}}(\text{O})(\text{OH}_2)(\text{Pytacn})]^{2+}$. This result imply that the formation of O-O bond thought intermediate $[\text{Fe}^{\text{IV}}(\text{O})(\text{OH})(\text{Pytacn})]^+$ is very unlikely. Nevertheless, $[\text{Fe}^{\text{IV}}(\text{O})(\text{OH})(\text{Pytacn})]^+$ presents a OH ligand *cis* to the oxo group that could aid to the O-O bond formation by acting as an internal Brønsted base accepting a proton from the water molecule. To evaluate the kinetic viability of the processes, two possible O-O bond formation mechanisms were explored: an internal base assisted mechanism, where the OH ligand acts as a proton acceptor^{37,201} and an external base assisted mechanism where a water solvent molecule acts as an external base (Figure 86).

Internal base assisted mechanism: In this case, only a single water molecule is required to be explicitly modelled (see Fig. 86). The most stable structure for the $[\text{Fe}^{\text{IV}}(\text{O})(\text{OH})(\text{Pytacn})]^+ \cdot \text{H}_2\text{O}$ was found among the S = 2 spin state structures (**Ia_{qt}-(O)(OH_{int})**). Structures with spin states S = 1 and S = 0 are 2.0 kcal·mol⁻¹ and 22.1 kcal·mol⁻¹ higher in energy than the ground state. In the water adduct $[\text{Fe}^{\text{IV}}(\text{O})(\text{OH})(\text{Pytacn})]^+ \cdot \text{H}_2\text{O}$, the formation of two hydrogen bonds between the water molecule and the oxo and hydroxo ligands of $[\text{Fe}^{\text{IV}}(\text{O})(\text{OH})(\text{Pytacn})]^+$ yields the most stable structure. From this intermediate, the reaction proceeds *via* nucleophilic attack of the O atom of the water molecule to

the oxo group to form the transition state **TSa_{qt}-(O)(OH_{int})** ($\Delta G^\ddagger = 32.2 \text{ kcal}\cdot\text{mol}^{-1}$). At this stage, a proton is transferred from the water molecule to the OH ligand with concomitant O-O bond formation. The reorganization enlarge the Fe-oxo bond in 0.189 Å and shortened the O-O bond distance in 1.086 Å. Mulliken population analysis of the **TSa_{qt}-(O)(OH_{int})** showed a spin density value of -0.21 at the oxygen atom of the water molecule, a spin density decrease of 0.36 at the oxo ligand and an increase of 0.66 at the iron center (Table 6). These spin densities reorganizations suggests a partial electron transfer from the water molecule to the iron-oxo moiety along the reaction coordinate, responsible of the reduction of the iron oxidation state. The concerted transition state leads to the formation of the Fe^{II} hydroperoxo product (**Ia_{qt}-(O)(OH_{int})**) with a O-O bond length of 1.499 Å. The process is endergonic, with a ΔG value of 28.3 kcal·mol⁻¹. Indeed, the ΔG^\ddagger of the O-O bond formation through $[\text{Fe}^{\text{IV}}(\text{O})(\text{OH})(\text{Pytacn})]^+\cdot\text{H}_2\text{O}$ increase to 40.3 kcal·mol⁻¹ if the most stable $[\text{Fe}^{\text{IV}}(\text{O})(\text{OH}_2)(\text{Pytacn})]^{2+}$ species is consider as reactant.

To this point, we have only considered the O-O bond formation mechanism performed by the tautomer **a** of the $[\text{Fe}^{\text{IV}}(\text{O})(\text{OH})(\text{Pytacn})]^+$. The free energy difference between the ground spin state of the two tautomers of $[\text{Fe}^{\text{IV}}(\text{O})(\text{OH})(\text{Pytacn})]^+\cdot\text{H}_2\text{O}$ intermediate indicates that **Ia_{qt}-(O)(OH_{int})** is slightly more stable than **Ib_t-(O)(OH_{int})** species ($\Delta G^\ddagger = 0.6 \text{ kcal}\cdot\text{mol}^{-1}$). Therefore, to analyse the kinetic feasibility of the process, is important to evaluate also the same event conducted by the tautomer **b**. The spin state energy profiles for tautomer **b** show the same reactivity trend already described for **a**, with an O-O bond formation energy barrier slightly higher of $\Delta G^\ddagger = 32.8 \text{ kcal}\cdot\text{mol}^{-1}$ (See Figure SI.3 of ref. 213). In summary, from the kinetic point of view the barrier of this reaction is too high to occur at room temperature, and from the thermodynamic point of view is clearly disfavored due to the strong endergonic character.

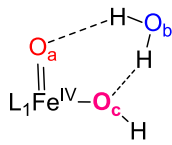
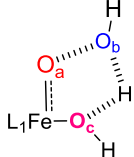
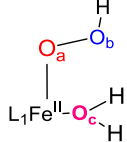
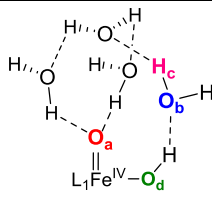
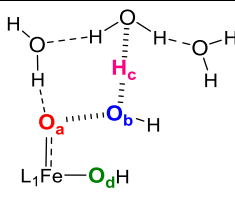
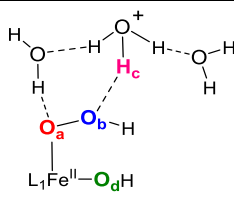
External base assisted mechanism: This mechanism requires the inclusion of at least four explicit water molecules to correctly reproduce the stabilization of the formed hydronium ion by means of hydrogen bonds. In the same line, a large influence respect to the number of explicit water molecules composing the first solvation shell on the O-O bond formation event has been also found in previous theoretical studies.²⁹⁻³³ The $[\text{Fe}^{\text{IV}}(\text{O})(\text{OH})(\text{Pytacn})]^+\cdot 4\text{H}_2\text{O}$ external base assisted O-O bond formation by the tautomeric form **a** also occurs through a $S = 2$ concerted transition state (**TSa_{qt}-(O)(OH)**, $\Delta G^\ddagger = 50.5 \text{ kcal}\cdot\text{mol}^{-1}$), 19.0 and 20.6 kcal·mol⁻¹ lower in Gibbs energy than the $S = 0$ and $S = 1$ transition states, respectively (see Figure 86 and Figure SI.4 of ref. 213). The high Gibbs energy barrier found and the Gibbs energy reaction (48.9 kcal·mol⁻¹) obtained for the **Ia_{qt}-(O)(OH)** indicates that O-O bond formation is kinetically and thermodynamically unviable through this mechanism.

Unexpectedly, the energy barrier found for the external attack of the water molecule to the oxo group on $[\text{Fe}^{\text{IV}}(\text{O})(\text{OH}_2)(\text{Pytacn})]^{2+}\cdot 4\text{H}_2\text{O}$ is slightly higher than for $[\text{Fe}^{\text{IV}}(\text{O})(\text{OH})(\text{Pytacn})]^+\cdot 4\text{H}_2\text{O}$, despite that the former is expected to be more electrophilic owing to charge considerations. This phenomenon could have its origin in the hydrogen bond formed between the nucleophilic water molecule and the *cis* ligand to the oxo group. The O(nucleophilic water)-H(*cis* ligand) hydrogen bond is stronger in **Ia_{qt}-(O)(OH₂)** ($d_{(\text{O}-\text{H})} = 1.576 \text{ \AA}$) than in **Ia_{qt}-(O)(OH)** ($d_{(\text{O}-\text{H})} = 1.761 \text{ \AA}$), producing a less nucleophilic water molecule and then a higher energy barrier when a *cis*-aqua ligand is present.

On the other hand and more remarkably, when the *cis*-OH ligand acts as an internal base, the O-O bond formation barrier is reduced in large extend with respect to the external mechanism ($\Delta\Delta G^\ddagger = 18.3 \text{ kcal}\cdot\text{mol}^{-1}$). Even taking into account the free energy required for the deprotonation equilibrium

of [Fe^{IV}(O)(OH₂)(Pytacn)]²⁺ under catalytic conditions (12.0 kcal·mol⁻¹), the O-O bond formation barrier for the internal mechanism remains lower in energy by $\Delta\Delta G^\ddagger = 6.3$ kcal·mol⁻¹. This result has implications in the future ligand design for the development of iron catalyst for the water oxidation reaction, as the introduction of internal bases clearly reduces the energy of the barrier. But in this case, the energy reduction of the barrier is not enough to allow the reaction of [Fe^{IV}(O)(OH)(Pytacn)]⁺ with water to occur at room temperature. Finally, an analysis of the magnitude of the enthalpic and entropic contributions to the O-O bond formation free energy barrier was performed at B3LYP/6-31G*/SMD level to elucidate the origin of the internal base effect. For the internal mechanism, the enthalpy and entropy of activation are 37.2 kcal·mol⁻¹ and 2.9 cal·mol⁻¹K⁻¹ respectively, while for the external mechanism, $\Delta H^\ddagger = 56.8$ kcal·mol⁻¹ and $\Delta S^\ddagger = 0.6$ cal·mol⁻¹K⁻¹. Then this event is mainly controlled by the enthalpic term. Indeed, the difference between the barriers of the internal and external mechanism can be rationalized by the preference of the final Fe^{II}-OOH·4H₂O product to act as a Brønsted base (pK_a = 16.0), locating the positive charge present on the ejected proton at the complex instead to delocalize it to the bulk water solvent.

Table 6: Selected Mulliken spin densities and bond distances for the S = 2 stationary points involved in the O-O bond formation mechanism from [Fe^{IV}(O)(OH)(Pytacn)]⁺ species.

			
	Ia_{qt}-(O)(OH_{int})	TSa_{qt}-(O)(OH_{int})	IIa_{qt}-(O)(OH_{int})
$\rho(\text{Fe})$	3.25	3.91	3.81
$\rho(\text{O}_a)$	0.44	0.08	0.06
$\rho(\text{O}_b)$	0.00	-0.21	0.00
$\rho(\text{O}_c)$	0.12	0.03	0.02
$d(\text{Fe}-\text{O}_a)^b$	1.642	1.831	1.961
$d(\text{O}_a-\text{O}_b)^b$	2.803	1.717	1.499
			
	Ia_{qt}-(O)(OH)	TSa_{qt}-(O)(OH)	IIa_{qt}-(O)(OH)
$\rho(\text{Fe})$	3.29	3.84	3.80
$\rho(\text{O}_a)$	0.36	0.02	0.03
$\rho(\text{O}_b)$	0.00	-0.09	-0.01
$\rho(\text{O}_d)$	0.14	0.10	0.09
$d(\text{Fe}-\text{O}_a)^b$	1.656	1.933	2.075
$d(\text{O}_a-\text{O}_b)^b$	3.181	1.603	1.497
$d(\text{Fe}-\text{O}_d)^b$	1.817	1.967	1.968
$d(\text{O}_b-\text{H}_c)^b$	0.993	1.455	1.538

[a] L₁ stands for the Pytacn ligand. [b] Bond lengths are given in Å.

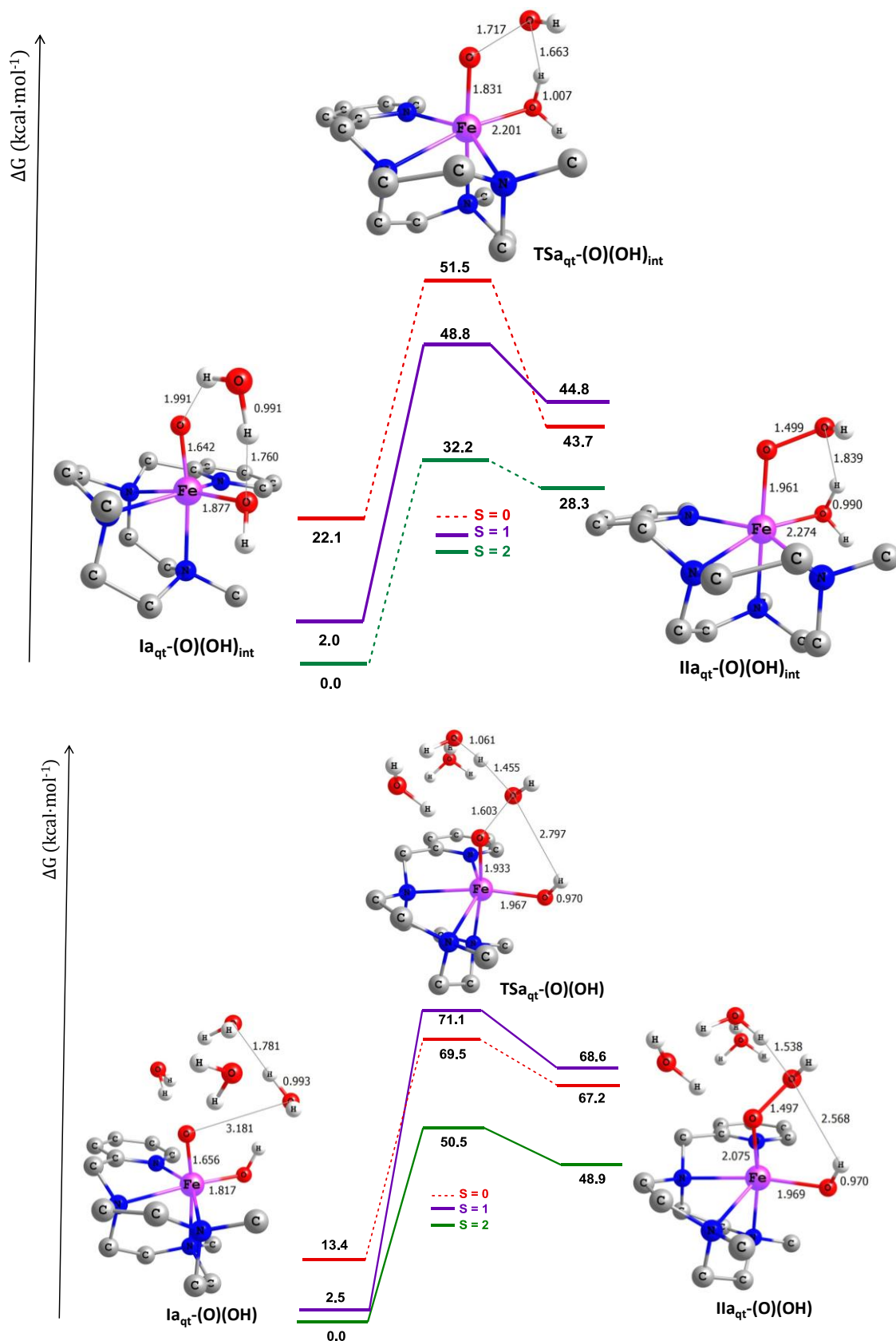


Figure 86: Internal (top) and external (bottom) base assisted O-O bond formation mechanisms from the tautomer **a** [Fe^{IV}(O)(OH)(Pytacn)]⁺ intermediate. Gibbs energy values are given in kcal·mol⁻¹. Selected bond distances in Å are indicated in the figures corresponding to the stationary points of the S = 2 reaction profile.

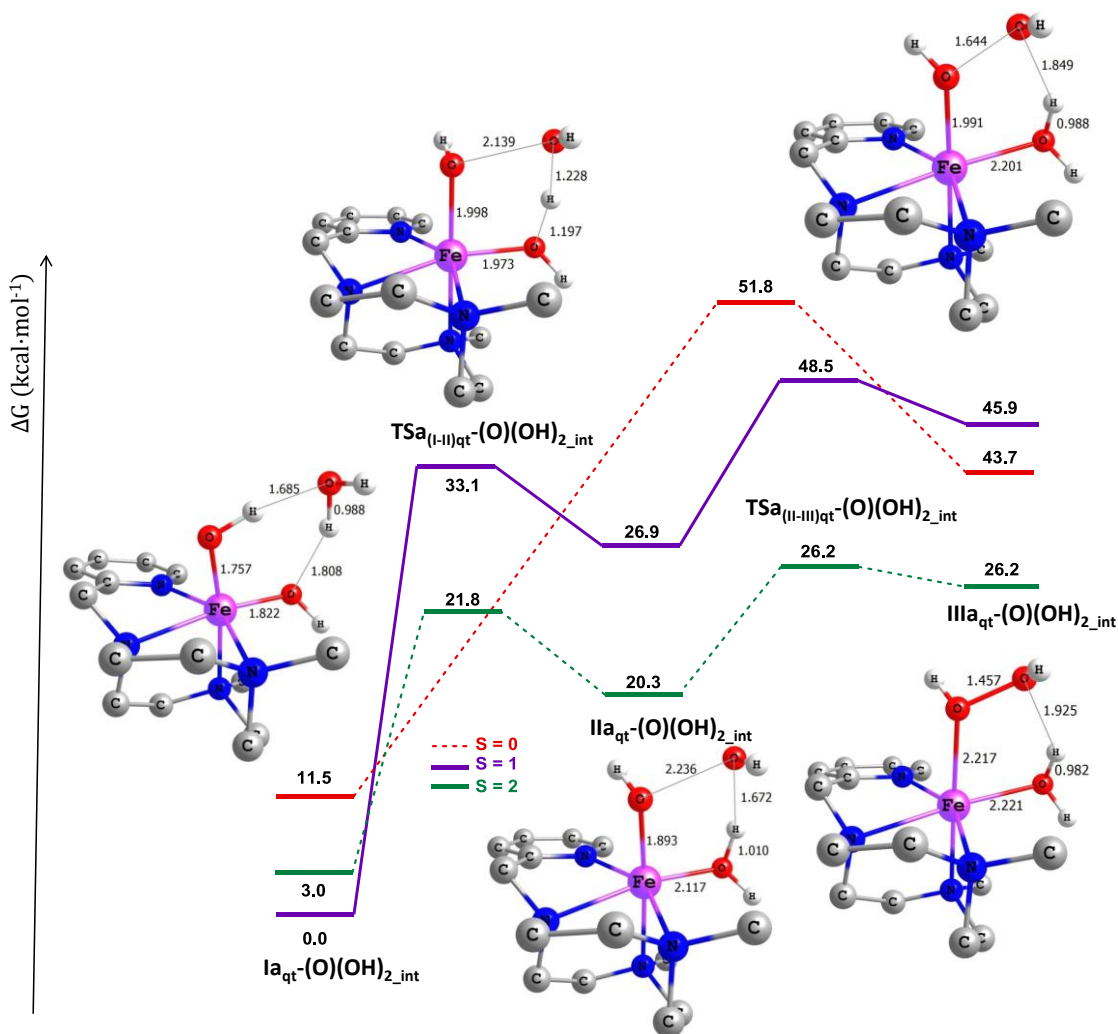


Figure 87: Internal base assisted O-O bond formation mechanisms from the tautomer **a** of $[\text{Fe}^{\text{IV}}(\text{OH})(\text{OH})(\text{Pytacn})]^{2+}$ intermediate. Gibbs energy values are given in $\text{kcal}\cdot\text{mol}^{-1}$. Selected bond distances (\AA) of stationary points on the $S = 2$ reaction profile are indicated in the figures.

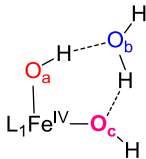
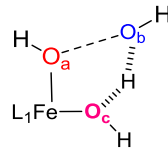
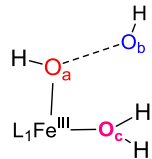
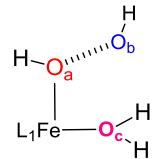
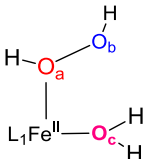
5.2.3 O-O bond formation mechanism through $[\text{Fe}^{\text{IV}}(\text{OH})(\text{OH})(\text{Pytacn})]^{2+}$

Finally the last Fe^{IV} complex to be considered is the bis-hydroxo $[\text{Fe}^{\text{IV}}(\text{OH})(\text{OH})(\text{Pytacn})]^{2+}$, which is a structural isomer of $[\text{Fe}^{\text{IV}}(\text{O})(\text{OH}_2)(\text{Pytacn})]^{2+}$. Indeed, $[\text{Fe}^{\text{IV}}(\text{OH})(\text{OH})(\text{Pytacn})]^{2+}$ is only $2.1 \text{ kcal}\cdot\text{mol}^{-1}$ higher in free energy than the Fe^{IV} -aqua complex (one explicit water molecule interacting with the oxygen moieties of the complexes was considered in the models). Therefore, the O-O bond formation mechanism through the Fe^{IV} -bishydroxo complex has also been investigated. In this case, only one explicit water molecule is enough to ensure a correct description of the internal base assisted mechanism. We have explored the mechanism for both possible tautomers **a** and **b**, which are virtually isoenergetic ($0.5 \text{ kcal}\cdot\text{mol}^{-1}$). We firstly explored the O-O bond formation event with the tautomer **a**, allowing proper comparison with the previous mechanisms. The $[\text{Fe}^{\text{IV}}(\text{OH})(\text{OH})(\text{Pytacn})]^{2+}\cdot\text{H}_2\text{O}$ complex presents a $S = 1$ ground spin state ($\text{Ia}_t\text{-(OH)}_2\text{_{int}}$). The $S = 2$ and $S = 0$ spin states lie $3.0 \text{ kcal}\cdot\text{mol}^{-1}$ and $11.5 \text{ kcal}\cdot\text{mol}^{-1}$ higher in free energy than the triplet ground state, respectively (See Figure SI.5 of ref. 213). The starting $\text{Ia}_t\text{-(OH)}_2\text{_{int}}$ includes the interaction of the two hydroxo ligands with one hydrogen and the oxygen atom of the water molecule through two hydrogen bonds (Figure 87). In contrast with the previous discussed

mechanism, the proton transfer and the O-O bond formation does not occur simultaneously. Instead, we have observed a two-step mechanism. All attempts to obtain the concerted mechanism failed. The first step involves the rotation of one O_aH group of **Ia_{qt}-(OH)₂_{int}** to allow the interaction between O_a and the O_b of the water molecule, and the proton transfer from the nucleophilic water molecule to the O_cH group (**TSa_{(I-II)qt}-(OH)₂_{int}**: $\Delta G^\ddagger = 21.8 \text{ kcal}\cdot\text{mol}^{-1}$). This yields the intermediate **IIa_{qt}-(OH)₂_{int}** ($\Delta G = 20.3 \text{ kcal}\cdot\text{mol}^{-1}$) (Table 7 and Figure 87). In **IIa_{qt}-(OH)₂_{int}**, the proton is completely transferred forming a second water molecule. The spin densities on the iron centre of **IIa_{qt}-(OH)₂_{int}** ($\rho(\text{Fe}) = 4.30$) and on the oxygen atom of the former nucleophilic water molecule ($\rho(\text{O}_b) = -0.79$), reveal an antiferromagnetically coupling between O_bH and {Fe(OH)(OH₂)} fragments. This suggests an electron transfer between the two previous groups leading to a formal Fe^{III} centre. The difference in mechanism found among isomers could be rationalized with the electrophilicity of the iron complex. For instance, difference in energy between [Fe^{IV}(OH)(OH)(Pytacn)]²⁺ and [Fe^{IV}(O)(OH₂)(Pytacn)]²⁺ isomers is translated into a reduction potential difference of 100 mV. Therefore [Fe^{IV}(OH)(OH)(Pytacn)]²⁺ is relatively more oxidant than [Fe^{IV}(O)(OH₂)(Pytacn)]²⁺, which could explain the preference for a direct hydrogen transference that leads to a formal reduction of Fe^{IV} to Fe^{III} before the O-O bond formation step. This is consistent with the O-O bond formation mechanism found for Fe^V(O)(OH) species, which are also more oxidant than Fe^{IV}(O)(OH₂).^{69,201}

Finally, in the second step, **IIa_{qt}-(OH)₂_{int}** connects with the **IIIa_{qt}-(OH)₂_{int}** Fe^{II} complex via the transition state **TSa_{(II-III)qt}-(OH)₂_{int}**, which is the TDTS ($\Delta G^\ddagger = 26.2 \text{ kcal}\cdot\text{mol}^{-1}$) and virtually isoenergetic with **IIIa_{qt}-(OH)₂_{int}**, forming the O-O bond. Considering the lowest Fe^{IV}-oxo isomer ([Fe^{IV}(O)(OH₂)(Pytacn)]²⁺) as the starting point of the reaction, the barrier increases up to 28.3 kcal·mol⁻¹. Thus, this mechanism is kinetically unviable. The reaction evolves through the S = 2 potential energy surface. For the S = 0 energy surface, only the concerted transition state (**TSa_{qt}-(OH)₂_{int}**: $\Delta G^\ddagger = 51.8 \text{ kcal}\cdot\text{mol}^{-1}$, Figure SI.5 of ref. 213) has been located, which is too high in energy to be directly involved in the O-O bond formation event. Finally, the **b** tautomer of [Fe^{IV}(OH)(OH)(Pytacn)]²⁺ presents a very similar free energy profile with a free energy barrier for the O-O bond formation step of 33.3 kcal·mol⁻¹ (see Figure SI.6 of ref. 213), which again is too high to occur at room temperature.

Table 7: Selected Mulliken spin densities and bond distances for the stationary points obtained in the formation of the O-O bond by external water nucleophilic attack to S = 2 [Fe^{IV}(OH)(OH)(Pytacn)]²⁺ complex.

					
	Ia_{qt}-(OH)₂_{int}	TSa_{(I-II)qt}-(OH)₂_{int}	IIa_{qt}-(OH)₂_{int}	TSa_{(II-III)qt}-(OH)₂_{int}	IIIa_{qt}-(OH)₂_{int}
$\rho(\text{Fe})$	3.49	4.29	4.30	3.97	3.82
$\rho(\text{O}_a)$	0.13	-0.34	-0.05	0.00	0.01
$\rho(\text{O}_b)$	0.01	-0.56	-0.79	-0.23	0.00
$\rho(\text{O}_c)$	0.18	0.13	0.07	0.03	0.02
$d(\text{Fe}-\text{O}_a)^b$	1.76	2.00	1.89	1.99	2.22
$d(\text{O}_a-\text{O}_b)^b$	2.67	2.14	2.12	1.64	1.46

[a] L₁ stands for the Pytacn ligand. [b] Bond lengths are given in Å.

5.2.4 Comparison with the catalytic cycle proposed by Kasapbasi *et al.*

While our computations are quite conclusive in showing that the iron(IV)-oxo species [Fe^{IV}(O)(OH)(Pytacn)]⁺, [Fe^{IV}(O)(OH₂)(Pytacn)]²⁺ and [Fe^{IV}(OH)(OH)(Pytacn)]²⁺ cannot form the O-O bond and oxidize the water molecule, a recent report by Kasapbasi *et al* indicated otherwise (Figure 84). A close analysis of this work shows that the thermodynamic driving force of the catalytic cycle depends on the energy gain of the protonation of nitrate anions. The authors proposed that a nitrate anion present at the coordination sphere of the reduced CAN acts as a Brønsted base to form the [Fe^{IV}(O)(OH)(Pytacn)]⁺ complex. This species performs the O-O bond formation event, through the nucleophilic attack of a solvent water molecule to the Fe^{IV}=O moiety. The protonation of the formed hydroperoxo ligand leads to the release of hydrogen peroxide, which is oxidized to molecular oxygen by Ce^{IV}, and generates an open vacant site on the iron center. In the next step, the water molecule occupies the free vacant site to form a [Fe^{IV}(OH₂)₂(Pytacn)]⁴⁺ intermediate. Finally, the nitrate ions abstract two protons of the Fe^{IV} aqua complex to recover the resting state species.

From a methodological point of view, one of the main differences between the present work and that of Kasapbasi *et al* is how the solvent effect has been computed. In the latter case, the conductor polarizable continuum model (CPCM) was employed,²¹⁶ without consideration of any explicit water molecule. However, this methodology cannot describe accurately the hydrogen bonds and dispersion effects present in the water media. The hydrogen bonding needs to be considered, especially when protic solvents are involved directly in the reaction and the studied mechanistic step releases or captures protons.^{27,196} Furthermore, the enthalpy and entropy corrections, which may be decisive to ensure an accurate description of the thermodynamics and kinetics of the WO reaction, were not included in Kasapbasi calculations. To clarify these points, we have examined and found a very strong dependence of the DFT reaction free energy of the nitrate protonation depending on the number of explicit water molecules included in the proton first solvation shell. The influence of the number of explicit water molecules of the proton first solvation shell on the acidic character of the HNO₃ in aqueous phase is summarized in Table 8 (see Figure SI.7 of ref. 213) for the proton hydrated cluster geometries).

Table 8: Free energy differences (ΔG) and pK_a values for the proton dissociation of HNO₃ assisted by several water clusters.

	ΔG (kcal·mol ⁻¹)	pK _a ^a
HNO₃	125.7 (270) ^b	93.5 (199.4) ^b
HNO₃ + H₂O	10.0	7.4
HNO₃ + 2H₂O	2.1	1.5
HNO₃ + 3H₂O	-1.9	-1.4
Exp.	-1.9	-1.4

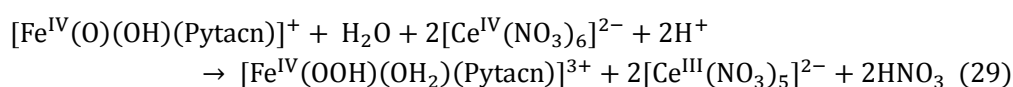
[a] The pK_a values are evaluated at room temperature and atmospheric pressure. [b] In parenthesis are shown the electronic energy difference obtained from ref. 208 and the corresponding pK_a value. [c] Experimental pK_a obtained from reference 217.

The pK_a of the gas phase deprotonation process is very far from the experimental value due to the description of the proton as a free ion. This large deviation is even true if solvent effects are included only through an implicit solvation model, showing the weakness of the SMD model for this case of study. Neither addition of enthalpy and entropy corrections allows reproducing the experimental observed behavior. The results clearly improve by the inclusion of one explicit water

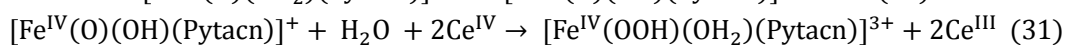
molecule, but still unreliable pK_a values (7.4) were obtained. A more accurate pK_a result (1.5) was obtained by the inclusion of two water molecules, already reproducing the strong acidic behavior of the nitric acid. But with three explicit water molecules the experimental HNO₃ pK_a value is nicely reproduced. Furthermore, the HNO₃ pK_a values show a clear rapid convergence respect to the number of explicit water molecules included in the proton solvation shell.

Consideration of the enthalpy and entropic corrections and three explicit water molecules into the calculations makes nitrate ions poor hydrogen atom acceptors, as it may actually be expected considering the low experimental pK_a of HNO₃ (-1.4). It must be emphasized that the origin of the acid/base character of nitrate species specifically falls in the correct description of the solvated free protons in the bulk water solvent, not in the solvation effects on the NO₃⁻ itself. The microsolvation on the whole system (nitrate + proton) was also explored, leading to its expected acid character when the number of explicit molecules increases (See Table SI.2 and Figures SI.8-9 of ref. 213). The consequence of the inclusion of explicit water molecules in the calculations is that the driving force for the water oxidation reaction proposed by Kasapbasi and co-workers, i.e. the protonation of nitrate anions, is removed. Then, the reaction of [Fe^{IV}(O)(OH)(Pytacn)]⁺ and [Fe^{IV}(O)(OH₂)(Pytacn)]²⁺ with water becomes computationally unfeasible under ambient experimental conditions.

Although the present study discards the WNA mechanism on a Fe^{IV}=O moiety, we cannot ignore the possible involvement of CAN species in the O-O bond formation event. Kasapbasi *et al* proposed that [Ce^{IV}(NO₃)₆]²⁻ could accept the two electrons transferred during the WNA on the oxo moiety of [Fe^{IV}(O)(OH)(Pytacn)]⁺, allowing the formation of a [Fe^{IV}(OOH)(OH₂)(Pytacn)]³⁺ intermediate (Eq. 29). Thus, to corroborate the viability of this process, we evaluated the free energy of this reaction at our more accurate level of calculation, obtaining indeed the exergonic character observed by Kasapbasi *et. al.* (ΔG = -283.0 kcal·mol⁻¹). However, as explained above, the free energy of solvation for a free proton is not correctly described in the SMD model, and the experimental value must be used, which strongly decreases the exergonic character of the reaction (ΔG = -23.1 kcal·mol⁻¹). Nevertheless, from a thermodynamic point of view, this reaction is feasible at room temperature.

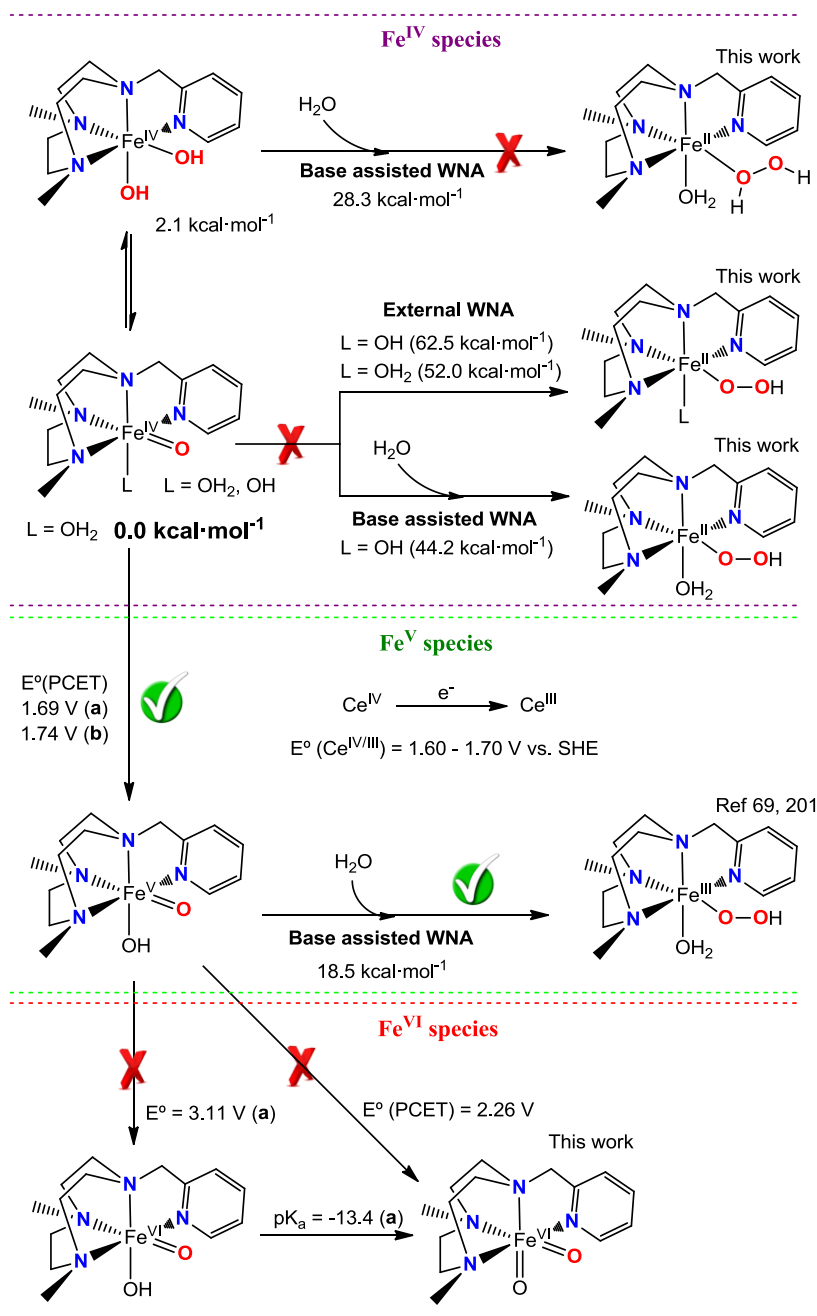


But the nature of Ce nitrate species in aqueous solution are not well known, and then free energy change obtained from the DFT calculation of [Ce^{IV}(NO₃)₆]²⁻ and [Ce^{III}(NO₃)₅]²⁻ may not be reliable. A more realistic energy balance can be obtained taking into account the free energy obtained from the experimental Ce reduction potential (E° = 1.61 V vs. SHE at pH = 1), giving a slightly endergonic but still feasible process when the deprotonation step is considered (Eq. 30-31, ΔG = 3.4 kcal·mol⁻¹). However, as we have previously shown, the O-O bond formation catalyzed by [Fe^{IV}(O)(OH)(Pytacn)]⁺, is kinetically not allowed at catalytic conditions.



The theoretical data suggest a WO catalytic cycle where the oxidizing power of the Ce^{IV} is the driving force of the reaction. This sacrificial oxidant may allow the generation of highly electrophilic Fe^V=O species, which catalyzes the O-O bond formation event. This hypothesis was corroborated

evaluating the energetic accessibility of the V oxidation state through the calculation of the PCET redox potential from $[\text{Fe}^{\text{IV}}(\text{O})(\text{OH}_2)(\text{Pytacn})]^{2+}$ to $[\text{Fe}^{\text{V}}(\text{O})(\text{OH})(\text{Pytacn})]^{2+}$ species. The $E^\circ(\text{PCET})$ value at $\text{pH} = 1$ does not change significantly between tautomer **1** (1.69 V vs. SHE) and **1b** (1.74 V vs. SHE), and fall into the interval of 1.6-1.7 V vs. SHE associated with the reduction potential of Ce^{IV} under catalytic conditions.²⁰¹ Therefore, CAN presents enough oxidizing power to reach the $[\text{Fe}^{\text{V}}(\text{O})(\text{OH})(\text{Pytacn})]^{2+}$ species. We had previously presented that $[\text{Fe}^{\text{V}}(\text{O})(\text{OH})(\text{Pytacn})]^{2+}$ species have a viable energy barrier for the O-O bond formation of $18.5 \text{ kcal}\cdot\text{mol}^{-1}$.²⁰¹ Finally, the oxidation potential to reach the $[\text{Fe}^{\text{VI}}(\text{O})(\text{OH})(\text{Pytacn})]^{3+}$ and $[\text{Fe}^{\text{VI}}(\text{O})(\text{O})(\text{Pytacn})]^{2+}$ species were also calculated, obtaining values of $E^\circ = 3.11 \text{ V}$ and 2.26 V , which are far from the oxidizing capacity of CAN ($E^\circ = 1.61 \text{ V}$ at $\text{pH} = 1$). Altogether, the data presented clearly illustrate that the O-O bond formation likely could not directly occur by the $\{\text{Fe}^{\text{IV}}(\text{Pytacn})\}$ nor by $\{\text{Fe}^{\text{VI}}(\text{Pytacn})\}$ species. Thus, both experimental and DFT evidences point $[\text{Fe}^{\text{V}}(\text{O})(\text{OH})(\text{Pytacn})]^{2+}$ species as the most likely responsible for the O-O bond formation event under catalytic conditions.



Scheme 5: Summary of all the O-O bond formation pathways involving $\text{Fe}^{\text{IV}}(\text{O})$ and $\text{Fe}^{\text{V}}(\text{O})$ species. The lowest energy barrier for the O-O bond formation starting from $\{\text{Fe}^{\text{IV}}\}$ species is around 28 kcal·mol⁻¹. In addition, we also reported that the redox couple $\text{Fe}^{\text{V/VI}}$ is not accessible under catalytic conditions. The redox values are relative to the SHE electrode at pH = 1. The free energies of the TS are relative to the $[\text{Fe}^{\text{IV}}(\text{O})(\text{OH}_2)(\text{Pytacn})]^{2+}$ and $[\text{Fe}^{\text{V}}(\text{O})(\text{OH})(\text{Pytacn})]^{2+}$, respectively. The WNA stands for Water Nucleophilic Attack.

Our computational results confirm the kinetic unviability of $[\text{Fe}^{\text{IV}}(\text{O})(\text{OH})(\text{Pytacn})]^+$, $[\text{Fe}^{\text{IV}}(\text{O})(\text{OH}_2)(\text{Pytacn})]^{2+}$ and $[\text{Fe}^{\text{IV}}(\text{OH})(\text{OH})(\text{Pytacn})]^{2+}$ species to perform the O-O bond formation event at room temperature, as well as the high endergonic nature of the intermediates formed after the O-O bond formation. These results are in complete agreement with the experimentally observed inactivity of $[\text{Fe}^{\text{IV}}(\text{O})(\text{OH}_2)(\text{Pytacn})]^{2+}$ species in aqueous solution, and discarding the formation of H_2O_2 . Thus, our results also reject the viability of WOC cycles based on

the feasibility of monomeric and dimeric $\text{Fe}^{\text{IV}}(\text{O})$ species to catalyze the formation of the O-O bonds. Furthermore, our results show that Fe^{VI} species are not accessible under catalytic conditions. On the contrary, our investigations have previously highlighted the need to access the high oxidation state $[\text{Fe}^{\text{V}}(\text{O})(\text{OH})(\text{Pytacn})]^{2+}$ species in order to yield the O-O bond formation, providing more confidence on the WOC mechanistic proposal involving $\text{Fe}^{\text{V}}(\text{O})$ as the active species (Scheme 3). Moreover, the results indicate that the introduction of an internal base in the coordination sphere of the iron complex reduces the energy of the O-O bond formation barrier. These results clearly have implications on the future design of iron based catalysts for WO.

This work also highlights the key importance of the explicit treatment of the hydrogen bonding network between the solvent molecules and the protons to achieve a good correlation with experimental data. Finally, our results demonstrated that the proposed catalytic cycle of Kasapbasi *et al* do not correctly describe the WO mechanism performed by iron complex **1** in condensed phase.

CHAPTER 6:

WATER OXIDATION REACTION MECHANISM WITH N-PENTADENTATE IRON CATALYSTS^a

^a This chapter is based on the publication: Codolà, Z.; Acuña-Parés, F.; Casadevall, C.; Luis, J.M.; Costas, M.; Lloret-Fillol, J. A new N-pentadentate iron (II) complex as an active homogeneous catalyst for water oxidation. *In manuscript*.

6. Water oxidation reaction mechanism with N-pentadentate iron catalysts.

The effect of a *cis* anionic group and the ligand coordination mode on the energetic feasibility of the iron catalysed WO reaction was considered to *in silico* design the first WO iron complex based on a *N*-pentadentate ligand. In this chapter, the WO mechanism by the new iron system, $[\text{Fe}^{\text{II}}(\text{AQ}^{\text{Me}_2}\text{tacn})](\text{OTf})$ ($\text{AQtacn} = N$ -(quinolin-8-yl)acetamidyl) has been explored. The complex $[\text{Fe}^{\text{III}}(\text{dpaq})(\text{H}_2\text{O})]^{2+}$ is also considered to understand the effect of the *trans/cis* relative position of the anionic group respect to the oxo ligand on the O-O bond formation event.

CHAPTER 7:

IRON-CERIUM ADDUCTS AS INTERMEDIATES IN THE WATER OXIDATION REACTION^a

^a This chapter is based on the publication: Acuña-Parés, F.; Luis, J.M.; Lloret-Fillol, J.; Christopher, C. Iron-cerium adducts as intermediates in the water oxidation reaction. *In manuscript*.

7. Iron-Cerium adducts as intermediates in the water oxidation reaction.

In chapters 4 and 5, we unravel that $\text{Fe}^{\text{V}}=\text{O}$ species may be generated under catalytic conditions when CAN is used as a sacrificial oxidant. It is always supposed that CAN behave as an outer sphere one electron oxidant. However, our group recently reported the first example of a well-characterized an inner-sphere metal-Ce(IV) complex active in water oxidation. The complex is formed in water oxidation conditions and composed by a non-heme iron complex ($\alpha\text{-}[\text{Fe}^{\text{II}}(\text{CF}_3\text{SO}_3)_2(\text{mcp})]$) and cerium(IV). The aim of this chapter is the computational study of the structure of this unprecedented Fe-Ce adduct (with general formula $[(\text{mcp})\text{Fe}^{\text{IV}}(\text{O})(\mu\text{-O})(\text{Ce}^{\text{IV}})(\text{H}_2\text{O})_n(\text{OH})_m]$) and their possible involvement in the WO catalysis. This model includes an essential feature not fully understood in the natural photosynthesis, a Lewis acid cation (Ce^{IV} or Ce^{III}).

CHAPTER 8:

H₂ VERSUS ORGANIC SUBSTRATE OXIDATION BY HIGH VALENT NON-HEME IRON SPECIES^a

^a This chapter is based on the publication: Hassanpour, A.; Acuña-Parés, F.; Luis, J.M.; Cussó, O.; Morales-delaRosa, S.; Campos Martín, J.M.; Fierro, J.L.G.; Costas, M.; Lloret-Fillol, J.; Mas Balleste, R. *Chem. Commun.* **2015**, *51*, 14992.

8. H₂ versus organic substrate oxidation by high valent non-heme iron species.

The theoretical data exposed in the previous chapters reveals that Fe^V(O) species with *cis* or *trans* anionic positions relative to the oxo group are capable to catalyse the water oxidation reaction. Herein, the quantum mechanical study focuses on the capacity of the α -[Fe^{II}(CF₃SO₃)₂(mcp)] upon reaction with H₂O₂ to oxidize H₂ to H₂O. The generated [Fe^V(O)(OH)(mcp)]²⁺ species may activate the molecular hydrogen, even in presence of organic substrates, while the addition of acetic acid in the reaction media leads to the generation of formal [Fe^V(O)(OAc)(mcp)]²⁺ species incapable to cleavage the H-H bond. This computational study corroborates the powerful oxidative character of high-valent iron non-heme complexes to activate small molecules. However, the capacity of Fe^V species to oxidize H₂ could suppose an inconvenient if these kinds of compounds are incorporated in water splitting devices.

8.1. State-of-the-art

In the last decade, several bioinspired iron and manganese complexes based on aminopyridine ligands have been developed as catalysts for oxidation reactions.²⁴⁸ Among these compounds, tetradentate iron complexes with two *cis* labile positions have been widely used to catalyse a variety of reactions like water oxidation, the stereospecific hydroxylation of alkanes and the *cis*-dihydroxylation of olefins.¹⁹¹ The proposed mechanism for olefin and C-H hydroxylation by putative [Fe^V(O)(OH)]²⁺ species involves a non-concerted 2+3 transition state to generate the alcohol product.^{249,250} A similar but concerted 2+3 mechanism has been proposed for H₂ activation by tetradentate nitrogen based OsO₄ complexes.²⁵¹ Moreover, it is known that other metal-oxo species can break the H-H bond through an analogous concerted mechanism,²⁵² in which no metal-hydrogen interaction occurs during the strong H-H bond cleavage. Taking into account the mechanistic resemblance between OsO₄ and [Fe^V(O)(OH)]²⁺, Mas-Ballesté and coworkers proposed that the latter species may be also capable to oxidize the H₂ molecule to water through a 2+3 concerted mechanism.²⁵³

This hypothesis was corroborated analyzing the changes in the yields of well-known model reactions such as C-H hydroxylation, epoxidation and sulfide oxidation experimented by cyclohexane, cyclooctene and thioanisole substrates, when H₂ gas is introduced in the reaction media. The experiments carried out with α -[Fe^{II}(CF₃SO₃)₂(mcp)] as catalyst and H₂O₂ as oxidant, in 1 atm of H₂ in acetonitrile, reveal that the yields of oxidation of cyclohexane and cyclooctene are reduced by more than 60% and approx. 40%, respectively. However, the yield of oxidation of thioanisole only decreased by 20%. These differences are consistent with the H₂ competitive oxidation reaction, which clearly reduces the yield of oxidation of less reactive substrates (cyclohexane and cyclooctene). In contrast, the easiest sulphide oxidation reaction is not significantly affected by the presence of H₂. The competitive substrate role of molecular hydrogen was also confirmed repeating the same experiments under different H₂ pressures, revealing that the generation of cyclohexanol decreases as the H₂ pressure increases until no cyclohexanol production was detected at 10 atm of H₂. Further confirmation of the inhibiting effect of H₂ was determined through isotopic labelling studies. The product of the hydrogen oxidation by the active high-valent iron species Fe^V(O)(OH) should be a water molecule and experiments with D₂ clearly revealed the production of HDO deuterated water molecules.

The addition of acid acetic in the reaction mixture at 1 atm of H₂ pressure hinders the oxidation of H₂ by α -[Fe(CF₃SO₃)₂(mcp)]. On the contrary, the acetic acid addition has no significant effect on

α -[Fe(CF₃SO₃)₂(mcp)] catalytic oxidation activity of cyclohexane, cyclooctene and thioanisole substrates. Furthermore, the catalytic cyclohexane oxidation in presence of acetic acid at different H₂ pressures reveals that the generation of cyclohexanol is not totally inhibited even at 10 atm of H₂. In light of previous observations, it was postulated the formation of Fe^V(O)(OAc) species capable of C-H hydroxylation and olefin epoxidation reactions²⁵⁴ but not enough reactive to activate the molecular hydrogen gas. Therefore, the experimental data suggest that, although Fe^V(O)(OH) and Fe^V(O)(OAc) species are good catalysts to oxidize organic substrates, only the *cis*-(O)(OH) intermediate has an enhanced oxidative power to activate the molecular hydrogen (Figure 109).

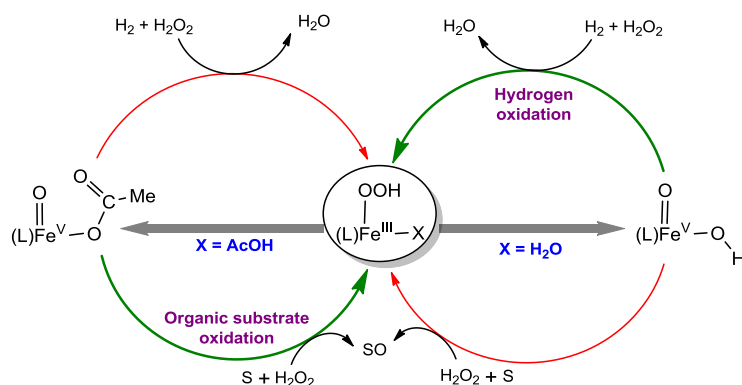
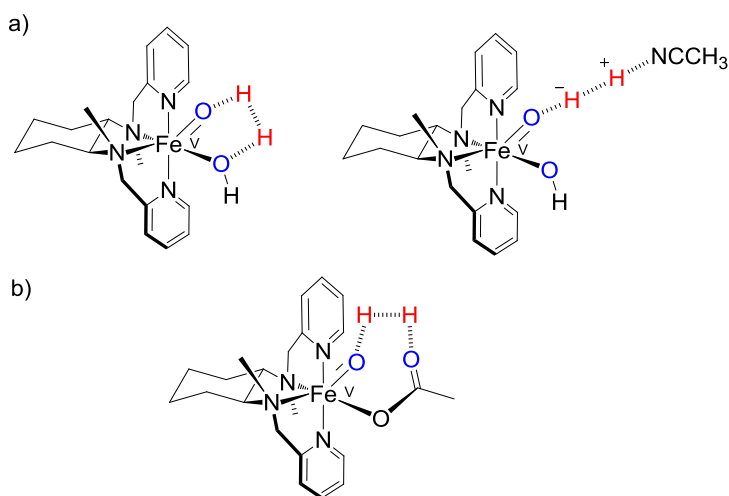


Figure 109: Experimentally proposed oxidation reactions and active species when acetic acid is present (left) or absent (right) in the reaction media. Green arrows indicate the most favorable reaction pathways. L stands for the mcp ligand.

To rationalize the inhibition of organic substrate oxidation reactions in presence of H₂ and the reverse reactivity trend observed when acetic acid is present, the hydrogen activation mechanisms by high valent iron species [Fe^V(O)(X)(mcp)]²⁺ (X = OH⁻ or AcO⁻) have been analyzed by means of DFT calculations (Scheme 7). Related with the previous chapters, the consequences of this catalytic behavior in the development of water splitting devices based on aminopyridine iron complexes are also discussed.



Scheme 7: a) Possible 2+3 homolytic H-H and heterolytic bond breaking mechanisms catalyzed by [Fe^V(O)(OH)(mcp)]²⁺ species. b) 2+4 homolytic mechanism for [Fe^V(O)(OAc)(mcp)]²⁺.

8.2. Results and discussion

The density functional theory study was carried out using the Gaussian09 software package²⁵⁵ and the B3LYP hybrid exchange-correlation functional.¹⁷⁶ Optimizations were performed with the 6-31G(d,p) 6d basis set for all atoms. Solvent effects were taken into account in geometry optimizations and energies through the SMD polarizable continuum model, with acetonitrile as implicit solvent.¹⁸⁰ Dispersion effects were also introduced with the Grimme-D₂ correction.¹⁸¹ The nature of the located stationary points was established by frequency calculations in solvent phase, where transition states have only one imaginary frequency. The electronic potential energies were further refined by single-point calculations with the cc-pVTZ Dunning basis set for all atoms. All calculations employed the spin-unrestricted formalism and spin-contaminated energies were systematically corrected ($E_{\text{spin corr.}}$) using the equations described in reference 187. The final free energy (G) was obtained by adding the following terms to the spin corrected potential energy $E_{\text{spin corr.}}$:

$$G = E_{\text{spin corr.}} + G_{\text{solv.}} + G_{\text{corr.}} + G_{\text{disp.}} \quad (37)$$

where $G_{\text{solv.}}$ and $G_{\text{disp.}}$ are the solvation and dispersion corrections, respectively. Thermal plus entropy corrections at 298.15 K were obtained from solvent phase frequency calculations at B3LYP/6-31G(d,p) level ($G_{\text{corr.}}$). In the H₂ activation energy profiles, all calculated solvation free energies use a standard state liquid phase concentration of 1 M, but for acetonitrile itself a 19.1 M standard state was employed. The free energy change associated with moving from a standard-state gas phase pressure of 1 atm to a standard state gas phase concentration of 1 M (19.1 M for acetonitrile) was calculated ($\Delta G^{o/*}$). The value of $\Delta G^{o/*}$ at 298.15 K is 1.9 kcal·mol⁻¹ for 1 M standard state solutes and 3.6 kcal·mol⁻¹ for 19.1 M standard state acetonitrile.

Labels **I**, **TS** and **II** were used as short nomenclature of reactant complexes, transition states and products involved in the H-H bond breaking event. The **homo** and **heter** notations are related to the homolytic or heterolytic nature of the H-H bond cleavage. Labels **d**, **q** and **sext** are used to specify the doublet, quartet and sextuple spin state of the iron center.

8.2.1 H-H bond cleavage mechanisms for $[\text{Fe}^{\text{V}}(\text{O})(\text{OH})(\text{mcp})]^{2+}$

By analogy with the H₂ activation mechanism followed by high valent metal-oxide species of group VIII,²⁵² the putative Fe^V(O)(OH) may trigger the H-H bond cleavage through a base assisted 2+3 homolytic or heterolytic reaction pathways (see Scheme 7). In the former, the H₂ molecule interacts simultaneously with the oxo and the hydroxo/acetate internal base and it breaks into its atomic constituents. In the later mechanism, an acetonitrile solvent molecule is explicitly considered to act as an external proton acceptor and a hydride fragment is transferred to the Fe=O moiety. In Figure 110, the lowest free energy profiles of the two H-H bond cleavage mechanisms are represented. The heterolytic mechanism mainly evolves in the $S = 3/2$ spin state free energy profile. The reaction starts with the simultaneous interaction between the oxo moiety of $[\text{Fe}^{\text{V}}(\text{O})(\text{OH})(\text{mcp})]^{2+}$, the H₂ and the acetonitrile molecule (Figure 111). The generation of the reactive complex **I_heter_q** has a free energy cost of 7.3 kcal·mol⁻¹ caused by the loss of entropy, with oxo-H₂ and H₂-NCCH₃ distances of 2.53 Å and 2.60 Å, respectively. Then, the hydrogen molecule begins to break in a heterolytic manner until the system reaches the transition state **TS_heter_q** ($\Delta G^{\ddagger} = 21.0$ kcal·mol⁻¹), in which the hydride fragment is being transferred to the oxo ligand ($d(\text{O}-\text{H}) = 1.17$ Å), and the proton starts to migrate to the cyano group of the acetonitrile molecule ($d(\text{H}-\text{NCCH}_3) = 2.36$ Å). Finally, a

reduced iron(III)-bishydroxide intermediate, **II_heter_q**, is generated in a clearly exergonic way ($\Delta G = -36.7 \text{ kcal}\cdot\text{mol}^{-1}$).

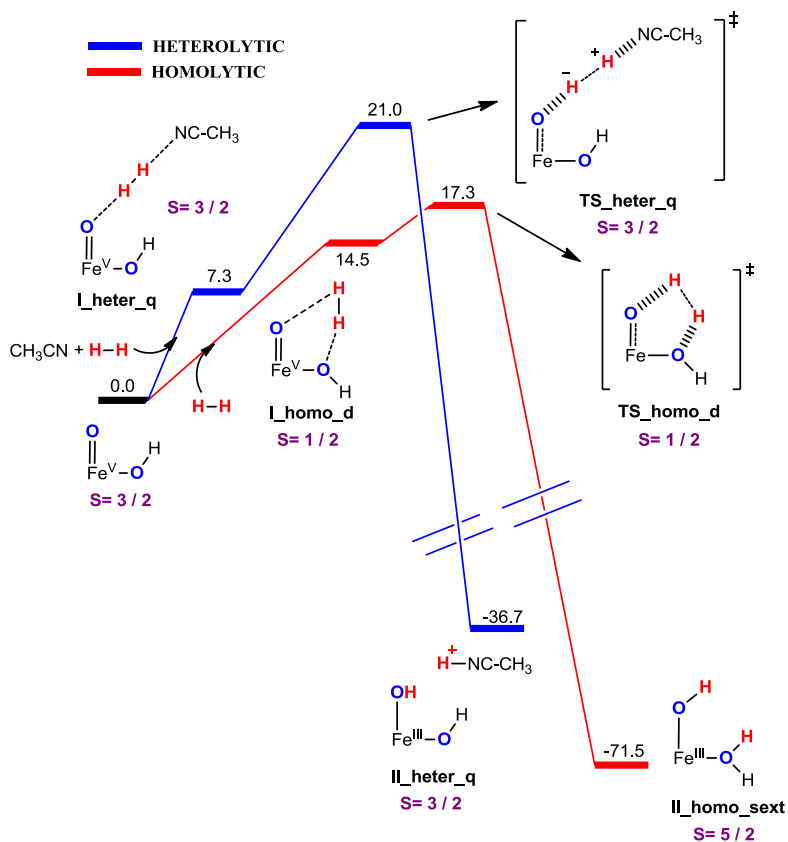


Figure 110: Homolytic vs heterolytic minimum free energy profiles for the H₂ oxidation by [Fe^V(O)(OH)(mcp)]²⁺. All species are labeled with its ground spin state. Gibbs energy values are given in kcal·mol⁻¹.

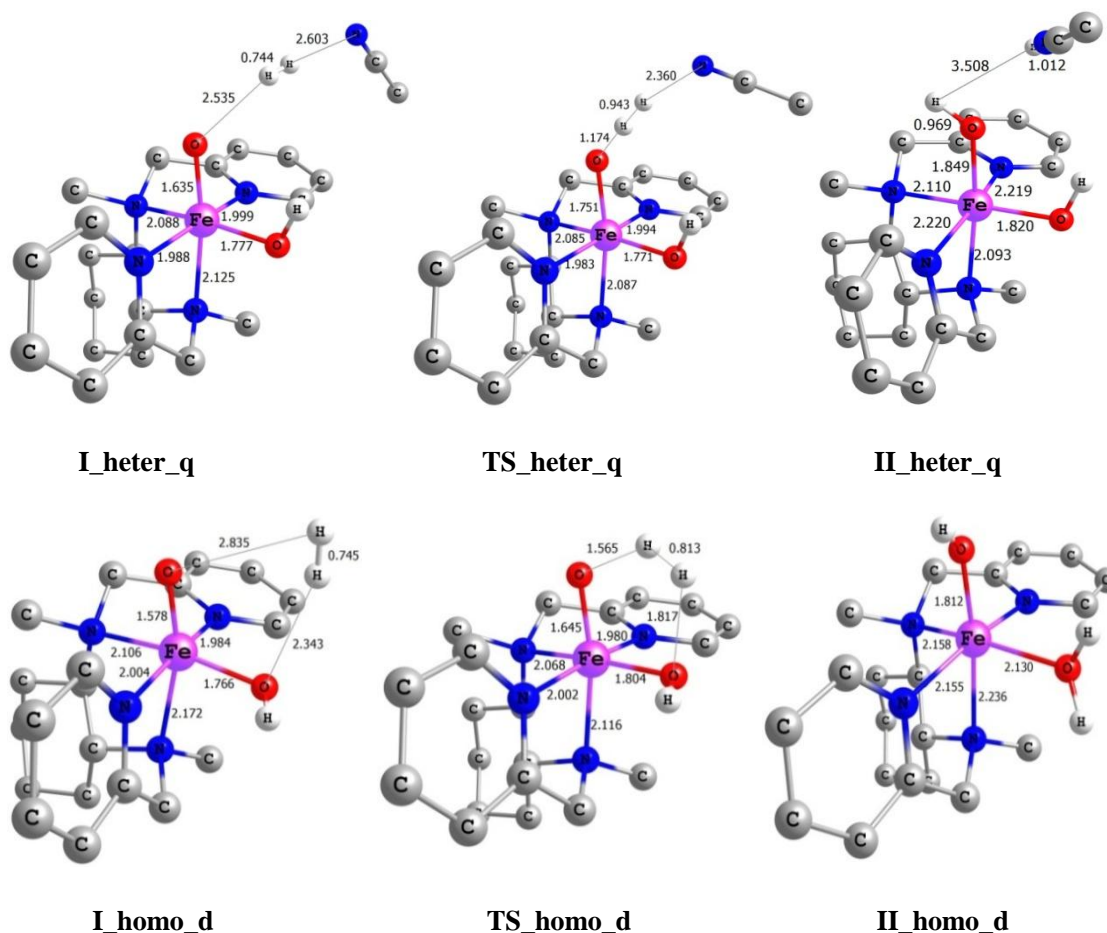
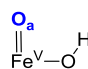
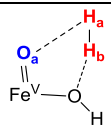
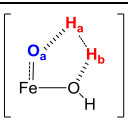
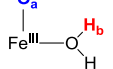


Figure 111: Optimized structures of the ground spin state intermediates and transition states involved in the heterolytic and 2+3 homolytic H-H cleavage mechanisms by $[\text{Fe}^{\text{V}}(\text{O})(\text{OH})(\text{mcp})]^{2+}$. Bond distances in Å. Irrelevant hydrogen atoms are omitted for clarity.

On the other hand, the homolytic mechanism proceeds in the $S = 1/2$ spin state free energy profile. The reactive complex **I_homo_d** presents a H_2 molecule in a parallel disposition respect to the $\text{Fe}=\text{O}$ moiety (Table 10: $d(\text{Fe}=\text{O}_a) = 1.58 \text{ \AA}$ and $\rho(\text{Fe}) = 0.77$), establishing hydrogen bonds with the $-\text{OH}$ and oxo groups ($\Delta G = 14.5 \text{ kcal}\cdot\text{mol}^{-1}$). The previous interaction precedes the cleavage of H_2 and the acceptance of the atomic hydrogen fragments by the oxo and OH terminal ligands (**TS_homo_d**: $\Delta G^\ddagger = 17.3 \text{ kcal}\cdot\text{mol}^{-1}$). The activation of the hydrogen molecule and the concomitant two electron reduction of the $\text{Fe}(\text{O})(\text{OH})$ moiety are reflected by the increase of the $\text{H}_a\text{-H}_b$ and $\text{Fe}=\text{O}_a$ bond distances to 0.81 \AA and 1.64 \AA , respectively, and the increase of the spin density on the metal center ($\rho(\text{Fe}) = 1.48$). After a spin crossing point, the reaction ends with the generation of a $S = 5/2$ $[\text{Fe}^{\text{III}}(\text{OH})(\text{OH}_2)(\text{mcp})]^{2+}$ intermediate in a very exergonic way (**II_homo_sext**: $\Delta G = -71.5 \text{ kcal}\cdot\text{mol}^{-1}$).

Table 19: Mulliken spin population, Fe-O_a and H_a-H_b bond distances for key species involved in the 2+3 homolytic H-H bond activation mechanism for [Fe^V(O)(OH)(mcp)]²⁺ active species.

				
	S = 3 / 2	I_homo_d	TS_homo_d	II_homo_sext
ρ(Fe) ^a	2.13	0.77	1.48	4.24
ρ(O _a) ^a	0.85	0.42	-0.14	0.31
ρ(H _a) ^a	-	0.00	-0.03	0.01
ρ(H _b) ^a	-	0.00	-0.14	0.00
d(Fe-O _a) ^b	1.64	1.58	1.64	1.81
d(H _a -H _b) ^b	-	0.74	0.81	3.01

[a] All values are calculated at the B3LYP(SMD)/6-31G(d,p) level in acetonitrile as solvent. [b] Bond distances are in Å.

The comparison between the homolytic and heterolytic H-H cleavage mechanisms indicate that the internal base assisted behavior of the -OH ligand reduces significantly the barrier for molecular hydrogen activation ($\Delta\Delta G^\ddagger = 3.7 \text{ kcal}\cdot\text{mol}^{-1}$). Therefore, DFT calculations suggest that [Fe^V(O)(OH)(mcp)]²⁺ intermediate is able to promote the H-H cleavage reaction through a 2+3 homolytic mechanism when H₂ gas is added to the reaction mixture, in agreement with experimental data.

8.2.2 Internal base assisted H-H bond cleavage mechanism for [Fe^V(O)(OAc)(mcp)]²⁺

Since [Fe^V(O)(OH)(mcp)]²⁺ follows a 2+3 homolytic H-H bond cleavage mechanism, the capacity of acetate group in [Fe^V(O)(AcO)(mcp)]²⁺ species to accept an hydrogen atom was also explored (Figure 112). The heterolytic H-H bond mechanism performed by [Fe^V(O)(OH)(mcp)]²⁺ species has not been considered, since the acetate group is not enough basic to extract a proton from the H₂ molecule. When acetic acid (AcOH) is added to the reaction crude, the interaction of [Fe^V(O)(OH)(mcp)]²⁺ with AcOH leads to the generation of a S = 1/2 [Fe^{III}(OOAc)(mcp)]²⁺ intermediate (d(O-O) = 1.48 Å) and the release of a water molecule ($\Delta G = -3.9 \text{ kcal}\cdot\text{mol}^{-1}$). After the O-O bond cleavage in [Fe^{III}(OOAc)(mcp)]²⁺, the injected H₂ gas may interact with the Fe^V(O)(OAc) fragment and form **I_homo_AcO_d** ($\Delta G = 4.8 \text{ kcal}\cdot\text{mol}^{-1}$). The kinetic feasibility of the O-O cleavage mechanism was determined by Shaik, Que and co-workers at a similar computational level for the analogous iron complex [Fe^{III}(OOAc)(S,S-PDP)]²⁺.²⁵⁴ The Mulliken spin density analysis on **I_homo_AcO_d** reveal that the Fe^V(O)(OAc) fragment is best described as a Fe^{IV}(O)(AcO·) with a radical delocalized in the acetate ligand, as has been described in previous computational studies (Table 20).²⁵⁴ However, the quartet spin state **I_homo_AcO_q** intermediate is best represented as high valent iron V complex.

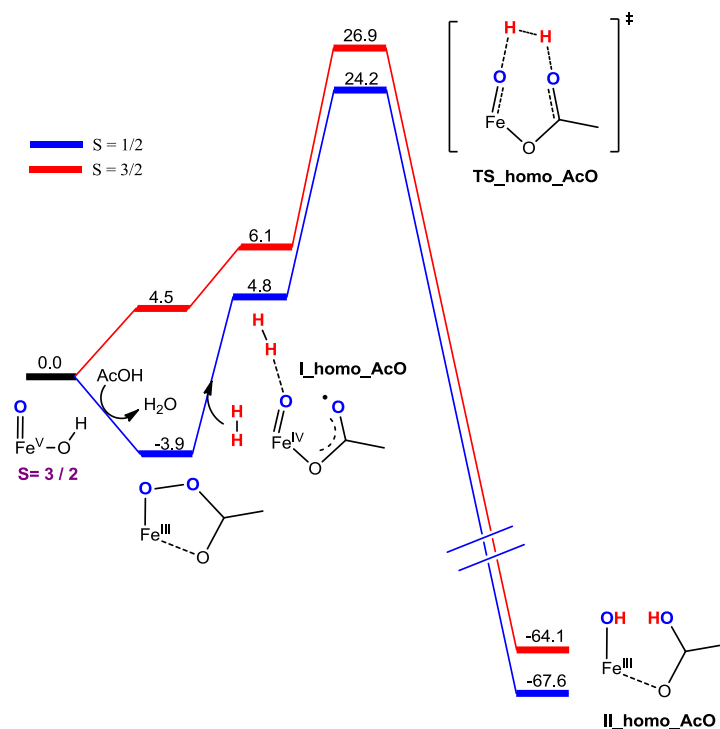


Figure 112: Homolytic H₂ oxidation free energy profiles found for $[\text{Fe}^{\text{IV}}(\text{O})(\cdot\text{OAc})(\text{mcp})]^{2+}$ in the $S = 1/2$ and $3/2$ spin states. Gibbs energy values are given in $\text{kcal}\cdot\text{mol}^{-1}$.

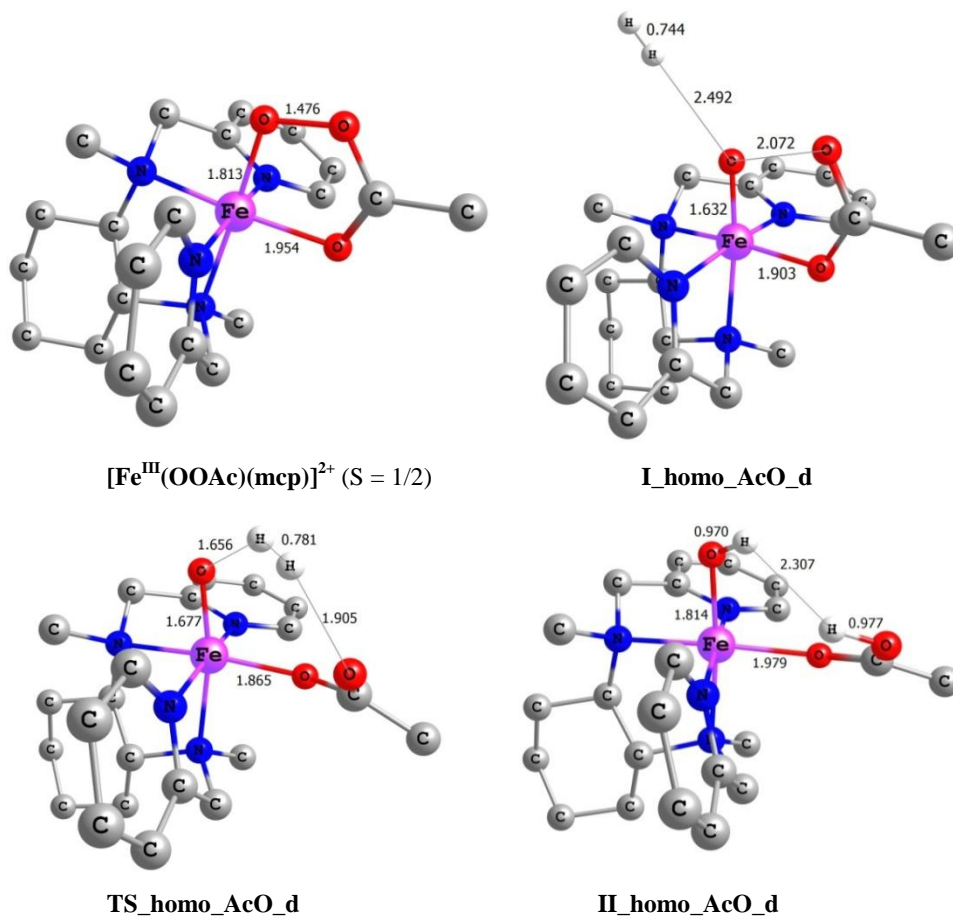
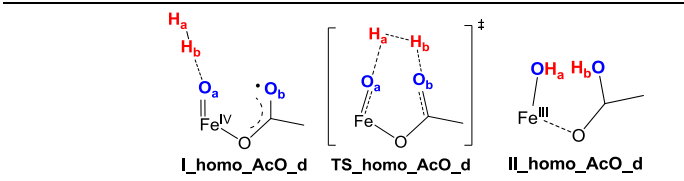


Figure 113: Optimized structures of the ground spin state intermediates and transition states involved in the 2+4 homolytic H-H cleavage mechanism by $[\text{Fe}^{\text{IV}}(\text{O})(\cdot\text{OAc})(\text{mcp})]^{2+}$. Bond distances in Å. Irrelevant hydrogen atoms are omitted for clarity.

The homolytic H-H cleavage mechanism proceeds exclusively in the $S = 1/2$ spin state free energy profile. In the reactive complex **I_homo_AcO_d**, the hydrogen molecule is connected with the Fe=O moiety through a hydrogen bond (Figure 113). Then, the H₂ molecule may rotate to establish a hydrogen bonding interaction with the acetate group and reach the transition state **TS_homo_AcO**, in which the 2+4 homolytic H-H bond cleavage is assisted by the Fe=O and AcO· groups ($\Delta G^\ddagger = 24.2 \text{ kcal}\cdot\text{mol}^{-1}$). The **TS_homo_AcO** presents only slightly elongated H_a-H_b and Fe=O_a bond distances (1.68 Å and 0.78 Å, respectively) respect to their equilibrium values and only 0.28 spin density units have been transferred from H₂ to the Fe=O moiety. In contrast to **TS_homo_d**, the significant free energy associated to **TS_homo_AcO** is related with the distortion of the H-H bond and no appreciable electron density is transferred to the metal complex at this stage of the reaction. Interestingly, the radical character of the acetate ligand in the doublet spin state makes the energy barrier of the H₂ activation ($24.2 \text{ kcal}\cdot\text{mol}^{-1}$) lower than in the quartet spin state ($26.9 \text{ kcal}\cdot\text{mol}^{-1}$). Finally, the H₂ breaks and O-H bond distances gradually decrease until reach the final $[\text{Fe}^{\text{III}}(\text{OH})(\text{AcOH})(\text{mcp})]^{2+}$ species (**II_homo_AcO_d**). The H-H bond cleavage reaction is strongly exergonic ($\Delta G = -67.6 \text{ kcal}\cdot\text{mol}^{-1}$).

Table 20: Mulliken spin populations Fe-O_a and H_a-H_b bond distances for key species involved in the 2+3 homolytic H-H bond activation mechanism for complex $[\text{Fe}^{\text{IV}}(\text{O})(\cdot\text{OAc})(\text{mcp})]^{2+}$.



	I_homo_AcO_d	TS_homo_AcO_d	II_homo_AcO_d
$\rho(\text{Fe})^a$	1.58	1.86	0.99
$\rho(\text{O}_a)^a$	0.00	-0.46	0.09
$\rho(\text{O}_b)^a$	-0.40	-0.05	0.00
$\rho(\text{H}_a)^a$	0.00	-0.02	0.00
$\rho(\text{H}_b)^a$	0.00	-0.13	0.00
$d(\text{Fe}-\text{O}_a)^b$	1.63	1.68	1.81
$d(\text{H}_a-\text{H}_b)^b$	0.74	0.78	2.31

[a] All values are calculated at the B3LYP(SMD)/6-31G(d,p) level in acetonitrile as solvent. [b] Bond distances are in Å.

The most stable species involved in the 2+4 homolytic H-H bond cleavage mechanism is $[\text{Fe}^{\text{III}}(\text{OOAc})(\text{mcp})]^{2+}$. The free energy barrier respect to the previous intermediate is above the kinetic limit at room temperature ($28.1 \text{ kcal}\cdot\text{mol}^{-1}$). Therefore, the computational study clearly indicates that $[\text{Fe}^{\text{IV}}(\text{O})(\cdot\text{OAc})(\text{mcp})]^{2+}$ species cannot catalyse the molecular hydrogen activation reaction. This result is in agreement with the experimentally observed preference of $[\text{Fe}^{\text{IV}}(\text{O})(\cdot\text{OAc})(\text{mcp})]^{2+}$ to oxidize organic molecule even if H₂ is present in the reaction media.

To conclude, it is known experimentally that the reaction of $\alpha\text{-}[\text{Fe}^{\text{II}}(\text{CF}_3\text{SO}_3)_2(\text{mcp})]$ with H₂O₂ lead to the generation of formal $[\text{Fe}^{\text{V}}(\text{O})(\text{OH})(\text{mcp})]^{2+}$ species. The previous intermediate is enough electrophilic to abstract hydrogen atoms from the organic substrates. However, when H₂ gas is added to the reaction mixture, the oxidation reaction is inhibited. DFT calculations suggest that the origin of this phenomenon may be related with the competition between H₂ and organic substrate oxidation. The mechanistic study indicates that $[\text{Fe}^{\text{V}}(\text{O})(\text{OH})(\text{mcp})]^{2+}$ species is capable to catalyze the molecular hydrogen oxidation following a 2+3 homolytic mechanism, in which the oxo and OH ligands act as internal bases. On the other hand, when acetic acid is added, the oxidation of organic

substrates always occurs, even if H₂ is present in the reaction media. The computational data indicates that the AcOH promotes the generation of radical $[\text{Fe}^{\text{IV}}(\text{O})(\cdot\text{OAc})(\text{mcp})]^{2+}$ species. The 2+4 homolytic H-H bond cleavage mechanism by $[\text{Fe}^{\text{IV}}(\text{O})(\cdot\text{OAc})(\text{mcp})]^{2+}$ is kinetically unfeasible under reaction conditions. Therefore, when $[\text{Fe}^{\text{IV}}(\text{O})(\cdot\text{OAc})(\text{mcp})]^{2+}$ is the active species, no competition may exist between H₂ and organic substrate oxidation and the later reaction is always preferred.

This study shows the capacity of high valent iron aminopyridine complexes to activate small molecules. However, the oxidation of H₂ by the Fe^V(O)(OH) fragment could suppose an inconvenience for the construction of water splitting devices. The decomposition of water into H₂ and O₂ implies a synergetic effect between water and proton reduction catalysts. If the water oxidation catalyst interacts with the H₂ generated in the reductive side, then the water splitting device becomes inoperative for molecular hydrogen production. Therefore, a new generation of iron complexes must be designed to overcome this deficiency and take advantage of the high reactivity of Fe^V(O) species.

CHAPTER 9:

INFLUENCE OF THE METAL IDENTITY AND SOLVENT ON THE PROTON REDUCTION ACTIVITY OF AMINOPYRIDINE COMPLEXES^a

^a This chapter is based on the publication: Call, A.; Codolà, Z.; Acuña-Parés, F.; Lloret-Fillol, J. *Chem Eur J.* **2014**, *20*, 6171.

9. Influence of the metal identity and solvent on the proton reduction activity of aminopyridine complexes.

In the first part of the thesis, the effect of the ligand coordination and mode on the WO activity of iron aminopyridine complexes has been unraveled by means of computational methods. DFT calculations show how the high chelating and electro-donating ability of aminopyridine complexes promotes the stabilization of a high oxidation state on the iron center. The chelating ability of the ligand may be also beneficial for the design of metal complexes with proton reduction activity. Moreover, the development of water splitting devices requires the synergism between the WO and proton reduction homogenous catalysts and analogous structural motifs for both systems may enhance compatibilities among them. However, most of the proposed proton reduction mechanisms by polypyridine based metal complexes usually involve intermediates in a low oxidation state (M^I or M^0). Therefore, the introduction of electron-withdrawing substituents results necessary to stabilize the low oxidation states without disrupting the high chelating nature of the ligand.

With this consideration in mind, our group synthesized the pentadentate ligand 1,4-di(picoly)-7-(*p*-toluenesulfonyl)-1,4,7-triazacyclononane ($Py_2^{Ts}tacn$) and the corresponding cobalt, nickel and iron complexes. The combination of experimental data and computational studies has revealed the effect of the solvent and the identity of the metal center on the proton reduction activity. The extracted information from these systems provides valuable information about the metal-ligand cooperation and its influence on the proton reduction reaction.

9.1. State-of-the-art

Recently, Lloret et. al. reported the synthesis, characterization and proton/water reduction activity of new cobalt (**1Co^{II}**), nickel (**1Ni^{II}**) and iron (**1Fe^{II}**) aminopyridine complexes based on the pentadentate $Py_2^{Ts}tacn$.¹⁴¹ The three complexes are excellent electrochemical catalysts for proton reduction in acetonitrile when using trifluoroacetic acid (TFA) as source of protons, while only cobalt complexes are efficient photochemical active catalysts in a solvent CH_3CN/H_2O (3:7) mixture, using $[Ir(ppy)_2(bpy)]PF_6$ (**PSIr^{III}**) as photosensitizer and Et_3N as electron donor.

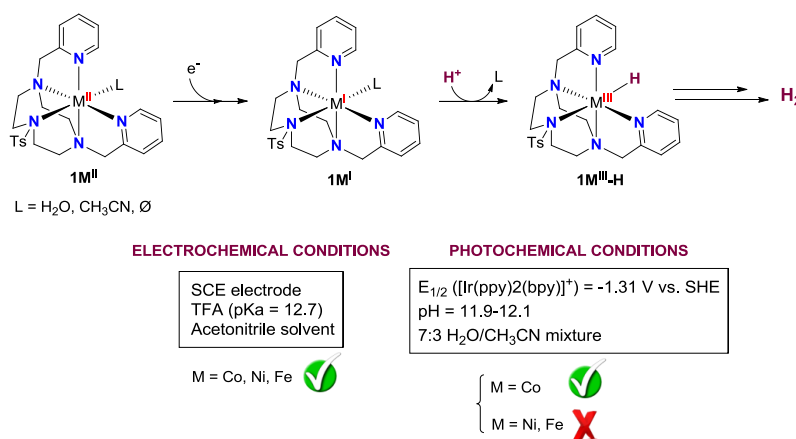


Figure 115: Experimentally proposed mechanism for the generation of metal-hydride active species under photochemical and electrochemical conditions. The reactivity differences between **1Co^{II}**, **1Ni^{II}** and **1Fe^{II}** complexes are shown.

The water reduction activity of the aminopyridine metal complexes under photochemical conditions was analyzed by UV-Vis spectroscopy. The monitoring of the **PSIr^{III}** reductive quenching to form **PSIr^{II}**, and the subsequent addition of one equivalent of **1Co^{II}**, **1Ni^{II}** or **1Fe^{II}**,

reveal that the formation of reduced species $\mathbf{1Co}^I$ and $\mathbf{1Ni}^I$ is favored. However, the $\mathbf{1Ni}^I$ intermediate may not evolve to the corresponding hydride active species (Figure 115). In contrast, it was proposed that the inability of \mathbf{PSIr}^{II} to generate the $\mathbf{1Fe}^I$ intermediate makes the iron complex photochemically inactive in H_2 generation. To provide some light on the reactivity differences among the $\mathbf{1M}$ series of complexes under photochemical conditions, the structures of M^I , M^{II} , M^I-L , $M^{II}-L$ ($L = H_2O$ or CH_3CN) and $M^{III}-H$ species were modelled by means of density functional theory (DFT) calculations. The theoretical efforts have been focused on the evaluation of the $M^{III}-L$ reduction potentials and the pK_a values of hydride species to explore the energetic accessibility of the proposed intermediates and their stability. The geometric and electronic structures of $M^{III}-L$ complexes were also characterized to rationalize their divergent chemical behavior. The synergism between computational and experimental efforts will provide some clues about the metal-ligand interactions and their influence on the proton/water reduction mechanisms. This information may be used as a guide for the synthesis of more efficient proton reduction catalysts based on aminopyridine ligands.

9.2. Results and discussion

The DFT calculations were carried out using the Gaussian09 software package²³² with the B3LYP hybrid exchange-correlation functional.¹⁷⁶ X-ray structures of $\mathbf{1Co}$ and $\mathbf{1Ni}$ were used as starting point for the geometry optimizations, using 6-31G* 6d basis set for all atoms. The effect of water solvation and dispersion interactions were included in geometry optimizations through the SMD polarizable continuum model¹⁸⁰ and the Grimme-D₂ correction,¹⁸¹ respectively. The nature of stationary points was established by vibrational frequency calculations in condensed phase, where minima have no imaginary frequencies. Free energies values (G) were obtained by including solvent and dispersion corrections to energy computed with 6-311+G** basis set on the equilibrium geometries:

$$G = E_{6-311+G^{**}} + G_{\text{corr.}} + G_{\text{solv.}} + E_{\text{disp}} \quad (38)$$

where the Gibbs correction ($G_{\text{corr.}}$) was obtained from gas phase frequency calculations at B3LYP/6-31G* level, the solvation energy ($G_{\text{solv.}}$) was calculated as the difference of the total free energy in gas phase and in water at the same level of theory and geometry and E_{disp} is the Grimme dispersion correction.

All calculations employ the spin-unrestricted formalism. Since some of the studied intermediates present important spin contamination, the spin-contaminated 6-311+G** electronic energies were systematically corrected using the methodology described in ref. 187. This strategy was used to achieve a reliable comparison of the energetics between the different metal complexes. The radical character of some molecular fragments and its effects upon the structure of the complexes remain when the geometries were reoptimized at the B3LYP/SMD/6-311+G** level of theory. Therefore, the size of the basis set has no influence on the spin delocalization pattern.

All the computed reduction potentials were reported versus the SHE electrode, where ΔG_{SHE} (-4.24 eV) was derived using the Fermi-Dirac statistics for the treatment of electron thermodynamics.^{200d}

Natural bond orbital (NBO) analysis was performed to estimate the strengths of the donor-acceptor orbital interactions between the metal and ligands.²⁵⁶ The energetic effects of these charge transfer interactions were evaluated by second-order perturbation theory as:

$$\Delta E_{ij} = n_i \frac{\langle i|F|j \rangle^2}{\epsilon_j - \epsilon_i} \quad (39)$$

where n_i is the donor orbital occupancy; $\langle i|F|j \rangle$ is an off-diagonal element of the NBO Fock operator matrix; and ϵ_i and ϵ_j are the energies of orbital donor and orbital acceptor, respectively (diagonal elements).

To rationalize the solvent ligand coordination preference by each metal and oxidation state, the electronegativity (χ), hardness (η) and electrophilicity (ω) descriptors derived from the conceptual DFT HSAB theory²⁵⁷ have been computed by the following equations:

$$\eta = \epsilon_{LUMO} - \epsilon_{HOMO} \quad (40)$$

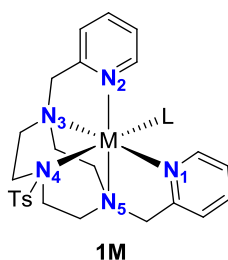
$$\chi = -\frac{(\epsilon_{HOMO} + \epsilon_{LUMO})}{2} \quad (41)$$

$$\omega = \frac{\chi^2}{2\eta} \quad (42)$$

9.2.1 Geometrical description of M^{II} -L intermediates

The nature of the L ligand occupying the coordination sphere of the **1M** complexes under photochemical conditions is unknown (Figure 115). The optimum $\text{CH}_3\text{CN}:\text{H}_2\text{O}$ mixture enables the metal center to interact with both kinds of solvent molecules and the redox activity of the resulting aqua or acetonitrile complexes could be very different. Therefore, the identification of the most stable aqua/acetonitrile intermediate for each metal oxidation state results necessary to ensure a correct description of the initial redox step.

First, we optimized all the possible M^{II} -L and M^I -L species to characterize their molecular geometry (Table 21). The M^{II} -L intermediates yield two kinds of distorted octahedral like complexes in which the solvent ligand L occupies the axial vacant position. In the Co^{II} -L structures, the aqua ligand is coordinated to metal center in the quartet ground spin state $\text{Co}^{II}\text{-OH}_2$ with a bond distance of 2.196 Å. The water molecule disposes in such a way that establishes a hydrogen bond with one oxygen atom of the tosyl group. The geometric orientation of the water molecule is characteristic of all $M^{II}\text{-OH}_2$ and $M^I\text{-OH}_2$ intermediates. The $\text{Co}^{II}\text{-OH}_2$ bond (2.196 Å) is longer than the one observed for the coordination of the π -acceptor acetonitrile ligand at $\text{Co}^{II}\text{-NCCH}_3$, 2.040 Å and the same trend is exhibited by the quintuplet $\text{Fe}^{II}\text{-NCCH}_3$ and triplet $\text{Ni}^{II}\text{-NCCH}_3$ ground spin state intermediates. This phenomenon reflexes the stronger interaction that exists between the metal and the acetonitrile molecule. Indeed, a longer (shorter) M-NCCH₃ bond distance correlates with a less (more) lineal arrangement of the acetonitrile ligand respect to the metal center. For example, the angle between the cyano group and the metal center is clearly bent in $\text{Fe}^{II}\text{-NCCH}_3$ (2.105 Å, 163.648°) and $\text{Co}^{II}\text{-NCCH}_3$ (2.040 Å, 168.392°) species, but an almost lineal arrangement is present in the $\text{Ni}^{II}\text{-NCCH}_3$ intermediate (2.000 Å, 175.908°) which has the shorter M-NCCH₃ bond. Therefore, the structural analysis suggests that the Co^{II} and Ni^{II} complexes may prefer an acetonitrile solvent molecule occupying the free coordination site (see next section for the energetics of the $\text{H}_2\text{O}/\text{CH}_3\text{CN}$ ligand exchange).

Table 21: Relevant bond distances (Å) of the most stable spin states for M^{II} -L geometries:^a

M =	Fe ^I (S = 3/2)	Fe ^{II} (S = 2)	Co ^I (S = 1)	Co ^{II} (S = 3/2)	Ni ^I (S = 1/2)	Ni ^{II} (S = 1)
L = CH ₃ CN						
d(M-N ₁)	2.177	2.174	2.044	2.096	2.059	2.050
d(M-N ₂)	1.996	2.171	2.045	2.122	2.080	2.075
d(M-N ₃)	2.262	2.261	2.222	2.162	2.092	2.110
d(M-N ₄)	2.739	2.380	2.534	2.309	2.025	2.276
d(M-N ₅)	2.289	2.262	2.235	2.169	2.130	2.113
d(M-L)	2.005	2.105	1.914	2.040	2.046	2.000
L = H ₂ O						
d(M-N ₁)	2.002	2.137	1.947	2.102	2.036	2.042
d(M-N ₂)	2.134	2.144	2.070	2.086	2.031	2.061
d(M-N ₃)	2.338	2.255	2.239	2.179	2.119	2.109
d(M-N ₄)	2.423	2.521	2.374	2.307	2.401	2.257
d(M-N ₅)	2.283	2.284	2.190	2.158	2.100	2.108
d(M-L)	2.205	2.213	2.273	2.196	2.195	2.014

[a] The bond distances of the most stable aqua or acetonitrile complex for each metal are labelled in black (see next section).

After the one electron reduction of the metal complex, the formal I oxidation state is achieved. The acceptance of electron density by $Co^{II}-OH_2$ and $Ni^{II}-OH_2$ provokes the elongation of the M-OH₂ bond but almost no change is experienced by $Fe^{II}-OH_2$. Instead, the change in the M-NCCH₃ bond distance depends on the metal identity. The Co-NCCH₃ bond distance in S = 1 Co^I-NCCH_3 species decreases 0.126 Å respect to $Co^{II}-NCCH_3$ since the one electron reduction enables the occupation of a π-bonding orbital. The latter bond contraction is also experienced by the S = 3/2 Fe^I-NCCH_3 intermediate which reduces the iron-acetonitrile bond in 0.100 Å respect to $Fe^{II}-NCCH_3$. In contrast, the trend in nickel species is reversed. This behavior is related with the different structures that can adopt the nickel(I)-NCCH₃ intermediate. Two geometries of Ni^I-NCCH_3 have been found (Figure 116): i) one analogous to Co^I-NCCH_3 and Fe^I-NCCH_3 species ($Ni^I_A-NCCH_3$) and ii) a second one ($Ni^I_B-NCCH_3$) with the N-Tosyl bond broken (2.750 Å), which has not been located for the other metals. The $Ni^I_B-NCCH_3$ structure is -13.4 kcal·mol⁻¹ more stable than $Ni^I_A-NCCH_3$ and present a 0.128 Å larger Ni-NCCH₃ bond. The origin of the $Ni^I_B-NCCH_3$ stability is mainly due to the substantial spread of the spin density on the N atom directly attached to the tosyl group ($\rho(N_4) = -0.64$). The spin delocalization on the tacn group favors a $Ni^{II}-tacn\cdot$ radical electronic structure ($\rho(Ni) = 1.61$) and the antiferromagnetic coupling between the nickel and the ligand radical reinforces the Ni-N₄ connectivity but weakens the N₄-tosyl and Ni-NCCH₃ bonds. This geometric distortion provides a more stable octahedral environment for the Ni^{II} center in $Ni^I_B-NCCH_3$ respect to $Ni^I_A-NCCH_3$. However, for comparison reasons, only $Ni^I_A-NCCH_3$ was considered in the analysis of the electronic and geometric structural changes that suffer the $M(Py_2^{Ts}tacn)$ system when the effective nuclear charge of the metal increases.

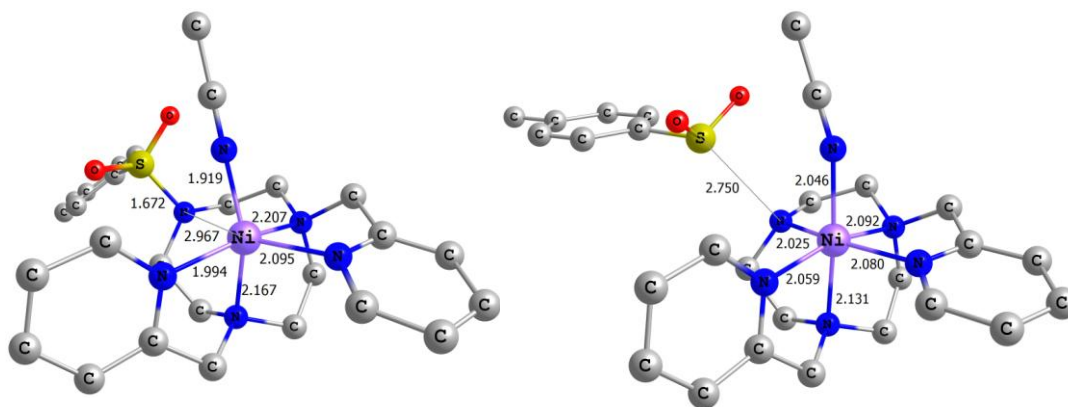


Figure 116: Optimized geometries of $\text{Ni}^{\text{I}}_{\text{A}}\text{-NCCH}_3$ (left) and $\text{Ni}^{\text{I}}_{\text{B}}\text{-NCCH}_3$ (right) intermediates. The bond distances values are in angstroms (\AA). Irrelevant hydrogen atoms are omitted for clarity.

9.2.2 Origin of the solvent ligand coordination preference

Despite structural data suggests which is the ligand coordination preference for each metal and oxidation state, the nature of this interaction and its energetics were also explored in detail. The free energy values for the ligand exchange reaction of H_2O by CH_3CN indicate that for both **1Co** and **1Ni** complexes the incorporation of an acetonitrile ligand in the open vacant site is an exergonic process for each oxidation state (Table 22). Moreover, the interaction between a water molecule and the Co^{I} , Co^{II} and Ni^{I} intermediates with a free coordination site is an endergonic process, while the acetonitrile coordination is clearly favored. Instead, the most stable iron intermediates presents an aqua group occupying the sixth position of the metal coordination sphere, although the small free energy differences fall into the mean error of the used methodology. To understand the ligand coordination preferences, the nature of the metal-solvent interaction was first examined through a NBO analysis. The metal ions are poor donors, thus the orbital interactions energies reported in Table 23 correspond to the dominant charge transfers of a lone pair of the donor species (i.e $\text{L} = \text{H}_2\text{O}$ or CH_3CN) to an antibonding lone pair acceptor metal orbital ($n_{\text{L}} \rightarrow n_{\text{M}}^*$). The stabilization energies for the acetonitrile coordination ($\Delta E_{\text{LM}} \approx 20\text{-}30 \text{ kcal}\cdot\text{mol}^{-1}$) are always higher than the same interaction with a water molecule ($\Delta E_{\text{LM}} \approx 6\text{-}12 \text{ kcal}\cdot\text{mol}^{-1}$). Indeed, the π -acceptor character of the acetonitrile ligand may contribute to the metal-ligand bond strength. This result correlates with the shorter bond distance between the acetonitrile ligand and the metal center respect to the aqua ligand in all the studied complexes.

Table 22: Computed free energy (ΔG) for coordination of CH_3CN and H_2O to **1M** and for ligand exchange reactions:^a

M =	ΔG (kcal·mol ⁻¹)					
	Fe ^I	Fe ^{II}	Co ^I	Co ^{II}	Ni ^I	Ni ^{II}
$[\text{M}^{\text{I/II}}(\text{Py}_2^{\text{Ts}}\text{tacn})] + \text{L} \rightarrow [\text{M}^{\text{I/II}}(\text{Py}_2^{\text{Ts}}\text{tacn})(\text{L})]$						
L = CH_3CN	2.9	3.4	0.2	-2.8	-7.9	-5.1
(5.5) ^b						
L = H_2O	2.2	1.8	3.9	3.4	9.6	-1.9
$\text{CH}_3\text{CN} + [\text{M}^{\text{I/II}}(\text{Py}_2^{\text{Ts}}\text{tacn})(\text{OH}_2)] \leftrightarrow [\text{M}^{\text{I/II}}(\text{Py}_2^{\text{Ts}}\text{tacn})(\text{NCCH}_3)] + \text{H}_2\text{O}$						
	0.7	1.6	-3.8	-6.2	-17.5	-3.2
(-4.1) ^b						

[a]All values have been obtained using the ground spin state for each structure. [b] In parenthesis, the free energy differences considering the $\text{Ni}^{\text{I}}\text{-NCCH}_3$ structure.

Table 23: Stabilization energies (ΔE_{LM}) for the dominant donor-acceptor interactions ($n_{\text{L}} \rightarrow n_{\text{M}^*}$) between **1M** complexes and L solvent ligands:^a

M =	Fe ^I	Fe ^{II}	Co ^I	Co ^{II}	Ni ^I	Ni ^{II}
ΔE_{LM} (kcal·mol ⁻¹)						
L = CH_3CN	23.4	19.1	31.8	23.4	30.8	25.8
(27.6)						
L = H_2O	6.0	8.4	8.0	10.2	11.8	13.7

[a]All values have been obtained using the ground spin state for each structure. In parenthesis, the stabilization energies for the $\text{Ni}^{\text{I}}\text{-NCCH}_3$ structure.

The discordant ligand coordination preference for **1Fe** complex may be rationalized with the quantum chemical properties of electronegativity (χ) and the electrophilicity index (ω) derived from the conceptual DFT Hard-Soft Acid-Base (HSAB) theory (see computational details). According to Pearson, the electron transfer in a metal complex will occur from the organic ligand (lower χ) towards the metal center (higher χ). Moreover, low values of ω imply a more reactive nucleophile character while the inverse statement is valid for an electrophile. In Table 24 the χ and ω values are listed for the M^{I} species and solvent ligands. The HSAB parameters indicate that Co^{I} and Ni^{I} centres have less electrophilic character than Fe^{I} . The unexpected increasing of the chemically soft character with the raise of the effective nuclear charge of the metal is related with the increasing number of d electrons, which outweighs increasing electronegativity.^{257b} The water molecule is a harder base than acetonitrile, as it presents a lower value of ω . Thus, a stronger interaction is expected between a water molecule nucleophile and an electrophilic Fe^{I} center than in the other $\text{M}^{\text{I}}\text{-OH}_2$ species. Similar conclusions can be extracted from the II oxidation state. Therefore, the free energy difference for the exchange of H_2O by CH_3CN in **1Fe** becomes endergonic. The Ni^{II} center presents an unexpected high electrophilic character, which correlates with the higher affinity of the Ni^{II} structure for both the water and acetonitrile ligands respect to the Fe^{II} intermediate (see Table 22).

Table 24: Electronegativity (χ) and electrophilicity (ω) descriptors for cobalt, nickel and iron complexes and solvent ligands:^a

M =	Fe ^I	Co ^I	Ni ^I	Fe ^{II}	Co ^{II}	Ni ^{II}	H ₂ O	CH ₃ CN
ϵ_{HOMO}^b	-0.09805	-0.11145	-0.11367	-0.19142	-0.20894	-0.23089	-0.29766	-0.32686
ϵ_{LUMO}^b	-0.04261	-0.04111	-0.04091	-0.06370	-0.05836	-0.07610	0.08858	0.03932
χ	0.0703	0.0763	0.0773	0.1276	0.1336	0.1535	0.1045	0.1438
ω	0.0446	0.0413	0.0410	0.0637	0.0593	0.0761	0.0141	0.0282

[a] The calculations take into account the metal complexes without any water or acetonitrile solvent ligand. [b] The frontier molecular orbital energies (ϵ) are in atomic units (a.u.).

9.2.3 Influence of solvent ligands on the proton reduction activity

The solvent ligand coordination preference will induce a perturbation on the electronic structure of each metal complex, changing their reactivity patterns. To get insight into these effects, the reduction potentials for the same metal and different L groups were calculated and the resultant electronic structure was examined. This study may allow us to understand how the solvent molecules modulate the redox behavior of these metal complexes and therefore the thermodynamically feasibility of the proton reduction reaction.

Table 25: DFT computed reduction potentials (V) and pK_a values of the proposed iron, cobalt and nickel intermediates.^a

	M = Fe	M = Co	M = Ni
$E^{\circ}(\text{M}^{\text{II}}\text{-NCCH}_3)^b$	-1.51	-1.11	-0.97 (-1.55) ^f
$E^{\circ}(\text{M}^{\text{II}}\text{-OH}_2)^c$	-1.55	-1.01	-1.59
$E^{\circ}(\text{M}^{\text{II}})^d$	-1.54	-0.98	-1.08
pK _a (M ^{III} -H) ^e	1.8	7.0	-0.4

[a] All values have been obtained using the ground spin state for each structure. E° values correspond to the standard reduction potentials relative to the SHE electrode. [b] The calculations take into account the presence of an **acetonitrile ligand** in the coordination sphere of the metal complexes. [c] The calculations take into account the presence of an **aqua ligand** in the coordination sphere of the metal complexes. [d] The calculations take into account the metal complexes without any **water or acetonitrile solvent ligands** [e] pK_a values (at 298 K) have been calculated taking into account the metal complexes without any **water or acetonitrile solvent ligand**. [f] In parenthesis, the reduction potential considering the Ni^I_A-NCCH₃ structure.

Table 25 summarizes the influence of ligand L on the M^{I/II} reduction potentials. The substitution of an aqua ligand for an acetonitrile molecule supposes a cathodic shift of about 100 mV in **1Co**, while **1Fe** complex experiment only a decrease of the reduction potential of 40 mV. Surprisingly, this shift increases to 620 mV when a water molecule is coordinated to **1Ni**. The reduction potentials obtained for the iron and cobalt complexes without any coordinated solvent ligand and with L = H₂O are very similar. The differences in the redox behavior may be understood analyzing the geometric and electronic changes imposed by the axial ligand L in the M^I intermediates. A Mulliken population analysis indicates that the non-innocent redox ligand behavior plays an important role on the geometric features of all M^I-OH₂ intermediates (Figure 117). These systems present an important spin electron delocalization over a pyridine group, suggesting that during the one electron reduction the pyridine ligand accepts most of the injected electron density. The metal-ligand electron transfer is responsible for the weakening/elongation of the aromatic C-C bonds and the folding of the pyridine group respect to the equatorial plane. The pyridine non-

innocent redox behavior can be envisaged through the frontier molecular orbitals topology of M^{II} -OH₂ intermediates (Figure 117). In M^{II} -OH₂ species the frontier orbitals illustrate how the pyridine rings can accommodate electron density in the π system after a reduction process. Moreover, in M^I -OH₂ species a bonding interaction between the d orbitals manifold of the M^I center and the pyridine π -system is observed. The latter electronic channel between the metal and the Py₂^{Ts}tacn ligand enable the system to achieve $M^{II}(\text{OH}_2)(\cdot\text{Py}_2^{\text{Ts}}\text{tacn})$ radical species. The spin density flow to the pyridine rings is also observed for all formal M^I structures when no solvent ligand is present. The non-innocent redox behavior of pyridine and pyrazine moieties was recently observed in other nickel¹⁵³ and cobalt²⁵⁸ water reduction catalysts.

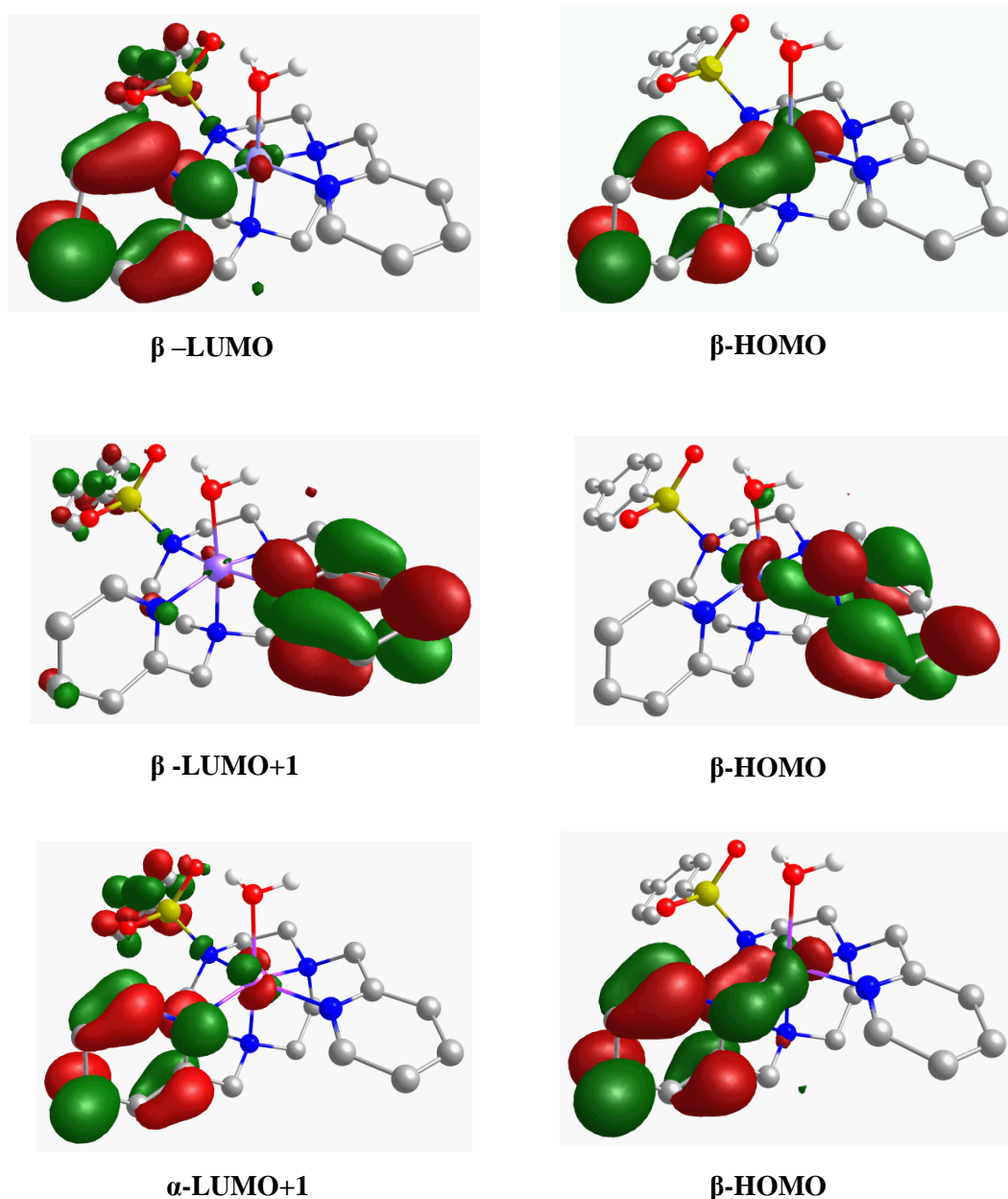
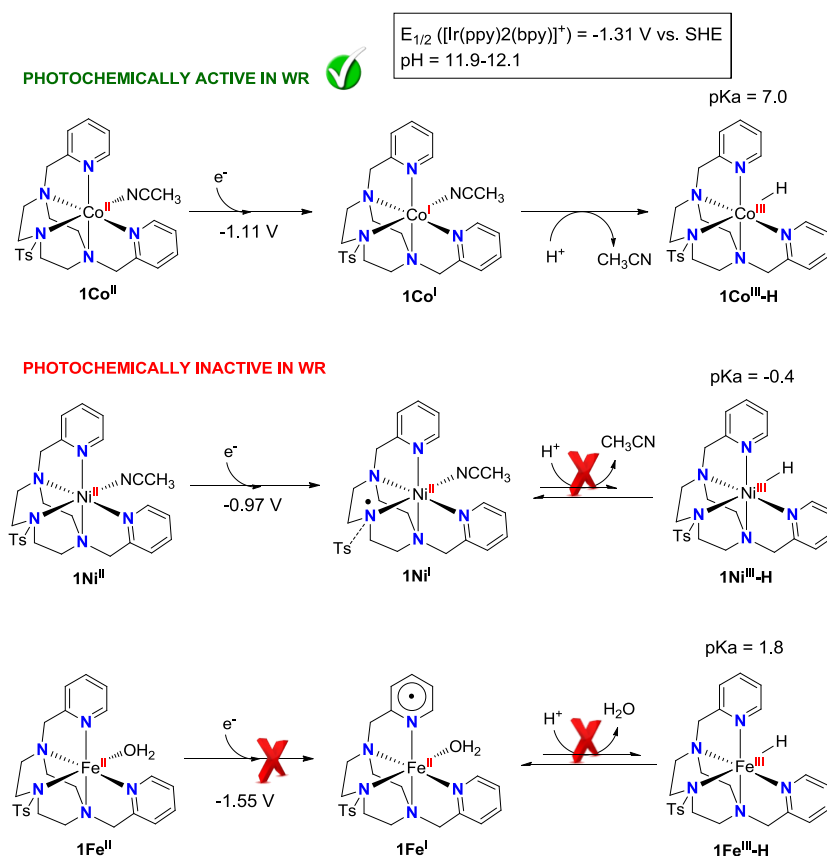


Figure 117: Single occupied molecular frontier orbitals of Co-OH₂ (top), Ni-OH₂ (middle) and Fe-OH₂ (bottom) intermediates (isovalue of 0.0432) involved in the reduction step from M^{II} to M^I . The M^{II} -OH₂ and M^I -OH₂ structures are inserted in the left and right columns, respectively.

The spin delocalization phenomenon does not follow the same trend in $M^I\text{-NCCH}_3$ intermediates. In contrast with the aqua complexes, only the $\text{Fe}^I\text{-NCCH}_3$ intermediate show substantial electronic spin delocalization on a pyridine group with a formal Fe^{II} center in a quartet spin state ($\rho(\text{Fe}) = 3.53$). Instead, $\text{Co}^I\text{-NCCH}_3$ and $\text{Ni}^I_{\text{A}}\text{-NCCH}_3$ species have no marked radical character on the tacn ligand, being best represented as triplet Co^I ($\rho = 2.18$) and doublet Ni^I ($\rho = 1.06$) compounds. The lack of spin density spread through the system may be correlated with the absence of orbital overlapping between the metal and the π acceptors groups.

The non-innocent redox behaviors of the pyridine groups in $M\text{-OH}_2$ and M intermediates facilitate the reduction reaction of **1Co**. Instead, in the most stable nickel acetonitrile species, the previously discussed geometrical distortion that presents $\text{Ni}^I_{\text{B}}\text{-NCCH}_3$ due to the existence of a radical on the tacn framework decrease the reduction potential necessary to achieve $\text{Ni}^I_{\text{B}}\text{-NCCH}_3$ ($E^\circ = -0.97$ V) respect to $\text{Ni}^I\text{-OH}_2$ ($E^\circ = -1.55$ V). The one electron potentials for **1Fe** are almost independent of the L solvent ligand identity, since in the two Fe^I structures there is electron spin density delocalized on a pyridine ring.

Taking into account the most stable aqua/acetonitrile species for each metal and oxidation state, we observed that the theoretical reduction potentials of the couples $\text{Co}^{I/II}\text{-NCCH}_3$, $\text{Ni}^{I/II}\text{-NCCH}_3$ and $\text{Fe}^{I/II}\text{-OH}_2$ are -1.11 V, -0.97 V and -1.55 V, respectively. The trends show by this values agree with the experimental one given by -0.99 V, -0.96 V and -1.34 V results obtained, respectively, for $\text{Co}^{I/II}$, $\text{Ni}^{I/II}$ and $\text{Fe}^{I/II}$ from a $\text{H}_2\text{O}:\text{CH}_3\text{CN}$ (7:3) solvent mixture. The divergence between theoretical and experimental values may be rationalized by the intrinsic errors of the DFT method, the implicit treatment of the aqueous solvent and the neglect of the bulk acetonitrile solvent present in the reaction mixture. Therefore, the experimental and computational studies confirm that both **1Co**^{II} and **1Ni**^{II} complexes can achieve the M^I oxidation state using **PSIr**^{II} as a photosensitizer ($E^0 \approx -1.31$ V vs. SHE), while $\text{Fe}^I\text{-OH}_2$ species may not be photochemically generated, inhibiting the capacity of **1Fe** to catalyze the H_2 evolution (Scheme 8). Finally, the origin of the inactivity of nickel species in H_2 evolution may be the instability of the $\text{Ni}^{III}\text{-H}$ species under the basic media imposed by Et_3N (Table 25). This hypothesis is supported by the pK_a value of -0.4 for $\text{Ni}^{III}\text{-H}$, which clearly emphasizes a more acidic character than the $\text{Co}^{III}\text{-H}$ intermediate ($\text{pK}_a = 7.0$).



Scheme 8: Summary of reactivity differences between 1Co^{II} , 1Ni^{II} and 1Fe^{II} complexes under photochemical conditions. Reduction potentials (vs. SHE electrode) and pK_a values have been derived by DFT calculations.

To conclude, DFT calculations allowed us to elucidate the coordination sphere constitution of 1Co^{II} , 1Ni^{II} and 1Fe^{II} complexes under photochemical conditions and its influence on the proton reduction activity. The structural data for $\text{M}^{\text{III}}\text{-L}$ ($\text{L} = \text{H}_2\text{O}$, CH_3CN) intermediates always show a stronger bonding between the acetonitrile solvent ligand and the metal center respect to M-OH_2 interaction. The NBO analysis reveals that the charge transfer energy for a lone pair donation from CH_3CN to the metal is the origin of the M-NCCH_3 stability. However, the free energy balances for the exchange of a H_2O molecule by a CH_3CN indicate that the sixth coordinative position of 1Co^{III} and 1Ni^{III} is occupied by CH_3CN . In contrast, the 1Fe^{III} species present a H_2O ligand. The solvent ligand coordination preference is rationalized with the conceptual DFT HSAB theory. According to this theory, the iron center is more electrophilic (harder acid) than the cobalt and nickel atoms. Indeed, the water molecule is more nucleophilic (more basic) than the acetonitrile ligand. Therefore, a major chemical affinity is expected between water and iron than with an acetonitrile ligand.

The one electron reduction potentials to reach the M^{I} oxidation state were also computed for each L ligand. The identity of the L ligand modifies the magnitude of the reduction potentials. Frontier molecular orbitals and the spin density clearly indicate that in $\text{M}^{\text{I}}\text{-OH}_2$ the pyridine rings may act as non-innocent redox ligands, leading to the formation of $\text{M}^{\text{II}}(\text{OH}_2)(\text{Pytac}\cdot)$ radical species. Despite, in M-NCCH_3 species, only $\text{Fe}^{\text{I}}\text{-NCCH}_3$ has spin delocalization on the $\text{Py}_2^{\text{Ts}}\text{tacn}$ organic framework.

The computational reduction potentials of $\text{Co}^{\text{II}}\text{-NCCH}_3$, $\text{Ni}^{\text{II}}\text{-NCCH}_3$ and $\text{Fe}^{\text{II}}\text{-OH}_2$ and the pK_a values of the corresponding $\text{M}^{\text{III}}\text{-H}$ species show that only cobalt species are efficient catalysts

for water reduction under catalytic conditions, in agreement with the experimental data. In contrast, under the same conditions, $\text{Ni}^{\text{II}}\text{-NCCH}_3$ presents a low photochemical water reduction activity due to the instability of the $\text{Ni}^{\text{III}}\text{-H}$ species under basic media. Finally, the $\text{Fe}^{\text{II}}\text{-OH}_2$ intermediate is inactive since the I oxidation state is unreachable by the reduced photosensitizer PSIr^{II} .

Altogether, this quantum mechanical study reveals the important influence of solvent ligand coordination on the electronic structure of metal complexes. The metal-ligand interactions may be tuned introducing new perturbations on the vacant sites of the metal coordination sphere, enabling the ligands to act as electron reservoir and thus, modulating the redox activity of the complex. This opens a new way for the *in silico* design of more efficient new proton reduction catalysts with redox non-innocent ligands.

CHAPTER 10:

**COMPUTATIONAL STUDY OF
ELECTROCHEMICAL HYDROGEN
PRODUCTION BY COBALT CATALYSTS BASED
ON AN AMINOPYRIDINE LIGAND^a**

^a This chapter is based on the publication: Acuña-Parés, F.; Luis, J.M.; Lloret-Fillol, J. Computational study of electrochemical hydrogen production mechanisms by cobalt catalysts based on an aminopyridine ligand. *In manuscript.*

10. Computational study of electrochemical hydrogen production mechanisms by cobalt catalysts based on an aminopyridine ligand.

In this chapter, the hydrogen evolution mechanism catalyzed by complex $[\text{Co}^{\text{II}}(\text{OTf})(\text{Py}_2^{\text{T}_s}\text{tacn})]$ in acetonitrile is explored through density functional theory calculations. The thermodynamic and kinetic aspects of the proton reduction reaction are elucidated through the computation of reduction potentials, pK_a values, hydricities, bond dissociation energies (BDE) and global free energy profiles. The inner sphere reorganization energies for protonation reactions accounting intramolecular rearrangements are also derived.

CHAPTER 11:

**COMPUTATIONAL STUDY OF
PHOTOCHEMICAL HYDROGEN PRODUCTION
BY COBALT CATALYSTS BASED ON AN
AMINOPYRIDINE LIGAND^a**

^a This chapter is based on the publication: Acuña-Parés, F.; Luis, J.M.; Lloret-Fillol, J. Computational study of photochemical hydrogen production mechanisms by cobalt catalysts based on an aminopyridine ligand. *In manuscript*.

11. Computational study of photochemical hydrogen production mechanisms by cobalt catalysts based on an aminopyridine ligand.

Here, the computational study of the hydrogen generation mechanism catalyzed by the photochemical system formed by $[\text{Co}^{\text{II}}(\text{OTf})(\text{Py}_2^{\text{T}_3}\text{tacn})]$, $[\text{Ir}(\text{ppy})_2(\text{bpy})]\text{PF}_6$ and Et_3N in water is presented. The thermodynamic and kinetic aspects of the proton reduction mechanism are clarified through the calculation of reduction potentials and reaction free energy profiles. The energy barriers of electron transfer reactions between the cobalt complex, the photosensitizer $[\text{Ir}(\text{ppy})_2(\text{bpy})]\text{PF}_6$ and the sacrificial donor Et_3N are also computed using the Marcus theory. Finally, the source of protons was modelled by water or hydronium's clusters.

CHAPTER 12:

GENERAL CONCLUSIONS

12. GENERAL CONCLUSIONS

The main conclusions of this thesis may be split in two main groups: *mechanistic studies of water oxidation catalyzed by non-heme iron complexes* and *mechanistic studies of proton/water reduction catalyzed by aminopyridine first-row transition metals complexes*

1) Mechanistic studies of water oxidation catalyzed by non-heme iron complexes

First:

DFT calculations have been carried out to evaluate the energetic accessibility and water oxidation activity of $[\text{Fe}^{\text{V}}(\text{O})(\text{OH})]^{2+}$ species. Assuming that CAN acts as an outer-sphere oxidant, the computed $[\text{Fe}^{\text{IV}}(\text{O})(\text{OH}_2)]^{2+}/[\text{Fe}^{\text{V}}(\text{O})(\text{OH})]^{2+}$ oxidation potentials for complexes $[\text{Fe}^{\text{II}}(\text{OTf})_2(\text{Pytacn})]$ (**1**), $[\text{Fe}^{\text{II}}(\text{OTf})_2(\text{mep})]$ (**2**), $[\text{Fe}^{\text{II}}(\text{OTf})_2(\text{tmc})]$ (**3**) and $[\text{Fe}^{\text{II}}(\text{NCCCH}_3)(\text{Py}_2\text{CH-tacn})(\text{OTf})_2]$ (**4**) indicate that $[\text{Fe}^{\text{V}}(\text{O})(\text{OH})]^{2+}$ species are only accessible by iron tetradentate catalysts **1** and **2**, which contain two labile ligands in a *cis* relative orientation. Thus, the addition of a water molecule in a *cis* position to the oxo ligand allows the coupled transfer of protons and electrons, reducing the oxidation potential required to achieve oxidation state V on the metal center. The mechanism of the O-O bond formation by catalysts **1-4** has been also explored. In the case of **1** and **2**, the nucleophilic attack of a water molecule to the oxo group of $[\text{Fe}^{\text{V}}(\text{O})(\text{OH})]^{2+}$ is accompanied by the transfer of a proton from the molecule water to the *cis* OH group, which acts as an internal base. The resulting free energy profiles indicate that the reaction is kinetically favorable and the theoretical parameters of activation for catalyst **1** are in excellent agreement with the experimental values. The absence of an internal base (OH) in *cis* position to the $\text{Fe}^{\text{V}}=\text{O}$ group in complexes **3** and **4** implies that water solvent molecules should assist the O-O bond formation event. The results show that if the intermediate $\text{Fe}^{\text{V}}=\text{O}$ was reached then it would be highly reactive with a low energy barrier, because complexes **3** and **4** do not present a *cis* negative charge (OH^-) capable to stabilize the high oxidation state on the metal. In the specific case of complex **1** the complete catalytic cycle of the water oxidation reaction has been determined and the global free energy profile confirms that the rate limiting step of the reaction is the O-O bond formation event.

Second:

The possible involvement of iron(IV) species such $[\text{Fe}^{\text{IV}}(\text{O})(\text{OH}_2)]^{2+}$, $[\text{Fe}^{\text{IV}}(\text{OH})(\text{OH})]^{2+}$ and $[\text{Fe}^{\text{IV}}(\text{O})(\text{OH})]^+$ in the O-O bond formation event has been explored for catalyst **1**. It has been considered that the nucleophilic attack of a water molecule on the $\text{Fe}^{\text{IV}}=\text{O}$ moiety can be assisted by an internal base ($-\text{OH}$) or the bulk aqueous solvent. The energy profiles for the three intermediates show energy barriers inaccessible at room temperature, indicating the inactivity of these compounds in the water oxidation reaction. The energetic accessibility of $\text{Fe}^{\text{VI}}=\text{O}$ intermediates have also been investigated, showing that $\text{Fe}^{\text{V}}=\text{O}$ is the higher oxidized species accessible under catalytic conditions.

Third:

We have studied the water oxidation capacity anionic pentadentate iron complex, $[\text{Fe}^{\text{II}}(\text{AQ}^{\text{Me}_2}\text{tacn})(\text{OTf})]$ (**5**), which was designed *in silico*. Theoretical studies have enabled the identification of the first electrochemical steps of the water oxidation reaction and the elucidation of the O-O bond formation mechanism. Calculations reveal that, in contrast with the reactivity observed for the *cis*-tetradentate complexes, the incorporated anionic group in *cis* relative position to

the oxo ligand in formal $[\text{Fe}^{\text{V}}(\text{O})(\text{AQ}^{\text{Me}_2}\text{taccn})]^{2+}$ species does not act as an internal Brønsted base. Instead, a solvent molecule accepts a proton from the water molecule involved in the nucleophilic attack on the $\text{Fe}=\text{O}$ group. Electronic structure analysis of the $[\text{Fe}^{\text{V}}(\text{O})(\text{AQ}^{\text{Me}_2}\text{taccn})]^{2+}$ show that the $\text{AQ}^{\text{Me}_2}\text{taccn}$ ligand is *redox non-innocent*, being the active species best represented as $[\text{Fe}^{\text{IV}}(\text{O})(\cdot\text{AQ}^{\text{Me}_2}\text{taccn})]^{2+}$. The radical ligand increases the electrophilic character of the complex, and therefore their reactivity, without the need to access the V oxidation state on the metal. Complex $[\text{Fe}^{\text{III}}(\text{dpaq})(\text{H}_2\text{O})]^{2+}$ (**6**) has been also considered to analyze the effect of the *trans/cis* position of the anionic group on the water oxidation activity. The *trans* influence that exerts the amidate on the oxo ligand in **6** reduces the O-O bond formation barrier respect to **5**. The presence of redox non-innocent ligands and the *trans/cis* relative position of the anionic group add new variables to be considered in the design of more efficient water oxidation catalysts. Our theoretical results were validated by experimental measurements.

Fourth:

The behavior of the sacrificial oxidant CAN under water oxidation reaction conditions, as well as the formation and reactivity of the $\text{Fe}^{\text{IV}}\text{-O-Ce}^{\text{IV}}$ adduct from complex $\alpha\text{-}[\text{Fe}^{\text{II}}(\text{OTf})_2(\text{mcp})]$ have been studied. The systematic analysis of a representative group of aqua, hydroxo and oxo Ce^{IV} mononuclear complexes and $\text{Ce}^{\text{IV}}\text{-O-Ce}^{\text{IV}}$ dimers suggest that the $[(\text{H}_2\text{O})_7\text{Ce}^{\text{IV}}\text{-O-Ce}^{\text{IV}}(\text{OH})(\text{H}_2\text{O})_6]^{5+}$ structure is the most stable form of CAN under catalytic conditions. The DFT data also show that the formation of the $\alpha\text{-}[(\text{mcp})\text{Fe}^{\text{IV}}(\text{O})(\mu\text{-O})(\text{Ce}^{\text{IV}})(\text{H}_2\text{O})_7]^{4+}$ adduct, derived from the previous cerium dimer and $\alpha\text{-}[\text{Fe}^{\text{IV}}(\text{O})(\text{OH}_2)(\text{mcp})]^{2+}$, is favored from a thermodynamic point of view. This result is fully consistent with the experimental detection of the α -adduct. Therefore, the availability of *cis* relative positions in an iron complex is necessary to facilitate the interaction between the two metals. In contrast, the adduct generation by the topological isomer $\beta\text{-}[\text{Fe}^{\text{IV}}(\text{O})(\text{OH}_2)(\text{mcp})]^{2+}$ is an endergonic process, due to the important steric hindrance between the iron complex and the cerium fragment. Since the α -adduct may exist in other protonation states, all the possible $\alpha\text{-}[(\text{mcp})\text{Fe}^{\text{IV}}(\text{O})(\mu\text{-X})(\text{Ce}^{\text{IV}})(\text{H}_2\text{O})_6(\text{OH})]^{3+/4+}$ ($\text{X} = \text{OH}$ or O) cerium-hydroxide adducts have been optimized. The computation of the corresponding $\text{pK}_a(\text{H}_2\text{O-Ce})$ show that H_2O deprotonation is exergonic only when $\text{X} = \text{OH}$. To achieve a better understanding of the water oxidation mechanism, we have explored the intramolecular and intermolecular O-O bond formation pathways performed by $\alpha\text{-}[(\text{mcp})\text{Fe}^{\text{IV}}(\text{O})(\mu\text{-OH})(\text{Ce}^{\text{IV}})(\text{H}_2\text{O})_6(\text{OH})]^{4+}$ species. However, the nucleophilic attack of a water molecule on $\text{Fe}=\text{O}$ is only kinetically feasible for the intermolecular O-O bond formation mechanism, in which the group Ce-OH acts as an internal base. The $\alpha\text{-}[(\text{mcp})\text{Fe}^{\text{IV}}(\text{O})(\mu\text{-OH})(\text{Ce}^{\text{IV}})(\text{H}_2\text{O})_6(\text{OH})]^{4+}$ intermediate presents a lower O-O bond formation energy barrier than $\alpha\text{-}[\text{Fe}^{\text{V}}(\text{O})(\text{OH})]^{2+}$ monomer. This suggests that $\text{Fe}^{\text{IV}}\text{-Ce}^{\text{IV}}$ intermediates are the active species in the water oxidation reaction instead of the oxidized $\alpha\text{-}[\text{Fe}^{\text{V}}(\text{O})(\text{OH})]^{2+}$ free species. Finally, it was found that the reduced water oxidation activity of the β -complex is related with the favored decomposition of the mcp ligand by $\beta\text{-}[\text{Fe}^{\text{V}}(\text{O})(\text{OH})]^{2+}$ species over the O-O bond formation reaction. This work represents the first approach to the inner-sphere interaction problem.

Fifth:

The capacity of the $\alpha\text{-}[\text{Fe}^{\text{II}}(\text{OTf})_2(\text{mcp})]$ complex upon reaction with H_2O_2 to oxidize the molecular hydrogen to water has been computationally analyzed. The mechanistic study indicates that $\alpha\text{-}[\text{Fe}^{\text{V}}(\text{O})(\text{OH})(\text{mcp})]^{2+}$ species oxidize the H_2 molecule, in which the oxo and OH ligands act as internal bases. This result is in agreement with the inhibition of organic substrates oxidation by $\alpha\text{-}[\text{Fe}^{\text{V}}(\text{O})(\text{OH})(\text{mcp})]^{2+}$ when the H_2 gas is injected in the reaction mixture. In contrast, no appreciable

decrease of the organic substrate oxidation activity is observed when acetic acid is added. DFT calculations reveal that α -[Fe^V(O)(OH)(mcp)]²⁺ react with the acetic acid to generate α -[Fe^{IV}(O)(·OAc)(mcp)]²⁺ species, which should overcome a high energy barrier to activate the hydrogen molecule. Therefore, the α -[Fe^{IV}(O)(·OAc)(mcp)]²⁺ intermediate exclusively works as an organic substrate oxidation catalyst. The capacity of Fe^V(O)(OH) species to activate the H₂ molecule makes incompatible their use in water splitting devices.

Mechanistic studies of proton/water reduction catalyzed by aminopyridine first-row transition metals complexes

Sixth:

The origin of the proton reduction activity differences between complexes [Co^{II}(OTf)(Py₂^{Ts}tacn)] (**1Co^{II}**), [Ni^{II}(OTf)(Py₂^{Ts}tacn)] (**1Ni^{II}**) and [Fe^{II}(OTf)(Py₂^{Ts}tacn)] (**1Fe^{II}**) under photochemical conditions ([Ir(ppy)₂(bpy)]PF₆ photosensitizer/Et₃N electron donor, pH = 12) has been analyzed by means of DFT calculations. In the 7:3 H₂O/CH₃CN solvent mixture used in catalysis, the OTf group may exchange by a solvent molecule. According to our calculations, the acetonitrile coordination is favored for complexes **1Co^{II}** and **1Ni^{II}** while the labile coordination position in **1Fe^{II}** is occupied by a water molecule. We have also found that the metal or ligand centered character of the photo-driven one-electron reduction to formal M^I-L (L = H₂O, CH₃CN) species depend on the nature of the L ligand. Thus, the pyridine moieties in Py₂^{Ts}tacn may act as redox non-innocent ligands when a water molecule is coordinated to the metal. Furthermore, the computation of the M^{III/I} reduction potentials and the pK_a values of the postulated M^{III}-H active species show that the experimentally observed reduced activity of **1Ni^{II}** is due to the unfavorable formation of the Ni^{III}-H intermediate under basic media. On the contrary, the iron complex **1Fe^{II}** is inactive because the formal I oxidation state is unreachable by the reduced form of the photosensitizer. This quantum mechanical study reveals the important influence of the metal identity and the solvent ligand coordination on the proton reduction activity.

Seventh:

The electrochemical proton reduction catalytic cycle by [Co^{II}(OTf)(Py₂^{Ts}tacn)] has been investigated by DFT means. Our results indicate that the reaction starts with one electron reduction of the cobalt complex ([Co^I(NCCH₃)(Py₂^{Ts}tacn)]⁺). Then, under electrochemical conditions (acetonitrile solvent, TFA as a source of protons), the pyridine rings of the [Co^I(NCCH₃)(Py₂^{Ts}tacn)]⁺ intermediate may capture a proton, generating [Co^{II}(·H-Py₂^{Ts}tacn)]⁺ pyridine radical species. The intramolecular hydrogen atom transfer from the protonated pyridine to the cobalt center leads to the formation [Co^{III}(H)(Py₂^{Ts}tacn)]²⁺ intermediate, which ultimately is reduced to [Co^{II}(H)(Py₂^{Ts}tacn)]⁺ active species. The subsequent protonation of a pyridine moiety ([Co^{II}(H)(H-Py₂^{Ts}tacn)] and the intramolecular coupling between the Co-H and pyr-H fragments permit the H₂ evolution. The global energy profile of the catalytic cycle reveals that the TDTS corresponds to the [Co^{III}(H)(Py₂^{Ts}tacn)]²⁺ generation and the associated free energy barrier is in agreement with the experimental TOF. This computational study concludes that the dynamical and redox active Py₂^{Ts}tacn ligand plays an important mechanistic role in the proton reduction reaction and not only develops a purely structural function.

Eighth:

The photochemical proton reduction catalytic cycle by $[\text{Co}^{\text{II}}(\text{OTf})(\text{Py}_2^{\text{Tstacn}})]$ has been explored. In contrast with the electrochemical mechanism, the proton capture by a pyridine moiety is kinetically banned due to the basic media. Instead, the reduced $[\text{Co}^{\text{I}}(\text{NCCH}_3)(\text{Py}_2^{\text{Tstacn}})]^+$ species capture a proton from a hydronium cation to directly generate the $[\text{Co}^{\text{III}}(\text{H})(\text{Py}_2^{\text{Tstacn}})]^{2+}$ hydride. The one electron reduction of the previous intermediate generates the $[\text{Co}^{\text{II}}(\text{H})(\text{Py}_2^{\text{Tstacn}})]^+$ species. The cobalt(II)-hydride is able to interact with the aqueous protons to produce molecular hydrogen. Indeed, under the photochemical conditions, the $[\text{Co}^{\text{II}}(\text{H})(\text{Py}_2^{\text{Tstacn}})]^+$ has also enough reductive power to catalyze the H-H bond formation through the cleavage of a water O-H bond. The significant differences between the electrochemical and photochemical mechanisms reveal that reaction conditions (solvent, pH, etc.) can change drastically the proton reduction operational mechanism.

REFERENCES

- 1) *Key World Energy Statistics 2015*, International Energy Agency (IEA), Paris, France.
- 2) Conti, J.; Holtberg, P. *International Energy Outlook 2013*, Energy Information Administration (EIA), Washington DC, USA.
- 3) Lewis, N. S.; Nocera, D. G. *Proc. Natl. Acad. Sci. U.S.A.*, **2006**, *103*, 15729-15735.
- 4) Rodriguez, C.A.; Modestino, M.A.; Psaltis, D.; Moser, C. *Energy Environ. Sci.*, **2014**, *7*, 3828-3835.
- 5) (a) Barber, J. *Int. J. Photonenergy*, **2004**, *6*, 43-51. (b) Ferreira, K.N.; Iverson, T.M.; Maghlaoui, K.; Barber, J.; Iwata, S. *Science*, **2004**, *303*, 1831-1838.
- 6) Lubitz, W.; Reijerse, E.J.; Messinger, J. *Energy Environ. Sci.*, **2008**, *1*, 15-31.
- 7) Barber, J. *Inorg. Chem.*, **2008**, *47*, 1700-1710.
- 8) (a) McEvoy, J. P.; Brudvig, G. W. *Chem. Rev.*, **2006**, *106*, 4455-4483. (b) Dau, H.; Limberg, C.; Reier, T.; Risch, M.; Roggan, S.; Strasser, P. *ChemCatChem*, **2010**, *2*, 724-761.
- 9) a) Yano, J.; Yachandra, V. K. *Inorg. Chem.*, **2008**, *47*, 1711-1726; (b) Ananyev, G. M.; Dismukes, G. C., *Photosynth. Res.*, **2005**, *84*, 355-365.
- 10) Duan, L.; Bozoglian, F.; Mandal, S.; Stewart, B.; Privalov, T.; Llobet, A.; Sun, L. *Nat. Chem.*, **2012**, *4*, 418-423.
- 11) Barnett, S.M.; Goldberg, K.I.; Mayer, J.M. *Nat. Chem.*, **2012**, *4*, 498-502.
- 12) Yasufumi, U.; Keisuke, K.; Jian-Ren, S.; Nobuo, K. *Nature*, **2011**, *473*, 55-60.
- 13) (a) Rüttinger, Y.; Dismukes, G. C. *Chem. Rev.*, **1997**, *97*, 1-24; (b) Tommos, C.; Babcock, G. T. *Acc. Chem. Res.*, **1998**, *31*, 18-25; (c) Yagi, M.; Kaneko, M. *Chem. Rev.*, **2001**, *101*, 21; (d) Diner, B. A.; Rappaport, F. *Annu. Rev. Plant Biol.*, **2002**, *53*, 551-580; (e) Mukhopadhyay, S.; Mandal, S.K.; Bhaduri, S.; Armstrong, W. H. *Chem. Rev.*, **2004**, *104*, 3981-4026; (f) Haumann, M.; Müller, C.; Liebisch, P.; Iuzzolino, L.; Dittmer, J.; Grabolle, M.; Neisius, T.; Meyer-Klaucke, W.; Dau, H. *Biochemistry*, **2005**, *44*, 1894-1908; (g) McEvoy, J. P.; Brudvig, G. W. *Chem. Rev.*, **2006**, *106*, 4455-4483; (h) Kern, J.; Renger, G. *Photosynth. Res.*, **2007**, *94*, 183; (i) Renger, G. *Photosynth. Res.*, **2007**, *92*, 407-425.
- 14) Betley, T. A.; Wu, Q.; Van Voorhis, T.; Nocera, D. G. *Inorg. Chem.*, **2008**, *47*, 1849-1861.
- 15) (a) Brudvig, G. W.; Crabtree, R. H. *Proc. Natl. Acad. Sci. U.S.A.*, **1986**, *83*, 4586-4588. (b) Brudvig, G. W. *Phil. Trans. R. Soc. B* **2008**, *363*, 1211-1219. (c) Brudvig, G. W.; Thorp, H. H.; Crabtree, R. H. *Acc. Chem. Res.*, **1991**, *24*, 311-316.
- 16) (a) Dempsey, J. L.; Esswein, A. J.; Manke, D. R.; Rosenthal, J.; Soper, J. D.; Nocera, D. G., *Inorg. Chem.*, **2005**, *44*, 6879-6892; (b) Duan, L. *Artificial water splitting: ruthenium complexes for water oxidation*. KTH Chemical Science and Engineering, Royal Institute of Technology, Stockholm (2011).
- 17) Romain, S.; Bozoglian, F.; Sala, X.; Llobet, A. *J. Am. Chem. Soc.*, **2009**, *131*, 2768-2769.
- 18) Betley, T.A.; Surendranath, Y.; Childress, M.V.; Alliger, G.E.; Fu, R.; Cummins, C.C.; Nocera D.G. *Phil. Trans. R. Soc. B*, **2008**, *363*, 1293-1303.
- 19) Gilbert, J. A.; Eggleston, D. S.; Murphy, W. R.; Geselowitz, D. A.; Gersten, S. W.; Hodgson, D. J.; Meyer, T. J. *J. Am. Chem. Soc.* **1985**, *107*, 3855-3864.
- 20) (a) Concepcion, J.; Jurss, J. W.; Brennaman, M. K.; Hoertz, P. G.; Patrocínio, A. O. T.; Iha, N. Y. M.; Templeton, J. L.; Meyer, T. J. *Acc. Chem. Res.*, **2009**, *42*, 1954-1965; (b) Romain, S.; Vigara, L.; Llobet, A. *Acc. Chem. Res.*, **2009**, *42*, 1944-1953; (c) Romero, I.; Rodríguez, M.; Sens, C.; Mola, J.; Kollipara, M. R.; Francàs, L.; Mas-Marza, E.; Escriche, L.; Llobet, A. *Inorg. Chem.*, **2008**, *47*, 1824-1834. (d) Sens, C.; Romero, I.; Rodríguez, M.; Llobet, A.; Parella, P.; Benet-Buchholz, J. *J. Am. Chem. Soc.*, **2004**, *126*, 7798-7799; (e) Concepcion, J. J.; Jurss, J. W.; Templeton, J. L.; Meyer, T. J. *Proc. Natl. Acad. Sci. U.S.A.* **2008**, *105*, 17632-17635; (f) Sala, X.; Romero, I.; Rodríguez, M.; Escriche, L.; Llobet, A. *Angew. Chem., Int. Ed.* **2009**, *48*, 2842-2852; (g) Duan, L.; Fischer, A.; Xu, Y. H.; Sun, L. C. *J. Am. Chem. Soc.*, **2009**, *131*, 10397-10398; (h) Hurst, J. K.; Cape, J. L.; Clark, A. E.; Das, S.; Qin, C. Y. *Inorg. Chem.*, **2008**, *47*, 1753-1764; (i) Concepcion, J. C.; Jurss, J. W.; Norris, M. R.; Chen, Z.; Templeton, J. L.; Meyer, T. J. *Inorg. Chem.*, **2010**, *49*, 1277-1279. (j) Concepcion, J. J.; Tsai, M. K.; Muckerman, J. T.; Meyer, T. J. *J. Am. Chem. Soc.* **2010**, *132*, 1545-1557.
- 21) Bozoglian, F.; Romain, S.; Ertem, M.Z.; Todorova, T.K.; Sens, C.; Mola J.; Rodríguez, M.; Romero, I.; Benet-Buchholz, J.; Fontrodona, X.; Cramer, C.J.; Gagliardi, L.; Llobet, A. *J. Am. Chem. Soc.*, **2009**, *131*, 15176-15187.
- 22) (a) Binstead, R.A.; Chronister, C. W.; Ni, J.; Hartshorn, C. M.; Meyer, T. J. *J. Am. Chem. Soc.*, **2000**, *122*, 8464-8473; (b) Yamada, H.; Siems, W. F.; Koike, T.; Hurst, J. K. *J. Am. Chem. Soc.*, **2004**, *126*, 9786-9795; (c) Geselowitz, D.; Meyer, T. J. *Inorg. Chem.*, **1990**, *29*, 3894-3896.
- 23) Li, X.; Chen, G.; Schinzel, S.; Siegbahn, P.E.M. *Dalton Trans.*, **2011**, *40*, 11296-11307.
- 24) Zong, R.; Thummel, R. P. *J. Am. Chem. Soc.*, **2005**, *127*, 12802-12803.
- 25) Tseng, H.-W.; Zong, R.; Muckerman, J.T.; Thummel, R.P. *Inorg. Chem.*, **2008**, *47*, 11763-11773.
- 26) Concepcion, J. J.; Jurss, J. W.; Templeton, J. L.; Meyer, T. J. *J. Am. Chem. Soc.* **2008**, *130*, 16462-16463.
- 27) Wang, L.-P.; Wu, Q.; Voorhis, V.T.; *Inorg. Chem.* **2010**, *49*, 4543-4553.
- 28) Lin, X.; Hub, X.; Concepcion, J.J.; Chenc, Z.; Liud, S.; Meyer, T.J.; Yang, W. *Proc. Natl. Acad. Sci. U.S.A.*, **2012**, *109*, 15669-15672.
- 29) Chen, Z.; Concepcion J.J.; Hu, X.; Yang, W.; Hoertz, P.G.; Meyer T.J. *Proc Natl Acad Sci U S A.* **2010**, *107*, 7225-7229.
- 30) Badiei, Y. M.; Polyansky, D. E.; Muckerman, J. T.; Szalda, D. J.; Haberdar, R.; Zong, R.; Thummel, R. P.; Fujita, E. *Inorg. Chem.*, **2013**, *52*, 8845-8850.
- 31) Dobson, J.C.; Meyer, T.J.; *Inorg. Chem.* **1988**, *27*, 3283-3291.

- 32) Sala, X.; Ertem, M.Z.; Vigarà, L.; Todorova, T.K.; Chen, W.; Rocha, R.C.; Aquilante, F.; Cramer, C.J.; Gagliardi, L.; Llobet, A. *Angew. Chem. Int. Ed.* **2010**, *49*, 7745-7747.
- 33) (a) Kimoto, A.; Yamauchi, K.; Yoshida, M.; Masaoka, S.; Sakai, K. *Chem. Commun.*, **2012**, *48*, 239-241. (b) Yoshida, M.; Masaoka, S.; Abe, J.; Sakai, K. *Chem. Asian J.* **2010**, *5*, 2369-2378. (c) Masaoka, S.; Sakai, K. *Chem. Lett.* **2009**, *38*, 182-183.
- 34) Lòpez, I.; Ertem, M.Z.; Maji, S.; Benet-Buchholz, J.; Keidel, A.; Kuhlmann, U.; Hildebrandt, P.; Cramer, C.J.; Batista, V.S.; Llobet, A. *Angew. Chem. Int. Ed.* **2013**, *52*, 205-209.
- 35) Pushkar, Y.; Moonshiram, D.; Purohit, V.; Yan, L.; Alperovich, I.; *J. Am. Chem. Soc.* **2014**, *136*, 11938-11945.
- 36) McDaniel, N.D.; Coughlin, F. J.; Tinker, L.L.; Bernhard, S. *J. Am. Chem. Soc.* **2008**, *130*, 210-217.
- 37) Vilella, L.; Vidossich, P.; Balcells, D.; Lledós, A. *Dalton Trans.* **2011**, *40*, 11241-11247.
- 38) (a) Hull, J.F.; Balcells, D.; Blakemore, J.D.; Incarvito, C.D.; Eisenstein, O.; Brudvig, G.W.; Crabtree, R.H. *J. Am. Chem. Soc.*, **2009**, *131*, 8730-8731; (b) Blakemore, J.D.; Schley, N.D.; Balcells, D.; Hull, J.F.; Olack, G.W.; Incarvito, C.D.; Eisenstein, O.; Brudvig, G.W.; Crabtree, R.H. *J. Am. Chem. Soc.*, **2010**, *132*, 16017-16029.
- 39) Hettterscheid, D.G.H.; Reek, J.N.H. *Eur. J. Inorg. Chem.*, **2014**, *4*, 742-749.
- 40) Codolà, Z.; Cardoso, J.M.S.; Royo, B.; Costas, M.; Lloret-Fillol, J. *Chem. Eur. J.*, **2013**, *19*, 7203-7213
- 41) Graepner, J.; Hintermair, U.; Huang, D.L.; Thomsen, J.M.; Takase, M.; Campos, J.; Hashmi, S.M.; Elimelech, M.; Brudvig, G.W.; Crabtree, R.H. *Organometallics*, **2013**, *32*, 5384-5390.
- 42) Grotjahn, D. B.; Brown, D. B.; Martin, J. K.; Marelus, D. C.; Abadjian, M.-C.; Tran, H. N.; Kalyuzhny, G.; Vecchio, K. S.; Specht, Z. G.; Cortes-Llamas, S. A.; Miranda-Soto, V.; van Niekerk, C.; Moore, C. E.; Rheingold, A. L. *J. Am. Chem. Soc.*, **2011**, *133*, 19024-19027.
- 43) Savini, A.; Belanzoni, P.; Bellachioma, G.; Zuccaccia, C.; Zuccaccia, D.; Macchioni, A. *Green Chem.*, **2011**, *13*, 3360-3374.
- 44) Schley, N.D.; Blakemore, J. D.; Subbaiyan, N. K.; Incarvito, C. D.; D'Souza, F.; Crabtree, R. H.; Brudvig, G. W. *J. Am. Chem. Soc.*, **2011**, *133*, 10473-10481.
- 45) Blakemore, J.D.; Mara, M.W.; Kushner-Lenhoff, M.N.; Schley, N.D.; Konezny, S.J.; Rivalta, I.; Negre, C.F.A.; Snoeberger, R.C.; Kokhan, O.; Huang, J.; Stickrath, A.; Tran, L.A.; Parr, M.L.; Chen, L.X.; Tiede, D.M.; Batista, V.S.; Crabtree, R.H.; Brudvig, G.W. *Inorg. Chem.*, **2013**, *52*, 1860-1871.
- 46) Hintermair, U.; Sheehan, S. W.; Parent, A. R.; Ess, D. H.; Richens, D. T.; Vaccaro, P. H.; Brudvig, G. W.; Crabtree, R. H. *J. Am. Chem. Soc.*, **2013**, *135*, 10837-10851.
- 47) Wang, C.; Wang, J.-L.; Lin, W. *J. Am. Chem. Soc.*, **2012**, *134*, 19895-19908.
- 48) Liao, R.-Z.; Siegbahn, P.E.M. *ACS Catal.*, **2014**, *4*, 3937-3949.
- 49) Naruta, Y.; Sasayama, M.; Sasaki, T. *Angew. Chem. Int. Ed. Eng.* **1994**, *33*, 1839-1841.
- 50) Shimazaki, Y.; Nagano, T.; Takesue, H.; Ye, B.-H.; Tani, F.; Naruta, Y. *Angew. Chem., Int. Ed.* **2004**, *43*, 98-100.
- 51) Limburg, J.; Vrettos, J. S.; Liable-Sands, L. M.; Rheingold, A. L.; Crabtree, R. H.; Brudvig, G. W. *Science* **1999**, *283*, 1524-1527.
- 52) Limburg, J.; Vrettos, J. S.; Chen, H. Y.; de Paula, J. C.; Crabtree, R. H.; Brudvig, G. W. *J. Am. Chem. Soc.* **2001**, *123*, 423-430.
- 53) Lundberg, M.; Blomberg, M.R.A.; Siegbahn, P.E.M. *Inorg. Chem.* **2004**, *43*, 264-274.
- 54) Lundberg, M.; Siegbahn, P.E.M. *Chem. Phys. Lett.*, **2005**, *401*, 347-351.
- 55) Hatakeyama, M.; Nakata, H.; Wakabayashi, M.; Yokojima, S.; Nakamura, S. *J. Phys. Chem. A* **2012**, *116*, 7089-7097.
- 56) Vallés-Pardo, J.L.; de Groot, H. J. M.; Buda, F.; *Phys. Chem. Chem. Phys.*, **2012**, *14*, 15502-15508.
- 57) (a) Chen, H.; Faller, J. W.; Crabtree, R. H.; Brudvig, G. W. *J. Am. Chem. Soc.* **2004**, *126*, 7345-7349; (b) Chen, H.; Collomb, M.-N.; Duboc, C.; Blondin, G.; Rivière, E.; Faller, J. W.; Crabtree, R. H.; Brudvig, G. W. *Inorg. Chem.* **2005**, *44*, 9567-9573.
- 58) (a) Baffert, C.; Romain, S.; Richardot, A.; Lepretre, J.-C.; Lefebvre, B.; Deronzier, A.; Collomb, M.-N. *J. Am. Chem. Soc.* **2005**, *127*, 13694-13704; (b) Gao, Y.; Crabtree, R. H.; Brudvig, G. W. *Inorg. Chem.* **2012**, *51*, 4043-4050.
- 59) Yagi, M.; Narita, K. *J. Am. Chem. Soc.* **2004**, *126*, 8084-8085.
- 60) Baffert, C.; Collomb, M.-N.; Deronzier, A.; Kjaergaard-Knudsen, S.; Latour, J.-M.; Lund, K. H.; McKenzie, C. J.; Mortensen, M.; Preuss Nielsen, L.; Thorup, N. *Dalton Trans.* **2003**, *9*, 1765-1772.
- 61) (a) Poulsen, A. K.; Rempel, A.; McKenzie, C. J. *Angew. Chem., Int. Ed.* **2005**, *44*, 6916-6920; (b) Seidler-Egdal, R. K.; Nielsen, A.; Bond, A. D.; Bjerrum, M. J.; McKenzie, C. J. *Dalton Trans.* **2011**, *40*, 3849-3858.
- 62) Sameera, W.M.C.; McKenzie, C.J.; McGrady, J.E.; *Dalton Trans.*, **2011**, *40*, 3859-3870.
- 63) Gao, Y.; Liu, J.; Wang, M.; Na, Y.; Åkermark, B.; Sun, L. *Tetrahedron* **2007**, *63*, 1987.
- 64) Privalov, T.; Sun, L.; Åkermark, B.; Liu, J.; Gao, Y.; Wang, M. *Inorg. Chem.* **2007**, *46*, 7075-7086.
- 65) Ellis, W.; McDaniel, M. D.; Bernhard, S.; Collins, T. J. *J. Am. Chem. Soc.* **2010**, *132*, 10990-10991.
- 66) Panda, C.; Debgupta, J.; Díaz, D.D.; Singh, K.K.; Gupta, S.S.; Dhar, B.B. *J. Am. Chem. Soc.*, **2014**, *136*, 12273-12282.
- 67) (a) Ertem, M. Z.; Gagliardi, L.; Cramer, C. J. *Chem. Sci.* **2012**, *3*, 1293-1299; (b) Liao, R.-Z.; Li, X.-C.; Siegbahn, P. E. M. *Eur. J. Inorg. Chem.* **2014**, 728-741.
- 68) Fillol, J. L.; Cordolà, Z.; Garcia-Bosch, I.; Gómez, L.; Pla, J. J.; Costas, M. *Nat. Chem.* **2011**, *3*, 807-813.
- 69) Codolà, Z.; Garcia-Bosch, I.; Acuña-Parés, F.; Prat, I.; Luis, J. M.; Costas, M.; Lloret-Fillol, J. *Chem. Eur. J.* **2013**, *19*, 8042-8047.
- 70) Codolà, Z.; Gómez, L.; Kleespies, S.T.; Que L, Jr.; Costas, M.; Lloret-Fillol, J. *Nat Commun.* **2015**, *6*, 5865-5873.

- 71) Hong, D.; Mandal, S.; Yamada, Y.; Lee, Y.-M.; Nam, W.; Llobet, A.; Fukuzumi, S. *Inorg. Chem.*, **2013**, *52*, 9522-9531.
- 72) Tan, P.; Kwong, H.-K.; Lau, T.-C. *Chem. Commun.*, **2015**, *51*, 12189-12192.
- 73) To, W.-P.; Chow, T.W.-S.; Tse, C.-W.; Guan, X.; Huang, J.-S.; Che, C.-M. *Chem. Sci.*, **2015**, *6*, 5891-5903.
- 74) Wang, D.; Que L, Jr. *Chem. Commun.*, **2013**, *49*, 10682-10684.
- 75) Liu, Y.; Xiang, R.; Du, X.; Ding, Y.; Ma, B. *Chem. Commun.*, **2014**, *50*, 12779-12782.
- 76) (a) Elizarova, G. L.; Matvienko, L. G.; Lozhkina, N. V.; Parmon, V. N.; Zamaraev, K. I. *React. Kinet. Catal. Lett.* **1981**, *16*, 191-194; (b) Elizarova, G. L.; Matvienko, L. G.; Lozhkina, N. V.; Parmon, V. N. *React. Kinet. Catal. Lett.* **1984**, *26*, 67-72.
- 77) Kanan, M. W.; Nocera, D. G. *Science* **2008**, *321*, 1072-1075.
- 78) Jiao, F.; Frei, H. *Angew. Chem., Int. Ed.* **2009**, *48*, 1841-1844.
- 79) Yin, Q.; Tan, J. M.; Besson, C.; Geletti, Y. V.; Musaev, D. G.; Kuznetsov, A. E.; Luo, Z.; Hardcastle, K. I.; Hill, C. L. *Science*. **2010**, *328*, 342-345.
- 80) Wasylenko, D.J.; Ganesamoorthy, C.; Borau-Garcia, J.; Berlinguette, C.P. *Chem. Commun.*, **2011**, *47*, 4249-4251.
- 81) Wasylenko, D.J.; Palmer, R.D.; Schott E.; Berlinguette, C.P. *Chem. Commun.*, **2012**, *48*, 2107-2109.
- 82) Winkler, J. R.; Gray, H. B. *Struct. Bond.* **2012**, *142*, 17-28.
- 83) Crandell, D.W.; Ghosh, S.; Berlinguette C.P.; Baik, M.H. *ChemSusChem*. **2015**, *8*, 844-852.
- 84) Dowers, T.S.; Rock, D.A.; Rock, D.A.; Jones, J. P. *J. Am. Chem. Soc.* **2004**, *126*, 8868-8869.
- 85) Dogutan, D.K.; McGuire, R.; Nocera, D. G. *J. Am. Chem. Soc.*, **2011**, *133*, 9178-9180.
- 86) Ertem, M. Z.; Cramer, C. J. *Dalton Trans.*, **2012**, *41*, 12213-12219.
- 87) Lei, H.; Han, A.; Li, F.; Zhang, M.; Han, Y.; Du, P.; Lai, W.; Cao, R. *Phys. Chem. Chem. Phys.* **2014**, *16*, 1883-1893.
- 88) Rigsby, M. L.; Mandal, S.; Nam, W.; Spencer, L. C.; Llobet, A.; Stahl, S. S. *Chem. Sci.* **2012**, *3*, 3058-3062.
- 89) Wang, L.-P.; Voorhis, T.V. *J. Phys. Chem. Lett.* **2011**, *2*, 2200-2204.
- 90) Leung, C.-F.; Ng, S.-M.; Ko, C.-C.; Man, W.-L.; Wu, J.; Chen, L.; Lau, T.-C. *Energy Environ. Sci.* **2012**, *5*, 7903-7907.
- 91) Pizzolato, E.; Natali, M.; Posocco, B.; Montellano López, A.; Bazzan, I.; Di Valentin, M.; Galloni, P.; Conte, V.; Bonchio, M.; Scandola, F.; Sartorel, A. *Chem. Commun.* **2013**, *49*, 9941-9943.
- 92) Zhang, M.; Zhang, M.-T.; Hou, C.; Ke, Z.-F.; Lu, T.-B. *Angew Chem Int Ed Engl.* **2014**, *53*, 13042-13048.
- 93) Han, Y.; Wu, Y.; Lai, W.; Cao, R. *Inorg. Chem.*, **2015**, *54*, 5604-5613.
- 94) Wang, L.; Duan, L.; Ambre, R.B.; Quentin, D.; Chen, H.; Sun, J.; Das, B.; Thapper, A.; Uhlig, J.; Dinér, P.; Sun, L. *Journal of Catalysis*, **2016**, *335*, 72-78.
- 95) Barnett, S.M.; Goldberg, K.I.; Mayer, J.M. *Nature Chem.* **2012**, *4*, 498-502.
- 96) Zhang, M.-T.; Chen, Z.; Kang, P.; Meyer, T.J. *J. Am. Chem. Soc.*, **2013**, *135*, 2048-2051.
- 97) Zhang, T.; Wang, C.; Liu, S.; Wang, J.-L.; Lin, W. *J. Am. Chem. Soc.* **2014**, *136*, 273-281.
- 98) Garrido-Barros, P.; Funes-Ardoiz, I.; Drouet, S.; Benet-Buchholz, J.; Maseras, F.; Llobet, A. *J. Am. Chem. Soc.* **2015**, *137*, 6758-6761.
- 99) Su, X.-J.; Gao, M.; Jiao, L.; Liao, R.-Z.; Siegbahn, P.E.M.; Cheng, J.-P.; Zhang, M.-T. *Angew. Chem. Int. Ed.* **2015**, *54*, 4904-4909.
- 100) Pershad, H.R.; Duff, J. L. C.; Heering, H. A.; Duin, E. C.; Albracht, S. P. J.; Armstrong, F. A. *Biochemistry*, **1999**, *38*, 8992-8999.
- 101) a) Vignais, P.M.; Billoud, B.; Meyer, J. *FEMS Microbiol. Rev.*, **2001**, *25*, 455-501; b) Fontecilla-Camps, J.C.; Volbeda, A.; Cavazza, C.; Nicolet, Y. *Chem. Rev.*, **2007**, *107*, 4273-4303.
- 102) Cornish, A.J.; Gärtner, K.; Yang, H.; Peters, J.W.; Hegg, E.L. *J. Biol. Chem.* **2011**, *286*, 38341-38347.
- 103) Siegbahn, P.E.M.; Tye, J.W. Hall, M.B. *Chem. Rev.*, **2007**, *107*, 4414-4435.
- 104) Greco, C.; Bruschi, M.; De Gioia, L.; Ryde, U. *Inorg. Chem.*, **2007**, *46*, 5911-5921.
- 105) Lauermaun, G.; Häussinger, P.; Lohmüller, R.; Watson, A. M. 2013 Hydrogen, 1. Properties and Occurrence. Ullmann's Encyclopedia of Industrial Chemistry. 1-15.
- 106) Scott, M. S.; Idriss, H. Heterogeneous Catalysis for Hydrogen Production. Handbook of Green Chemistry. **2010**, *2*, 223-246.
- 107) Tard, C.; Pickett, C.J.; *Chem. Rev.*, **2009**, *109*, 2245-2274.
- 108) Xu, T.; Chen, D.; Hu, X.; *Coord. Chem. Rev.*, **2015**, *303*, 32-41.
- 109) Thoi, V.S.; Sun, Y.; Long, J.R.L.; Chang, C.J. *Chem. Soc. Rev.*, **2013**, *42*, 2388-2400.
- 110) Dutta, A.; Roberts, J.A.S.; Shaw, W.J.; *Angew. Chem. Int. Ed.* **2014**, *53*, 6487-6491.
- 111) Luca, O.R. Crabtree, R.H. *Chem. Soc. Rev.*, **2013**, *42*, 1440-1459.
- 112) (a) Canty, A. J.; Fritsche, S. D.; Jin, H.; Honeyman, R. T.; Skelton, B. W.; White, A. H. *J. Organomet. Chem.* **1996**, *510*, 281-286; (b) Canty, A. J.; Fritsche, S. D.; Jin, H.; Patel, J.; Skelton, B. W.; White, A. H. *Organometallics* **1997**, *16*, 2175-2182.
- 113) (a) Monaghan, P. K.; Puddephatt, R. J. *Inorg. Chim. Acta* **1982**, *65*, L59. (b) Monaghan, P. K.; Puddephatt, R. J. *Organometallics* **1984**, *3*, 444-449.
- 114) (a) Sakai, K.; Matsumoto, K. *J. Coord. Chem.* **1988**, *18*, 169-172; (b) K. Sakai, K. Matsumoto, *J. Mol. Catal.* **1990**, *62*, 1-14; (c) K. Sakai, Y. Kizaki, T. Tsubomura, K. Matsumoto, *J. Mol. Catal.* **1993**, *79*, 141-152; (d) K. Sakai, H. Ozawa, *Coord. Chem. Rev.* **2007**, *251*, 2753-2766.

- 115) Ogawa, M.; Ajayakumar, G.; Masaoka, S.; Kraatz, H.-B.; Sakai, K. *Chem. Eur. J.* **2011**, *17*, 1148-1162.
- 116) (a) Canty, A. J.; Fritsche, S. D.; Jin, H.; Skelton, B. W.; White, A. H. *J. Organomet. Chem.* **1995**, *490*, C18; (b) Canty, A. J.; van Koten, G. *Acc. Chem. Res.* **1995**, *28*, 406-413.
- 117) Milet, A.; Dedieu, A.; Canty, A.J. *Organometallics* **1997**, *16*, 5331-5341.
- 118) (a) James, B.R. *Coord. Chem. Rev.*, **1966**, *1*, 505-524. (b) Bakac, A.; *Dalton Trans.*, **2006**, 1589-1596.
- 119) Lehn, J.M.; Sauvage, J.P. *Nouv. J. Chim.* **1977**, *1*, 449-451.
- 120) (a) Brown, G.M.; Chan, S.F.Creutz, C.C.; Schwarz, H.A. Sutin, N. *J. Am. Chem. Soc.*, **1979**, *101*, 7638-7640; (b) Chan, S.F.; Chou, M.; Creutz, C.; Matsubara, T.; Sutin, N. *J. Am. Chem. Soc.* **1981**, *103*, 369-379.
- 121) Kirch, M.; Lehn, J.-M.; Sauvage, J.-P. *Helv. Chim. Acta.* **1979**, *62*, 1345-1384.
- 122) Cline, E.D.; Adamson, S.E.; Bernhard, S. *Inorg. Chem.* **2008**, *47*, 10378-10388.
- 123) Stoll, T.; Gennari, M.; Serrano, I.; Fortage, J.; Chauvin, J.; Odobel, F.; Rebarz, M.; Poizat, O.; Sliwa, M.; Deronzier, A.; Collomb, M.-N. *Chem. Eur. J.* **2013**, *19*, 782-792.
- 124) Kayanuma, M.; Stoll, T.; Daniel, C.; Odobel, F.; Fortage, J.; Deronzierbc, A.; Collomb, M.-N. *Phys.Chem.Chem.Phys.*, **2015**, *17*, 10497-10509.
- 125) Tanaka, S.; Masaoka, S.; Yamauchi, K.; Annaka, M.; Sakai, K. *Dalton Trans.* **2010**, *39*, 11218-11226.
- 126) Fisher, B.J.; Eisenberg, R. *J. Am. Chem. Soc.*, **1980**, *102*, 7361-7363.
- 127) R. M. Kellett and T. G. Spiro, *Inorg. Chem.*, 1985, *24*, 2373-2377.
- 128) R. Abdel-Hamid, H. M. El-Sagher, A. M. Abdel-Mawgoud and A. Nafady, *Polyhedron*, **1998**, *17*, 4535-4541.
- 129) McCrory, C. C. L.; Uyeda, C.; Peters, J. C. *J. Am. Chem. Soc.*, **2012**, *134*, 3164-3170.
- 130) Connolly, P.; Espenson, J. H. *Inorg. Chem.*, **1986**, *25*, 2684-2688.
- 131) Razavet, M.; Artero, V.; Fontecave, M. *Inorg. Chem.* **2005**, *44*, 4786-4795.
- 132) Solis, B. H.; Hammes-Schiffer, S. *Inorg. Chem.* **2014**, *53*, 6427-6443.
- 133) Solis, B. H.; Hammes-Schiffer, S. *Inorg. Chem.* **2011**, *50*, 11252-11262.
- 134) Muckerman, J. T.; Fujita, E. *Chem. Commun.* **2011**, *47*, 12456-12458.
- 135) (a) Jacques, P.-A.; Artero, V.; Pécaut, J.; Fontecave, M. *Proc. Natl. Acad. Sci. U.S.A* **2009**, *106*, 20627-20632; (b) Fourmond, V.; Jacques, P. A.; Fontecave, M.; Artero, V. *Inorg. Chem.* **2010**, *49*, 10338-10347.
- 136) Bhattacharjee, A.; Andréiadis, E.S.; Chavarot-Kerlidou, M.; Fontecave, M.; Field, M.J.; Artero, V. *Chem. Eur. J.* **2013**, *19*, 15166-15174.
- 137) Solis, B. H.; Hammes-Schiffer, S. *J. Am. Chem. Soc.* **2012**, *134*, 15253-15256.
- 138) Sun, Y.; Bigi, J. P.; Piro, N. A.; Tang, M. L.; Long, J. R.; Chang, C. J. *J. Am. Chem. Soc.*, **2011**, *133*, 9212-9215.
- 139) Singh, W. M.; Baine, T.; Kudo, S.; Tian, S.; Ma, X. A. N.; Zhou, H.; DeYonker, N. J.; Pham, T. C.; Bollinger, J. C.; Baker, D. L.; Yan, B.; Webster, C. E.; Zhao, X. *Angew. Chem., Int. Ed.* **2012**, *51*, 5941-5944.
- 140) Lewandowska-Andralojc, Anna, Baine, T.; Zhao, X.; Muckerman, J.T.; Fujita, E.; Polyansky, D. E. *Inorg Chem.* **2015**, *54*, 4310-4321.
- 141) Call, A.; Codolà, Z.; Acuña-Parés, F.; Lloret-Fillol, J. *Chem. Eur. J.* **2014**, *20*, 6171-6183.
- 142) Collin, J.P.; Jouaiti, A.; Sauvage, J.P. *Inorg. Chem.*, **1988**, *27*, 1986-1990.
- 143) Pool, D.H.; DuBois, D. L.; *J. Organomet. Chem.*, **2009**, *694*, 2858-2865.
- 144) M. Rakowski DuBois and D. L. DuBois, *Chem. Soc. Rev.*, **2009**, *38*, 62-72.
- 145) Wilson, A.D.; Newell, R. H.; McNevin, M. J.; Muckerman, J. T.; DuBois, M. R.; DuBois, D. L. *J. Am. Chem. Soc.*, **2005**, *128*, 358-366.
- 146) Dubois, M.R.; Dubois, D. L. *Acc. Chem. Res.*, **2009**, *42*, 1974-1982.
- 147) Bullock, R.M.; Appela, A.M.; Helm, M.L.; *Chem. Commun.*, **2014**, *50*, 3125-3143.
- 148) (a) Wilson, A. D.; Newell, R. H.; McNevin, M. J.; Muckerman, J. T.; DuBois, R.M.; DuBois, D. L. *J. Am. Chem. Soc.* **2006**, *128*, 358-366; (b) Wilson, A. D.; Shoemaker, R. K.; Miedaner, A.; Muckerman, J. T.; DuBois, D. L.; DuBois, R. M. *Proc. Natl. Acad. Sci. U.S.A.* **2007**, *104*, 6951-6956; (c) Chen, S.; Raugei, S.; Rousseau, R.; Dupuis, M.; Bullock, R. M. *J. Phys. Chem. A* **2010**, *114*, 12716-12724.
- 149) Fernandez, L.E.; Horvath, S.; Hammes-Schiffer, S. *J. Phys. Chem. Lett.* **2013**, *4*, 542-546.
- 150) Kilgore, U. J.; Roberts, J. A.; Pool, D. H.; Appel, A. M.; Stewart, M. P.; Rakowski DuBois, M.; Dougherty, W. G.; Kassel, W. S.; Bullock, R. M.; DuBois, D. L. *J. Am. Chem. Soc.* **2011**, *133*, 5861-5872.
- 151) Helm, M. L.; Stewart, M. P.; Bullock, R. M.; Rakowski DuBois, M.; DuBois, D. L. *Science* **2011**, *333*, 863-866.
- 152) Ho, M.-H.; Raugei, S.; Rousseau, R.; Dupuis, M.; Bullock, R.M. *J. Chem. Theory Comput.* **2013**, *9*, 3505-3514.
- 153) Luca, O. R.; Konezny, S.J. James; Blakemore, D.; Colosi, D. M.; Saha, S.; Brudvig, G.W.; Batista, V. S.; Crabtree, R. H. *New J. Chem.*, **2012**, *36*, 1149-1152.
- 154) Karunadasa, H. I.; Chang, C. J.; Long, J. R. *Nature*, **2010**, *464*, 1329-1333.
- 155) Thoi, V.S.; Karunadasa, H. I.; Surendranath, Y.; Long, J. R.; Chang, C. J. *Energy and Environ. Sci.* **2012**, *5*, 7762-7770.
- 156) Sundstrom, E.J.; Yang, X.; Thoi, V. S.; Karunadasa, H.I.; Chang, C.J.; Long, J. R. Head-Gordon, M. *J. Am. Chem. Soc.* **2012**, *134*, 5233-5242.
- 157) Eckenhoff, W.T.; Brennessel, W.W.; Eisenberg, R.; *Inorg. Chem.*, **2014**, *53*, 9860-9869.
- 158) Porcher, J.-P.; Fogeron, T.; Gomez-Mingot, M.; Derat, E.; Chamoreau, L.-M.; Li, Y.; Fontecave, M. *Angew Chem Int Ed Engl.* **2015**, *54*, 14090-14093.

- 159) Fu, L.-Z.; Fang, T.; Zhou, L.-L.; Zhan, S.-Z. *RSC Adv.*, **2014**, *4*, 53674-53680.
- 160) Zhou, L.-L.; Fang, T.; Cao, J.-P.; Zhu, Z.-H.; Su, X.-T.; Zhan, S.Z. *Journal of Power Sources*, **2015**, *273*, 298-304.
- 161) Fang, T.; Fu, L.-Z.; Zhou, L.-L.; Zhan, S.-Z. *Electrochimica Acta*, **2015**, *161*, 388-394.
- 162) Zhang, P.; Wang, M.; Yang, Y.; Yao, T.; Sun, L. *Angew. Chem. Int. Ed.* **2014**, *53*, 13803-13807.
- 163) Liao, R.Z.; Wang, M.; Sun, L.; Siegbahn, P.E. *Dalton Trans.* **2015**, *44*, 9736-9739.
- 164) Cramer, C. J. *Essentials of Computational Chemistry*, Chichester: John Wiley & Sons, Ltd., **2002**.
- 165) (a) Szabo, A.; Ostlund, N. S. *Modern quantum chemistry: introduction to advanced electronic structure theory*, Courier Dover Publication, **1996**; (b) Wang, Y. *Theoretical Studies on Water Splitting Using Transition Metal Complexes*, KTH Chemical Science and Engineering, Royal Institute of Technology, Stockholm (2014).
- 166) Møller, C.; Plesset, M. S. *Phys. Rev.*, **1934**, *46*, 618-622.
- 167) Pople, J.A. Seeger, R.; Krishnan, R. *Int. J. Quantum Chem.*, **1977**, *11*, 149-163.
- 168) (a) Werner, H.-J.; Knowles, P.J. *J. Chem. Phys.*, **1985**, *82*, 5053; (b) Knowles, P.J.; Werner, H.-J. *Chem. Phys. Lett.*, **1985**, *115*, 259-267.
- 169) Bartlett, R.J.; Purvis III, G.D. *Int. J. Quantum Chem.*, **1978**, *14*, 561-581.
- 171) (a) Thomas, L. H. *Proc. Cambridge Phil. Soc.*, **1927**, *23*, 542-548; (b) Fermi, E. *Rend. Accad. Naz. Lincei.*, **1927**, *6*, 602-607; (c) Dirac, P. A. M. *Proc. Cambridge Phil. Soc.*, **1930**, *26*, 376-385.
- 172) (a) Levine, I.N. *Química Cuántica*, Prentice Hall, **2001**. (b) Parr, R.G.; Yang, W. *Density-Functional Theory of Atoms and Molecules*, **1994**.
- 172) Hohenberg, P.; Kohn, W. *Phys. Rev.*, **1964**, *136*, B864-B871.
- 173) Kohn, W.; Sham, L.J. (1965). *Physical Review*, **1965**, *140*, A1133-A1138.
- 174) J. C. Slater, *The Self-Consistent Field for Molecular and Solids, Quantum Theory of Molecular and Solids, Vol. 4* (McGraw-Hill, New York, 1974).
- 175) Perdew, J. P. *Phys. Rev. B.*, **1986**, *33*, 8822-8824.
- 176) (a) Becke, A. D. *J. Chem. Phys.*, **1993**, *98*, 5648-5652; (b) Becke, A.D. *J. Chem. Phys.* **1993**, *98*, 1372-1377; (c) Lee, C.; Yang, W.; Parr, R. G. *Phys. Rev. B.*, **1988**, *37*, 785-789.
- 177) Truhlar, D. G.; Morokuma, K.; (eds.) **1999**, *Transition State Modelling for Catalysis*, ACS Symposium Series, 721, ACS, Washington, D. C.
- 178) (a) Siegbahn, P. E. *Electronic Structure Calculations for Molecules Containing Transition Metals* in *Advances in Chemical Physics XCIII*, Prigogine, I. and Rice (eds.), **1996** Wiley, Chichester. (b) Ziegler, T. *Density-Functional Theory as a Practical Tool in Studies of Transition Metal Chemistry and Catalysis 1997*, Springborg, M. (ed.), Wiley, Chichester.
- 179) (a) Curtiss, L.A.; Raghavachari, K.; Redfern, R.C.; Pople, J.A. *J. Chem. Phys.* **2000**, *112*, 7374-7383; (b) Curtiss, L. A.; Raghavachari, K.; Redfern, P. C.; Pople, J. A., *J. Chem. Phys.* **1997**, *106*, 1063-1079
- 180) Marenich, A.V. ; Cramer, C.J.; Truhlar, D.G. *J. Phys. Chem. B* **2009**, *113*, 6378-6396.
- 181) Grimme, S. *J. Comp. Chem.*, **2006**, *27*, 1787-1799.
- 182) Winget, P.; Cramer, C.J.; Truhlar, D.G. *Theor. Chem. Acc.* **2004**, *112*, 217-227.
- 183) Kelly, C.P.; Cramer, C.J.; Truhlar, D.G. *J. Phys. Chem. A* **2006**, *110*, 2493-2499.
- 184) a) Marcus, R.A. *Annu. Rev. Phys. Chem.* **1964**, *15*, 155-196; b) Marcus, R. A. *J. Chem. Phys.* **1956**, *24*, 966-978; c) Marcus, R. A. *J. Chem. Phys.* **1965**, *43*, 679-701.
- 185) Klimkans, A.; Larson, S. *Chem. Phys.* **1994**, *189*, 25-31.
- 186) Cramer, C.J.; Truhlar, D.G. *Phys. Chem. Chem. Phys.*, **2009**, *11*, 10757-10816.
- 187) a) Swart, M; Güell, M.; Luis, J.M.; Solà, M. *J. Phys. Chem. A* **2010**, *114*, 7191-7197. b) Yamaguchi, K.; Jensen, F.; Dorigo, A.; Houk, K. N. *Chem. Phys. Lett.* **1988**, *149*, 537-542. c) Wittbrodt, J. M.; Schlegel, H. B. *J. Chem. Phys.* **1996**, *105*, 6574-6577.
- 188) Noodleman, L.; Peng, C.Y.; Case, D.A.; Mouesca, J. -M. *Coord. Chem. Rev.*, **1995**, *144*, 199-244.
- 189) Harvey, J.N. *Struct. Bonding*, **2004**, *112*, 151-183.
- 190) Neese, F.; *Coord. Chem. Rev.*, **2009**, *253*, 526-563.
- 191) Garcia-Bosch, I.; Codolà, Z.; Prat, I.; Ribas, X.; Lloret-Fillol, J. Costas, M. *Chem. Eur. J.* **2012**, *18*, 13269-13273.
- 192) Kozuch, S.; Shaik, S. *Acc. Chem. Res.* **2010**, *44*, 101-110.
- 193) Gaussian 09, Revision A.1, Frisch, M. J.; Trucks, G. W.; Schlegel, H. B.; Scuseria, G. E.; Robb, M. A.; Cheeseman, J. R.; Scalmani, G.; Barone, V.; Mennucci, B.; Petersson, G. A.; Nakatsuji, H.; Caricato, M.; Li, X.; Hratchian, H. P.; Izmaylov, A. F.; Bloino, J.; Zheng, G.; Sonnenberg, J. L.; Hada, M.; Ehara, M.; Toyota, K.; Fukuda, R.; Hasegawa, J.; Ishida, M.; Nakajima, T.; Honda, Y.; Kitao, O.; Nakai, H.; Vreven, T.; Montgomery, Jr., J. A.; Peralta, J. E.; Ogliaro, F.; Bearpark, M.; Heyd, J. J.; Brothers, E.; Kudin, K. N.; Staroverov, V. N.; Kobayashi, R.; Normand, J.; Raghavachari, K.; Rendell, A.; Burant, J. C.; Iyengar, S. S.; Tomasi, J.; Cossi, M.; Rega, N.; Millam, J. M.; Klene, M.; Knox, J. E.; Cross, J. B.; Bakken, V.; Adamo, C.; Jaramillo, J.; Gomperts, R.; Stratmann, R. E.; Yazyev, O.; Austin, A. J.; Cammi, R.; Pomelli, C.; Ochterski, J. W.; Martin, R. L.; Morokuma, K.; Zakrzewski, V. G.; Voth, G. A.; Salvador, P.; Dannenberg, J. J.; Dapprich, S.; Daniels, A. D.; Farkas, Ö.; Foresman, J. B.; Ortiz, J. V.; Cioslowski, J.; Fox, D. J. Gaussian, Inc., Wallingford CT, **2009**.
- 194) Ribeiro, R.F.; Marenich, A.V.; Cramer, C.J.; Truhlar, D.G. *J Phys. Chem. B* **2011**, *115*, 14556-14562.
- 195) Vigara, L.; Ertem, M.Z.; Planas, N.; Bozoglian, F.; Leidel, N.; Dau, H.; Haumann, M.; Gagliardi, L.; Cramer, C.J.; Llobet, A. *Chem. Sci.* **2012**, *3*, 2576-2586.
- 196) Bianco, R.; Hay, P.J.; Hynes, J.T.J. *Phys. Chem. A*, **2011**, *115*, 8003-8016.

- 197) Hirahara, M.; Ertem, M.Z.; Komi, M.; Yamasaki, H.; Cramer, C.J.; Yagi, M. *Inorg. Chem.* **2013**, *52*, 6354-6364.
- 198) Vardhaman, A.K.; Sastri, C.V.; Kumar, D.; de Visser, S.P. *Chem. Commun.* **2011**, *47*, 11044-11046.
- 199) de Visser, S.P.; Quesne, M.G.; Martín, B.; Comba, P.; Ryde, U. *Chem. Commun.* **2014**, *50*, 262-282.
- 200) (a) Isse, A.A.; Gennaro, A. *J. Phys. Chem. B*, **2010**, *114*, 7894-7899; (b) Winget, P.; Cramer, C.J.; Truhlar, D.G. *J. Phys. Chem. B* **2007**, *111*, 408-422; (c) Baik, M.H.; Friesner, R.A. *J. Phys. Chem. A* **2002**, *106*, 7407-7412; (d) Bartmess, J.E. *J. Phys. Chem.* **1994**, *98*, 6420-6424.
- 201) Acuña-Parés, F.; Codolà, Z.; Costas, M.; Luis, J.M.; Lloret-Fillol, J. *Chem. Eur. J.* **2014**, *20*, 5696-5707.
- 202) Wadsworth, E.; Duke, F.R.; Goetz, C.A. *Anal. Chem.* **1957**, *29*, 1824-1825.
- 203) The IRC calculations on **TS(II-III)_a** for complex **1** show that the **III_a** intermediate is a minima in the lower energy reaction pathway. However, these species are not minima in the free-energy scale. This fact reveals the asynchronicity in which the proton transfer and the O-O bond-formation events take place.
- 204) Bassan, A.; Blomberg, M.R.; Siegbahn, P.E.M.; Que, L. Jr. *J. Am. Chem. Soc.* **2002**, *124*, 11056-11063.
- 205) Prat, I.; Company, A.; Postils, V.; Ribas, X.; Que, L.; Luis, J.M.; Costas, M. *Chem. Eur. J.* **2013**, *19*, 6724-6738.
- 206) Hirao, H.; Li, F.; Que, L.; Morokuma, K. *Inorg. Chem.* **2011**, *50*, 6637-6648.
- 207) The redox potential for water oxidation to O₂ production carried out at pH = 1.0 is 1.17 V. The redox potential that we set for Ce^{IV}/Ce^{III} is 1.72 V, at the same pH. This leads a total exergonicity for the entire water oxidation process of 50.7 kcal·mol⁻¹. As expected the experimental and theoretical (46.5 kcal·mol⁻¹) driving force for water oxidation are in good agreement.
- 208) Kasapbasi, E. E.; Whangbo, M.H. *Inorg. Chem.* **2012**, *51*, 10850-10855.
- 209) Kundu, S.; Matito, E.; Walleck, S.; Pfaff, F. F.; Heims, F.; Rábay, B.; Luis, J. M.; Company, A.; Braun, B.; Glaser, T.; Ray, K. *Chem. Eur. J.* **2012**, *18*, 2787-2791.
- 210) Kodera, M.; Kawahara, Y.; Hitomi, Y.; Nomura, T.; Ogura, T.; Kobayashi, Y.; *J Am Chem Soc.* **2012**, *134*, 13236-13239.
- 211) Parent, A.R.; Nakazono, T.; Lin, S.; Utsunomiya, S.; Sakai, K. *Dalton Trans.*, **2014**, *43*, 12501-12513.
- 212) Due to the extraordinary magnitude of the energy barrier and the very similar free energy between the two possible *cis*-Fe^{IV}(O)(OH₂)(Pytacn) tautomers ($\Delta G = 0.2$ kcal·mol⁻¹), only one catalytic potential tautomer has been considered. We selected the most stable one, in which the Fe=O moiety is in *trans* relative position to one of the Me-substituted amines (**a**). We also selected the tautomer **a** for comparison proposals, because this is the most stable form for the *cis*-Fe^{IV}(O)(OH)(Pytacn) complex (see next section).
- 213) Acuña-Parés, F.; Costas, M.; Luis, J. M.; Lloret-Fillol, J. *Inorg. Chem.* **2014**, *53*, 5474-5485.
- 214) Comba, P.; Rajaraman, G.; Rohwer, H. *Inorg. Chem.* **2007**, *46*, 3826-3838.
- 215) Lundberg, M.; Borowski, T. *Coord. Chem. Rev.* **2013**, *257*, 277-289.
- 216) Barone, V.; Cossi, M. *J. Phys. Chem. A* **1998**, *102*, 1995-2001.
- 217) Bell, R. P. (1973), *The Proton in Chemistry* (2nd ed.), Ithaca, NY: Cornell University Press.
- 218) (a) Hetterscheid, D.; Kotttrup, K. *Chem. Commun.*, **2015**, DOI: 10.1039/C5CC10092E; (b) Hitomi, Y.; Arakawa, K.; Funabiki, T.; Kodera, M. *Angew. Chem. Int. Ed.* **2012**, *51*, 3448-3452.
- 219)
- 220) Coggins, M. K.; Zhang, M. T.; Vannucci, A. K.; Dares, C. J.; Meyer, T. J. *J. Am. Chem. Soc.* **2014**, *136*, 5531-5534.
- 221) Codolà, Z.; Acuña-Parés, F.; Casadevall, C.; Luis, J.M.; Costas, M.; Lloret-Fillol, J., *unpublished results*.
- 222) Shaik, S.; Kumar, D.; de Visser, S.P.; Altun, A.; Thiel, W. *Chem Rev.* **2005**, *105*, 2279-2328.
- 223) Chen, H.; Lai, W.; Yao, J.; Shaik, S. *J. Chem. Theory Comput.* **2011**, *7*, 3049-3053.
- 224) Czarnecki, K.; Nimri, S.; Gross, Z.; Proniewicz, L.M.; Kincaid, J.R. *J. Am. Chem. Soc.* **1996**, *118*, 2929-2935.
- 225) Shen, J.-R. *Annu. Rev. Plant Biol.* **2015**, *66*, 4.1-4.26.
- 226) a) Saito, K.; Ishikita, H. *Biochim. Biophys. Acta* **2014**, *1837*, 159-166. b) Siegbahn, P.E. *Phys. Chem. Chem. Phys.* **2014**, *16*, 11893-11900.
- 227) Kawakami, K.; Umena, Y.; Kamiya, N.; Shen, J.R. *J. Photochem. Photobiol. B* **2011**, *104*, 9-18.
- 228) Fukuzumi, S.; Itoh, S. *Antioxid. Redox Signaling* **2001**, *3*, 807-824.
- 229) (a) Koua, F.H.; Umena, Y.; Kawakami, K.; Shen, J.R. *Proc Natl Acad Sci U S A* **2013**, *110*, 3889-3894; (b) Ugur, I.; William, R.A.; Kaila, V.R. *Biochim Biophys Acta* **2016**, DOI: 10.1016/j.bbabi.2016.01.015.
- 230) Fukuzumi, S.; Ohkubo, K.; Lee, Y.-M.; Nam, W. *Chem. Eur. J.* **2015**, *21*, 17548-17559.
- 231) Ma, L.; Lam, W.W.; Lo, P.K.; Lau, K.C.; Lau, T.C. *Angew. Chem. Int. Ed.* **2016**, *55*, 3012-3016.
- 232) Wasylenko, D.J.; Ganesamoorthy, C.; Koivisto, B.D.; Osthoff, H.D.; Berlinguette, C.P. *J. Am. Chem. Soc.* **2010**, *45*, 16094-16106.
- 233) Gaussian 09, Revision D.01, Frisch, M. J.; Trucks, G. W.; Schlegel, H. B.; Scuseria, G. E.; Robb, M. A.; Cheeseman, J. R.; Scalmani, G.; Barone, V.; Mennucci, B.; Petersson, G. A.; Nakatsuji, H.; Caricato, M.; Li, X.; Hratchian, H. P.; Izmaylov, A. F.; Bloino, J.; Zheng, G.; Sonnenberg, J. L.; Hada, M.; Ehara, M.; Toyota, K.; Fukuda, R.; Hasegawa, J.; Ishida, M.; Nakajima, T.; Honda, Y.; Kitao, O.; Nakai, H.; Vreven, T.; Montgomery, Jr., J. A.; Peralta, J. E.; Ogliaro, F.; Bearpark, M.; Heyd, J. J.; Brothers, E.; Kudin, K. N.; Staroverov, V. N.; Kobayashi, R.; Normand, J.; Raghavachari, K.; Rendell, A.; Burant, J. C.; Iyengar, S. S.; Tomasi, J.; Cossi, M.; Rega, N.; Millam, J. M.; Klene, M.; Knox, J. E.; Cross, J. B.; Bakken, V.; Adamo, C.; Jaramillo, J.; Gomperts, R.; Stratmann, R. E.; Yazyev, O.; Austin, A. J.; Cammi, R.; Pomelli, C.; Ochterski, J. W.; Martin, R. L.; Morokuma, K.; Zakrzewski, V. G.; Voth, G. A.; Salvador, P.; Dannenberg, J. J.

- Dapprich, S.; Daniels, A. D.; Farkas, Ö.; Foresman, J. B.; Ortiz, J. V.; Cioslowski, J.; Fox, D. J. Gaussian, Inc., Wallingford CT, **2009**.
- 234) a) Becke, A. D. *Phys. Rev. A*, **1988**, *38*, 3098-3100; b) Perdew, J.P. *Phys. Rev. B*, **1986**, *33*, 8822-8224.
- 235) Grimme, S.; Ehrlich, S.; L. Goerigk, L. *J. Comp. Chem.* **2011**, *32*, 1456-1465.
- 236) Dunlap, B. I. *J. Mol. Struct. (Theochem)*, **2000**, *529*, 37-40.
- 237) Poater, A. Vummaletti, S.V.C., Cavallo, L. *Dalton Trans.*, **2014**, *43*, 11190-11194.
- 238) a) Blaustein, B.D.; Gryder, J.W. *J. Am. Chem. Soc.*, **1957**, *79*, 540-547. b) Miller, J.T.; Irish, D.E. *Canadian Journal of Chemistry* **1967**, *45*, 147-155. c) Nelson, D.L.; Irish, D.E. *J. Chem. Soc., Faraday Trans. 1*, **1973**, *69*, 156-160. d) Kanno, H.; Hiraishi, J. *J. Phys. Chem.*, **1984**, *88*, 2787-2792.
- 239) Tuazon, Lourdes Ocampo, "The nature of cerium (IV) in aqueous nitric acid solution" (1959). *Retrospective Theses and Dissertations*. Paper 2167.
- 240) Ikeda-Ohno A.; Tsushima S.; Hennig C.; Yaita T.; Bernhard G. *Dalton Trans.*, **2012**, *41*, 7190-7192.
- 241) Demars, T.J.; Bera, M.K.; Seifert, S.; Antonio, M.R.; Ellis R.J. *Angew Chem Int Ed. Engl.*, **2015**, *54*, 7534-7538.
- 242) Lutz, O.M.D.; Hofer, T. S.; Randolf, B. R.; Weiss, A. K. H.; Rodenorg, B. M. *Inorg. Chem.* **2012**, *51*, 6746-6752.
- 243) a) Dinescu, A.; Clark, A.E. *J. Phys. Chem. A* **2008**, *112*, 11198-11206. b) Lutz, O.M.D.; Hofer, T.S.; Randolf, B.R.; Bernd, R.; Rode, M. *Chem Phys Lett.* **2012**, *539-540*, 50-53.
- 244) Smith, G.F.; Getz, C.A. *Ind. Eng. Chem. Anal. Ed.*, **1940**, *12*, 339-340.
- 245) Wong, C.L.; Kochi, J.K. *J. Am. Chem. Soc.*, **1979**, *101*, 5593-5603.
- 246) Gamba, I. et. al. *Unpublished results*.
- 247) Codolà Duch, Zoel. Iron and Iridium complex for water oxidation catalysis [online]. Girona: Universitat de Girona. Chemistry Department, 2014. <<http://hdl.handle.net/10803/276172>> [Consult: 11 July 2014].
- 248) Codola, Z.; Lloret-Fillol, J.; Costas, M. *Prog. in Inorg. Chem.* Vol. 59, John Wiley & Sons, Inc., **2014**, 447-532.
- 249) Prat, I.; Mathieson, J.S.; Güell, M.; Ribas, X.; Luis, J.M.; Cronin, J.; Costas, M. *Nat. Chem.*, **2011**, *3*, 788-793.
- 250) (a) Bassan, A.; Blomberg, M. R. A.; Siegbahn, P. E. M.; Que, L. Jr. *Angew. Chem. Int. Ed.* **2005**, *44*, 2939-2941; (b) Chen, K.; Costas, M.; Kim, J.; Tipton, A.K.; Que, L. Jr. *J. Am. Chem. Soc.* **2002**, *124*, 3026-3035.
- 251) Dehestani, A.; Lam, W.H.; Hrovat, D.A.; Davidson, E.R.; Borden, W.T.; Mayer, J.M. *J. Am. Chem. Soc.* **2005**, *127*, 3423-3432.
- 252) (a) Collman, J.P.; Slaughter, L.M.; Eberspacher, T.A.; Strassner, T.; Brauman, J.I. *Inorg. Chem.* **2001**, *40*, 6272-6280; (b) Bi, S.; Wang, J.; Liu, L.; Li, P.; Lin, Z. *Organometallics*, **2012**, *31*, 6139-6147.
- 253) Hassanpour, A.; Acuña-Parés, F.; Luis, J.M.; Cusso, O.; Morales de la Rosa, S.; Campos-Martín, J.M.; Fierro, J.L.G.; Costas, M.; Lloret-Fillol, J.; Mas-Ballesté, R. *Chem. Commun.* **2015**, *51*, 14992-14995.
- 254) Wang, Y.; Janardanan, D.; Usharani, D.; Han, K.; Que, L. Jr.; Shaik, S. *ACS Catal.* **2013**, *3*, 1334-1341.
- 255) Gaussian 09, Revision C.01, Frisch, M. J.; Trucks, G. W.; Schlegel, H. B.; Scuseria, G. E.; Robb, M. A.; Cheeseman, J. R.; Scalmani, G.; Barone, V.; Mennucci, B.; Petersson, G. A.; Nakatsuji, H.; Caricato, M.; Li, X.; Hratchian, H. P.; Izmaylov, A. F.; Bloino, J.; Zheng, G.; Sonnenberg, J. L.; Hada, M.; Ehara, M.; Toyota, K.; Fukuda, R.; Hasegawa, J.; Ishida, M.; Nakajima, T.; Honda, Y.; Kitao, O.; Nakai, H.; Vreven, T.; Montgomery, Jr., J. A.; Peralta, J. E.; Ogliaro, F.; Bearpark, M.; Heyd, J. J.; Brothers, E.; Kudin, K. N.; Staroverov, V. N.; Kobayashi, R.; Normand, J.; Raghavachari, K.; Rendell, A.; Burant, J. C.; Iyengar, S. S.; Tomasi, J.; Cossi, M.; Rega, N.; Millam, J. M.; Klene, M.; Knox, J. E.; Cross, J. B.; Bakken, V.; Adamo, C.; Jaramillo, J.; Gomperts, R.; Stratmann, R. E.; Yazyev, O.; Austin, A. J.; Cammi, R.; Pomelli, C.; Ochterski, J. W.; Martin, R. L.; Morokuma, K.; Zakrzewski, V. G.; Voth, G. A.; Salvador, P.; Dannenberg, J. J.; Dapprich, S.; Daniels, A. D.; Farkas, Ö.; Foresman, J. B.; Ortiz, J. V.; Cioslowski, J.; Fox, D. J. Gaussian, Inc., Wallingford CT, **2009**.
- 256) (a) NBO Version 3.1, E. D. Glendening, A. E. Reed, J. E. Carpenter, and F. Weinhold; (b) Foster, J.P.; Weinhold, F. *J. Am. Chem. Soc.* **1980**, *102*, 7211-7218.
- 257) (a) Pearson, R. *J. Chem. Sci.*, **2005**, *117*, 369-377; (b) Pearson, R. *J. Chem. Educ.* **1968**, *45*, 581-587.
- 258) Jurss, J.W.; Khnayzer, R.S.; Panetier, J.A.; El Roz, K.A.; Nichols, E.M.; Head-Gordon, M.; Long, J.R.; Castellano, F.N.; Chang, C.J. *Chem. Sci.* **2015**, *6*, 4954-4972.
- 259) (a) Solis, B.H.; Hammes-Schiffer, S. *J. Am. Chem. Soc.* **2011**, *133*, 19036-19039; (b) Solis, B.H.; Yu, Y.; Hammes-Schiffer, S. *Inorg. Chem.* **2013**, *52*, 6994-6999; (c) Jiang, Y.-K.; Liu, J.-H. *Int. J. Quantum Chem.*, **2012**, *112*, 2541-2614.
- 260) Virca, C.N.; McCormick, T. M. *Dalton Trans.*, **2015**, *44*, 14333-14340.
- 261) Liu, Y.-C.; Chu, K.-T.; Jhang, R.-L.; Lee, G.-H.; Chiang, M.-H. *Chem. Commun.*, **2013**, *49*, 4743-4745.
- 262) Xie, J.; Zhou, Q.; Li, C.; Wang, W.; Hou, Y.; Zhang, B.; Wang, X. *Chem. Commun.* **2014**, *50*, 6520-6522.
- 263) Warren, J. J.; Tronic, T. A.; Mayer, J. M. *Chem. Rev.* **2010**, *110*, 6961-7001.
- 264) Xue, L.; Ahlquist, M.S.G. *Inorg. Chem.* **2014**, *53*, 3281-3289.
- 265) Sutin, N. *Acc. Chem. Res.* **1982**, *15*, 275-282.
- 266) Heiden, Z.M.; Lathem, A.P. *Organometallics*, **2015**, *34*, 1818-1827.
- 267) (a) Matsubara, Y.; Fujita, E.; Doherty, M. D.; Muckerman, J. T.; Creutz, C. *J. Am. Chem. Soc.* **2012**, *134*, 15743-15757; (b) Muckerman, J.T.; Achord, P.; Creutz, C.; Polyansky, D.E.; Fujita, E. *Proc. Natl. Acad. Sci. U.S.A.* **2012**, *109*, 15657-15662.
- 268) Galan, B. R.; Schoffel, J.; Linehan, J. C.; Seu, C.; Appel, A. M.; Roberts, J. A.; Helm, M. L.; Kilgore, U. J.; Yang, J. Y.; DuBois, D. L.; Kubiak, C. P. *J. Am. Chem. Soc.* **2011**, *133*, 12767-12779.

- 269) Price, A.J.; Ciancanelli, R.; Noll, B.C.; Curtis, C.J.; DuBois, D.L.; DuBois, M.R. *Organometallics* **2002**, *21*, 4833-4839.
- 270) Siewert, I. *Chem. Eur. J.* **2015**, DOI: 10.1002/chem.201501684.
- 271) Nippe, M.; Khnayzer, R.S.; Panetier, J.A.; Zee, D.Z.; Olaiya, B.S.; Head-Gordon, M.; Chang, C.J.; Castellano, F.N.; Long, J.R. *Chem. Sci.* **2013**, *4*, 3934-3945.
- 272) Schlimgen, A.W.; Heaps, C.W.; Mazziotti, D.A. *J. Phys. Chem. Lett.* **2016**, *7*, 627-631.
- 273) Tong, L.; Zong, R.; Thummel, R. P. *J. Am. Chem. Soc.* **2014**, *136*, 4881-4884.
- 274) Zhang, P.; Wang, M.; Gloaguen, F.; Chen, L.; Quentel, F.; Sun, L. *Chem. Commun.* **2013**, *49*, 9455-9457.
- 275) Brown, G. M.; Brunshwig, B. S.; Creutz, C.; Endicott, J. F.; Sutin, N. *J. Am. Chem. Soc.* **1979**, *101*, 1298-1300.
- 276) Krishnan, C. V.; Sutin, N. *J. Am. Chem. Soc.* **1981**, *103*, 2141-2142.
- 277) Khnayzer, R. S.; Thoi, V. S.; Nippe, M.; King, A. E.; Jurss, J. W.; El Roz, K. A.; Long, J. R.; Chang, C. J.; Castellano, F. N. *Energy Environ. Sci.* **2014**, *7*, 1477-1488.
- 278) Singh, W. M.; Mirmohades, M.; Jane, R. T.; White, T. A.; Hammarstrom, L.; Thapper, A.; Lomoth, R.; Ott, S. *Chem. Commun.* **2013**, *49*, 8638-8640.
- 279) Shan, B.; Baine, T.; Ma, X. A. N.; Zhao, X.; Schmehl, R. H. *Inorg. Chem.* **2013**, *52*, 4853-4859.
- 280) Rodenberg, A.; Oraziotti, M.; Probst, B.; Bachmann, C.; Alberto, R.; Baldrige, K. K.; Hamm, P. *Inorg. Chem.* **2015**, *54*, 646-657.
- 281) Varma, S.; Castillo, C. E.; Stoll, T.; Fortage, J.; Blackman, A. G.; Molton, F.; Deronzier, A.; Collomb, M.-N. *Phys. Chem. Chem. Phys.* **2013**, *15*, 17544-17552.
- 282) Mayer, I. *Int. J. Quantum Chem.*, **1984**, *26*, 151-154.
- 283) Mayer, I. *Chem. Phys. Lett.*, **1983**, *97*, 270-274.
- 284) (a) Neubauer, A.; Grell, G.; Friedrich, A.; Bokarev, S.I.; Schwarzbach, P.; Gärtner, F.; Surkus, A.-E.; Junge, H.; Beller, M.; Kühn, O.; Lochbrunner, S. *J. Phys. Chem. Lett.* **2014**, *5*, 1355-1360; (b) Bokarev S.I.; Hollmann, D.; Pazidis, A.; Neubauer, A.; Radnik, J.; Kuehn, O.; Lochbrunner, S.; Junge, H.; Beller, M.; Brueckner, A. *Phys. Chem. Chem. Phys.*, **2014**, *16*, 4789-4796.
- 285) Sandhya, K. S.; Suresh, C.H. *Dalton Trans.* **2014**, *43*, 12279-12287.